UTPP-33

MEASUREMENT OF THE INTERMEDIATE-VECTOR-BOSON PRODUCTION CROSS SECTION AND MASS AT THE FERMILAB PROTON-ANTIPROTON COLLIDER

January 1989

Youhei Morita

Submitted in partial fulfillment of the requirements
for the degree of Doctor of Science
in Doctoral program in
University of Tsukuba

UTPP–33

MEASUREMENT OF THE INTERMEDIATE-VECTOR-BOSON PRODUCTION CROSS SECTION AND MASS AT THE FERMILAB PROTON-ANTIPROTON COLLIDER

January 1989

Youhei Morita

Submitted in partial fulfillment of the requirements

for the degree of Doctor of Science

in Doctoral program in

University of Tsukuba

Abstract

Production cross sections and masses of the charged and the neutral intermediate vector bosons (IVB's) have been determined through their electron decay channel using the CDF detector at the Fermilab Tevatron, which is the world largest $\bar{p}p$ collider at the moment. These are the first measurements of this kind at $\sqrt{s}$ = 1.8 TeV. The data correspond to a total integrated luminosity of 27.4 nb^{-1}. A total of 31 events were observed as candidates of the $W \rightarrow e\nu$ decay in the pseudorapidity range $|\eta| < 2.3$ and 6 events as candidates of the $Z^0 \rightarrow e^+e^-$ decay. The measured production cross sections of the IVB's are compared with those which were measured at the UA1/UA2 experiments at $\sqrt{s}$ = 546 GeV and 630 GeV, and the results are in good agreement with the expectations from the Standard Model predictions and the Q^2-evolution of the parton distribution functions.

In recent high energy experiments such as in the hadron colliders, the electromagnetic calorimeters play an important role because of their superior energy resolution for high energy electrons. The identification of electrons is an essential key in the hadron collider experiments, especially in studying the electroweak sector of the Standard Model, or its counter part in the Supersymmetry Theory if such symmetry were to exist. As shown by the UA1/UA2 experiments at CERN in 1984, $\bar{p}p$-collider experiments have proven the capability of investigating the high mass objects, such as the W/Z bosons, via their electronic decay channels.

The CDF detector has three components of the electromagnetic calorimeters. The Central electromagnetic calorimeter covers the pseudorapidity range of -1.1 to +1.1, while the Endplug covers –2.4 to –1.1 and +1.1 to +2.4, and the forward/backward electromagnetic detectors covers –4.0 to –2.4 and +2.4 to +4.0, respectively. By using the Central and the Endplug calorimeters, 76% of the electron from the $W \rightarrow e\nu$ decay and 37% of the $Z^0 \rightarrow e^+e^-$ decay can be detected. These numbers should be compared to the ones which are obtained when we use the Central calorimeter only; 49% for $W \rightarrow e\nu$ and 22% for $Z^0 \rightarrow e^+e^-$, respectively. (These numbers reflect the geometric acceptance only.) Therefore the data from the Endplug calorimeter is essential to increase the statistics and to provide a wider range in measuring the angular distribution of the electrons.

The Endplug electromagnetic calorimeter consists of 34 layers of lead sheets and proportional chambers. Each proportional chamber consists of a planer array of proportional counters made of conductive plastic tube cathode, and pick-up electrodes placed outside the array. The DC field is formed between the anode wire and the conductive plastic tube, while the RF signals are picked up by the readout electrodes outside the tubes. This tube structure enabled us to form rigid proportional chambers with optimized pattern of readout electrodes. The outline of electrodes are not restricted by the shape of the cathode tubes, and therefore a complete projective tower geometry has been achieved with minimal dead region. This fine and versatile segmentation of the readout channels allows us to help discriminating the electromagnetic shower from the hadronic shower, as described below.

Due to the huge difference in the cross section between the QCD process and the IVB production with subsequent semi-leptonic decay, the discrimination of the fake electron signal which is caused by the overlapping of photons with charged hadrons becomes crucial. The cuts used to create the W/Z event sample were as follows. First, the clusters from the calorimetry cells were reconstructed by using informations from the electromagnetic calorimeters only. Then the ratio of the hadronic energy to the electromagnetic energy in the cluster was required to be less than 5%. A loose cut requiring the isolation of the electrons rejected the QCD background which had jet activities near the electrons. The matching of the electron energy measured by the calorimeters and the momentum measured by the central tracking chamber helped to reduce such overlapping background to a great extent in the Central calorimeter region, while in the plug region the longitudinal and the lateral shower chi-squares

were used since the error in the momentum measurement in this region was relatively large. The position matching of the calorimeter signal and the extrapolated track was also required.

After applying all of these cuts, 134 events were selected with electron candidates in the Endplug calorimeter region (*Plug electrons*). Some fraction of these events contained inclusive electron, but they were still dominated by the QCD background. A Dijet cut, which suppresses events having back-to-back jet to the electron in the azimuth, a tight isolation cut, and the missing E_T cut were required to produce a pure W data sample, while for the Z sample another electron cluster with relatively loose cuts were required. The number of events survived after these cuts was 9 for W with electrons in the Endplug calorimeter, and was 6 with electrons in the whole CDF calorimetry for Z. The number of QCD background events to the W candidates was estimated to be 0.6 ± 0.4 from the shape of the distribution of the normalized missing E_T. The contribution of the $W \rightarrow \tau\nu \rightarrow e\nu\nu$ process was calculated with ISAJET Monte Carlo program and was 0.3 ± 0.1 events. After correcting the trigger efficiency, the detector acceptance and the efficiency of the cuts, these W candidate events with Plug electrons were combined with the ones with the Central electrons. The product of the production cross section of the W boson and the branching ratio to the electron decay channel was obtained as 2.3 ± 0.4 (stat.) ± 0.5 (syst.) nb. Similarly, the cross section of the Z boson times the branching ratio of the electron channel was obtained to be 0.4 ± 0.2 (stat.) ± 0.1 (syst.) nb. The mass of the W boson was determined to be 82.1 ± 2.0 (stat.) ± 1.2 (syst.) GeV/c^2. These results are in good agreement with the predictions of the Standard Model within the error.

Acknowledgments

I would greatly like to thank Prof. K. Kondo for his guidance and encouragement throughout my graduate career. I have learned from his attitude toward physics that how one should confront a huge amount of tasks and conduct a careful experiment.

The construction of the Endplug electromagnetic calorimeter would have been impossible without the limitless efforts and advice of the collaborators: Professor S. Miyashita, Drs. S. Kim, Y. Hayashide, M. Shibata, Messrs M. Ito, S. Kanda, T. Suzaki and Miss M. Masuzawa.

Professors K. Takikawa, M. Mishina, S. Mori, S. Mikamo, Drs. Y. Fukui and F. Abe are appreciated for their continuous encouragement and criticism.

I owe to Drs. K. Yasuoka and C. Blocker for constructing the CDF electron analysis code. They are also appreciated for their useful discussion.

Reconstruction of the tracking data which played an essential role in the electron analysis would have been impossible without the collaboration of Prof. A. Para, Drs. J. P. Berge, M. Sekiguchi, Messrs A. Mukherjee and T. Mimashi.

I was deeply enlightened in fruitful discussions with Drs. T. Kamon, A. Yamashita, Y. Takaiwa and H. Miyata.

Messrs. F. Ukegawa, S. Ogawa and M. Takano gave a lot of useful cooperation and guidance throughout the data taking and the analysis and are gratefully appreciated.

Drs. A. Baden, M. Franklin, C. Haber, Messrs. D. Brown, E. Kearns and R. St. Denis gave extraordinary contributions to make the beam test at the M-Bottom beam line possible.

I deeply appreciate the work of other CDF collaborators whose names appear in the list of Appendix A and many other engineers and technicians who do not appear in the list. It was really a great pleasure for me to work with them during my stay at Fermilab.

This work would not have been possible without the skill and hard work of the Accelerator Division of Fermilab.

The experiment described in this thesis has been done under the accord of U.S.-Japan collaboration in high energy physics. I gratefully acknowledge the support of the Ministry of Education, Science and Culture of Japan and the U.S. DOE. I wish to express my special thanks to Dr. A. Tollestrup (CDF co-leader), Prof. R. Schwitters (CDF co-leader), Drs. K. Stanfield (Head of Research Division) and L. Lederman (Director) of Fermilab.

This work was supported by the Ministry of Education, Science and Culture of Japan (KEK, Tsukuba); the U.S. Department of Energy, Contract Nos. W-31-109-ENG-38 (ANL); DE-ACO2-76ER03230 (Brandeis); DE-ACO2-76CH03000 (Fermilab); DE-ACO2-76ER03064 (Harvard); DE-ACO2-76ER01196 (Illinois); DE-ACO2-76SF00098 (LBL); DE-ACO2-76ER3071 (Pennsylvania); DE-ACO2-76ER0-1428 (Purdue); DE-ACO2-87ER40325 (Rockefeller); DE-AS05-81ER40039 (Texas A & M); DE-ACO2-76ER00881 (Wisconsin); the National Science Foundation, Grant No. NSF-PHY 86-01628 (Chicago), NSF-PHY-85-14193 (Rutgers); and Istituto Nazionale di Fisica Nucleare (Frascati, Pisa).

Contents

Chapter 1 INTRODUCTION

This thesis describes the production cross sections and the masses of the charged and the neutral intermediate vector bosons observed at the Collider Detector at Fermilab (CDF) in 1987 run at a center of mass energy of 1.8 TeV.

1.1 Physics of the Intermediate Vector Bosons

A major achievement in the recent high energy physics is the discovery that the three fundamental forces, the strong, weak, and electromagnetic forces, have an underlying unity in terms of the gauge theory [Ref.1-1]. It now appears that the strong interaction is described with SU(3) gauge theory, so called Quantum Chromodynamics (QCD), and the weak and electromagnetic interactions with unified SU(2)×U(1) gauge theory, which was developed by Glashow, Weinberg and Salam [Ref.1-2]. The unification of the electromagnetic and the weak forces was firmly established by observing leptonic decay modes of the charged and the neutral intermediate vector bosons by the CERN $S\bar{p}pS$ collider experiments. The UA1 and UA2 groups have observed the decay of the charged and neutral intermediate vector bosons, or W and Z bosons, to the electronic and muonic channel in 1983 and 1984 run [Ref.1-3].

The conventional mechanism for the production of the W/Z bosons in high energy $\bar{p}p$ collision is the Drell-Yan process (Fig.1-1) – the annihilation of a quark and an antiquark into the W/Z. The first-order production cross sections of the IVB's are directly calculated from the quark momentum distribution functions in the proton and from the weak coupling constant. Higher order α_s corrections have also been calculated [Ref.1-4]. Measuring the production cross section of the IVB's at various center of mass energies therefore gives a good opportunity

to test the higher order QCD correction and the Q^2-evolution of the various sets of parton distribution functions [Ref.1-5~7].

The ratio of the production cross sections times the branching ratio of the W/Z bosons can yield important information on the number of light neutrinos and the mass of the top quark [Ref.1-8];

$$R = \frac{\sigma_W}{\sigma_Z}\frac{B(W\rightarrow e\nu)}{B(Z^0\rightarrow e^+e^-)} \equiv R_\sigma R_{BR} . \qquad (1\text{-}1)$$

Through the total width, R_{BR} is a function of the number of light neutrinos N_ν and the top quark mass m_t. Thus precise measurements of R and precise calculations of R_σ can yield information on these quantities assuming: (i) there are N_ν (≥3) light neutrinos which contribute to Z decay, (ii) apart from $Z \rightarrow \nu_L\bar{\nu}_L$ the fourth (L, ν_L, U, D) and higher generations do not contribute to W or Z decay, and (iii) there are no other non-standard (e.g. supersymmetric) decay modes.

The theoretical uncertainties in choosing among various sets of structure functions in calculating σ_W and σ_Z mostly cancel when one takes the ratio R_σ [Ref.1-9~10]. It was shown in the literature that the ratio R_σ can be directly derived from a measurement of F_2^n/F_2^p in deep-inelastic μp and μD scattering at EMC and BCDMS [Ref.1-11]. Also it should be noted that the experimental uncertainty decreases in calculating Eq.1-1 due to the fact that the systematic errors of the integrated luminosity, and a part of electron finding efficiencies cancel in $\sigma_W \cdot B$ and $\sigma_Z \cdot B$. With the combined value of R currently available from the UA1 and UA2 data, Halzen *et al* have argued that $N_\nu = 3$ and $m_t < 60$ GeV/c^2 at 95% CL [Ref.1-10]. (See Fig.1-2) Their conclusion is still somewhat controversial due to the discrepancies in the ratio F_2^n/F_2^p between the EMC and BCDMS data [Ref.1-12], but the increase in the statistics of W/Z events will solve the situation. At the Tevatron energy of 1.8 TeV, one expects an approximately threefold increase in the W/Z boson production cross section compared to the previously measured results at the CERN collider energy of 630 GeV. Although the integrated luminosity

of the data used in this analysis is rather limited, one expects that we CDF will accumulate more than 2 pb^{-1} of data in the 1988 run. The expected number of $Z^0 \rightarrow e^+e^-$ events is about 350 at 2 pb^{-1} and thus the statistical error of R will reduce to 5% or less, putting stricter limit on the combination of top quark mass and the number of light neutrinos, or existence of any other "exotic" particles [Ref.1-13].

Measuring the masses of the IVB's is free from the ambiguity of the production mechanism and therefore it is an independent measurement from the determination of the $\sigma \cdot B$ and R. Systematic errors of the $\sigma \cdot B$ is dominated by the errors in the calculation of the electron detection efficiencies and in the luminosity calculations, while the error in the energy scale calibration dominates in the systematic error of the mass determination. Comparing the measured IVB masses to the theoretical prediction thus serves as another opportunity of the verification of the Standard Model.

In the Standard Model, masses of the IVB's are given as follows [Ref.1-14],

$$m_w = A/sin\theta_w \tag{1-2}$$

$$m_z = 2A/sin2\theta_w \tag{1-3}$$

$$m_z = m_w/cos\theta_w \tag{1-4}$$

where,

$$A = \left[\frac{\pi\alpha}{\sqrt{2}G_\mu}\right]^{1/2}\left[\frac{1}{1-\Delta r}\right]^{1/2} = \frac{37.281\text{GeV}}{\sqrt{1-\Delta r}} \tag{1-5}$$

with $\alpha = 1 / 137.03596$

$$G_\mu = 1.16632 \times 10^{-5}\ \text{GeV}^{-2},$$

and θ_w is the weak mixing angle. Here Δr denotes the $O(\alpha)$ radiative corrections to make Eq.1-4 exact. Then the mass difference of W and Z is expressed as,

$$m_z - m_w = m_z\left[\ 1\ -\ \sqrt{\frac{1 + (1 - 4A^2/m_z^2)^{1/2}}{2}}\ \right] \tag{1-6}$$

From Eqs.1-5 and 1-6, the radiative correction factor Δr can be written as a function of m_w and m_z :

$$\Delta r = 1 - \frac{(37.281\text{GeV})^2}{m_w^2(1 - m_w^2/m_z^2)} \tag{1-7}$$

A theoretical evaluation leads to

$$\Delta r = 0.0696 \pm 0.0020 \tag{1-8}$$

for $sin\theta_w = 0.217$, Higgs mass $m_\phi = m_z$ and top quark mass $m_t = 36\ \text{GeV/c}^2$.

The production cross sections times the branching ratio of $W \rightarrow e\nu$ decay which were measured at UA1/UA2 experiments were [Ref.1-15],

UA1	$\sigma_W B(W\rightarrow e\nu) = 0.55 \pm 0.08 \pm 0.09$ nb	at $\sqrt{s} = 546$ GeV
UA1	$\sigma_W B(W\rightarrow e\nu) = 0.63 \pm 0.05 \pm 0.10$ nb	at $\sqrt{s} = 630$ GeV
UA2	$\sigma_W B(W\rightarrow e\nu) = 0.61 \pm 0.10 \pm 0.07$ nb	at $\sqrt{s} = 546$ GeV
UA2	$\sigma_W B(W\rightarrow e\nu) = 0.57 \pm 0.04 \pm 0.07$ nb	at $\sqrt{s} = 630$ GeV

and the production cross sections times the branching ratio of $Z^0 \rightarrow e^+e^-$ decay were,

UA1	$\sigma_Z B(Z\rightarrow ee) = 42\ ^{+33}_{-20} \pm 6$ pb	at $\sqrt{s} = 546$ GeV
UA1	$\sigma_Z B(Z\rightarrow ee) = 74 \pm 14 \pm 11$ pb	at $\sqrt{s} = 630$ GeV
UA2	$\sigma_Z B(Z\rightarrow ee) = 116 \pm 39 \pm 11$ pb	at $\sqrt{s} = 546$ GeV
UA2	$\sigma_Z B(Z\rightarrow ee) = 73 \pm 14 \pm 7$ pb	at $\sqrt{s} = 630$ GeV

Weak boson masses are summarized as [Ref.1-16],

UA1	$M_W = 83.5\ ^{+1.1}_{-1.0} \pm 2.7\ \text{GeV/c}^2$

UA2 $M_W = 81.2 \pm 1.1 \pm 1.3$ GeV/c^2

UA1 $M_Z = 93.0 \pm 1.4 \pm 3.0$ GeV/c^2

UA2 $M_Z = 92.5 \pm 1.3 \pm 1.5$ GeV/c^2

1.2 General Design of the CDF Detector

1.2.1 Detector Design

The CDF [Ref.1-17] is a general purpose detector assembled at the B0 straight section of Fermilab Tevatron. A perspective view of the detector is shown in Fig.1-3. It consists of a central detector and forward/backward detectors. Each angular range of the CDF consists of components with different functions, namely, tracking detectors, calorimeters and muon detectors. The calorimeters are constructed in tower geometry with each tower aiming at the interaction point. The total weight is approximately 5000 tons, half of which is in the central detector. The approximate size of the central detector is that of a box 9.4 m high, 7.6 m wide and 7.3 m long. A cut through one half of the detector is shown in Fig.1-4. The interaction region is in the center of the detector. The description for each part is given below.

Magnets

The CDF has two types of magnets to measure the momenta of the charged particles. One is a superconducting solenoid in the central detector and the other is the forward/backward toroidal magnets for the forward/backward muon detectors.

The superconducting solenoidal coil is 3 m in diameter and 5 m long, and produces a uniform magnetic field of 1.5 Tesla at 5 kA. The coil is made of 1164 turns of an aluminum stabilized NbTi/Cu superconductor, fabricated by the EFT (extrusion with front tension) method in which high purity aluminum is friction welded to the superconducting wire during the extrusion process. The return flux of the magnetic

field goes through the steel plates of the Endplug and the Endwall hadron calorimeters and then goes separately into the steel return yokes outside the central calorimeters and the muon chambers. The coil has 0.85 radiation length in thickness.

Each of the forward and backward muon detectors has two large magnetized steel toroids. They are 7.6 m in diameter and 1 m in thick. Four coils per toroid generate a 1.8 Tesla field within the steel.

Charged Particle Tracking

Various types of the tracking chambers are used in the CDF to achieve the high precision momentum measurement over the large coverage of the solid angle. All tracking detectors except for the forward silicon detectors overlap with the calorimeter acceptance (angles greater than 2° with respect to the beam direction). Also, the combination of each subsystem of the tracking detectors covers each other to improve the three-dimensional track reconstruction at the various angle.

Central Tracking Chamber

The Central Tracking Chamber (CTC) [Ref.1-18] is a large cylindrical drift chamber with excellent spatial and momentum resolution used to measure charged tracks in the central region. It is a 1.3 m radius and 3.2 m long cylindrical drift chamber and covers the angular region $40° < \theta < 140°$ ($-1 < \eta < 1$). In this region the momentum resolution is better than $\Delta p_T/p_T \leq 0.002$ (GeV/c)$^{-1}$. The chamber contains 84 layers of sense wires grouped into 9 "superlayers"; 5 of which are "axial" and 4 are "stereo." Each axial superlayer consists of 12 axial sense wire layers, and each stereo superlayer consists of 6 sense wire layers in which wires are tilted by ±3° relative to the beam direction. Each superlayer has a 45° tilt to the radial direction to correct the angle of the electron drift caused by the Lorentz force

of the magnetic field. An endplate of the CTC which shows the configuration of the super layers is given in Fig.1-5.

Central Drift Chambers

A system of Central Drift Tubes (CDT) with high resolution charge division surrounding the CTC provide a correlated R-φ-Z measurement. It consists of three layers of 3 m long, 1.27 cm diameter stainless steel tubes. Typical resolutions are 2.5 mm in the axial (beam) direction and 200 μm in the azimuthal direction.

Vertex Time Projection Chambers

A set of Vertex Time Projection Chambers (VTPC) [Ref.1-19] was implemented to determine the Z-position of the interaction vertex accurately and to measure charged particle multiplicities over a large solid angle. This system comprises eight separate time projection chamber modules which are mounted end-to-end along the beam direction. A total length of 2.8 m of the chamber system well covers the distribution of the interaction points ($\sigma_z \approx 35$ cm). The VTPC chambers contain a total of 3072 sense wires for the measurement of track coordinates in R-Z, where R is the radial distance from the beam and Z is the distance along the beam line from the center of the detector, and 3072 pads[1] for the measurement of coordinates in R-φ. Fig.1-6 is a schematic drawing of two octagonal VTPC modules. Each module has a central high voltage grid plane that divides it into two 15 cm-long drift regions. At the end of each drift region there are proportional chambers arranged in octants, each octant with 24 anode sense wires and 24 cathode pads. As viewed from the drift region, an octant consists of a cathode grid

[1]Only 768 pads were actually turned on and read out during the 1987 run due to cooling problems of VTPC pre-amplifier modules.

(screen) followed by a plane of field shaping wires, a plane of sense wires which alternate in the radial direction with the field wires, and a resistive cathode plane. Three rows of pads are located behind the resistive cathodes. The active area of the chamber extends from R = 6.8 cm to R = 21 cm.

Since particles detected by the calorimeters and other tracking chambers first pass through the VTPC, a considerable effort was made to minimize the mass of the VTPC and the beam pipe. The beam pipe, inside the VTPC, consists of the 5.08 cm diameter beryllium tube, with a wall thickness of 500 μm. Fig.1-7 is a plot of the amount of material in radiation lengths versus the polar angle as measured from the interaction point.

Forward Tracking Chambers

The forward tracking chamber (FTC) is a radial drift chamber which, in conjunction with the VTPC, is responsible for tracking in the angular region $2° < \theta < 10°$. The 72 wedge shaped cells of an FTC are shown schematically in Fig.1-8. The chamber contains planes of radial anode and field shaping wires which alternate with planes of cathode strips. The planes are slanted by 2° relative to the beam axis so that left-right ambiguities can be resolved by demanding that tracks point back to the primary event vertex. Each anode plane has 21 sense wires and 26 field shaping wires. Four of the 21 sense wires are instrumented for charge division, so that an R-φ-Z measurement can be made for each track.

Forward Silicon Detectors

A set of silicon detector, scintillation counters and drift chambers are located at the seven stations along the accelerator ring to track particles produced at very small angles. A purpose of this detector is to study the elastic and diffractive scatterings. Each station contain a single silicon detector with both horizontal and vertical strips,

giving 50 μm resolution in the horizontal plane and 300 μm in the vertical. Each combination of the different subsystem of the stations tracks particles of various angles, ranging from 0.2 mrad to 35 mrad. Because the spectrometers in the antiproton direction uses the Tevatron dipoles as well as the low-β quadrupoles, the resolution of the momentum measurement is better ($\Delta p/p \approx 0.1\%$) than in the proton direction. The resolution in the proton direction depends on the angle of the particle and is 2% at $\theta = 1.0$ mrad.

Trigger Counters

There is a plane of scintillation counters on the front face of each of the forward and the backward shower counters. These scintillators, called the beam-beam counters (BBC), provide a "minimum-bias" trigger for the detector, and are also used as the primary luminosity monitor. The counters are arranged in a rectangle around the beam pipe as shown in Fig.1-9. They have excellent timing properties ($\sigma < 200$ psec), and so provide the best measurement of the time of the interaction. A crude (± 4 cm) measurement of the vertex position is also obtained from the timing.

Calorimetry

Both electromagnetic (EM) and hadron calorimeters are outside of the tracking detectors. All the calorimeters are of the sampling type. The EM calorimeters contain lead plates as the absorber, whereas the hadron calorimeters have steal plates instead. The active medium is scintillator for the polar angle region of $30° < \theta < 150°$ and gas proportional tubes for small angles of $2° < \theta < 30°$ and $150° < \theta < 178°$.

The angular coverage of the calorimeter is 2π in the azimuth φ and from -4 to +4 in the pseudorapidity η. The calorimeters are all subdivided into many cells. Because of the importance of hadronic jets in the high energy $\bar{p}p$ collisions, a pyramidlike "tower" geometry pointing to the center of the detector was chosen for all calorimeters. The

coverage of the calorimeter towers in η-φ space is shown in Fig.1-10. Each tower has an electromagnetic shower counter in front of a corresponding hadron calorimeter, so that one can make a detailed comparison of electromagnetic to hadronic energy on a tower-by-tower basis. The tower size is approximately 0.1 in pseudorapidity and 0.26 (15°) in azimuth for the scintillator calorimeters, while it is 0.1 by 0.09 (5°) for the proportional tube calorimeters. Summary of the CDF calorimetry is given in Table 1-1 and the brief description for each calorimeter follows.

Central Calorimeters

A total of 48 "wedge" modules are built into four "arches" to consist the central calorimeters. A wedge module contains both electromagnetic and hadron calorimeters. The electromagnetic calorimeters (CEM) contain lead plates as the shower medium, whereas the hadron calorimeters (CHA) have steel plates instead. The sampling medium is scintillator. The total thickness of the CEM and CHA are 18 radiation lengths and $4.7/sin\theta$ absorption lengths respectively. Fig.1-11 is a schematic drawing of a CEM module in one wedge.

Endwall Hadron Calorimeters

The Endwall hadron calorimeter (WHA) uses the same shower and sampling medium as those of CHA, and has $4.5/cos\theta$ absorption lengths in total. They are mounted on the steel Endwalls of the magnet yoke, and work as a part of the flux return path as well.

Endplug Calorimeters

Both the Endplug electromagnetic (PEM) and the hadron (PHA) calorimeters use gas proportional tubes with cathode pad readout for the shower localization and the energy measurement. The PEM and the first few layers of the PHA calorimeters

are located inside the solenoid field. The longitudinal depths of the PEM and the PHA are 18 radiations length and 6.0 absorption lengths, respectively. The PEM calorimeter will be described in Chapter 2 in more detail.

Forward/Backward Calorimeters

The forward/backward electromagnetic (FEM) and hadron (FHA) calorimeters are located between 6 m and 10 m from the interaction region on both sides of the central detector. They also use proportional tubes with cathode pad readout for the sampling medium. The longitudinal depth of the calorimeters are 26 radiation lengths and 8.5 absorption lengths for FEM and FHA respectively.

Muon Chambers

CDF has two muon detection system. One is the central muon detector and the other is the forward/backward muon detector. Both of these detectors are put outside of the calorimeters. The central muon detector has three drift chambers located between the last two steel plates of the central wedge calorimeters. The azimuthal position of the charged particle is determined by its drift time, while the z-coordinate is measured by its charge division on the sense wire.

1.2.2 Readout Electronics

The CDF detector has a total of approximately 100,000 electronic channels consisting of photomultiplier tubes, strip/wire/pad chambers, drift chambers, drift chambers with current division readout, and silicon strip detectors. The calorimetry requires a very large dynamic range of the electronic readout, extending from a few tens of MeV for detecting minimum ionizing particles, to many hundreds of GeV for the high P_T jet detection. A special crate-based analog front-end system called the RABBIT System [Ref.1-20] was developed to satisfy these requirements. The RABBIT system consists of 129 crates

mounted on the detector which service all of the calorimeters, about 60,000 channels of the 100,000 total. The drift chambers make up the bulk of the remainder: their signals are shaped at the detector and brought up from the collision hall to commercial Fastbus TDC modules in the counting room.

The measurement method upon which the RABBIT system is based involves sampling two voltage levels for each event to avoid pileup and common mode noise: one just before the interaction time to establish a reference level and another after the interaction. The difference between voltage levels is proportional to the integrated signal charge. This approach makes use of the bunched structure of the beams. Normally, the Tevatron operates with three or six approximately equally spaced bunches of protons and antiprotons. Thus, interactions take place at relatively well defined "windows" in time, separated by 7 or 3.5 μsec. This general approach is referred to as "before-after" sampling. Digitization is performed in each crate.

As the RABBIT channels are digitized, they are read out by fast intelligent scanners called MX's [Ref.1-20]. The scanners interface these digitized data to the Fastbus data acquisition system. Most of the tracking systems use commercial Fastbus modules for the detector readout and digitization, which in turn are read out by a second type of intelligent scanners called the SSP [Ref.1-21]. Each scanner can buffer four events, and handles approximately 1000 channels. There are approximately 60 MX scanners and 25 SSP scanners in the system.

The Fastbus network which comprises the Data Acquisition (DAQ) system consists of 53 crates, 16 cable segments, and 66 segment-interconnect modules. Many custom designed Fastbus modules, such as a hardware event builder, allow for the bandwidth necessary to transmit the data for each event. For a nominal event size of 100 Kbytes the DAQ system reads out events at 20~30 Hz into the Level 3 system (see below). A detailed technical description is given in the reference 1-21.

1.2.3 Trigger System

The CDF has three stages of the trigger system. The Level 1 and Level 2 triggers are hardwired systems [Ref.1-22], and the Level 3 system is a set of multi-processor computer system which is capable of using software filterings written in FORTRAN-77 [Ref.1-23]. The Level 2 and Level 3 trigger systems were not ready in the 1987 run, and only the Level 1 trigger was actually employed in the data used in this analysis.

Level 1 trigger

The calorimetry trigger is designed to exploit the projective geometry of the calorimeter towers. Both hadron and EM calorimeter towers are summed into trigger towers with a width in pseudorapidity of $\Delta\eta = 0.2$ and a width in azimuth of $\Delta\varphi = 15°$. Outputs from all phototubes are brought to the counting room individually and summed, four tubes per channel, into the $\Delta\varphi = 15°$ and $\Delta\eta = 0.2$ trigger towers. All gas calorimeter pad signals are summed at the detector into the trigger towers. The signals are weighted by $sin\theta$ to represent the "transverse energy", or E_T, deposited in each tower.

The Level 1 calorimetry triggers require that the sum of E_T for all calorimeter towers which are individually over a lower threshold (STT: Single Tower Threshold, typically 1 GeV for jet triggers) be greater than a higher threshold (typically 30 - 40 GeV). Both electromagnetic and hadronic energy, or either one, can be summed in a given tower. These two thresholds are programmable, and up to four such comparisons can be made independently in a given beam crossing. The results of these comparisons are combined in a trigger "look-up" table with the beam-beam counter coincidence, the muon triggers, a stiff track trigger from a fast hardware track processor, and other optional signals to generate the Level 1 decision to accept or reject the event. Different

patterns can be rate-limited so that minimum bias events, for example, can be taken intermixed with jet or electron triggers.

Level 2 trigger

The Level 2 trigger starts after a Level 1 trigger has accepted an event. Level 2 uses the same hardware to search the 42×24 array of towers in η–φ, both for clusters of total energy, or of electromagnetic energy. Towers with contents below a programmable threshold are ignored; a hardware cluster finder identifies clusters of energy with a speed of about 200 nsec/cluster. The total E_T and the E_T weighted first and second moments of η and φ positions of each cluster are digitized and presented as a list of clusters to a fast hardware Level 2 processor. For each cluster a match is made to tracks found in the CTC by the fast (10 μsec) hardware tracking processor, and a coarse P_T measurement appears in the list if a match is found. Each muon found by the muon processor is matched to the CTC tracks, and it also appears in the cluster list in the Level 2 processor with the matched CTC track momenta.

The final trigger is then a selection on muons, electrons, photons, jets and missing E_T by the programmable Level 2 processor. Many combinations of the above can be programmed in parallel.

Level 3 trigger

The Level 3 System is designed to execute FORTRAN-77 filter algorithms as the last stage of on-line trigger selection. Level 3 uses 32-bit processors, developed at Fermilab as Advanced Computer Program (ACP), installed in VME crates with VME bus control and interface modules. An interface allows a Fastbus master to transfer data to a processor memory at 20 Mbytes/sec. The processors are double height VME cards based on the Motorola 68020 CPU and 68881 floating point coprocessor. A total of 50 of such processors will be installed in the next run: each processor will have 6 Mbytes

of DRAM. Events which pass the Level 3 filter algorithm will be written on tapes for offline analysis.

1.3 Outline of the Article

The present article is organized as follows: Chapter 2 describes the design, construction and performance of the CDF Endplug EM calorimeter, on which the author has been working. In Chapter 3, the beam test calibrations of the calorimeters (mainly the Endplug EM calorimeters) are evaluated in the light of energy scale which in turn contributes to the systematic error of the vector boson masses. The actual data taking environment and the trigger conditions in the 1987 run are described in Chapter 4. Chapter 5 is devoted to the offline analysis on the electron initiated analysis stream. The W and Z events are selected here. A Monte Carlo study to evaluate the detector acceptance and the background contamination is presented in Chapter 6. Given the events of W and Z decays, the cross sections and masses of the IVB's are studied in Chapter 7. Finally, summary and conclusions are provided in Chapter 8.

Chapter 2 THE ENDPLUG EM CALORIMETER

2.1 Detector Design

The Endplug electromagnetic calorimeter [Ref.2-1] covers both ends of the 3 m diameter 5 m long solenoid in the central detector system of CDF leaving a concentric conical hole of an opening angle of 10° with respect to the beam axis in either direction. Each of the two calorimeter modules occupies a cylindrical volume of an outer diameter of 280 cm and a depth of 53 cm between 173 cm and 226 cm in the z-coordinate along the beam axis. The angular coverage is from 10° to about 36° in the polar angle θ, or in the pseudorapidity η from about 1.1 to 2.4, with full depth up to 32°. A cross sectional view of the CDF Endplug region is shown in Fig.2-1.

Since the Endplug electromagnetic calorimeter resides completely inside the solenoid coil, a scintillator system is not appropriate for this calorimeter due to the presence of a strong magnetic field and the difficulty in designing a proper light guide system to achieve desired fine segmentation in lateral and longitudinal directions. This constraint leads to a choice of a proportional chamber based system. By reading cathode induced signals with etched electrodes on printed circuit boards, virtually any shape of tower geometry can be achieved with no dead space. Relatively inferior energy resolution of the gas calorimetry system compared to the scintillator system is not a significant problem, if one compares the resolution in transverse energy, not in bare energy.

Each of the PEM modules consists of four quadrants, and each of quadrants consists of 34 layers of proportional tube arrays interleaved with 2.7 mm thick lead absorber panels filling about 50 cm in depth in the z direction. An exploded view of such a layer is sketched in Fig.2-

2. The proportional tubes were made of conductive plastic tubes of a square inner cross section of 7 mm x 7 mm with 0.8 mm thick wall and anode wires of 50 μm gold-plated tungsten supported by Y-shaped molded plastic pieces at both ends, as sketched in Fig.2-3. The conductive plastic tubes were extruded out of polystyrene loaded with fine grain carbon powder. The surface resistance was chosen to be in a range of 60 to 100 kΩ/*square*. Since the gain of a proportional tube is quite sensitive to the physical dimensions of the components, the tolerance of the inner dimension was kept within ±100 μm. The wall thickness was maintained within ±50 μm. The tolerance of the anode wire diameter was specified to ±0.5% and the plastic molding for the wire support was specified to ±100 μm in the dimensional tolerance of the position of the saddle point. The wire tension was about 150 g.

Each plane of the tube arrays was assembled into a fan-shaped quadrant in the azimuth in which all 156 tubes were vertical or horizontal in a plane perpendicular to the beam axis, but were trimmed tube by tube to form a circular arc of $\Delta\varphi = 90°$at the inner conical wall of $\theta = 10°$ and the outer cylindrical boundary above r = 136 cm. Since the tube arrays were pushed against one of the orthogonal straight edges parallel to the tubes, there was virtually no dead space along that edge, while along the other straight edge orthogonal to the tube orientation there were about 5 mm wide dead zone for terminating the anode wires and another several mm wide zone of reduced sensitivity inherent to the end of a proportional tube. However, by rotating the orientation of the tubes by 90° layer by layer, real dead zone is only the physical gap between contiguous quadrants which were kept to within 3 mm. The tube arrays were sandwiched by a pair of 1.6 mm thick G-10 panels with structural adhesive. Since the gain of the proportional tubes is sensitive to the anode wire displacement from the center of the tube, great caution was taken to keep the tubes straight within the chamber plane when the tube panels were assembled.

Material thickness of each layer is listed in Table 2-1. The total material thickness varies according to the polar angle θ, which is proportional to $1/cos\theta$ up to θ = 30°, and then decreases rapidly due to the penetration of the shower particles to the cylindrical side periphery.

The readout electrodes were etched into either "pad" or "strip" shape out of the copper plating clad on G-10 panels. The pads are on one side of every proportional tube panels directly facing to the tube array, and the strips are on the other side of the tube panels but only through the sixth to fifteenth layer, around the shower maximum depth. The shape of the pads is shown in Fig.2-4(a), and two different patterns of the strips, θ-strips and φ-strips, which are orthogonal to each other, in (b) and (c), respectively. The lateral and the longitudinal segmentations of the pads and the strips are summarized in Table 2-2 and Table 2-3.

The anode wires in each of the quadrant panels were ganged together through a 100 Ω resistor on individual wire. The signals from each layer were then picked up with a 50 Ω coaxial cable which feeds high voltage to each quadrant panel. The signals were decoupled from the high voltage by blocking capacitors of 0.01 μF.

A 50% - 50% mixture of argon-ethane gas with a small percentage of ethyl alcohol admixture has been used throughout the test and the calibration runs. Since a recent study [Ref.2-2] has shown that isopropyl alcohol is superior as a quenching agent, it is used in the final CDF detector instead of ethyl alcohol. This change of the alcohol admixture, however, does not pose a problem in maintaining the absolute energy scale calibration because the energy scale is solely maintained by the signals from radioactive sources embedded within the same gas environment as will be discussed in Chapter 3.

The alcohol percentage is regulated by feeding the inlet gas through a bubbler immersed in alcohol in a refrigerating bath whose temperature is kept within ±0.1°C around –3°C.

2.2 Construction

A local gain variation in a calorimeter increases a systematic uncertainty of the energy measurement. Therefore a great caution was taken in constructing the Endplug electromagnetic calorimeter to minimize the nonuniformity of the proportional tube arrays. The tube dimensions and the anode wire diameters were carefully controlled as described in the previous section. Since the gain variation ΔG can be expressed as a function of the anode wire displacement D (mm) by the following empirical formula [Ref.2-1],

$$\left|\frac{\Delta G}{G}\right| = (0.214 \pm 0.006) D^{(2.33 \pm 0.06)} \qquad (2\text{-}1)$$

the wire displacement has to be kept within 270 μm to keep the gain nonuniformity less than 1%.

As shown in Fig.2-2, a proportional tube array was sandwiched by G-10 boards. The tubes and the boards were fixed with epoxy glue. First, one side of three G-10 boards were glued with the tube array. At this point, a special jig shown in Fig.2-5 was used to measure the straightness of the tubes in the horizontal direction. The straightness in the vertical direction was ensured by pressing the tubes and the boards during the curing time with a water tank of 50 cm deep on a 3 cm thick iron plate. The average horizontal bend and the vertical flatness variation were kept within 60 μm and 100 μm, respectively.

Anode wires were stretched before gluing the other side of the G-10 boards to the tube array. The wire tension was kept within the range of 100 to 200 g by measuring it with a computer controlled checking system. A magnetic field was applied to each tube and then the resonance frequency was measured.

After gluing the other side of the G-10 boards, high voltage loading test was applied in open air. The dark current was required to be less than 1 μA at 2.5 kV. Various wiring failure and tiny fragments of metal causing breakdown were found at this stage.

An assembly of the proportional tube array and the G-10 boards is called "Chamber". The Chamber is a unit of shower sampling medium. Each Chamber was tested with cosmic rays as described in the next section to check the performance and the gain uniformity. These assembly and tests were done in Japan and then all Chambers were exported to Fermilab. At Fermilab, four or five Chambers were grouped and then glued with 2.7 mm thick lead plates layer by layer. Finally, each block of chambers was stacked into gas vessel to construct a doughnut shape calorimeter module. The cable connections of more than 8,000 channels were checked out by observing cathode signals induced by a step pulse signal imposed on anode. Several pads were found dead because of a circuit disconnection at the through-hole of the G-10 board, or a short circuit to the ground.

2.3 Cosmic Ray Test

Each Chamber was tested on its function with cosmic rays before being shipped to Fermilab. A main objective of the cosmic ray test was twofold: (1) confirm the stable operation of the Chamber in argon-ethane gas, and (2) check whether the quality control standards at the production stage were satisfied.

Fig.2-6 shows the setup of the cosmic ray testing system. A set of hodoscope shown in Fig.2-7 triggered on a cosmic ray event. Up to 24 Chambers were stacked into a gas vessel and tested simultaneously. Anode signals were amplified by LeCroy TRA1000 preamplifier and digitized by LeCroy 2285 ADC. Chambers were operated in fifty-fifty mixture of argon-ethane gas with 1% admixture of ethyl alcohol.

One batch of the test lasted typically 4 days to a week, thus the gas gain had to be monitored by a proportional tube with Fe^{55} radioactive source throughout the data taking period. Fig.2-8(a) shows a gas gain variation as a function of time tracked by Fe^{55} signal during a typical run, while (b) is a response of a typical Chamber to the cosmic ray during the

same period of time. These two types of signals trace each other as shown in Fig.2-8(c), indicating the validity of the gas gain monitoring system.

The anode signals from each Chamber were accumulated through the data taking period together with the hit pattern of the trigger hodoscope. This hit pattern was analyzed event by event at offline and the position of the cosmic ray was determined by 8 cm × 8 cm meshes.

The energy-loss of a minimum ionizing particle in thin media has a well-known Landau distribution [Ref.2-3],

$$f(\lambda) = \frac{1}{\sqrt{2\pi}} e^{-1/2\,(\lambda + e^{-\lambda})} \tag{2-2}$$

where the reduced energy variable λ represents the normalized deviation from the most probable energy loss ΔE_{mp} defined by

$$\lambda = \frac{\Delta E - \Delta E_{mp}}{\xi} \tag{2-3}$$

where ΔE is actual energy loss and ξ is the average energy loss given by

$$\xi = K \frac{Z}{A} \frac{\rho}{\beta^2} X, \qquad K = \frac{2\pi N z^2 e^4}{mc^2} \tag{2-4}$$

Here N is the Avogadro number, m and e are the electron mass and charge, Z, A and ρ are the atomic number, mass, the density of the medium, respectively, and z is the charge and β the velocity of the projectile in units of the speed of light c.

The pulse height distributions from each mesh of the Chambers were fitted with a Landau-like function,

$$f(x) = A\, e^{-1/2\,(ax + b + e^{-(ax+b)})} \tag{2-5}$$

and the gain variation of the Chamber ΔG was evaluated by,

$$\Delta G = \frac{\sqrt{\frac{1}{N}\sum_{i=1}^{N}(G_i - \langle G \rangle)^2}}{\langle G \rangle}, \quad G_i = \frac{1.27 - b_i}{a_i} \tag{2-6}$$

where G_i is the gain of i-th mesh of the Chamber, $\langle G \rangle$ is the mean gain of the Chamber and N is the number of meshes inside the Chamber. This gain variation was typically 2 to 6%, as shown in Fig.2-9. This was slightly worse than expected from the quality control of the Chamber production, but could be attributed to the poor flatness of the bottom plate of the gas vessel. Since several Chambers are glued to rigid lead plates in the final form of the calorimeter, the final gain nonuniformity of the calorimeter is not so bad as in this cosmic ray test, as will be shown in Chapter 3.

2.4 Readout electronics: CARROT cards

As described in Chapter 1, the RABBIT (Redundant Analog Bus Based Information Transfer) system is used to read pad, strip and wire signals from the calorimeter. The RABBIT module HRW (High Range Wire) cards are used to read the wire signals, while the pad and the signals are read out by CARROT (Cathode signal Amplifier and Read Out) cards. HRW card was designed and produced by PIG (Particle Instrumentation Group) of CDF, while CARROT card was originally designed at PIG, modified at Harvard University and produced at Meisei Co. Ltd. in Japan. The author was in charge of building the quality control system of this CARROT card. Some of the CARROT cards were modified to accept negative polarity signal and used as wire signal readout at the M-Bottom beam line as described in Chapter 3, since no HRW cards were available at the time.

The RABBIT system is a front-end electronics in reading out the calorimetry signals. It has to be located next to the detector, namely in the collision hall. Access to the collision hall for the maintenance service is highly limited during the run, therefore the system is required to be very reliable. It has two sets of redundant buses. Most of operations can be achieved through either bus on most of RABBIT modules. Another remarkable characteristic of the system is

"Test on Threshold" (TOT). In analyzing each event, not all the calorimetry channels (towers) are necessary. Only a fraction of towers above a certain threshold are needed and the rest of vast amount of channels need not be digitized. A EWE (Event Write Encoder) module controls the modules in a RABBIT Hutch (Fig.2-10) and can digitize only the signals above programmable threshold. This scheme allows us to minimize the number of expensive ADC chips and also the amount of calorimetry data size, thus minimizing the time for reading out the data.

A CARROT card consists of 24 channels of charge sensitive amplifiers with fast outputs for the main trigger system, a self-charge injection circuit for the calibration, and two sample-and-hold circuits for each channel, as shown in Fig.2-11. There are two types of charge amplifier circuits used in CARROT. Fig.2-12(a) shows the one used for the PEM and PHA calorimeters (Type-I), and (b) shows the one used for the FEM and FHA (Type-II). Lists of parts used for both Type-I and Type-II of CARROT are given in Table 2-4 (a) and (b), respectively. The main difference between the two types of the circuits is the input threw rate. The Endplug calorimeters have lager source capacitances compared to the Forward/Backward calorimeters. The Type-I amplifier was designed to have faster threw rate to cope with this larger source capacitance.

The feedback capacitor and the feedback resister used in Type-I are 200 pF and 500 kΩ, respectively. The fall time of the integrated signal is thus $C_f R_f$ = 100 μsec and is longer than typical beam crossing time 7 μsec.[1] Fig.2-13 shows the timing chart of the gate signals used in the CARROT card. One sample-and-hold circuit "Return" holds the output level before the beam crossing, and the other circuit "Signal" holds the level after the crossing. Thus the net amount of the signal from the crossing is the difference of the two levels "Signal" and "Return". This difference is calculated with analog OP-amplifier and sent to the trigger

[1] Beam crossing time in the three bunch operating mode.

processor. Upon the decision of the trigger processor to readout this event, the next cycle of the gate signal "Before" and "After" is inhibited and the two levels "Signal" and "Return" are held until the difference of the levels is digitized by EWE module.

Several parameters had to be controlled in the CARROT card mass production. The linearity was required to be within 0.2% without source capacitance. The absolute gain need not be so precise since it can be calibrated with the internal charge injection circuit. However, it does affect the trigger gain since the signals from six to nine channels were summed on the board and used as trigger fast-out signal. The gain of each channel cannot be calibrated on channel by channel basis in this trigger tower. Therefore the gain variation on each channel was controlled to be within 5%. Other parameters such as pedestal width and droop of the sample-and-hold circuit were also controlled in the production.

Fig.2-14 shows the setup of the quality checking system for the CARROT card. In this system, signal was generated with on-board self-charge injection circuit (Fig.2-15). A step pulse whose pulse height is proportional to the twice of the analog bus line voltage VCAL is generated at the timing of TCAL at the drain of the FET T_{63}. This step pulse is then differentiated by a calibration capacitor C_{69} and delivered to the desired channel by analog multiplexer U_{60} to U_{62}. The net charge Q generated by this circuit is thus given by

$$Q = 2\, C_{69} \times \mathrm{VCAL}. \tag{2-7}$$

We used dipped mica capacitor of 0.5% precision for C_{69} and adjusted the turn pot resister RP_1 so that the output voltage of U_{63} becomes exactly the twice of VCAL within 0.5% of accuracy. Thus the calibration of each channel of the CARROT is ensured within 1% level from card to card. This calibration circuit is also used during the run when the cards are connected to the detector.

As a EWE-sim module triggers a NIM pulse, gate generator modules generate Before, After and TCAL timing signals and feed them to the RABBIT backplane via Slave-BAT (Before-

After Timing) module. A CAMAC controlled 10-bit DAC module generates DC level voltage and feed it to the backplane as VCAL. The EWE-sim module is interfaced to a CAMAC crate via PIG-tail module and the CAMAC crate is controlled with a PDP-11 computer.

Measurements of the amplifier gain, linearity, pedestal and pedestal width were done as follows. The amount of the input charge was controlled by changing the VCAL voltage with DAC module. The DAC voltage at each data taking point was calibrated with a digital volt meter within 0.5% accuracy. At each VCAL point, 50 sets of NIM pulses were generated to each channel of the card and the difference of the Before and After was digitized by the EWE module. Taking the mean and the r.m.s. of the 50 sets of digitized data, output of each channel was fitted to a straight line through the pedestal point. The output of the amplifier at zero VCAL voltage was regarded as pedestal, and the pedestal width was given by r.m.s. of the same point. A slope of the fitted line gives a channel gain, and the residuals of the data points from the linear line were required to be within 0.2% or 50 ADC counts (~1.91 mV).

The droop is defined as a voltage drop of the output of the sample-and-hold circuits during 1 sec period. As the EWE module scans through the crate, it takes about 6 msec to digitize all the channels in the crate.[1] If the droops of the sample-and-hold circuits are large, they give systematic gain differences to the channels according to their crate addresses. To control the systematic gain differences to be within 0.5%, the droop has to be controlled within 200 mV/sec.

The rise time of the gate signals Before and After which control the gate FET SD5000N are kept to 50 nsec or less.

[1]In the real data taking environment, it is unlikely to digitize all the channels in the crates. However, in some calibration runs such as self-charge injection (EQI) and pedestal runs, all channels have to be readout.

Six or nine channels of the output of "Signal" and "Return" are summed onboard and readout as an unit of trigger fast out signal. This summation is done at an analog OP-amplifier chip AD518J as shown in the circuit diagram [Fig.2-12(c)]. The calorimeter response was readout as a differential signal of the lines TRI^+ and TRI^-. The variation of the gains of trigger fastout channels was controlled within 5% and the rise time was to 300 nsec or less.

Quantities and their tolerances controlled in the CARROT mass production are summarized in Table 2-5.

Chapter 3 DETECTOR CALIBRATION: BEAM TEST

Since the precision of the $W^{\pm}$ and Z^0 mass determination is dependent on the accurate measurement of the electron energies, the calibration of the energy scale of each calorimeter plays a crucial role. The CDF calorimeters were calibrated at two beam lines of Fermilab. The central electromagnetic and the hadronic (including Endwall) calorimeters were tested at the NW (neutrino west) beam line at Fermilab, and the rest of calorimeters (Endplug and Forward) at the M-Bottom beam line. Calibration of the central electromagnetic calorimeter is described in reference 3-1. In this chapter, calibration of the Endplug electromagnetic calorimeter is discussed.

3.1 Experimental Setup

At the M-Bottom beam line, electron and hadron beams in the energy range of 20 to 200 GeV were available. The hadron beam was generated by shooting an aluminum target with a primary 800 GeV proton beam[1]. The electron beam was obtained by sweeping out secondary charged hadrons with a magnet and converting residual γs into e^+e^- pairs with a lead converter. Layout of the M-Bottom beam line is shown in Fig.3-1. The momentum of each particle was measured by a combination of four sets of multiwire proportional chambers and a couple of dipole magnets. The horizontal and vertical resolutions of the MWPC system were 0.5 mm and 1 mm, respectively. The momentum resolution of this system was 0.47% for 100 GeV electrons [Ref.3-2].

[1]Tevatron was operated at 800 GeV in 1985 when this beam test was performed.

The Endplug electromagnetic calorimeter was mounted on a rotating stand in front of the 30° sector of the Endplug hadron calorimeter. The stand was controlled by a computer PDP-11 and was rotated around a pivot point on a horizontal plane. The beam scanning in the azimuthal direction was achieved by rotating the electromagnetic calorimeter module around its designed beam axis. (The hadron calorimeter was not scanned in the azimuthal direction.) The beam incident position was monitored and recorded by a polar angle encoder and an azimuthal angle encoder.

The trigger was defined by three trigger counters F2, F3, F4, and a veto counter V, as F2·F3·F4·$\bar{V}$·Beam Gate. Nominal trigger rate was about 1×10^4 events/burst.

Unlike the $\bar{p}p$-collider run, the exact incidence timing of the particle to the calorimeter is unpredictable in the fixed target experiment. Therefore a standard BAT cannot be used in the beam test and a CAMAC module DING-BAT has been developed instead, to generate the Before and After signals at a proper timing. Upon the completion of the readout of the previous event, DING-BAT brings the levels of both Before and After lines to high. Before then goes low after ~800 nsec interval, while After goes low at 2.6 μsec after the beam trigger. Both timing is programmable. These timing signals are then fed to RABBIT backplanes through Slave-BAT modules. HRW cards for the anode signal readout (negative polarity) were not available at the time of the beam test, so several CARROT cards were modified on their polarity and used for the anode signal.

Gas gain during the beam test was monitored by the same proportional tubes as used in the calorimeter. As listed in Table 2-2, 24 such tubes were mounted per calorimeter module. A 1 μCi Fe^{55} line source was attached to each tube and the signals were readout with LeCroy TRA1000. One of the two outputs of the amplifier was connected to LeCroy 2285 ADC via a 105 nsec delay line. The other output, which had opposite polarity, was fed to the discriminator via an inverter and a main amplifier to obtain high enough pulse height against the

threshold of the discriminator. The trigger of the Fe^{55} source signal was defined by the logical OR of these discriminator outputs in the interval of successive beam spills.

3.2 Electronics Calibration

The pads of the Endplug electromagnetic calorimeter have fairly large source capacitances, which impose a severe defect to charge amplifiers. The measured values of the pad capacitances are consistent with the following parallel plate formula

$$C = 8.855\,\varepsilon\,\frac{S}{d} \quad (pF), \tag{3-1}$$

where S is the area of the pads in [m^2], d is the distance between the surface of the plastic tube and the pad in [m], and ε is the dielectric constant of the material between the tube and the pad. In the case of the PEM calorimeter, typical values for S, d and ε are 3×3 cm^2 to 10×19 cm^2, ~70 μm, and 4, respectively. The maximum source capacitance comes from the second longitudinal segment, where 24 pads are ganged together in the longitudinal direction. Fig.3-2 shows the typical source capacitances of three longitudinal segments of the pads as functions of the pseudorapidity. It ranges from about 20 nF to 120 nF for the second segment, 3 nF to 20 nF for the first and the third segments. The gain of the charge amplifier with source capacitance C_S is given by the following formula [Ref.3-3]

$$G = G_0\,\frac{G_{OPEN}\,C_F}{G_{OPEN}\,C_F + C_S}\,\left(1 - exp\left(-\frac{t}{C_S\,R_{in}}\right)\right), \tag{3-2}$$

where G_0 is the amplifier gain without source capacitance and G_{OPEN} is the open loop gain, C_F is the feedback capacitance, R_{in} and t are the input impedance and the sampling time, respectively.

The open loop gain and the input impedance of the PEM CARROT card were measured to be [Ref.3-3]

$$G_{OPEN} = 5180 \qquad \delta G_{OPEN} = 280 \tag{3-3a}$$

$$R_{in} = 11.1\ \Omega \qquad \delta R_{in} = 0.6\ \Omega \tag{3-3b}$$

Thus the gain of typical CARROT channel with 100 nF source capacitance is reduced by about 15% at 2.6 μsec of the sampling time. Therefore the electronics gain of each channel should be calibrated with the source capacitance. It also causes a nonlinear effect so the calibration must be done at least to the quadratic term of the readout charge.

The sampling time t had to be changed from 2.6 μsec in the M-Bottom beam test to 1.6 μsec in the real CDF run due to the requirement from the Level 1 trigger decision time. A sampling time of 2.6 μsec was determined from a typical time constant of the PEM pad signal and used throughout the beam test. However, the calorimetry fastout signal at the trigger counting room had a ringing of about 0.5 μsec, and to leave a sufficient settle time and decision time for the Level 1 trigger, it had to be changed to 1.6 μsec. The gain change due to this change of the sampling time can directly be measured by injecting test charge. However, as seen from Eq.3-2, non-linear effect of the electronics responses gives a systematic uncertainty in the electronics gain calibration since the open loop gain, the source capacitance and the input impedance of the amplifier were not well controlled channel by channel.

3.3 Beam Test Results

The systematic error in measuring the electron/photon energies can be divided into three parts: (1) systematic error in transferring the observed charge into the energy (energy scale), (2) systematic error in calibrating the non-linear response of the detector and the electronics (linearity), and (3) systematic error in correcting for a local gain variation of the detector (mapping). In this section, these systematic errors in the energy measurement are evaluated with the beam test results.

3.3.1 Energy Scale

Determination of the energy scale is subject to several factors in converting the M-Bottom beam test to the real data taking environment. The operating high voltage has been changed from 1.8 kV of the beam test to 1.7 kV in the real data taking to get proper trigger

fastout gain preset by electronics. The gate width for the charge integration has been changed from 2.6 μsec to 1.6 μsec as described above. Charge calibration of the readout electronics for the gas gain monitoring system also gives a systematic error.

High Voltage Dependence

The high voltage curve of the PEM calorimeter can be fitted well with a function $Q = Q_0 \exp(AV)$, where Q is the total charge of the calorimeter at 100 GeV in pC and V is the supplied high voltage in kV. Fig.3-3 shows the high voltage dependence of the induced charge for anode and pad signals. Fitted results are [Ref.3-3]

$$Q_0^{anode} = (0.175 \pm 0.002) \times 10^{-4} \quad (pC/100GeV) \qquad (3\text{-}4a)$$

$$A^{anode} = 9.50 \pm 0.01 \quad (kV^{-1}) \qquad (3\text{-}4b)$$

for anode signals and,

$$Q_0^{pad} = (0.127 \pm 0.001) \times 10^{-4} \quad (pC/100GeV) \qquad (3\text{-}4c)$$

$$A^{pad} = 9.55 \pm 0.01 \quad (kV^{-1}) \qquad (3\text{-}4d)$$

for pads.

The total charge from the calorimeter is 370 pC per 100 GeV at 1.8 kV. On the other hand, the calorimetry trigger hardware requires this charge-to-energy scale be 125 pC per 100 GeV. The operational high voltage was chosen to be 1.7 kV for this reason and the trigger calibration constants were adjusted so that the charge-to-energy ratio becomes 125 pC per 100 GeV. Therefore the systematic error due to this gain change with the high voltage is given by,

$$\left|\frac{\delta Q}{Q}\right|_{HV} = \frac{\sqrt{\left|\frac{\partial Q}{\partial Q_0}\Delta Q_0\right|^2 + \left|\frac{\partial Q}{\partial A}\Delta A\right|^2}}{Q}$$

$$= 2.67 / 143 = 1.88 \times 10^{-2} \qquad (3\text{-}5)$$

Source Capacitance Dependence

The electronics gains of channels were calibrated with the onboard charge injection circuit shown in Fig.2-15 on channel-by-channel basis. Therefore the systematic error in the energy scale due to the source capacitance variance on each channel was minimized. Systematic errors due to the differences in the position of the charge generated with respect to the 4 m 12 Ω cable, and in the shape (especially the rise time) of the signal was estimated by injecting various signals with benchmark test and were inclusively estimated to be about 1%.

Gas Gain Monitoring System

Through the 1987 CDF run, total of 48 gas gain monitor tubes were monitored and it was observed that each of the signals were tracking closely to each other. The r.m.s. of each of the tubes from the average response of the tubes was 0.4%. However, due to the fact that different sets of monitor tube electronics were used in the 1985 beam test, systematic uncertainty of the overall gas gain was limited by the electronics gain, which was calibrated by charge injection circuit with 5% precision capacitor.

3.3.2 Mapping

Gain correction factor for each pad was obtained using scanning beam data as follows:

1) The sum of the signals from three longitudinal segments of each tower was taken as the minimum unit for gain correction. The summed signal for the k-th event is defined as A_{ik}^m for the i-th tower, and is corrected with a gain factor a_i, where beam was aimed at the center of the m-th tower. The calorimeter was moved to the next tower during the beam spills, scanning the whole detector. Average number of events accumulated at each tower was about 500.

2) The gain factor was obtained by solving the following equation:

$$\sum_{i=1}^{N} a_i \left(\frac{1}{K} \sum_{k=1}^{K} A_{ik}^{m} \right) = M \qquad (m = 1,...N) \qquad (3\text{-}6)$$

where M is the mean total charge which is a fixed constant. In the above calculation, range of the suffix i was constrained to $1.26 < |\eta| < 2.22$, while the suffix m ran through the whole range of the PEM calorimeter. This means that the gain factors of the innermost two η-rings and the outermost two were fixed to 1.

The gain correction (mapping) factors obtained by the above method are given in Table 3-1. Responses of the detector before and after this gain correction are given in Fig.3-4 (a) and (b) as a function of the polar angle. Data shown in Fig.3-4 (b) is the same sample as used for the calculation of Eq.3-6 (data set A), while the data in which beam was aimed at the pad boundaries (data set B) are shown in Fig.3-5. Standard deviation of the detector response in the range $12° < \theta < 30°$ was 1.3% in the data set B. Since the data set B was not used in the determination of the gain correction factors, it gives an inclusive error in the mapping correction.

Systematic uncertainties in the PEM energy scale are summarized in Table 3-2.

Chapter 4 THE CDF 1987 RUN

The first data-taking run for CDF took place during January–May, 1987. The Tevatron Collider delivered a total integrated luminosity of about 74 nb^{-1}. This chapter describes the online data taking environments and the event triggers used in this run. The CDF recorded approximately 4.8×10^5 events with the runs of electron and jet trigger, which corresponds to an integrated luminosity of 32.4 nb^{-1}. The amount of data used in this analysis is 4.1×10^5 events, or 27.4 nb^{-1}, after having eliminated the runs with detector problems or recording problems.

4.1 Online Control System

Fig.4-1 shows a simplified diagram of the CDF data acquisition system. As described in Chapter 1, raw signals from the CDF detector are converted into a flow of digital numbers and handled by the online Fastbus system. The data is read out by a mini-computer VAX11/785 (B0HOST) through the Unibus-Fastbus interface module, UPI. The process RUN_CONTROL, which runs on the VAX, gives a man-machine interface to the operator to control reading of events, detector calibrations and hardware diagnostics. A Fastbus module Event_Builder formats the raw data to YBOS bank structure [Ref.4-1]. YBOS is a name of memory management scheme and allows one to easily access the data from each subsystem of the detector. One YBOS data bank typically corresponds to one subsystem. The data banks which contain the raw detector response are called D-banks [Ref.4-2].

Buffer_Manager is a VAX process and governs the traffic of each event record. Several other VAX processes, so called "consumer processes", run in the typical CDF run. As described in Chapter 1, the Level 1, 2 and 3 processors examine each event record and put the

result of the examination into the trigger look-up table. Each trigger processor and consumer process give a list of requested events to the Buffer_Manager prior to the data taking, and Buffer_Manager then delivers each event record to each process according to the list. *V.I.P. consumer processes* such as Data_Logger and each trigger processor can take all events which satisfy the requested list, while normal consumer processes such as YMON can take only a fraction of the events.

Data_Logger receives all the events which passed all stages of trigger and put them onto 6250 bpi magnetic tape. The logging rate is limited by the hardware throughput and is 1 Hz at maximum. One 2400 ft of 6250 bpi tape finishes recording in about 15 minutes, and four tape drivers are switched back and forth to minimize the dead time due to tape logistics.

To monitor a performance of each subsystem of the detector on-line, a consumer process YMON collects a fraction of events during the data taking. The operator can determine whether each subsystem is functioning properly based on the monitor output. A similar monitoring process Trig_Mon is also used to monitor the performance of the trigger system and the trigger statistics.

4.2 Electron Trigger

Two types of Level 1 trigger sets were relevant to the electron analysis in analyzing the 1987 data. One was a jet trigger and the other was an electron trigger. As described in Chapter 1, the raw data from each calorimeter tower was summed into trigger towers. Each trigger tower was compared to Single Tower Threshold (STT) in the trigger table and then only the towers which exceed the threshold were summed into the total transverse energy sum (Total E_T). Then the Total E_T was examined with the threshold defined in the trigger table. The CDF Level 1 trigger system is able to examine four different sets of threshold at four different data summation timing ("summer"). Thus the same calorimetry data can be used up to four different combinations of thresholds and partition. In the 1987 run, the trigger summer A was dedicated

to the jet trigger and B and C summer were used for the electron trigger. Only the data from the electromagnetic calorimeter was used in the electron trigger and both electromagnetic and hadron calorimeters were used in the jet trigger. The combinations of the STT and the Total E_T varies with each component, trigger set, and the luminosity at the time data were taken. Table 4-1 summarizes the sets of jet and electron triggers used in the 1987 run, and the integrated luminosity of each trigger type is shown in Table 4-2. (See Appendix B for the calculation of the luminosity.)

Chapter 5 THE OFFLINE ANALYSIS: ELECTRON IDENTIFICATION

5.1 Overview

The structure of the CDF offline package was determined by the requirement that each physicist from the 17 institutions which constitute the collaboration should be able to do physics with fully corrected data from every CDF subsystem. The analysis is based on "parton level" algorithms, which identify jets, electrons, muons, and neutrinos (by missing E_T), and which incorporate the detailed knowledge of the experts for each subsystem.

Raw data go through a "production" analysis at Fermilab, which generates physics oriented output streams based on the above "parton" level analysis, such as jets above certain thresholds, multijets, electrons, minimum bias physics, etc. Data from each output streams are written to separate data summary tapes (DST's). This production job and the subsequent DST analysis were performed under the framework of "ANALYSIS_CONTROL" [Ref.5-1].

5.2 Event Reconstruction

The raw data written onto magnetic tapes are just the enumerations of digitized ADC or TDC counts of detector channels. To obtain a meaningful physics quantities, such as particle momenta or energies, one has to reconstruct each event from the raw data according to the detector structure. The formats of the data banks at various analysis stages are defined in "Data Analysis Structure" (DAIS) [Ref.5-2]. In this section, software modules which are used in the electron analysis path of the ANALYSIS_CONTROL are described.

Fig.5-1 shows the event analysis path of the electron analysis. Data flow between the modules is controlled by using YBOS [Ref.4-1] banks. Each module has a certain set of input/output banks.

5.2.1 D-to-E module and Noise Suppression

CADTOE module converts the calorimetry raw data banks, or D-banks, expressed in terms of ADC counts, to E-banks, the energy bank, in which the unit of the energy deposit is GeV. Each entry of the D- and E-banks corresponds to each channel of the calorimeter. For example, the raw data bank of the central EM calorimeter is CEMD and the corresponding E-bank is CEME. All the calorimetry E-banks are combined into monolithic E-bank TOWE by TOWECR module.[1]

Tracking D-banks, such as CTCD or VTWD banks, are calibrated for their T0's and drift time by TRKDTE module and the corrected data is stored into corresponding E-banks.

On an event by event basis, there exist several types of calorimetry problems affecting the data adversely. The TOWECR module has been modified to find such defects and eliminate them from the sum of the energies in each tower (sum over photo-multiplier tubes or over longitudinal segmentations). For the CEM, CHA, and WHA calorimeters, the most common problems are single photo-multiplier hits from either Čerenkov light produced in the light guides and/or PM discharge in one of the tubes [Ref.5-3].

[1] CADTOE and TOWECR modules are combined into CALORIMETRY module in the CDF offline package V-4.4 and later version.

A relatively naive algorithm was used to eliminate such occurrence of the single PM hits in the offline version 4.3 production and the post production analysis for the 1987 data.[1] A tower was suppressed when the lower energy of the tubes was less than 100 MeV and the higher energy was greater than 2 GeV.

In the gas calorimetry, similar unphysical events were observed, in which only one layer of the gas chambers had an energy deposit. This problem is known to be caused by slow neutrons (see Appendix C). In the PEM calorimeter, however, two more types of single layer hit events were observed (see Appendix D), both of which are understood as the detector discharge. As described in Chapter 2, the pad readout of the PEM calorimeter has three depth segments. Therefore this type of noise can easily be distinguished from the normal electromagnetic shower by looking into the ratio R of the energy deposit on each tower.

In the TOWECR module, all PEM towers which satisfy the following conditions,

$$E_i^{\max} \geq 5 \text{ GeV and } R_i^{\max} \geq 0.98, \tag{5-1a}$$

where

[1]Current version of the single PM spike suppression algorithm uses the cuts on the log of the ratio of the energy in the two tubes.

When E_0 and E_1 (the energy of the two tubes) are both > 0, then

$$|\log \frac{E_0}{E_1}| < \frac{\text{Width}}{\Lambda} + N_\sigma \frac{\sigma}{\sqrt{E}}$$

passes the cut where,

Width	is the width of the calorimeter module
Λ	is the attenuation length of the scintillator
N_σ	is the number of sigma to cut (4 for CEM and 3 for CHA, WHA)
σ	is the constant which represents the calorimeter energy resolution
E	is the energy (= $(E_0+E_1)/2$)

and when E_0 (E_1) is ≤ 0, then E_1 (E_0) < N_σ T passes the cut where T is a constant.

$$E_i^{\max} = \max(E_i^0, E_i^1, E_i^2) \tag{5-1b}$$

$$R_i^{\max} = \frac{E_i^{\max}}{E_i^0+E_i^1+E_i^2} \tag{5-1c}$$

were removed (set to zero). Here E_i^0, E_i^1 and E_i^2 are the energy deposit in the first, second and third longitudinal segment of the i-th tower, respectively. As shown in Fig.5-2, the real electromagnetic shower signals are safely kept by the above cuts.

The electronics gain correction of the calorimetry is performed online in the CDF experiment. As described in Chapter 3, CARROT system has a self-charge injection system and a charge calibration run (EQI) is typically taken once per week. These calibration constants are downloaded to MX's at each begin-run of the data taking, and the detector signal is calibrated online on channel-by-channel basis. However, the EQI constants for the gas calorimetry, PEM, PHA, FEM and FHA were inversely multiplied by mistake in the 1987 run, causing a systematic gain non-uniformity. It was not until mid-June of 1988 that this mistake became clear, therefore all the offline production paths have been completed with this systematics. To correct this mistake, FIX_DBANK module has been developed and it was applied to the output of the production tapes (DST's). This systematics has about 15 % effect in detector non-uniformity as shown in Fig.5-3. Fortunately this systematics does not cause any serious problem in selecting events at the production stage, because the Electron stream kept EM clusters of $E_T \geq 5$ GeV as described in Table 5-1 when associated tracks are present, while we are interested in relatively high E_T of electron (≥ 15 GeV) in this analysis.

5.2.2 Vertex finding

The event primary Z-vertex was determined from the VTPC wire data by VTVERT module. The E_T of each calorimeter tower was calculated with $\sin\theta$ which were corrected with the vertex offset. The vertex information obtained by VTVERT module was stored

into EVTA bank and the vertex corrected values of $sin\theta$ for η-rings of towers were stored into SETA bank.

5.2.3 Calorimeter Clustering

In the CDF electron algorithm, an electron was identified by a calorimeter cluster. Fig.5-4 illustrates how this clustering algorithm works. First, all the calorimeter towers of $E_T \geq 3$ GeV in the electromagnetic calorimeter were picked up and defined as "seed towers". Once a tower was picked up, it was called as "parent" and neighboring eight towers ("daughters") were then examined and included into the same cluster if their electromagnetic energies were $E_T \geq 0.1$ GeV and the parent-daughter ratio was ≤ 1. This step was continued until: (1) no more towers meeting the above criteria can be picked up, or (2) daughters search hits the size limit of the cluster window. The window size was defined as centered at the seed tower, spans three towers in η and one tower in φ at the CEM calorimeter, and five by five at the PEM/FEM calorimeters. Informations from the hadron calorimetry were not used at the clustering stage. The name of the module which performed this electromagnetic clustering was ELEANA in the CDF offline package V-4.3 and was EMCLST in V-4.4 or later.

5.2.4 Strip Reconstruction

In the CEM and PEM calorimeters, strip chambers give a precise information about the position of the electron. A clustering algorithm similar to EMCLST was performed in each θ and φ view, and the clusters in each view in the same detector module were "matched" according to their energies. Informations of one-view strip clusters were stored into CESS and PESS banks, and the view-matched clusters into CASS banks, both by the STPANA module. All strip clusters which overlap with the cluster towers were regarded as "associated strip clusters" and the position of the most energetic associated strip cluster was used as the electron position from the calorimeter.

5.2.5 Track Reconstruction

Track Reconstruction was done by TRCONTROL module. In the electron finding algorithm, a track reconstruction was required only for tracks which are within $\pm$ 15° in φ around the electromagnetic cluster. The minimum transverse momentum to be reconstructed was 2 GeV/c. Tracks whose extrapolated points were inside the cluster towers were regarded as "associated tracks". Some tracks were reconstructed only two dimensionally due to the limited number of hit points in the tracking chambers. For those tracks, only the φ coordinate was known in the CTC and the θ in the VTPC. These were picked up as associated tracks based on the known coordinate only.

5.3 Missing Et Analysis

In the CDF detector, energy carried by neutrino cannot be detected and appears as a missing transverse energy. (Note that the longitudinal component of the neutrino cannot be measured in the hadron collider since spectator jets carry away the longitudinal momentum balance.) The missing transverse energy vector, or $\vec{\not{E}}_T$, was measured as the opposite of the vector sum of the transverse energy over all calorimeter towers:

$$\vec{\not{E}}_T = - \sum_{i}^{\text{all towers}} \vec{E_T}^i , \qquad (5\text{-}2)$$

here i indicates the tower index and runs over all calorimeter towers except for the six rapidity rings of the forward and the backward calorimeters closest to the beam pipe, where the azimuthal coverage is not complete due to the intrusion of the low-β quadrupoles. This calculation was done with NAIVET module from TOWE bank and the results were stored into METS bank.

Because of the neutron problem as described earlier in this chapter, any cluster with less than 5% electromagnetic energy is regarded as background. A study of a sample of jet triggers

shows that (0.03 ± 0.03) % of real jet clusters would be eliminated by this cut. Also at the post production analysis, the TOWE bank was re-created with FIX_DBANK module which fixed the wrong EQI calibration in the gas calorimetry, and the METS bank was re-constructed with this new TOWE bank.

5.4 DST Production

As already mentioned, the CDF recorded approximately 4.8×10^5 events in the 1987 run. Raw data tapes were processed by the CDF Production Group by using the offline package V-4.3 at the Fermilab VAX cluster and the data was reduced to various kinds of physics data summary tapes (DST's). The electron data stream was reduced to 134 DST's. The cuts used in this stage are summarized in Table 5-1. The amount of raw events processed to produce these 134 tapes corresponds to about 4.1×10^5 events, which corresponds to an integrated luminosity of 27.4 nb^{-1}.

5.5 Data Reduction

A scheme of the cuts used in this electron analysis stream is sketched in Fig.5-5. Two different sets of cuts were used to identify electrons in the Central and the Endplug region respectively. If the cluster seed tower was in the CEM calorimeter, the cuts for the Central electron were applied, and if it was in the PEM calorimeter, the cuts for the Endplug electron were used. To ensure a complete energy measurement of the electron, a fiducial volume cut was applied to both calorimeters. In the CEM calorimeter, if the seed tower resided in the outermost ring of towers in η, that cluster was discarded (Tower 9 veto). Similarly the innermost one η-ring and the outermost two were discarded in the PEM calorimeter.

These cuts were applied to the 134 tapes of the electron DST data sample. DST analysis was done at University of Tsukuba using a mini-computer VAX 8800 and the CDF offline package V-4.4.

The Central electron sample obtained after these cuts were relatively clean compared to the one from the Endplug, and it was mainly because the measurement of the momenta of associated tracks was superior in this region. To reduce the copious background in the Endplug region, the lateral and the longitudinal shower shapes were taken into consideration.

5.5.1 Central electron cuts

The following quantities were examined to establish the inclusive Central electron sample above the electron transverse energy $E_T(e) \geq 15$ GeV. These cuts were established by the Central electron group and the distributions of these quantities can be found in references 3-3 and 5-4

Had/EM cut

Had/EM is the ratio of the cluster transverse energy measured by the hadron calorimetry and the electromagnetic calorimetry. Most of the energy in nominal electromagnetic shower is well contained to the electromagnetic calorimeter as shown in Fig.5-6. Cut was made at 0.1 at the production stage and at 0.05 in tight selection criteria.

Isolation cut

Isolation I is the scalar sum of extra transverse energy around the electron, normalized by the electron E_T:

$$I(\mathrm{R}=0.4) \equiv \frac{\sum_{\Delta R<0.4} E_T^i - E_T(e)}{E_T(e)} \qquad (5\text{-}3a)$$

where ΔR is the distance of a centroid of the EM cluster and a center of each tower,

$$\Delta R = \sqrt{\Delta\varphi^2 + \Delta\eta^2} \qquad (5\text{-}3b)$$

and E_T^i is the transverse energy of the i-th tower around the electron within the cone size $\Delta R<0.4$.

Number of tracks

Number of associated tracks were counted if the extrapolation of each track passes through one of the towers in the cluster. At least one associated track was required as an electron candidate.

E/p cut

E/p is the ratio of the transverse energy of the electron measured by calorimetry and the transverse momentum measured by the central tracking chamber.

A total of 142 events remained after the set of these "Central Electron Cuts" as shown in Fig.5-5.

5.5.2 Plug electron cuts

In the Endplug calorimeter region, the following quantities were examined to establish the inclusive plug electron sample above the electron transverse energy $E_T(e) \geq 15$ GeV.

Had/EM cut

The definition of the Had/EM is the same as in the central region. The Had/EM distributions of the test beam 100 GeV electrons and 200 GeV electrons are given in Fig.5-7. Cut is made at 0.1 for the loose cut and 0.05 for the tight cut.

Isolation cut

Isolation I is also defined similarly as in the central region (eq.5-3). Cut is made at 0.3 for the loose cut and 0.1 for the tight cut.

Number of tracks

In the plug region, coverage of the CTC chamber is not complete and therefore the VTPC tracks must also be taken into consideration. A fixed size window around the cluster centroid was used to pickup the CTC and VTPC tracks (CTCS and VTCS banks). Size of the window for the CTC tracks was $\pm 5°$ in the φ direction and $\pm$ 20 cm in the radial direction around the cluster centroid, and $\pm 5°$ and $\pm$ 10 cm for the VTPC tracks.

Longitudinal chi-square cut

The PEM calorimeter has three longitudinal segments in the pad readout as described in Chapter 2. The energy fraction of the first and second segments X_i (i = 0,1) was measured cluster-by-cluster and their deviation from the nominal electromagnetic shower obtained from the beam test was calculated as $\chi^2_{\text{longitudinal}}$, or ζ [Ref.5-5].

$$\zeta \equiv \sum_{i\ j} (X_i - \overline{X_i(E)}) M^{-1}_{ij}(E) (X_j - \overline{X_j(E)}) \qquad \text{(5-4a)}$$

where E is the cluster energy and $M^{-1}_{ij}(E)$ is an inverse matrix of generalized standard deviation matrix $M_{ij}(E)$ obtained from the beam test.

$$M_{ij}(E) = \frac{1}{N} \sum_{n=1}^{N} (X_i - \overline{X_i(E)})(X_j - \overline{X_j(E)}) \qquad \text{(5-4b)}$$

Distributions of ζ from test beam data at various beam energies are shown in Fig.5-8. As seen from the figure, the ζ distribution is nearly independent of the electron energy ranging from 20 GeV to 200 GeV. Cutting ζ at 4 retains 94.8% of electrons at 100 GeV and the variation of the efficiency is 1.0% in the range 20 ~ 200 GeV.

Lateral chi-square cut

The lateral electromagnetic shower shape was parameterized with an isometric exponential function around the cluster centroid and the deviations from the test function was calculated as a chi-square at 25 towers around the cluster seed tower (5 rows in η and 5 rows in φ).

A test function

$$F(\mathrm{R}) = Ae^{-\mathrm{R}/\sigma}, \qquad \text{where } A = \frac{E}{2\pi\sigma} \tag{5-5}$$

is assumed as the electromagnetic shower shape. Here E is the cluster energy, R is the distance between the point of interest and the shower centroid, and the shower width σ is fixed to 1.6 cm by test beam analysis. F is then integrated over each tower area S_i and compared to the actual data D_i. $\chi^2_{\mathrm{lateral}}$ is defined as the summation of the square of the residuals normalized by 10 % of the energy deposit[1] in each tower.

$$\chi^2_{\mathrm{lateral}} = \frac{1}{N_{\mathrm{tower}}} \sum_{i=1}^{N_{\mathrm{tower}}} \left| \frac{D_i - \int_{S_i} F(\mathrm{R})\mathrm{ds}}{\delta D_i} \right|^2 \tag{5-6}$$

where $\delta D_i = 0.1 D_i$

$N_{\mathrm{tower}} = 25$ for 5×5 window

A typical distribution of $\chi^2_{\mathrm{lateral}}$ is shown in Fig.5-9. Cutting electron data sample at $\chi^2_{\mathrm{lateral}} \leq 10$ retains about 94 % of electrons at electron energy 100 GeV and above, and decreases slowly as energy decreases as shown in Fig.5-10(a). It also has a

[1]"Error" of each tower used here was obtained empirically in analyzing electron test beam data. Therefore the absolute value of $\chi^2_{\mathrm{lateral}}$ does not necessary reflect the number of degree of freedom in its distribution.

systematics on the tower size S_i as the test function F does not reflect the actual shower shape completely. Thus the efficiency of the electron on this $\chi^2_{\mathrm{lateral}}$ cut is a function of the tower size S_i, namely the polar angle (Fig.5-10b). Both effects give systematics in the calculation of the electron efficiencies as will be discussed in Chapter 7.

Track-cluster position matching

As a resolution of the track momentum measurement was inferior in the Endplug calorimeter region, the track position matching cut was used instead of E/p cut to select electron data sample. The position of the cluster centroid was measured from the energy weighting method. If the cluster was in the region where strip chambers exist, the position obtained from the strip cluster analysis was used and compared to the extrapolated position from the associated CTC tracks in the azimuthal direction ($\Delta\varphi_{\mathrm{CTC}}$). Otherwise the position matching between the cluster position by the pad and the VTPC tracks were used in the radial direction (ΔR_{VTPC}).[1]

By applying the plug electron cuts shown in the Fig.5-5, 134 events of the plug inclusive electron candidates remained (*PEM e sample*).

5.5.3 "W cuts"

The electron cuts described above are general purpose criteria for identifying the electron and hence the events passed through these cuts are inclusive electron data sample. These samples are still dominated by QCD backgrounds. To get a pure W sample, following cuts were applied additionally.

[1]The position matching of the cluster and the track was done at the shower maximum plane of the PEM calorimeter which was perpendicular to the beam axis at $z = \pm 190$ *cm*.

Dijet cut

The QCD background events contained in the above inclusive electron sample mostly consist of two-jet events, in which one of the jets fakes an electron either by overlapping or by photon conversion. Therefore a cut based on back-to-back two-jet topology gives a powerful reduction of this kind, at a price of certain amount of the W events which have recoil jets coming from higher order diagrams.

The CDF standard jet clustering algorithm JCLST2 [Ref.5-6] was used to define jets for $E_T \geq 5$ GeV. The Dijet quantity D is the ratio of the scalar sum of the jet E_T within 30° in the azimuth angle with respect to the 180° opposite of the electron.

$$D \equiv \frac{\sum_{\Delta\varphi=180°\pm30°} E_T(\text{jet})}{E_T(e)} \qquad (5\text{-}7)$$

Cut was made at $D \leq 0.3$. The efficiency of this cut to the $W \rightarrow e\nu$ events was studied by using ISAJET Monte Carlo as will be shown in Chapter 7.

Missing Et cut

Another characteristics of the QCD background events is that they usually do not have real missing energy as opposed to the $W \rightarrow e\nu$ process, in which the neutrino carries a large fraction of the W energy. The missing E_T of the QCD background arises from the finite resolution of the energy measurement. Thus it is convenient to define the missing E_T significance χ :

$$\chi \equiv \not{E}_T^2 / \sum E_{Tpc}\,, \qquad (5\text{-}8)$$

where $\sum E_{Tpc}$ is a scalar sum of the transverse energy in the central and plug calorimetry. The reasons the forward/backward calorimetry is excluded from this calculation are: (1) the forward/backward calorimetry had pedestal shift problems in the electronics and the slow neutron problems described earlier, (2) we are focusing on the

$W \rightarrow e\nu$ events in which the electron goes into the central or plug calorimetry and the resolution of the electron E_T measurement dominates in the error of the missing E_T calculation. Thus normalizing $\not{E}_T$ with the sum E_T of central and plug region gives a looser cut than normalizing with the total E_T sum. Cut was made at $\chi \geq 7.8$ GeV.

Total of 22 events remained after the set of "Central Electron Cuts" and "W cuts" [Ref.3-3]. Fig.5-11 shows these 22 events in the $E_T(e)$-$\not{E}_T$ plane.

Fig.5-12 shows the scatter plot of the $\not{E}_T$ and the electron E_T of 134 events of the plug electron sample. One can see a shoulder or a tail in the $\not{E}_T$ and the electron E_T projection at around E_T = 40 GeV due to the W Jacobian peak, but it is also clearly seen from the figure that this event sample is still dominated by the background events at lower E_T. By looking these events by the Event_Display program, most of them appear as QCD overlap backgrounds. Fig.5-13 (a) shows a scatter plot of the missing E_T significance χ and the isolation I(R=0.4) for the event sample before making χ and I(R=0.4) cuts. By applying the "W cuts" described above, the number of events was reduced to 9. Scatter plot of $\not{E}_T$ versus $E_T(e)$ of these 9 events is shown in Fig.5-14. Table 5-2 is an event list of these 9 events. Event display of these 9 events are given in Fig.5-15.

Fig.5-16 shows the distribution of the various quantities used in this analysis for the loose cuts sample and the final 9 plug W candidates.

5.5.4 "Z cuts"

Z candidates were obtained by applying the additional second cluster cuts to the Central inclusive electron sample described above. Since we have limited statistics in data, a relatively loose set of cuts were applied to the secondary electron to keep the Z efficiency high.

Primary cluster cuts

Requires the same set of cuts as described in the section 5.5.1 to the electron cluster in the CEM region.

Second cluster cuts

Requires the second electron cluster of Had/EM ≤ 0.1 and $E_T(e) \geq 5$ GeV in any region of the detector. If it is in the central region or in the plug region, number of associated tracks ≥ 1 is also required and if it is in the central region, E/p ≤ 2 is required additionally.

Total of 15 events remained after the set of "Z cuts". There were 12 events above $M_{ee} \geq 20$ GeV/c^2 as shown in Fig.5-17, where the efficiency was not affected by the cluster E_T thresholds. By scanning these events with the Event_Display program, 6 events of $M_{ee} <$ 60 GeV/c^2 appeared to be QCD backgrounds. In fact, all of these events will disappear if we tighten the criteria on the second electron cuts. Remaining 6 events of $M_{ee} \geq 60$ GeV/c^2 appear to be the $Z^0 \rightarrow e^+e^-$ candidates. They are listed in Table 5-3. Event display of these 6 candidates are shown in Fig.5-18. As seen from Fig.5-18, the second electrons hit the detector boundaries in Run 7767, Event 940 and in Run 7744, Event 5364. In Run 7288, Event 1276, the second electron which went into the forward calorimeter had an associated photon. In Run 7769, Event 4235, an isolated hard photon was observed together with electron pairs (Fig.5-18f). The mass of the $ee\gamma$ system was obtained to be 95.2 GeV/c^2 for this particular event. The dielectron masses listed as M_{12} in Table 5-3 and plotted in Fig.5-17 are not corrected for these effects and just took two highest E_T clusters as an electron pair. The effects of the detector boundaries and the photon emission were taken into consideration in Chapter 7.

Chapter 6 MONTE CARLO STUDY OF THE BACKGROUND

Background contaminations in the W and Z sample were estimated separately on each background process.

6.1 Background Estimate to the W event sample

The following process were considered as the source of the background to the $W \rightarrow e\nu$ process and the numbers of contamination were estimated by using the real data or Monte Carlo simulations.

1) Electrons from Tau Decay

$W \rightarrow \tau\nu \rightarrow e\nu\nu$

2) Electrons from Z^0 decay and one of the electron is undetected or mismeasured

$Z^0 \rightarrow e^+e^-$

3) Electrons from semi-leptonic decay of heavy flavor quarks

$Q\bar{Q} \rightarrow$ jets + $e\nu$

4) Other QCD Background

Overlap of photons and charged hadrons

γ-conversions

The processes 1), 2) and 3) were evaluated by using ISAJET V-6.10 Monte Carlo event generator package [Ref.6-1] and CDFSIM, the CDF detector simulation package [Ref.6-2] V-4.4. (Tracking simulation code was linked from V-4.5.)

6.1.1 Electrons From Tau Decay

The process $W \rightarrow \tau\nu \rightarrow e\nu\nu\nu$ was generated by ISAJET V-6.10 and simulated with the CDFSIM V-4.4/4.5. Fig.6-1 shows the electron E_T distribution before the detector simulation (a) and after the simulation (b). By applying the same set of cuts described in Chapter 5, total of 208 events out of 2999 events remained in the Endplug region. This efficiency corresponds to 6.94 ± 0.50 %. (The error shown here is statistical only.) Scaling this efficiency to the observed number of $W \rightarrow e\nu$ candidates divided by $\tau \rightarrow e\nu\nu$ branching ratio (16.5 ± 0.9 % [Ref.6-3]), one gets 0.3 ± 0.1 background events.

6.1.2 Electrons From Z Decay

The process $Z^0 \rightarrow e^+e^-$ in which one of the electrons is mismeasured in energy or undetected due to the detector cracks can also fake $W \rightarrow e\nu$ signature. This type of background was evaluated by generating $Z^0 \rightarrow e^+e^-$ events with ISAJET V-6.10 and simulated with the CDFSIM V-4.4/4.5 package. By applying the same set of cuts used in the W analysis, 33 events remained out of 2995 events. Fig.6-2 is a scatter plot of the missing E_T versus the E_T of higher E_T electron which is found in the Endplug calorimeter. The efficiency was 1.1 ± 0.2 % and by using the $\sigma_Z B(Z^0 \rightarrow e^+e^-)$ which will be obtained in Chapter 7, the number of this background to the Endplug W sample was estimated to be 0.12 ± 0.06 events.

6.1.3 Electrons From Heavy Flavor Decay

Background from the heavy flavor quark decay was estimated for $b\bar{b}$ and $t\bar{t}$ production. Again, ISAJET V-6.10 and CDFSIM V-4.4/4.5 were used. Integrated luminosity 528 nb^{-1} equivalent of $b\bar{b}$ data was generated and 815 events had electrons with E_T above 10 GeV, none of which passed the same set of electron cuts as the $W \rightarrow e\nu$ candidates. Therefore the number of background from the bottom quark decay was estimated to be less than 0.05 events. For the $t\bar{t}$ production, two sets of data were

generated with the top quark masses of 40 GeV/c^2 and 60 GeV/c^2. The equivalent integrated luminosities were 247 nb^{-1} and 4.23 pb^{-1}, respectively. None of the events passed the W cuts in the 40 GeV/c^2 sample, and one event left in the 60 GeV/c^2 sample. Thus the contribution of the semi-leptonic decays of top quarks as a background was estimated to be less than 0.1 events.

6.1.4 Other QCD Background

Contamination of the QCD background to the $W \rightarrow e\nu$ sample was estimated from the real data. These are mostly the overlapping of the photons and the charged hadrons or γ-conversions which essentially has no real missing energy. A "Background Sample" was created by requiring the same set of calorimetry cuts described in Chapter 5, but had no associated tracks pointing to the cluster. Thus the data sample largely consists of isolated photons from π^0 or η in QCD jets. For nominal QCD events, the main source of the missing E_T comes from the energy mismeasurement due to limited detector resolution. The energy resolution of the calorimetry is proportional to the square root of the energy;

$$\Delta E = \alpha_0 \sqrt{E} \qquad (6\text{-}1)$$

where α_0 is 14~28% for electromagnetic calorimetry and ~125% for hadron calorimetry, as shown in Table 1-1. The resolution of the missing E_T measurement for the QCD background depends on the calorimetry resolution α (averaged over electromagnetic and hadronic components of jets), sum of the scalar E_T seen in the calorimetry, and the event topology.

$$\Delta \not{E}_T = k\,\alpha\sqrt{\Sigma E_T} \qquad \text{where } k = 1/\sqrt{2} \text{ for isometric event and } 1 \text{ for pencil-like event} \qquad (6\text{-}2)$$

Therefore the missing E_T significance χ defined by Eq.5-8 distributes as an exponential for the background events which have no real missing energy.

Fig.6-3 shows the χ distribution for the background event sample which passed the same set of the plug electron calorimetry cuts but had no associated tracks. As clearly seen from the figure, events are dominated at the low χ region and it has an exponential slope $y = Ae^{-a\chi}$. Here a corresponds to the detector resolution σ in the missing E_T as $\sigma = 1/\sqrt{2}a$. Assuming the χ distribution does not change significantly in the overlapped QCD background with the associated tracks and assuming none of the events having $\chi < 7.8$ GeV result from $W \rightarrow e\nu$ decays, one can estimate the contamination of this background to the plug W event sample from the following formula,

$$B = (N_1/N_2)\, n_2 \tag{6-3a}$$

$$\text{where} \quad N_1 = \int_0^{x_0} Ae^{-a\chi}\, d\chi = \frac{A}{a}\left[1 - e^{-ax}\right] \tag{6-3b}$$

$$N_2 = \int_{x_0}^{\infty} Ae^{-a\chi}\, d\chi = \frac{A}{a}e^{-ax} \tag{6-3c}$$

$$\text{with } x_0 = 7.8 \text{ GeV} \tag{6-3d}$$

and n_2 is the number of events having failed the cut $\chi \geq 7.8$ GeV in the plug electron data sample. Fitting to Fig.6-3 gives,

$$A = 1.62 \pm 0.25 \tag{6-4a}$$

$$a = 0.391 \pm 0.045 \quad [\text{GeV}^{-1}] \tag{6-4b}$$

and n_2 is 6 events from Fig.5-13(b). Therefore B is estimated to be 0.30 ± 0.16 events.

The number of estimated background events to the $W \rightarrow e\nu$ process are summarized in Table 6-1.

6.2 Background Estimate to the Z event sample

Two kinds of processes were considered as backgrounds to $Z^0 \rightarrow e^+e^-$ sample. One was the overlapping background of QCD two jet events, and the other was the semi-leptonic decay channel of the heavy flavor quarks. The overlapping QCD background was estimated using the

real data sample, while the heavy flavor background was estimated by ISAJET V-6.10 Monte Carlo simulation and CDFSIM V-4.4/4.5.

6.2.1 QCD Overlapping Background

To estimate the background contribution from two-jet final states to the distribution of the dielectron mass M_{ee} (Fig.5-17), a separate background data sample which passed the cuts shown in Table 6-2 were used. This background sample has two or more electromagnetic clusters per event which passes the calorimetry cuts but has no associated tracks. Therefore most of events in this sample are two-jet. Mass of the photon pair of these 343 events are plotted in Fig.6-4 for $M_{\gamma\gamma} \geq 20$ GeV/c^2. Assuming the shape of the "M_{ee}" distribution of the two-jet background sample does not change significantly by the associated tracking cuts, one can estimate the contribution of the two-jet background to the looser Z sample by the formula,

$$B = (N_1/N_2)\, n_2 \tag{6-5}$$

where $N_1(N_2)$ is the total number of events having passed (failed) the cut $M_{ee} \geq 60$ GeV/c^2 in the above background sample and n_2 is the number of events having failed the cut $M_{ee} \geq 60$ GeV/c^2 in the Z sample (Fig.6-4). From Fig.5-17 and Fig.6-4 N_1, N_2 and n_2 are 19, 324 and 6 events respectively and therefore B is estimated to be 0.35 ± 0.08 events.

6.2.2 Heavy Flavor Background

Events which contains electrons from the semi-leptonic decay of $b\bar{b}$ were generated with ISAJET V-6.10 and they were simulated with CDFSIM V-4.4/4.5 package. Integrated luminosity 8.6 pb^{-1} worth of $b\bar{b}$ events were generated and were applied the same set of cuts as the Z sample. None of the events remained after the cuts, accounting the number of this kind of background to the Z sample be less than 0.003 events.

The number of estimated background events to the $Z^0 \rightarrow e^+e^-$ process are summarized in Table 6-3.

Chapter 7 RESULTS AND DISCUSSIONS

The production cross sections and the masses of the charged and neutral intermediate vector bosons are evaluated from the event samples obtained in Chapter 5, after calculating various cut efficiencies and the energy scale correction.

7.1 Cross Sections of the W and Z

7.1.1 Cross Section of the W Boson

The production cross section of the W boson for the inclusive process $\bar{p}p \rightarrow W^{\pm} + anything$ times the branching ratio of the succeeding decay $W \rightarrow e\nu$ was obtained from the relation,

$$\sigma_W B(W \rightarrow e\nu)_{CEM} = \frac{N_{obs}^{CEM} - N_{bkgd}^{CEM}}{\varepsilon_{geom}^{CEM}\, \varepsilon_{algo}\, \varepsilon_{trig}\, L_{CEM}} \qquad (7\text{-}1a)$$

for the CEM electron and

$$\sigma_W B(W \rightarrow e\nu)_{PEM} = \frac{N_{obs}^{PEM} - N_{bkgd}^{PEM}}{\varepsilon_{geom}^{PEM}\, \varepsilon_{algo}\, (\varepsilon_{15} L_{15} + \varepsilon_{20} L_{20})} \qquad (7\text{-}1b)$$

for the PEM electron, where N_{obs}^{CEM} and N_{obs}^{PEM} are the observed numbers of $W \rightarrow e\nu$ candidates in which the electron/positron goes into the central and the plug calorimeter respectively. N_{bkgd}^{CEM} and N_{bkgd}^{PEM} are the numbers of background events in the corresponding region, ε_{geom}^{CEM} and ε_{geom}^{PEM} are the detector acceptance for each calorimeter, ε_{trig}, ε_{15}, ε_{20} are the trigger efficiencies for the CEM trigger, PEM trigger with total E_T threshold $\leq$ 15 GeV and 20 GeV, respectively (see Table 4-1). L_{CEM}, L_{15} and L_{20} are the integrated luminosity

of the corresponding trigger type, and ε_{algo} is the overall efficiency of the electron identification algorithm.

Some fraction of data was taken with triggers in which the PEM total E_T threshold was 20 GeV. Meanwhile the offline analysis was done at $E_T(e) \geq 15$ GeV cut and therefore the production cross section for the W boson have to be calculated separately in the CEM and the PEM detector. They are then combined into one cross section with

$$\sigma_W B(W \rightarrow e\nu) = \frac{(\sigma B)_{CEM} / (\Delta\sigma B_{CEM})^2 + (\sigma B)_{PEM} / (\Delta\sigma B_{PEM})^2}{1 / (\Delta\sigma B_{CEM})^2 + 1 / (\Delta\sigma B_{PEM})^2}, \qquad (7\text{-}2)$$

where $(\sigma B)_{CEM}$ and $(\sigma B)_{PEM}$ are the W production cross sections calculated from each detector component and $\Delta\sigma B_{CEM}$ and $\Delta\sigma B_{PEM}$ are their statistical errors.

The efficiencies for the various CEM electron cuts and the W production cross section $(\sigma B)_{CEM}$ was obtained by K. Yasuoka *et al* in the reference 5-4,

$$(\sigma B)_{CEM} = 2.6 \pm 0.6 \text{ (stat.)} \pm 0.5 \text{ (syst.) nb} \qquad (7\text{-}3)$$

and the efficiencies of the CEM analysis are summarized in Table 7-1.

Luminosity

Integrated luminosity was calculated from the number of events observed by BBC. (See Appendix B.) The numbers of BBC events were recorded run by run and the integrated luminosity was calculated for each trigger type (Table 4-2).

$$L_{CEM} = 27.4 \pm 4.1 \text{ nb}^{-1} \qquad (7\text{-}4a)$$

$$L_{15} = 13.5 \pm 2.0 \text{ nb}^{-1} \qquad (7\text{-}4b)$$

$$L_{20} = 13.9 \pm 2.1 \text{ nb}^{-1} \qquad (7\text{-}4c)$$

Here errors are 15% uncertainty which is in the BBC cross section calculation.

Geometrical Acceptance

The detector geometrical acceptance of the PEM calorimeter was obtained by running ISAJET V-6.10 Monte Carlo and CDFSIM V-4.4 detector simulation.

$$\varepsilon_{geom}^{PEM} = 0.30 \pm 0.01 \pm 0.02 \,. \tag{7-5}$$

The first error is statistical in the Monte Carlo calculation and the second is the systematic in choosing among different set of structure functions.

Trigger Efficiency

Trigger efficiencies were also calculated with ISAJET V-6.10 and CDFSIM V-4.4 detector simulation. The efficiencies that E_T of the electron from W decay exceeds 15 GeV and 20 GeV thresholds in the plug region are

$$\varepsilon_{15} = 0.90 \pm 0.04 \pm 0.03, \tag{7-6a}$$

$$\varepsilon_{20} = 0.82 \pm 0.04 \pm 0.03, \tag{7-6b}$$

respectively. Here the first errors are statistical in the Monte Carlo and the second are the systematic of the structure functions.

Algorithm Efficiency

Algorithm efficiency was broken into the efficiencies of each cut and they were individually evaluated either from the Monte Carlo data or from test beam data. They are summarized in Table 7-1. Overall algorithm efficiency for the PEM $W \rightarrow e\nu$ sample is

$$\varepsilon_{algo} = 0.49 \pm 0.07 \pm 0.04 \,. \tag{7-7}$$

The first error is statistical in estimating efficiencies from the Monte Carlo or from the test beam data, and the second is systematics of the energy or position dependence of

each cut, choice of the distribution functions and the uncertainty in the tracking fiducial volume.

From Eq.7-1b and Eqs.7-4 to 7-7, the production cross section from the PEM calorimeter was obtained to be,

$$(\sigma B)_{PEM} = 2.0 \pm 0.7 \text{ (stat.)} \pm 0.4 \text{ (syst.) nb.} \tag{7-8}$$

Statistical and systematic errors in Eqs.7-5 to 7-7 are added quadrature respectively and shown as systematic error in Eq.7-8. From Eqs.7-2 and 7-3, combined production cross section of the W production cross section is

$$\sigma_W B(W \rightarrow e\nu) = 2.3 \pm 0.4 \text{ (stat.)} \pm 0.5 \text{ (syst.) nb.} \tag{7-9}$$

Using the theoretical branching ratio $B(W \rightarrow e\nu) = 0.089$ (m_t = 40 GeV/c^2), total cross section of the W boson is put on Fig.7-1 together with the UA1/UA2 results [Ref.1-15] and the theoretical predictions by Altarelli *et al* [Ref.1-4]. The statistical and systematic errors are added quadrature in the figure. The experimental results briefly match with the theoretical predictions within the errors, but they are systematically above the theoretical predictions. This point will be discussed later in this chapter.

7.1.2 Cross Section of the Z Boson

The production cross section of the Z boson for the inclusive process $\bar{p}p \rightarrow Z^0 + anything$ times the branching ratio of the succeeding decay $Z^0 \rightarrow e^+e^-$ was obtained from the relation,

$$\sigma_Z B(Z^0 \rightarrow e^+e^-) = \frac{N_{obs}^Z - N_{bkgd}^Z}{\varepsilon_{geom}^Z \, \varepsilon_{algo} \, \varepsilon_{trig} \, L} \tag{7-10}$$

where N_{obs}^Z is the observed number of $Z^0 \rightarrow e^+e^-$ candidates, N_{bkgd}^Z is the number of background events, ε_{geom}^Z is the detector acceptance for the $Z^0 \rightarrow e^+e^-$ events, ε_{algo} and

ε_{trig} are the algorithm efficiency and the trigger efficiency with total E_T threshold ≥ 15 GeV, respectively. L is the luminosity of the electron sample used for the Z analysis (same as L_{CEM} in Eq.7-4a). They are summarized in Table 7-2 and $\sigma_Z B(Z^0 \rightarrow e^+e^-)$ is obtained as

$$\sigma_Z B(Z^0 \rightarrow e^+e^-) = 0.4 \pm 0.2 \text{ (stat.)} \pm 0.1 \text{ (syst.) nb} . \quad (7\text{-}11)$$

Using the theoretical branching ratio $B(Z^0 \rightarrow e^+e^-) = 0.032$ (m_t = 40 GeV/c^2), total cross section of the Z boson is put on Fig.7-2 together with the UA1/UA2 results [Ref.1-15] and the theoretical predictions by Altarelli *et al* [Ref.1-4]. The statistical and systematic errors are added quadrature in this figure. As in the case of the W total cross sections, the experimental results are slightly above the theoretical predictions.

7.1.3 R and number of neutrinos / top quark mass

From Eqs.7-9 and 7-11, the ratio of the cross sections defined by Eq.1-1 is given as

$$R = 5.8 \pm 3.1 \text{ (stat.)} \pm 1.1 \text{ (syst.)} . \quad (7\text{-}12)$$

Note that the 15% error of the integrated luminosity cancels here. Systematic error in Eq.7-12 consists only of the error of the efficiency calculation and the background estimation. This number is somewhat smaller than the theoretical prediction of R = 8.62 ± 0.28 at $\sqrt{s}$ = 2 TeV and m_t = 50 GeV/c^2 [Ref.1-10], but is consistent within the error. The data favors the number of light neutrino species to be three and relatively light top quark mass, but further statistics is necessary to draw any conclusion.

7.2 Mass of the W and Z Bosons

7.2.1 Energy Corrections

Before determining the *W/Z* boson masses from the obtained event sample, the detector responses were carefully studied with beam test results and electron energies were

corrected. These corrections include the calorimeter response map and the dead layers in the gas calorimetry sampling medium.

Mapping

Calorimetry non-uniformity was mapped with test beam data. The incident point of the electron was determined either from tracking information or from strip chamber information. Systematic uncertainty of the CEM response map was 1% [Ref.3-1], and for the PEM it was 1.3% as described in Chapter 3.

Dead Layer Correction

In the 1987 CDF run, we had several dead chamber layers in the PEM calorimeter. Since the pad readout is ganged longitudinally, these dead layers give a systematic energy mismeasurement in the quadrant. The position of the dead layers has been recorded run-by-run basis, and the correction factors for the cluster energies were obtained by interpolating anode signals of the adjacent two layers for each event. Error of this correction method was obtained by applying this algorithm to a live layer on beam test data and was obtained to be 1.2% at beam energies above 50 GeV.

7.2.2 Determination of the W mass

Fig.7-3 shows the transverse mass $M_T(e\nu)$ distribution of the 31 events of $W \rightarrow e\nu$ candidates. Transverse mass $M_T(e\nu)$ is defined by

$$M_T(e\nu) = \sqrt{2\, E_T^e\, \not{E}_T\, (1 - \cos\varphi_{e\nu})} , \quad (7\text{-}12)$$

where $\varphi_{e\nu}$ is the azimuthal angular difference between the electron and neutrino, E_T^e and $\not{E}_T$ are the transverse energy of the electron and neutrino, respectively. Events in which the electrons go into the Endplug calorimeter are shown in the hatched area. To determine the W boson mass, a set of Monte Carlo sample of $W \rightarrow e\nu$ was generated with ISAJET V-6.10 and CDFSIM V-4.4 at various M_W values. EHLQ Set 2 Structure function [Ref.1-6]

was used to produce the W longitudinal momentum. Dotted cross in this figure is the Monte Carlo data at M_W = 81 GeV/c^2. At each M_W, the χ^2 of the fitting to the data (solid line) was calculated. The results are given in Table 7-3 and Fig.7-4 shows the χ^2 of the fitting as a function of generated M_W. The W mass which gives this χ^2 minimum is obtained to be

$$M_W = 82.1 \pm 2.0 \pm 1.2 \text{ GeV/c}^2, \tag{7-13}$$

where first error is statistical which gives the unit rise in the χ^2 and the second error is systematic. The systematic error of M_W can be broken into two parts,

$$\left(\frac{\Delta M_W}{M_W}\right)^2 = \left(\frac{\Delta M_W}{M_W}\right)^2_{\text{scale}} + \left(\frac{\Delta M_W}{M_W}\right)^2_{\text{resol}} \tag{7-14}$$

Here $\left(\frac{\Delta M_W}{M_W}\right)_{\text{scale}}$ is the systematic scaling error in the calorimeter energy calibration,

$$\left(\frac{\Delta M_W}{M_W}\right)^2_{\text{scale}} = \left(\frac{\Delta M_T}{M_T}\right)^2_{\text{scale}}$$

$$= \frac{1}{N^2}\left[N_C{}^2\left(\frac{\Delta E}{E}\right)^2_{\text{CEM scale}} + N_P{}^2\left(\frac{\Delta E}{E}\right)^2_{\text{PEM scale}}\right]$$

$$= 1.5\ \% \tag{7-15}$$

where N_C and N_P are the number of the $W \rightarrow e\nu$ events in the central and plug region, and $\left(\frac{\Delta M_W}{M_W}\right)_{\text{resol}}$ is the systematic error due to the finite resolution of the calorimeters.

$$\left(\frac{\Delta M_W}{M_W}\right)^2_{\text{resol}} = \frac{1}{N^2}\sum_{i=1}^{N}\left(\frac{\Delta M_T}{M_T}\right)^2_{\text{resol}} = 0.3\ \% \tag{7-16a}$$

where,

$$\left(\frac{\Delta M_T}{M_T}\right)^2_{\text{resol}} = \left(\frac{1}{2}\frac{\Delta E_T^e}{E_T^e}\right)^2 + \left(\frac{1}{2}\frac{\Delta \not{E}_T}{\not{E}_T}\right)^2 \tag{7-16b}$$

Here $\left(\frac{\Delta E}{E}\right)_{\text{CEM scale}}$ is obtained from the reproducibility of the CEM module calibration in the test beam and is 0.6% [Ref.3-1], while $\left(\frac{\Delta E}{E}\right)_{\text{PEM scale}}$ is estimated to be 5% due to the uncertainty in the electronics gain calibration in the gas gain monitoring system. Calorimetry resolutions for $\frac{\Delta E_T^e}{E_T^e}$ is typically 2% for the W electrons (E_T^e ~ 40 GeV) and $\frac{\Delta \not{E}_T}{\not{E}_T}$ is determined from Eqs.5-8 and 6-4 (typically 20%). The error in measuring the azimuth opening angle between the electron and the missing E_T vector is negligible compared to these two.

The result Eq.7-13 is put in Fig.7-5 together with the UA1/UA2 results [Ref.1-16]. The statistical and systematic errors are added quadrature. They are consistent to each other within the error bars.

7.2.3 Electron Pair Mass Distribution of the Z Candidates

As described in Section 5.6.3, 2 events of the $Z^0 \rightarrow e^+e^-$ candidates have associated photons, and the energy measurements of the second electron cluster in other 2 events were relatively inferior due to their locations by the detector boundaries. For the events with a photon (Run 7288 Event 1276 and Run 7769 Event 4235), three-body masses were calculated instead of the electron pair mass. In Run 7377 Event 830, the cluster energy of the secondary electron was corrected with CTC momentum since it hit the tower 8 of the Central calorimeter, where the energy containment of the shower is incomplete. The electron hit the θ = 30° crack in Run 7767 Event 940. Only part of the electron energy is captured in the Endplug calorimeter. To estimate the undetected energy of this electron, the shower exit point was evaluated from the wire information and the shower function was integrated over the observed range of depth to estimate the leakage. Corrected electron

energies and pair mass of these 6 events are listed in Table 7-4 and Fig.7-6. The mass distribution is shown in Fig.7-7 together with the ISAJET V-6.10 Monte Carlo and the detector simulation for M_Z = 93 GeV/c^2. The distribution of the masses of these 6 events is consistent with the Monte Carlo. However no conclusion can be made on the Z^0 mass since the number of the events are limited and the energy corrections to these events are so large.

7.3 Discussions

As mentioned in section 7.1, the total cross sections of the W and Z obtained from this analysis and the UA1/UA2 experimental results are systematically higher than the predictions made by Altarelli *et al.* The discrepancies are of 15~30% level in the case of the W boson, and 40% or more for the Z boson. The branching ratios used in plotting the Figs.7-1 are 7-2 are assumed the top quark mass be 40 GeV/c^2. If the top quark mass is 70 GeV/c^2 or heavier, the discrepancy between the data and theoretical predictions in the W/Z total cross section would be explained. Lighter W boson mass than 83 GeV/c^2 would also raise the theoretical values, but it is unlikely that the mass of the W boson differs more than 5% according to Fig.7-5. Remaining uncertainties are the higher order QCD contributions and the parton distribution functions at small x values. As the statistics of the experimental data increases, efforts should be made to reduce these theoretical uncertainties.

Chapter 8 SUMMARY AND CONCLUSIONS

The production of the intermediate vector bosons $W^{\pm}$ and Z^0 and their decay to the electron channel have been observed at $\sqrt{s}$ = 1.8 TeV at the Fermilab Tevatron $\bar{p}p$ collider. The luminosity of the data used for this analysis was 27.4 nb^{-1} at $\sqrt{s}$ = 1.8 TeV. Total of 9 events which were consistent with the process $\bar{p} + p \rightarrow W^{\pm} + anything \rightarrow e^{\pm} + \nu(\bar{\nu}) + anything$ were observed at the Endplug calorimeter region of the CDF detector as well as 22 events in the central calorimeter. Total of 6 events which were consistent with $\bar{p} + p \rightarrow Z^0 + anything \rightarrow e^+ + e^- + anything$ were also observed. The production cross sections and the branching ratios for these process have been measured to be:

$$\sigma \cdot B(W^{\pm} \rightarrow e^{\pm} + \nu(\bar{\nu})) = 2.3 \pm 0.4 \text{ (stat.)} \pm 0.5 \text{ (syst.) nb},$$

$$\sigma \cdot B(Z^0 \rightarrow e^+ + e^-) = 0.4 \pm 0.2 \text{ (stat.)} \pm 0.1 \text{ (syst.) nb}.$$

These results are in reasonable agreement with theoretical predictions [Ref.1-4], and have reasonable dependence on $\sqrt{s}$, compared to the results from the UA1/UA2 experiments at CERN [Ref.1-16].

The transverse mass distribution of the 31 events of the $W \rightarrow e\nu$ candidates were fitted with the Monte Carlo events with the detector simulation, including the smearing of the energy resolution. The fitting result was:

$$M_W = 82.1 \pm 2.0 \text{ (stat.)} \pm 1.2 \text{ (syst.) GeV/c}^2$$

which was also in good agreement with the UA1/UA2 results within errors.

APPENDIX

Appendix A

The CDF Collaboration

F.Abe[p], D.Amidei[c], G.Apollinari[k], G.Ascoli[g], M.Atac[d], P.Auchincloss[n], A.R.Baden[f], A. Barbaro-Galtieri[i], V.E.Barnes[l], E.Barsotti[d], F.Bedeschi[k], S.Belforte[k], G.Bellettini[k], J.Bellinger[q], J.Bensinger[b], A.Beretvas[n], P.Berge[d], S.Bertolucci[e], S.Bhadra[g], M.Binkley[d], R.Blair[a], C.Blocker[b], J.Bofill[d], A.W.Booth[d], G.Brandenburg[f], A.Brenner[d], D.Brown[f], A.Byon[l], K.L.Byrum[q], M.Campbell[c], R.Carey[f], W.Carithers[i], D.Carlsmith[q], J.T.Carroll[d], R.Cashmore[1], F.Cervelli[k], K.Chadwick[l,d], T.Chapin[m], G.Chiarelli[k], W.Chinowsky[i], S.Cihangir[o], D.Cline[q], D.Connor[j], M. Contreras[b], J.Cooper[d], M.Cordelli[e], M.Curatolo[e], C.Day[d], R.DelFabbro[k], M.Dell'Orso[k], L.DeMortier[b], T.Devlin[n], D.DiBitonto[o], R.Diebold[a], F.Dittus[d], A.DiVirgilio[k], R.Downing[g], G. Drake[d], T.Droege[d], M.Eaton[f], J.E.Elias[d], R.Ely[i], S.Errede[g], B.Esposito[e], A.Feldman[f], B.Flaugher[n], E.Focardi[k], G.W.Foster[d], M.Franklin[f,g], J.Freeman[d], H.Frisch[c], Y.Fukui[h], S.Galeotti[k], I.Gaines[d], A.F.Garfinkel[l], P.Giannetti [k], N.Giokaris[m], P.Giromini[e], L.Gladney[j], M.Gold[i], K.Goulianos[m], J.Grimson[d], C.Grosso-Pilcher[c], C.Haber[i], S.R.Hahn[j], R.Handler[q], D.Hanssen[d], R.M.Harris[i], J.Hauser[c], Y.Hayashide[p], T.Hessing[o], R.Hollebeek[j], L.Holloway[g], P.Hu[n], B.Hubbard[i], P.Hurst[g], J.Huth[d], M.Ito[p], J.Jaske[q], H.Jensen[d], R.P.Johnson[d], U.Joshi[n], R.W.Kadel[d], T.Kamon[o], S.Kanda[p], I.Karliner[g], H.Kautzky[d], K.Kazlauskis[n], E.Kearns[f], R.Kephart[d], P.Kesten[b], H.Keutelian[g], Y.Kikuchi[p], S.Kim[p], L.Kirsch[b], S.Kobayashi[2], K.Kondo[p], U.Kruse[g], S.E.Kuhlmann[l], A.T.Laasanen[l], W.Li[a], T.Liss[c], N.Lockyer[j], F.Marchetto[o], R.Markeloff[q], L.A. Markosky[q], M.Masuzawa[p], P.McIntyre[o], A.Menzione[k], T.Meyer[o], S.Mikamo[h], M.Miller[j], T.Mimashi[p], S.Miscetti[e], M.Mishina[h], S.Miyashita[p], H.Miyata[p], N.Mondal[q], S.Mori[p], Y.Morita[p], A.Mukherjee[d], A.Murakami[2], Y.Muraki[3], C.Nelson[d], C.Newman-Holmes[d], L.Nodulman[a], J.O'Meara[d], G.Ott[q], T.Ozaki[p], S.Palanque[4], R.Paoletti[k], A.Para[d], D.Passuello[k], J.Patrick[d], R.Perchonok[d], T.J.Phillips[f], H.Piekarz[b], R.Plunkett[m], L.Pondrom[q], J.Proudfoot[a], G.Punzi[k], D.Quarrie[d], K.Ragan[j], G.Redlinger[c], R.Rezmer[a], J.Rhoades[q], L.Ristori[k], T.Rohaly[j], A.Roodman[c], H.Sanders[c], A.Sansoni[e], R.Sard[g], V.Scarpine[g], P.Schlabach[g], E.E.Schmidt[d], P.Schoessow[a], M.H.Schub[l], R.Schwitters[f], A.Scribano[k], S.Segler[d], M.Sekiguchi[p], P.Sestini[k], M.Shapiro[f], M.Sheaff[q], M.Shibata[p], M.Shochet[c], J.Siegrist[i], V.Simaitis[g], J.K.Simmons[l], P.Sinervo[j], M.Sivertz[5], J.Skarha[q], D.A.Smith[g], F.Snider[c], L.Spencer[b], R.St.Denis[f], A.Stefanini[k], Y.Takaiwa[p], K.Takikawa[p], S.Tarem[b], D.Theriot[d], J.Ting[c], A.Tollestrup[d], G.Tonelli[k], W.Trischuk[f], Y.Tsay[c], K.Turner[d], F.Ukegawa[p], D.Underwood[a], C.vanIngen[d], R.VanBerg[j], R.Vidal[d], R.G.Wagner[a], R.L.Wagner[d], J.Walsh[j], T.Watts[n], R.Webb[o], T.Westhusing[g], S.White[m], V.White[d], A.Wicklund[a], H.H.Williams[j], T.Winch[q], R.Yamada[d], T.Yamanouchi[d], A.Yamashita[p], K.Yasuoka[p], G.P.Yeh[d], J.Yoh[d], F.Zetti[k]

CDF Member Institutions

[a] Argonne National Laboratory- [b] Brandeis University- [c] University of Chicago
[d] Fermi National Accelerator Laboratory- [e] INFN, Laboratori Nazionali di Frascati, Italy
[f] Harvard University- [g] University of Illinois- [h] KEK, Japan
[i] Lawrence Berkeley Laboratory-[j] University of Pennsylvania
[k] INFN, University and Scuola Normale Superiore of Pisa, Italy- [l] Purdue University
[m] Rockefeller University- [n] Rutgers University- [o] Texas A&M University
[p] University of Tsukuba, Japan- [q] University of Wisconsin

Visitors

[1] Oxford University, England- [2] Saga University, Japan
[3] ICRR, Tokyo University, Japan- [4] CEN, Saclay, France-
[5] Haverford College, Haverford, PA.

Appendix B Calculation of the Integrated Luminosity

The integrated luminosity is calculated as the number of coincidences of both proton and the anti-proton direction of the BBC counters, divided by the part of the total $\bar{p}p$ cross section seen by the BBC. The original plan was to measure the BBC cross section by simultaneously using the Forward Silicon detector to get the total $\bar{p}p$ cross section. This scheme, however, did not work in the 1987 CDF run, since the Forward Silicon detector had a difficulty in observing elastic scattering events. Therefore the total cross section had to be estimated from the BBC information only [Ref.b-1].

To estimate the BBC cross section, the total cross section and the ratio of various components, elastic, single diffractive, double diffractive and hard core at $\sqrt{s}$ = 1.8 TeV was estimated based upon the extrapolation from the lower energy data and a Monte Carlo program. Then the acceptance of the BBC for each inelastic process was calculated with a detector simulation.

The extremes of the predicted total cross section at $\sqrt{s}$ = 1.8 TeV is 74 mb and 80 mb [Ref.b-2]. The smaller value is derived from the extrapolation from lower energy data and assuming that the cross section is asymptotically constant at very high energies but locally proportional to $\log^2 s$, while the larger value results from assuming the cross section to continue to evolve proportionally to $\log^2 s$. Taking the mean of these two extremes, the total cross section is,

$$\sigma_{tot} = (77 \pm 6) \text{ mb}$$

where the error is chosen simply to allow the value to comfortable span the entire range of the predictions.

The ratio σ_{el}/σ_{tot} is predicted as 0.229 by Goulianos for $\sqrt{s}$ = 1.8 TeV [Ref.b-3]. This gives

$$\sigma_{el} = (17.6 \pm 1.6) \text{ mb}$$

where the error results from the uncertainty in the total cross section above, and the uncertainty in the ratio σ_{el}/σ_{tot}.

Using these values of σ_{tot} and σ_{el}, the inelastic cross section is given by

$$\sigma_{in} = \sigma_{tot} - \sigma_{el} = (59.4 \pm 4.7) \text{ mb}$$

The inelastic cross section itself breaks up into three components, hard core, σ_o, and single and double diffractive, σ_{sd} and σ_{dd}, respectively. Here the components σ_{sd} and σ_{dd} were estimated based upon the UA5 measurement and the extrapolation, then σ_o was calculated. UA5 has measured [Ref.b-4] the single diffractive cross section to be (7.8 ± 1.2) mb at $\sqrt{s}$ = 900 GeV (The convention of the single diffractive cross section here is that it is the sum of the proton and anti-proton components, thus for comparison the values given by Goulianos, for example, must be multiplied by two). By the extrapolation from the lower energy data [Ref.b-1] and by the analysis of the BBC scalar done by Giokaris and Goulianos [Ref.b-5], the single diffractive cross section was taken to be

$$\sigma_{sd} = (15.0 \pm 5.0) \text{ mb}$$

and the double diffractive cross section to be

$$\sigma_{dd} = (4.2 \pm 1.0) \text{ mb}$$

Using these values, σ_o can be given as

$$\sigma_o = \sigma_{in} - \sigma_{sd} - \sigma_{dd} = (40.2 \pm 6.9) \text{ mb}$$

and using the Rockefeller Monte Carlo acceptances for the BBC we get

$$\sigma_{BBC} = 0.134\sigma_{sd} + 0.618\sigma_{dd} + 0.942\sigma_o = (42.5 \pm 6.0) \text{ mb}$$

Finally, the integrated luminosity is given by

$$\int L\, dt = \frac{\textit{Number of events observed by BBC}}{\sigma_{BBC}}$$

Appendix C Slow Neutron Noise in the Gas Calorimetry

In the 1987 CDF run, many events were observed in the gas calorimetry, especially in the forward hadron (FHA) calorimeter, at the trigger rates much more than expected. By looking into these events, it appeared that only one layer in the longitudinal segmentation had a hit at a time. This phenomenon, so called "Texas Tower", is understood as caused by a slow proton in the gas chamber knocked out by a slow neutron which is produced by the accelerator or by the uranium bars used in the crack filler detector between the central calorimeter modules:

$$n + p \rightarrow n + p \,.$$

Typically 1 MeV/c of proton releases its kinetic energy of about 1/3 MeV through ionization process in a gas medium. This released energy is several hundreds to several thousands times as much as in the minimum ionization process. Thus the number of the ion pairs produced by one slow proton is comparable to the one produced by a high energy shower. This problem has lead to the decision that the plug and the forward hadron calorimeters were taken out from the trigger system in the 1987 run.

Energy equivalent of a minimum ionization particle (MIP) and the impact of a slow proton ionization in the CDF calorimetry is estimated as follows:

	CEM	CHA	PEM	PHA	FEM	FHA
# of layers	30	30	34	20	28	13
Sensing medium	Scintillator	Scintillator	Gas	Gas	Gas	Gas
Medium thickness / layer [mm]	5	10	7	10	7	10
Actual energy loss of MIP in a layer [KeV]	1,005	2,010	2.7	3.8	2.7	3.8
Shower equivalent MIP energy [MeV]	300	2,200	~250	~3,000	~250	~4,000
Shower equivalent MIP energy / layer [MeV]	10	73	7.4	150	8.9	308
Shower equivalent slow proton (1/3 MeV) energy [GeV]	0.003	0.012	0.91	13	1.1	27

Appendix D PEM Spike Noise

In the 1987 CDF run, it turned out that a single chamber hit, so called *PEM spike noise* dominated over the real signal. By studying the characteristics of this noise, the sources were turned out to be two categories: (a) beam luminosity proportional (slow neutron) and (b) detector oriented (discharge).

Existence of the PEM spike noise is most evident in the scatter plot of the single layer anode energy versus the sum of the anode energies in the quadrant, as shown in Fig.D-1 (a). To localize the noise, it was defined as follows: For the anode signal,

$$E_i^{anode} > 5 \text{ GeV, and } E_{i-1}{}^{anode} + E_{i+1}{}^{anode} < 1 \text{ GeV} \qquad \text{(D-1a)}$$

where E_i^{anode} is the energy deposit of the i-th layer in GeV. For the pad signal,

$$E_i^{pad} > 5 \text{ GeV, and } \frac{E_i^{pad}}{\sum_{j=0}^{2} E_j^{pad}} > 0.98 \qquad \text{(D-1b)}$$

where E_i^{pad} is the energy deposit of the i-th depth in each tower. Fig.D-2 shows the scatter plot of the spike energies seen from pads and anodes. The pad energy of the spike was taken by picking up the JCLST2 cluster which contains the spike tower defined by Eq.D-1b. Three distinctive groups are obvious according to the pad to anode ratio. They are named as *Group 1*, *Group 2* and *Group 3*, from the larger pad/anode ratio to the smaller. These three groups have characteristic localization over the PEM calorimeter as shown in Fig.D-3. The Group 1 and 3 spikes are localized at smaller η rings, and have periodical distribution over the azimuthal angle, while the Group 2 spike seems to spread uniformly over the detector and is proportional to the trigger threshold and the beam luminosity.

These observations of the spike noise lead to the conclusions that the Group 2 spike is caused by the slow neutron as in the other gas calorimetry (Appendix C), while the Group 1 and 3 spikes are due to the discharge between the high voltage bus line and the G10 print circuit board at certain edge of the tube end board (see Fig.2-3).

REFERENCES

Ref.1-1 General review of the gauge theories is given in:
E. S. Abers and B. W. Lee, Phys. Rep. **9**(1973)1;
For general introductory texts to the high energy physics, see the following books and references therein:
D. H. Perkins, *Introduction to High Energy Physics*, Third Edition, Addison-Wesley, 1987
V. Barger, R. Phillips, *Collider Physics*, Addison-Wesley, 1987

Ref.1-2 S. Glashow, Nucl. Phys. **22**(1961)579;
S. Weinberg, Phys. Rev. Lett. **19**(1967)1264;
A. Salam, Elementary Particle Theory: Relativistic Groups and Analyticity (Nobel Symposium No.8), edited by N.Svartholm, Almqvist and Wiksell, Stockholm, 1968, p.367

Ref.1-3 UA1 Collab., G. Arnison *et al*, Phys. Lett. **122B**(1983)103;
UA2 Collab., M. Banner *et al*, Phys. Lett. **122B**(1983)476

Ref.1-4 G. Altarelli, K. Ellis, M. Greco and G. Martinelli, Nucl. Phys. **B246**(1984)12;
G. Altarelli, K. Ellis and G. Martinelli, Z. Phys. **C27**(1985)617

Ref.1-5 D. Duke and J. Owens, Phys. Rev. **D30**(1984)49

Ref.1-6 E. Eichten, I. Hinchliffe, K. Lane and C. Quigg, Rev. Mod. Phys. **56**(1984) 579; and Errata, preprint, Fermilab-Pub-86/75-T(1986)

Ref.1-7 M. Glück, E. Hoffmann and E. Reya, Z. Phys. **C13**(1982)119

Ref.1-8 F. Halzen and K. Mursula, Phys. Rev. Lett. **51**(1983)857;
K. Hikasa, Phys. Rev. **D29**(1984)1939;
N. G. Deshpande, G. Eilam, V. Barger and F. Halzen, Phys. Rev. Lett. **54**(1985)1757;
D. Dicus, S. Nandi and S. Willenbrock, Phys. Rev. Lett. **55**(1985)132

Ref.1-9 A. D. Martin, R. G. Roberts and W. J. Stirling, Phys. Lett. **B189**(1987)220

Ref.1-10 F. Halzen, C. S. Kim and S. Willenbrock, Phys. Rev. **D37**(1988)229

Ref.1-11 EMC Collab., J. J. Aubert *et al*, Nucl. Phys. **B259**(1985)189; Phys. Lett. **B123**(1983)123
BCDMS data is unpublished. See the references in Ref.1-9 and in Ref.1-10.

Ref.1-12 R. Phillips, preprint, RAL-88-076 (1988)

Ref.1-13 A. Datta, M. Drees, R. M. Godbole, X. R. Tata, Phys. Rev. **D37**(1988)1876

Ref.1-14 M. J. Marciano *et al*, Phys. Rev. **D29**(1984)945

Ref.1-15 UA1 Collab., C. Albajar *et al*, Phys. Lett. **198B**(1987)271;
UA2 Collab., R. Ansari *et al*, Phys. Lett. **194B**(1987)158

Ref.1-16 UA1 Collab., G. Arnison *et al*, Europhys. Lett. **1**(7)(1986)327;
UA2 Collab., J. Appel *et al*, Z. Phys. C **30**(1986)1

Ref.1-17 F. Abe *et al*, Nucl. Inst. and Meth. **A271**(1988)487

Ref.1-18 F. Bedeschi *et al*, Nucl. Inst. and Meth. **A268**(1988)50

Ref.1-19 F. Snider *et al*, Nucl. Inst. and Meth. **A268**(1988)75

Ref.1-20 G. Drake *et al*, Nucl. Inst. and Meth. **A269**(1988)68

Ref.1-21 E. Barsotti *et al*, Nucl. Inst. and Meth. **A269**(1988)82

Ref.1-22 D. Amedai *et al*, Nucl. Inst. and Meth. **A269**(1988)51

Ref.1-23 J. Carrol *et al*, Nucl. Inst. and Meth. **A263**(1988)199

Ref.2-1 Y. Fukui *et al*, Nucl. Inst. and Meth. **A267**(1988)280

Ref.2-2 M. Atac *et al*, CDF Note 477(1986)

Ref.2-3 F. Sauli, Principle of operation of multiwire proportional and drift Chambers, CERN 77-09(1977)

Ref.3-1 L. Balka *et al*, Nucl. Inst. and Meth. **A267**(1988)272
K. Yasuoka *et al*, Nucl. Inst. and Meth. **A267**(1988)315
S. R. Hahn *et al*, Nucl. Inst. and Meth. **A267**(1988)351
S. Bertolucci *et al*, Nucl. Inst. and Meth. **A267**(1988)301

Ref.3-2 Y. Fukui, CDF Note 266

Ref.3-3 M. Shibata, Doctoral Thesis, *Study of Charged Intermediate Vector Boson Production in Proton-Antiproton Collisions at* $\sqrt{s}$ *= 1.8 TeV*, Univ. of Tsukuba, UTPP-31(1988)

Ref.4-1 D. Quarrie, CDF Note 156

Ref.4-2 C. Blocker *et al*, CDF Note 152

Ref.5-1 M. Shapiro and D. Quarrie, CDF Note 384

Ref.5-2 F. Dittus, CDF Note 292

Ref.5-3 R. Wagner, CDF Note 433(1986)

Ref.5-4 K. Yasuoka *et al*, CDF Note 784(1988)
L. Nodulman *et al*, CDF Note 614(1988)

Ref.5-5 Y. Fukui *et al*, CDF Note 488(1986)
M. Shibata, CDF Note 599(1988)

Ref.5-6 S. Kim, CDF Note 439(1985) and references therein

Ref.6-1 F. Paige and S. D. Protopopescu, *ISAJET Monte Carlo*, BNL 38034(1986)

Ref.6-2 J. Freeman, *Guide to the CDF Detector Simulation*,
CDF file `C$DOC:SIMGUIDE.MEM`(1985);
T. Kamon, Y. Hayashide, J. Freeman, CDF Note 287(1985)

Ref.6-3 Particle Data Group, Phys. Lett. **170B**(1986)1

Ref.b-1 T. M. Liss, CDF Note 552(1987)

Ref.b-2 M. M. Block and R. N. Cahn, Phys. Lett. **188B**(1987)143

Ref.b-3 K. Goulianos, Private communication.

Ref.b-4 R. E. Ansorge *et al*, Z. Phys. C, 33(1986)175

Ref.b-5 N. Giokaris and K. Goulianos, Private communication.

TABLES

Table 1-1 The properties of the CDF calorimetry. [Ref.1-17]

CDF Electromagnetic Calorimetry

	Forward	Endplug	Central
Angular Range	$2° \sim 10°$	$10° \sim 37°$	$37° \sim 90°$
Tower Size	$\Delta\eta \sim 0.1$	$\Delta\eta = 0.045$ or 0.09	$0.087 < \Delta\eta < 0.13$
	$\Delta\varphi = 5°$	$\Delta\varphi = 5°$	$\Delta\varphi = 15°$
Absorber	Lead	Lead	Lead
Sampling medium	gas tubes	gas tubes	polystyrene scintillator
Radiation Length per Layer (X_o)	0.9	0.53	0.6
$\Delta E / E$	$\sim 27\% / \sqrt{E}$	$\sim 28\% / \sqrt{E}$	$\sim 14\% / \sqrt{E}$
Position Resolution (mm)	2 ~ 4	1 ~ 2	1.5 ~ 3

CDF Hadron Calorimetry

	Forward	Endplug	Endwall	Central
Angular Range	$2° \sim 10°$	$10° \sim 30°$	$30° \sim 45°$	$45° \sim 90°$
Tower Size	$\Delta\eta \sim 0.1$	$\Delta\eta = 0.09$	$.08 < \Delta\eta < .12$	$.1 < \Delta\eta < .15$
	$\Delta\varphi = 5°$	$\Delta\varphi = 5°$	$\Delta\varphi = 15°$	$\Delta\varphi = 15°$
Absorber	Iron	Iron	Iron	Iron
Sampling medium	gas tubes	gas tubes	acrylic scintillator	acrylic scintillator
$\Delta E / E$	$\sim 125\% / \sqrt{E}$	$\sim 14\%$ at 50 GeV	$\sim 14\%$ at 50 GeV	$\sim 70\% / \sqrt{E}$

Table 2-1 Material thickness of the CDF endplug calorimeter.

	Physical Thickness	Radiation Length (X_0)	Pion Absorption Length
Front Cover Plate : Fe (z = 173.99 ~ 175.26 cm)	12.7 mm	0.722	0.05971
Each Sampling Layer (z = 175.26 ~ 226.06 cm)			
Lead Panel (Ca : 0.065%, Sn : 0.7%)	2.69 mm	0.480	0.0134
Chamber Layer			
Cu-Clad G-10	1.6 mm	0.013	0.0033
Conductive Plastic Tube			
(Wall: 0.8 mm, ID: 7.0 mm × 7.0 mm)	8.6 mm	0.007	0.0037
Cu-Clad G-10	1.6 mm	0.013	0.0033
Epoxy	0.2 mm		0.0003
50 μm G-10	0.05 mm		0.0001
(Only on Chambers with Strips: 6th ~ 15th			
Subtotal	12.1 mm	0.034	0.0107
Total Thickness (Front Cover Plate + 34 Sampling Layers)			
$\theta = 0°$	51.4 cm	18.2	$0.88\ \lambda^{\pi}_{abs}$
$\theta = 11°$		18.5	$0.89\ \lambda^{\pi}_{abs}$
$\theta = 30°$		21.0	$1.01\ \lambda^{\pi}_{abs}$

CARROT AMP - Tsukuba/LBL version 2/25/85
5/30/86 corrected
USR$ROOT1:[SUZAKI.RABBIT.PLIST]PARTS_TYPE1.LIS
1/ 5/89 Final ver. (YM)

PARTS LIST

ITEM#	REF DES	TYPE	QTY/BD	
		RESISTORS		
1	R10,22	2K 1/4W	2	
2	R11,15,19,23,40-43,71,500,508	1K 1/4W	11	
3	R12-13,20-21,65	100 OHM 1/4W	5	
4	R14,18	1.5K 1/4W	2	
5	R17,24	10 OHM 1/4W	2	
6	R61,62	40.2K 1% 1/4W	2	
8	R63,64	80.6K 1% 1/4W	2	
9	R66,520	4.7K 1/4W	2	
10	R67	10K 1/4W	1	
11	R69-70	390 OHM 1/4W	2	
12	R72	See note #3	1	!*5)
12.1	R80	See note #5	jumper	!*10)
13	R101	See Note #3	12	
14	R102	100 OHM 1/4W	12	
15	R103	1.5K 1/4W	12	
16	R104	2K 1/4W	12	
17	R105	1K 1/4W	12	
18	R106	See Note #3	12	
19	R107	SEE NOTE #1	omit	
20	R201	See Note #3	12	
21	R202	100 OHM 1/4W	12	
22	R203	1.5K 1/4W	12	
23	R204	2K 1/4W	12	
24	R205	1K 1/4W	12	
25	R206	See Note #3	12	
26	R207	SEE NOTE #1	omit	
27	R601-612	SEE NOTE #2	12	
28	R701-712	SEE NOTE #2	12	
29	R801-812	SEE NOTE #2	12	
30	R901-912	SEE NOTE #2	12	
31	R613	See note #3	1	!*5)
32	R614	See note #3	1	!*5)
33	R615-616,715-716,915-916	51 OHM 1/4W	6	
33.1	R815-816	See Note #4	(2)	
34	R713	See note #3	1	!*5)
35	R714	See note #3	1	!*5)
36	R813	See Note #4	(1)	
37	R814	See Note #4	(1)	
38	R913	See note #3	1	!*5)
39	R914	See note #3	1	!*5)
40	RS1-2	1K 8 PIN SIP	2	
41	RS3	470 OHM 8 PIN SIP	1	
41.1	RS4-7	100K 8 PIN SIP	4	
42	RP1	5K 1 TURN POT	1	

!*5) Changed by Suzaki on 30MAY86.
!*10) Changed from 4.7K 1/4W to a jumper cord in Sep86

Table 2-4 (a)

Table 2-2 The types and the number of the signals.

Signal type	η	$\Delta\eta$	No. of η-segm.	No. of $\Delta\phi$ ϕ-segm.	No. of Long. Segm.	No. of Modules	Total No. of Channles
Pads	1.13 - 1.2	0.07					
	1.2 - 1.32	0.06	16	5°	72	2	6912
	1.32 - 1.41	0.045					
	1.41 - 2.40	0.09					
θ-Strips	1.2 - 1.84	0.02	32	30°	12	1	2 768
ϕ-strips	1.2 - 1.84	0.64	1	F	360	1	2 720
Anode Wires: 156 wires in a $\Delta\phi$ = 90° chamber are ganged together.							
			1	90°	4	34	2 272
Monitoring tubes		Every - 30°			Two places	2	48
Total							8720

Table 2-3 Longitudinal layer configuration.

Radiation Length X_0 at θ = 11°	30°	Layer No.		
1.24	1.41	1	----------	Pad Longitudinal
		2		
		...		
		5	----------	Segment I
3.33	3.78	6	θ-Strip No. 1 ----------	
3.86	4.37	7		ϕ-Strip No. 1
		8	θ-Strip No. 2	
		9		ϕ-Strip No. 2
		10	θ-Strip No. 3	
		11		ϕ-Strip No. 3
		12	θ-Strip No. 4	Pad Longitudinal
		13		ϕ-Strip No. 4
		14	θ-Strip No. 5	Segment II
		15		ϕ-Strip No. 5
		16		
		17		
		...		
15.89	18.01	29	----------	
16.41	18.60	30	----------	
		31		Pad Longitudinal
		...		Segment III
18.50	20.97	34	----------	

NOTE #1:COMPONENT TO BE OMITTED

NOTE #2:FIVE TYPES OF BOARDS , A-E. ALL RESISTOR VALUES IN KILOHMS, 1/4W 1%
(!*4) and C-D are changed to the nearest value.)

	VALUE	QTY/BD	
TYPE A (Tsukuba)			
R601-R612	3.17K	12	
R701-R712	2.67K	12	
R801-R812	2.26K	12	!*4)
R901-R912	1.89K	12	
TYPE B (Tsukuba)			
R601-R612	1.58K	12	!*4)
R701-R712, R801-803, R807-809	1.37K	18	!*4)
R804-806, R810-812, R901-912	1.15K	18	!*4)
TYPE C (LBL)			
R601-R612	6.34K	12	
R701-R712	5.36K	12	
R801-R812	4.53K	12	
R901-R912	3.83K	12	
TYPE D (LBL)			
R601-R612	3.24K	12	
R701-R712	2.74K	12	
R801-R812	6.34K	12	
R901-R912	5.36K	12	
TYPE E (LBL)			
R601-R612	4.53K	12	
R701-R712	3.83K	12	
R801-R812	3.24K	12	
R901-R912	2.74K	12	

Table 2-4 (a) cont'd

Note #3: Different values are used in type A-B and type C-E.

Type A-B: (Tsukuba version)		
R72	1.2K 1/4W 5%----------1	!*5) !*7)
R101,201	30 OHM 1/4W 5%----------24	
R106,206	500K 1/4W 1%----------24	
R613-614,R713-714, R913-914	2.00K 1/4W 1%----------6	!*5)
C69	100pF 1/2% TYPE E TEMPCO -20,+100 PPM/C----------1	
C101,201	680pF CERAMIC----------24	!*1)
C106,206	200pF 1% DIPPED MICA----------24	
Type C-E: (LBL version)		
R72	3.9K 1/4W 5%----------1	!*5)
R101,201	10 OHM 1/4W 5%----------24	!*6)
R106,206	500K OHM 1/4W 1%----------24	!*5)
R613-614,R713-714, R913-914	4.02K 1/4W 1%----------6	!*5)
C69	100pF 1/2% TYPE E TEMPCO -20,+100 PPM/C----------1	
C101,201	680pF CERAMIC----------24	
C106,206	200pF 1% DIPPED MICA----------24	

!*1) Changed from 2200pF by Morita on 25Dec85.
!*5) Changed by Suzaki on 30MAy85.
!*6) Changed from 30 ohm to 10 ohm in Oct86
!*7) Changed from 150 ohm in Jul86

Table 2-4 (a) cont'd

Note #4: Component to be omitted in type B

Type A

R813-814	2.00K 1/4W 1%----------2	
R815-816	51 OHM 1/4W----------2	
U801	AD518JH----------1	
C801-802	.1uF MONOCAP @50V----------2	
C813-814	47pF CERMIC DISC----------2	
C815	.1uF MONOCAP @50V----------1	

Type C-E:

R813-814	4.02K 1/4W 1%----------2	!*2)
R815-816	51 OHM 1/4W----------2	
U801	AD518JH----------1	
C801-802	.1uF MONOCAP @50V----------2	
C813-814	22pF CERMIC DISC----------2	!*3)
C815	.1uF MONOCAP @50V----------1	

Note #5: Component to be omitted and put a jumper instead

!*2) Changed from 2.00K by Suzaki on 11MAY86.
!*3) Changed from 47PF bu Suzaki on 11MAY86.

Table 2-4 (a) cont'd

CARROT AMP - Tsukuba/LBL version 2/25/85
PARTS LIST

ITEM#	REF DES	TYPE	QTY/BD	
		DIODES		
43	D1-8	1N5817	8	
44	D61-62	1N914	2	
45	D63	HSCH1001 (1N6263 EQUIVILENT)	1	(HEWLETT PACKARD)
47	D102	1N914	12	
48	D103	1N914	12	
50	D202	1N914	12	
51	D203	1N914	12	
52	CR101	CR470	12	(SILICONIX)
52.1	CR102	CR470	12	!*8)
53	CR201	CR470	12	(SILICONIX)
53.1	CR202	CR470	12	!*8)
		TRANSISTORS		
54	T10,13,18,20, 61-62	2N3904	6	
55	T11,14-17,21, 40-43	2N3906	10	
56	T12,19	SD210DE	2	(Semi Processes Inc)
57	T63	J270	1	(Siliconix)
58	T101	J309	12	(Siliconix) !*1)
59	T102	2N5087	12	
60	T103	2N2907	12	
60.1	T104	2N3904	12	
61	T201	J309	12	(Siliconix) !*1)
62	T202	2N5087	12	
63	T203	2N2907	12	
63.1	T204	2N3904	12	
		FUSE		
64	F1-8	1.5A TRACOR PICOFUSE	8	
		IC'S		
65	Z1	SD5000N NOTE: Item #65 from Semi Processes Inc. to be specially ordered for maximum tested leakeage current of 100pA. This will add approximately 20% to cost.	12	(QUAD MOSFET)
66	ZX0-23,U42-43	CA3240AE	26	(DUAL OP AMP)
67	U1-12	HEF4051BP	12	(SIGNETICS) (MOS MULTIPLEXER)
68	U40-41	HEF4052	2	(MOS MULTIPLEXER)
69	U60-62	HEF4051BP	3	(MOS MULTIPLEXER)
70	U63	LF356N	1	(OP AMP)
71	U64	MC10101P	1	(ECL)
72	U101	MC10116P	1	(ECL)
73	U102-103,106-107	MC10125P	4	(ECL/TTL)
74	U104-105	MC10109P	2	(ECL)
75	U108-109,115	74LS26	3	(TTL)

!*1) Changed from J310 by Inohata on 13Nov85.
!*8) Changed from J557 to CR470 on Aug86

Table 2-4 (a) cont'd

ITEM#	REF DES	TYPE	QTY/BD	
76	U110-111	74LS138	2	(TTL)
77	U112	74S288	1	(TTL)
78	U113-114	7407	2	(TTL)
79	U601,701,901	AD518JH	3	(FAST OP AMP) (Analog Devices Inc) (Norwood,Massachusetts)
79.1	U801	See Note #4	(1)	
		CAPACITORS		
80	C1	560PF 5% DIPPED MICA	12	!*9)
81	C2	560PF 5% DIPPED MICA	12	!*9)
82	C3	560PF 5% DIPPED MICA	12	!*9)
83	C4	560PF 5% DIPPED MICA	12	!*9)
84	C5	.1uF MONOCAP @50V	12	
85	C6	.1uF MONOCAP @50V	12	
86	C7	See Note #1	omit	!*1)
87	C8	See Note #1	omit	!*1)
88	C12-13,20-23, 30-31,36-38 40-43,63-65, 70-71,75-79	.1uF MONOCAP @50V	21	
89	C14-15	6.8uF TANTALUM @35V	2	
90	C61	100PF CERAMIC @500V	1	
91	C62	22PF CERAMIC @500V	1	
92	C66	.001uF CERAMIC @25V	1	
93	C68	OMIT		
94	C101	See Note #3	12	
95	C102	.1uF MONOCAP @50V	12	
96	C103	2.2uF TANTALUM @35V	12	(+7.5V)
97	C105	.1uF MONOCAP @50V	12	
98	C106	See Note #3	12	
99	C107	SEE NOTE #1	Omit	
100	C108	6.8 uF TANTALUM @35V	12	
100.1	C109	6.8 uF TANTALUM @35V	12	
100.2	C110	2.2uF TANTALUM @35V	12	
100.3	C201	See Note #3	12	
101	C202	.1uF MONOCAP @50V	12	
102	C203	2.2uF TANTALUM @35V	12	(-7.5V)
103	C205	.1uF MONOCAP @50V	12	
104	C206	See Note #3	12	
105	C207	SEE NOTE #1	Omit	
105.1	C208	6.8 uF TANTALUM @35V	12	
105.2	C209	6.8 uF TANTALUM @35V	12	
105.3	C210	2.2uF TANTALUM @35V	12	
106	C601-602,701-702,901-902	.1uF MONOCAP @50V	6	
106.1	C801-802	See Note #4	(2)	
107	C69	See Note #3	1	
107.1	C613,C614 C713,C714 C913,C914	22PF CERAMIC DISC	6	!*3)
107.2	C813,C814	See Note #4	(2)	
107.3	C615,715,915	.1uF MONOCAP @50V	3	
107.4	C815	See Note #4	(1)	

!*1) Deleted by Inohata on 14Nov85.
!*3) Changed from 47PF by Suzaki on 11MAY86.
!*9) Changed from 270pF to 560pF on Aug86

Table 2-4 (a) cont'd

CARROT AMP - Tsukuba/LBL version 2/25/85
PARTS LIST

ITEM#	REF DES	TYPE	QTY/BD
		EDGE CONNECTORS	
108	J1,4	BERG 66413-517	2
109	J2-3	BERG 66413-525	2
110	J5	Hirose RDAB-15P (TRW DAC 15P AD equivalent)	1 (TRIGGER OUTPUTS)
110.1	J5.1	Hirose HD-LNA (4-40)	1 (rock nut for RDAB-15P)
110.2	J6-12	BERG 65626-104	7 (4pin right angle)
110.3	J6.1-12.1	BERG 65474-001	8 (Jumper)
		PANEL	
111	Front panel	RABBIT standard front panel	1
111.1	Card ejector	CARD-O-PULL CARD EJECTOR No. CP-46	2 (BIVAR.INC)
		Socket	
112	IC socket	16 pin IC socket	1 (For PROM IC)

Table 2-4 (a) cont'd

CARROT AMP TYPE II 2/25/85
5/30/86 corrected
USR$ROOT1:[SUZAKI.RABBIT.PLIST]PARTS_TYPE2.LIS
1/ 5/89 Final ver. (YM)
Harvard/Texas version
PARTS LIST

ITEM#	REF DEF	TYPE	QTY/BD	
		RESISTORS		
1	R10,22	2K 1/4W	2	
2	R11,15,19,23, 40-43,71,500, 508	1K 1/4W	11	
3	R12-13,20-21, 65	100 OHM 1/4W	5	
4	R14,18	1.5K 1/4W	2	
5	R17,24	10 OHM 1/4W	2	
6	R61,62	40.2K 1% 1/4W	2	
8	R63,64	80.6K 1% 1/4W	2	
9	R66,520	4.7K 1/4W	2	
10	R67	10K 1/4W	1	
11	R69-70	390 OHM 1/4W	2	
12	R72	390 OHM 1/4W	1	!*5)
12.1	R80	See note #5	jumper	!*10)
13	R101	2.2 OHM 1/4W	12	
14	R102	200 OHM 1/4W	12	
15	R103	750 OHM 1/4W	12	
16	R104	2K 1/4W	12	
17	R105	1K 1/4W	12	
18	R106	SEE NOTE #3	12	
19	R107	SEE NOTE #1	omit	
20	R201	2.2 OHM 1/4W	12	
21	R202	200 OHM 1/4W	12	
22	R203	750 OHM 1/4W	12	
23	R204	2K 1/4W	12	
24	R205	1K 1/4W	12	
25	R206	SEE NOTE #3	12	
26	R207	SEE NOTE #1	omit	
27	R601-612	SEE NOTE #2	12	
28	R701-712	SEE NOTE #2	12	
29	R801-812	SEE NOTE #2	12	
30	R901-912	SEE NOTE #2	12	
31	R613	2.00K 1/4W 1%	1	
32	R614	2.00K 1/4W 1%	1	
33	R615-616,715-716,815-816, 915-916	51 OHM 1/4W	8	
34	R713	2.00K 1/4W 1%	1	
35	R714	2.00K 1/4W 1%	1	
36	R813	2.00K 1/4W 1%	1	
37	R814	2.00K 1/4W 1%	1	
38	R913	2.00K 1/4W 1%	1	
39	R914	2.00K 1/4W 1%	1	
40	RS1-2	1K 8 PIN SIP	2	
41	RS3	470 OHM 8 PIN SIP	1	
42	RP1	5K 1 TURN POT	1	
42.1	RS4-7		omit	!*1)

!*1) added by Inohata on 18Nov85.
!*5) Changed by Suzaki on 30MAY86.

Table 2-4 (b)

NOTE #1:COMPONENT TO BE OMITED

NOTE #2:TEN TYPES OF BOARDS, A-E, G-K. ALL RESISTOR VALUES IN OHMS, 1/4W 1%
(G-K are changed to the nearest value by Suzaki on 23MAY86.)

	VALUE	QTY/BD
TYPE A		
R601-612	18.7K	12
R701-712	15.4K	12
R801-812	12.7K	12
R901-912	10.2K	12
TYPE B		
R601-612	8.45K	12
R701-712	6.98K	12
R801-812	5.62K	12
R901-912	4.64K	12
TYPE C		
R601-612	3.83K	12
R701-712	3.24K	12
R801-812	18.7K	12
R901-912	15.4K	12
TYPE D		
R601-612	12.7K	12
R701-712	10.2K	12
R801-812	8.45K	12
R901-912	6.98K	12
TYPE E		
R601-612	5.62K	12
R701-712	4.64K	12
R801-812	3.83K	12
R901-912	3.24K	12
TYPE G		
R601-612	4.15K	12
R701-712	3.40K	12
R801-812	2.74K	12
R901-912	2.26K	12
TYPE H		
R601-612	1.89K	12
R701-712	1.54K	12
R801-812	1.24K	12
R901-912	1.02K	12
TYPE I		
R601-612	845	12
R701-712	732	12
R801-812	4.15K	12
R901-912	3.40K	12
TYPE J		
R601-612	2.74K	12
R701-712	2.26K	12
R801-812	1.89K	12
R901-912	1.54K	12
TYPE K		
R601-612	1.24K	12
R701-712	1.02K	12
R801-812	845	12
R901-912	732	12

Table 2-4 (b) cont'd

NOTE #3: Different values are used in type A-E and type G-K.
(Changed by Suzaki on 11MAY86.)

type A-E: (Harvard version)

R106,206	330K 1% 1/4W	24
C106,206	330pF 1% DIPPED MICA	24
C69	160pF 1/2% TYPE E TEMPCO -20,+100 PPM/C	1

type G-K: (Texas version)

R106,206	500K 5% 1/4W	24
C106,206	200pF 5% DIPPED MICA	24
C69	100pF 1/2% TYPE E TEMPCO -20,+100 PPM/C	1

Table 2-4 (b) cont'd

CARROT AMP TYPE II 2/25/85
Harvard/Texas version
PARTS LIST

ITEM#	REF DEF	TYPE	QTY/BD	
		DIODES		
43	D1-8	1N5817	8	
44	D61-62	1N914	2	
45	D63	HSCH1001 (1N6263 EQUIVALENT)	1	(HEWLETT PACKARD)
46	D101	1N914	12	
47	D102	1N914	12	
48	D103	1N914	12	
49	D201	1N914	12	
50	D202	1N914	12	
51	D203	1N914	12	
52	CR101	CR470	12	(SILICONIX)
53	CR201	CR470	12	(SILICONIX)
		TRANSISTORS		
54	T10,13,18,20, 61-62	2N3904	6	
55	T11,14-17,21, 40-43	2N3906	10	
56	T12,19	SD210DE	2	(Semi Process Inc)
57	T63	J270	1	(Siliconix)
58	T101	J309	12	(Siliconix) !*1)
59	T102	2N5087	12	
60	T103	2N5087	12	(Siliconix)
61	T201	J309	12	(Siliconix) !*1)
62	T202	2N5087	12	
63	T203	2N5087	12	(Siliconix)
		FUSE		
64	F1-8	1.5A TRACOR PICOPUSE	8	
		IC'S		
65	Z1	SD5000N NOTE: Item #65 from Semi Processes Inc. to be specially ordered for maximum tested leakage current of 100pA. This will add approximately 20% to cost.	12	(QUAD MOSFET)
66	ZX0-23,U42-43	CA3240AE	26	(DUAL OP AMP)
67	U1-12	HEF4051BP	12	(SICNETICS) (MOS MULTIPLEXER)
68	U40-41	HEF4052	2	(SICNETICS) (MOS MULTIPLEXER)
69	U60-62	HEF4051BP	3	(SICNETICS) (MOS MULTIPLEXER)
70	U63	LF356N	1	(OP AMP)
71	U64	MC10101P	1	(ECL)
72	U101	MC10116P	1	(ECL)
73	U102-103,106-107	MC10125P	4	(ECL/TTL)
74	U104-105	MC10109P	2	(ECL)

!*1) Changed from J310 by Inohata on 13Nov85.

Table 2-4 (b) cont'd

CARROT AMP TYPE II 2/25/85
Harvard/Texas version
PARTS LIST

ITEM#	REF DEF	TYPE	QTY/BD	
75	U108-109,115	74LS26	3	(TTL)
76	U110-111	74LS138	2	(TTL)
77	U112	74S288	1	(TTL)
78	U113-114	7407	2	(TTL)
79	U601,701,801, 901	AD518JH	4	(FAST OP AMP) (Analog Devices Inc) (Norwood,Massachusetts)
		CAPACITORS		
80	C1	560pF 5% DIPPED MICA	12	
81	C2	560pF 5% DIPPED MICA	12	
82	C3	560pF 5% DIPPED MICA	12	
83	C4	560pF 5% DIPPED MICA	12	
84	C5	.1uF MONOCAP @50V	12	
85	C6	.1uF MONOCAP @50V	12	
86	C7	See Note #1	omit	!*1)
87	C8	See Note #1	omit	!*1)
88	C12-13,20-23, 30-31,36-38, 40-43,63-65, 70-71,75-79	.1uF MONOCAP @50V	21	!*2)
89	C14-15	6.8uF TANTALUM @35V	2	
90	C61	100pF CERAMIC @500V	1	
91	C62	22pF CERAMIC @500V	1	
92	C66	.001uF CERAMIC @25V	1	
93	C68		omit	
94	C101	3.3uF TANTALUM @35V	12	
95	C102	.1uF MONOCAP @50V	12	
96	C103	2.2uF TANTALUM @35V	12	(+7.5V)
97	C105	.1uF MONOCAP @50V	12	
98	C106	SEE NOTE #3	12	
99	C107	SEE NOTE #1	omit	
100	C201	3.3uF TANTALUM @35V	12	
101	C202	.1uF MONOCAP @50V	12	
102	C204	2.2uF TANTALUM @35V	12	(-7.5V)
103	C205	.1uF MONOCAP @50V	12	
104	C206	SEE NOTE #3	12	
105	C207	SEE NOTE #1	omit	
106	C601-602,701-702,801-802, 901-902	.1uF MONOCAP @50V	8	
107	C69	SEE NOTE #3	1	
107.1	C613,C614, C713,C714, C813,C814, C913,C914	47pF CERMIC DISC	8	
107.3	C615,C715, C815,C915	.1uF MONOCAP @50V	4	

!*1) Deleted by Inohata on 14Nov85.
!*2) C72 deleted. C75-79 added by Inohata on 18Nov85.

Table 2-4 (b) cont'd

CARROT AMP TYPE II 2/25/85
Harvard/Texas version
PARTS LIST

ITEM#	REF DEF	TYPE	QTY/BD
		EDGE CONNECTORS	
108	J1,4	BERG 66413-517	2
109	J2-3	BERG 66413-525	2
110	J5	Hirose RDAB-15P (TRW DAC 15P AD equivalent)	1 (TRIGGER OUTPUTS)
110.1	J5.1	Hirose HD-LNA (4-40)	1 (rock nut for RDAB-15P)
110.2	J6-12	BERG 65626-104	7 (4pin right angle)
110.3	J6.1-12.1	BERG 65474-001	8 (Jumper)
		PANEL	
111	Front panel	RABBIT standard front panel	1
111.1	Card ejector	CARD-O-PULL CARD EJECTOR No. CP-46	2 (BIVAR.INC)
		Socket	
112	IC socket	16 pin IC socket	1 (For PROM IC)

Table 2-4 (b) cont'd

Table 2-5 CARROT amplifier card production specifications.

		CARROT Type I	CARROT Type II
Dynamic Range	[pC]	0 ~ 500	0 ~ 825
Gain	[V/nC]	5.00 ± 0.25	3.03± 0.15
Linearity (Relative)	[%]	≤ 0.2	≤ 0.2
Linearity (Absolute)	[mV]	≤ 1.91	≤ 1.91
Sample & Hold Droop	[mV/sec]	≤ 200	≤ 200
Pedestal	[mV]	≤ ± 19.1	≤ ± 19.1
Pedestal width	[μV]	≤ 458	≤ 458
Before/After Rise Time	[nsec]	≤ 50	≤ 50
Trigger Fastout Gain	[%]	≤ 5	≤ 5
Trigger Fastout Rise Time	[nsec]	≤ 300	≤ 300

Table 3-1 PEM gain correction factors

|| Quadrant# 0 ||

phi\eta	0	1	2	3	4	5	6	7	8	9	10	11	12	13	14	15
0	0.960	0.960	0.952	0.958	0.975	0.972	0.986	0.984	1.004	1.001	1.044	1.034	1.018	1.037	1.000	1.000
1	0.960	0.960	0.958	0.938	0.992	0.939	0.953	0.958	1.002	1.040	1.026	0.951	1.030	0.985	1.000	1.000
2	0.960	0.960	0.905	0.946	0.924	0.852	0.837	0.889	0.977	0.989	1.015	1.025	1.112	1.150	1.000	1.000
3	0.960	0.960	0.800	0.916	0.935	0.823	0.854	0.851	0.930	0.927	0.898	1.021	1.000	1.082	1.000	1.000
4	0.960	0.960	0.992	0.918	0.919	0.948	0.993	0.999	0.981	0.974	1.053	1.060	1.026	1.098	1.000	1.000
5	0.960	0.960	0.953	0.914	0.952	0.995	0.988	0.974	1.095	1.072	1.068	1.059	1.037	1.083	1.000	1.000
6	0.960	0.960	0.905	0.875	0.926	0.989	0.934	0.967	0.986	1.008	1.095	1.061	1.043	1.053	1.000	1.000
7	0.960	0.960	0.946	0.999	1.046	1.060	1.019	1.053	0.984	0.992	1.055	1.133	1.009	1.019	1.000	1.000
8	0.960	0.960	0.957	1.007	1.000	1.010	1.047	0.998	1.018	1.004	1.000	1.059	1.027	1.053	1.000	1.000
9	0.960	0.960	0.895	1.029	1.003	1.031	0.957	1.018	0.969	1.010	1.047	1.005	0.995	1.101	1.000	1.000
10	0.960	0.960	0.938	0.996	0.935	0.978	1.061	1.104	1.071	0.906	1.076	0.976	0.982	1.052	1.000	1.000
11	0.960	0.960	0.880	0.990	0.906	0.966	0.977	0.964	1.004	1.032	1.048	1.083	0.994	1.118	1.000	1.000
12	0.960	0.960	1.010	0.922	1.014	0.951	1.028	0.984	1.023	1.057	1.092	1.042	0.996	0.821	1.000	1.000
13	0.960	0.960	1.019	0.919	0.990	0.973	1.016	0.964	1.032	0.969	1.024	0.997	1.015	0.953	1.000	1.000
14	0.960	0.960	1.030	1.009	1.015	1.044	1.051	1.011	0.990	0.964	1.049	1.017	1.012	0.991	1.000	1.000
15	0.960	0.960	1.049	0.993	1.008	1.011	1.011	0.984	1.003	1.033	1.093	1.027	1.033	1.036	1.000	1.000
16	0.960	0.960	1.013	0.951	1.041	0.981	1.045	1.034	0.991	1.040	1.064	1.030	0.974	0.991	1.000	1.000
17	0.960	0.960	0.952	0.958	0.975	0.972	0.986	0.984	1.004	1.001	1.044	1.034	1.018	1.037	1.000	1.000

|| Quadrant# 1 ||

phi\eta	0	1	2	3	4	5	6	7	8	9	10	11	12	13	14	15
0	0.960	0.960	0.962	0.975	0.957	0.968	0.986	1.001	1.012	0.991	1.039	1.024	1.003	1.014	1.000	1.000
1	0.960	0.960	0.984	1.026	0.957	1.031	1.064	0.977	1.081	1.086	1.046	1.010	0.989	1.014	1.000	1.000
2	0.960	0.960	0.955	1.013	0.984	1.014	1.020	0.977	1.035	0.986	1.026	1.055	1.051	0.962	1.000	1.000
3	0.960	0.960	0.943	0.942	0.922	0.947	1.007	0.951	1.025	1.013	0.978	0.988	1.045	1.053	1.000	1.000
4	0.960	0.960	0.930	0.946	0.893	0.893	0.959	0.943	1.005	0.928	1.053	1.031	0.932	1.021	1.000	1.000
5	0.960	0.960	0.977	0.980	0.945	0.967	0.978	0.958	1.046	1.004	1.006	1.047	1.037	1.095	1.000	1.000
6	0.960	0.960	0.939	0.913	0.938	0.954	0.963	1.042	0.936	0.965	1.098	1.043	0.896	0.986	1.000	1.000
7	0.960	0.960	0.973	0.925	0.984	0.941	0.934	1.002	0.992	0.982	1.067	1.055	1.055	1.112	1.000	1.000
8	0.960	0.960	0.980	1.003	1.028	0.995	0.999	0.996	1.012	0.989	0.981	1.060	0.940	1.059	1.000	1.000
9	0.960	0.960	0.986	0.998	1.004	0.929	0.987	1.084	1.032	1.017	1.004	0.947	1.000	1.039	1.000	1.000
10	0.960	0.960	0.932	0.921	1.016	0.953	0.968	1.035	0.986	0.931	1.030	0.965	0.940	0.955	1.000	1.000
11	0.960	0.960	1.008	1.006	0.972	0.989	1.030	1.042	1.010	1.042	1.077	1.096	1.021	1.023	1.000	1.000
12	0.960	0.960	0.981	1.096	0.975	1.013	1.000	1.047	0.993	0.950	1.088	1.020	1.028	0.983	1.000	1.000
13	0.960	0.960	0.969	1.013	0.954	1.034	0.998	1.066	0.965	0.964	1.020	0.994	1.046	1.010	1.000	1.000
14	0.960	0.960	1.016	1.021	1.049	0.994	1.073	0.961	1.057	1.008	1.033	1.005	1.040	0.975	1.000	1.000
15	0.960	0.960	0.936	0.901	0.821	0.862	0.835	0.927	0.975	1.011	1.093	1.082	1.030	0.974	1.000	1.000
16	0.960	0.960	0.877	0.891	0.864	0.977	0.961	1.007	1.040	0.973	1.033	0.980	1.004	0.971	1.000	1.000
17	0.960	0.960	0.962	0.975	0.957	0.968	0.986	1.001	1.012	0.991	1.039	1.024	1.003	1.014	1.000	1.000

|| Quadrant# 2 ||

phi\eta	0	1	2	3	4	5	6	7	8	9	10	11	12	13	14	15
0	0.960	0.960	0.972	0.981	0.955	0.946	0.976	0.999	1.005	1.000	1.029	1.032	1.030	1.021	1.000	1.000
1	0.960	0.960	0.974	0.978	1.000	0.932	0.981	0.999	1.000	1.037	1.017	1.013	1.048	1.124	1.000	1.000
2	0.960	0.960	0.970	0.987	0.971	0.955	0.998	1.015	1.014	1.033	1.112	1.088	1.054	0.999	1.000	1.000
3	0.960	0.960	0.958	0.945	0.927	0.977	0.978	0.988	0.990	0.993	1.035	1.031	1.046	1.200	1.000	1.000
4	0.960	0.960	0.883	0.894	0.861	0.891	0.971	0.907	0.911	0.997	1.026	1.128	1.056	1.086	1.000	1.000
5	0.960	0.960	0.969	0.909	0.972	0.918	0.914	1.023	1.027	0.990	1.072	1.005	1.122	1.159	1.000	1.000
6	0.960	0.960	0.932	0.976	0.935	0.980	0.954	1.028	1.009	1.029	1.086	1.029	1.057	1.077	1.000	1.000
7	0.960	0.960	0.985	0.933	0.945	0.940	0.982	1.010	0.995	0.937	1.053	1.067	1.104	1.056	1.000	1.000
8	0.960	0.960	0.958	1.033	0.969	0.832	1.044	0.968	1.054	0.976	1.051	1.035	0.961	1.069	1.000	1.000
9	0.960	0.960	0.960	0.918	0.937	0.918	0.951	1.024	1.090	1.021	0.901	0.982	1.026	0.973	1.000	1.000
10	0.960	0.960	1.004	0.972	0.964	0.947	0.937	1.035	0.989	1.097	1.031	1.050	1.087	1.091	1.000	1.000
11	0.960	0.960	0.944	0.991	0.919	0.974	1.006	0.980	0.952	0.966	0.972	1.006	0.970	0.946	1.000	1.000
12	0.960	0.960	0.957	1.013	0.956	0.966	0.954	0.977	0.959	0.945	1.073	1.034	1.023	0.932	1.000	1.000
13	0.960	0.960	1.015	0.985	0.989	0.921	1.002	0.998	1.001	0.960	1.032	0.981	0.989	0.937	1.000	1.000
14	0.960	0.960	0.987	1.082	0.898	0.979	0.984	1.027	1.048	0.957	0.996	1.017	0.980	0.836	1.000	1.000
15	0.960	0.960	1.000	1.042	0.987	0.990	0.931	0.976	1.039	1.038	1.022	1.047	0.980	1.016	1.000	1.000
16	0.960	0.960	1.049	1.039	1.044	1.012	1.022	1.033	1.003	1.030	0.988	1.006	0.968	0.826	1.000	1.000
17	0.960	0.960	0.972	0.981	0.955	0.946	0.976	0.999	1.005	1.000	1.029	1.032	1.030	1.021	1.000	1.000

Table 3-1 PEM gain correction factors (cont'd)

|| Quadrant# 3 ||

phi\eta	0	1	2	3	4	5	6	7	8	9	10	11	12	13	14	15
0	0.960	0.960	0.955	0.963	0.962	0.973	0.993	0.997	1.021	1.003	1.040	0.994	1.028	1.015	1.000	1.000
1	0.960	0.960	0.938	0.915	1.008	0.973	1.009	1.074	1.065	1.100	1.030	1.085	0.990	1.048	1.000	1.000
2	0.960	0.960	0.919	1.012	0.860	0.972	0.979	0.970	1.002	1.039	1.087	0.902	1.034	0.971	1.000	1.000
3	0.960	0.960	0.910	0.949	0.944	0.971	1.045	1.021	1.057	1.015	1.020	1.014	1.039	1.078	1.000	1.000
4	0.960	0.960	0.907	0.907	0.907	0.949	0.835	0.984	1.016	0.967	1.092	0.879	1.081	0.976	1.000	1.000
5	0.960	0.960	0.884	0.904	0.891	0.927	0.949	0.964	1.049	0.922	1.120	1.043	1.130	1.102	1.000	1.000
6	0.960	0.960	0.988	0.991	0.992	0.962	1.046	0.996	1.077	1.014	1.062	1.010	1.067	1.055	1.000	1.000
7	0.960	0.960	0.989	0.956	0.903	0.979	0.977	1.019	1.029	1.026	1.004	1.010	0.999	0.996	1.000	1.000
8	0.960	0.960	0.976	0.957	1.021	1.036	1.030	1.032	1.037	0.987	1.068	0.993	1.088	1.130	1.000	1.000
9	0.960	0.960	1.004	0.963	1.012	0.975	1.037	1.053	1.046	1.056	0.986	1.006	0.963	1.054	1.000	1.000
10	0.960	0.960	1.048	1.044	0.989	0.979	0.989	1.011	1.056	0.957	1.019	1.031	1.072	1.028	1.000	1.000
11	0.960	0.960	0.942	0.999	0.981	0.974	0.982	0.955	0.947	0.959	1.001	0.940	1.009	0.927	1.000	1.000
12	0.960	0.960	0.947	0.976	0.963	0.926	0.934	0.982	0.983	1.019	0.981	0.981	0.991	1.006	1.000	1.000
13	0.960	0.960	0.920	0.982	0.963	0.960	1.005	0.988	0.938	1.000	1.052	0.912	1.080	1.034	1.000	1.000
14	0.960	0.960	0.994	0.955	0.973	1.005	1.007	0.942	1.041	1.045	1.015	1.114	0.952	0.970	1.000	1.000
15	0.960	0.960	0.918	0.964	1.003	0.999	1.040	0.995	0.973	1.018	1.073	0.994	0.986	0.908	1.000	1.000
16	0.960	0.960	0.992	0.936	0.989	0.987	1.020	0.970	1.027	0.922	1.026	0.990	0.970	0.966	1.000	1.000
17	0.960	0.960	0.955	0.963	0.962	0.973	0.993	0.997	1.021	1.003	1.040	0.994	1.028	1.015	1.000	1.000

|| Quadrant# 4 ||

phi\eta	0	1	2	3	4	5	6	7	8	9	10	11	12	13	14	15
0	0.970	0.970	0.931	0.952	0.982	1.036	1.021	1.014	1.011	0.988	1.059	1.020	1.006	0.996	1.000	1.000
1	0.970	0.970	0.979	1.019	1.006	1.101	1.036	1.138	1.033	0.941	0.979	1.023	1.002	0.985	1.000	1.000
2	0.970	0.970	0.859	0.849	0.975	1.049	1.034	0.924	0.995	0.916	0.965	0.935	0.894	0.916	1.000	1.000
3	0.970	0.970	0.807	0.950	0.857	1.004	0.971	0.940	0.899	0.871	1.000	0.894	0.894	0.926	1.000	1.000
4	0.970	0.970	0.847	0.892	0.900	0.965	0.999	0.989	0.974	0.948	0.989	1.037	0.944	1.008	1.000	1.000
5	0.970	0.970	0.944	0.938	1.022	1.135	1.008	0.988	1.028	1.029	1.091	1.034	1.015	1.076	1.000	1.000
6	0.970	0.970	0.963	0.998	1.039	1.138	1.101	1.072	1.022	0.996	1.068	1.108	1.037	1.008	1.000	1.000
7	0.970	0.970	0.870	0.868	0.952	0.994	0.987	1.016	0.901	0.855	0.913	1.018	0.950	0.894	1.000	1.000
8	0.970	0.970	1.010	1.052	1.127	1.045	1.014	0.988	1.068	1.015	0.967	0.952	0.901	0.984	1.000	1.000
9	0.970	0.970	0.945	0.947	0.946	1.022	1.020	1.007	1.021	0.977	1.125	0.997	1.056	1.039	1.000	1.000
10	0.970	0.970	0.978	0.975	0.951	1.044	1.054	1.016	1.040	1.000	1.132	1.003	1.113	1.113	1.000	1.000
11	0.970	0.970	0.908	0.810	0.939	1.012	0.977	0.946	1.026	1.027	1.105	1.123	1.037	1.012	1.000	1.000
12	0.970	0.970	0.973	0.880	0.989	0.981	1.024	1.019	1.004	1.051	1.147	1.033	1.150	1.081	1.000	1.000
13	0.970	0.970	0.870	0.912	0.908	0.986	0.946	1.011	0.952	0.937	0.965	1.000	0.933	0.941	1.000	1.000
14	0.970	0.970	0.964	1.058	1.066	1.081	1.104	1.056	1.090	1.074	1.077	1.047	1.074	1.070	1.000	1.000
15	0.970	0.970	1.003	0.945	1.127	1.022	1.084	1.066	1.045	1.071	1.083	1.087	1.035	0.894	1.000	1.000
16	0.970	0.970	0.974	0.946	0.910	0.995	0.976	1.023	1.078	1.091	1.101	1.033	1.092	1.047	1.000	1.000
17	0.970	0.970	0.931	0.952	0.982	1.036	1.021	1.014	1.011	0.988	1.059	1.020	1.006	0.996	1.000	1.000

|| Quadrant# 5 ||

phi\eta	0	1	2	3	4	5	6	7	8	9	10	11	12	13	14	15
0	0.970	0.970	1.004	0.994	0.995	1.055	1.033	0.998	0.979	0.970	1.012	0.986	0.972	1.021	1.000	1.000
1	0.970	0.970	0.951	0.956	0.967	1.100	1.032	1.008	1.042	0.997	0.983	1.116	0.981	1.054	1.000	1.000
2	0.970	0.970	1.139	0.952	1.064	1.113	1.026	1.021	1.024	0.902	0.981	0.896	0.932	0.908	1.000	1.000
3	0.970	0.970	0.916	0.992	1.042	1.081	1.088	1.048	0.914	0.978	0.960	0.964	0.946	1.110	1.000	1.000
4	0.970	0.970	1.049	1.072	1.014	0.979	1.008	0.986	0.958	0.959	1.017	1.013	1.014	1.023	1.000	1.000
5	0.970	0.970	1.029	0.933	0.871	1.049	0.970	0.968	0.971	1.027	0.906	1.063	1.039	1.089	1.000	1.000
6	0.970	0.970	1.024	1.037	1.024	1.061	1.067	1.022	1.116	1.009	1.137	1.063	1.029	1.033	1.000	1.000
7	0.970	0.970	1.025	0.985	1.027	1.093	1.055	1.060	0.886	0.978	0.963	0.923	0.927	0.896	1.000	1.000
8	0.970	0.970	0.974	1.001	1.025	1.059	1.041	0.974	0.931	0.952	1.000	0.896	0.896	1.084	1.000	1.000
9	0.970	0.970	0.993	0.952	0.917	1.065	1.009	0.899	0.956	0.899	0.956	0.896	0.896	1.022	1.000	1.000
10	0.970	0.970	1.049	1.096	1.069	1.078	1.062	0.995	0.974	0.935	1.104	1.031	1.137	0.984	1.000	1.000
11	0.970	0.970	1.006	0.979	0.990	1.062	1.018	0.974	0.909	0.960	1.026	0.942	1.004	1.094	1.000	1.000
12	0.970	0.970	0.874	1.058	0.979	1.017	1.053	1.042	1.081	0.989	1.050	1.105	1.050	1.103	1.000	1.000
13	0.970	0.970	0.917	0.970	0.976	1.044	0.991	1.029	0.966	0.886	0.896	0.981	0.896	0.988	1.000	1.000
14	0.970	0.970	1.032	1.010	1.015	1.079	1.048	0.974	0.931	0.998	0.962	1.002	0.938	0.991	1.000	1.000
15	0.970	0.970	0.951	0.904	0.971	1.000	1.023	0.983	0.981	1.017	0.939	0.995	0.944	0.938	1.000	1.000
16	0.970	0.970	0.999	1.011	0.978	0.998	1.045	0.990	1.018	1.031	1.018	0.942	0.896	1.040	1.000	1.000
17	0.970	0.970	1.004	0.994	0.995	1.055	1.033	0.998	0.979	0.970	1.012	0.986	0.972	1.021	1.000	1.000

Table 3-1 PEM gain correction factors (cont'd)

|| Quadrant# 6 ||

phi\eta	0	1	2	3	4	5	6	7	8	9	10	11	12	13	14	15
0	0.970	0.970	1.005	0.987	0.975	1.026	1.030	1.002	0.978	0.996	1.025	1.013	0.977	1.012	1.000	1.000
1	0.970	0.970	1.055	1.035	0.997	1.099	0.986	1.005	0.942	0.953	0.915	1.019	1.005	1.062	1.000	1.000
2	0.970	0.970	0.943	1.033	0.926	0.986	1.005	0.932	0.951	1.025	1.059	1.097	1.007	0.883	1.000	1.000
3	0.970	0.970	1.000	0.972	0.962	0.961	0.991	0.980	0.904	1.016	1.000	0.930	0.918	0.963	1.000	1.000
4	0.970	0.970	0.972	1.017	0.983	0.987	1.047	1.018	0.936	0.872	0.948	0.930	0.984	1.039	1.000	1.000
5	0.970	0.970	1.098	0.990	0.953	1.091	1.084	1.009	1.028	1.008	1.092	1.003	1.007	1.037	1.000	1.000
6	0.970	0.970	0.973	0.913	1.026	1.022	1.039	1.027	0.982	0.873	1.024	1.050	1.021	1.072	1.000	1.000
7	0.970	0.970	1.065	1.021	1.038	1.094	1.082	1.061	0.947	1.023	1.021	1.056	1.006	0.999	1.000	1.000
8	0.970	0.970	1.067	1.046	1.051	1.106	1.021	1.021	1.002	1.017	0.998	0.973	0.883	0.940	1.000	1.000
9	0.970	0.970	0.996	1.058	0.990	1.029	1.006	0.934	1.022	0.899	0.926	0.963	0.893	1.053	1.000	1.000
10	0.970	0.970	0.982	0.984	1.014	0.972	1.062	0.996	0.936	1.050	1.056	1.028	1.126	0.988	1.000	1.000
11	0.970	0.970	1.020	0.933	0.934	1.047	1.049	1.015	1.040	1.018	1.098	1.102	1.023	1.055	1.000	1.000
12	0.970	0.970	0.982	0.928	0.951	0.975	1.041	0.991	1.032	1.023	1.131	1.032	1.125	1.140	1.000	1.000
13	0.970	0.970	0.938	0.954	0.887	0.972	1.006	0.999	0.976	0.999	1.024	1.086	1.000	0.988	1.000	1.000
14	0.970	0.970	1.018	0.952	0.976	1.058	0.992	0.956	0.948	0.946	0.948	0.994	0.921	0.965	1.000	1.000
15	0.970	0.970	0.978	1.021	0.964	1.003	1.039	1.023	1.006	1.088	1.020	0.937	0.883	0.965	1.000	1.000
16	0.970	0.970	0.992	0.936	0.955	1.012	1.034	1.060	1.002	1.119	1.010	0.999	0.998	1.061	1.000	1.000
17	0.970	0.970	1.005	0.987	0.975	1.026	1.030	1.002	0.978	0.996	1.025	1.013	0.977	1.012	1.000	1.000

|| Quadrant# 7 ||

phi\eta	0	1	2	3	4	5	6	7	8	9	10	11	12	13	14	15
0	0.970	0.970	0.960	0.952	0.959	1.024	1.006	1.030	0.990	1.004	1.029	1.013	1.026	1.023	1.000	1.000
1	0.970	0.970	0.961	0.898	1.003	1.072	0.989	1.171	1.050	1.143	1.110	1.107	1.099	1.109	1.000	1.000
2	0.970	0.970	1.013	0.917	0.992	1.040	1.016	1.055	1.034	1.066	1.033	1.074	0.992	0.995	1.000	1.000
3	0.970	0.970	0.995	0.883	0.987	1.013	1.012	1.032	0.964	1.019	1.031	1.036	1.058	0.988	1.000	1.000
4	0.970	0.970	0.916	0.912	0.911	0.971	1.021	1.030	0.973	0.953	1.069	1.060	1.116	1.097	1.000	1.000
5	0.970	0.970	0.922	0.941	1.031	1.002	1.010	0.969	1.036	1.023	1.077	1.126	1.075	1.097	1.000	1.000
6	0.970	0.970	0.971	1.024	1.050	1.039	1.021	1.021	1.044	1.043	1.100	1.013	1.059	0.990	1.000	1.000
7	0.970	0.970	0.972	0.960	0.967	1.086	1.042	1.137	0.962	1.041	0.976	0.970	1.038	1.038	1.000	1.000
8	0.970	0.970	0.965	0.940	0.899	1.021	1.027	1.019	1.074	1.029	1.036	1.045	1.027	1.199	1.000	1.000
9	0.970	0.970	1.021	1.006	0.979	1.048	1.076	1.042	1.001	0.997	1.038	0.980	1.014	1.062	1.000	1.000
10	0.970	0.970	0.903	0.905	0.892	0.972	0.919	0.978	0.888	0.951	0.966	0.945	0.993	0.976	1.000	1.000
11	0.970	0.970	0.853	0.901	0.933	1.038	1.047	0.969	0.942	0.961	0.988	1.009	0.932	1.020	1.000	1.000
12	0.970	0.970	0.979	1.007	0.942	1.035	0.964	1.027	1.022	0.911	0.975	0.941	1.003	0.859	1.000	1.000
13	0.970	0.970	0.954	0.986	0.935	1.036	0.974	1.013	1.006	0.911	0.973	0.944	1.001	0.869	1.000	1.000
14	0.970	0.970	1.003	1.020	0.929	1.008	0.959	1.027	0.987	1.004	0.981	0.981	0.928	0.978	1.000	1.000
15	0.970	0.970	0.887	0.969	0.954	0.964	1.007	0.936	0.977	1.022	1.076	0.964	1.051	1.022	1.000	1.000
16	0.970	0.970	1.037	0.968	0.932	1.044	1.018	1.039	1.038	0.999	1.027	1.005	1.038	1.071	1.000	1.000
17	0.970	0.970	0.960	0.952	0.959	1.024	1.006	1.030	0.990	1.004	1.029	1.013	1.026	1.023	1.000	1.000

Table 4-1 Single Tower Threshold and Total Et Threshold of each trigger type

Trigger condition = 1	BUFFET_25			
STT - EM [GeV] : Sum	A	B	C	D
West forward	1	5	1	1
West plug	1	5	1	1
Central	1	5	1	1
East plug	1	5	1	1
East forward	1	5	1	1
STT - Hadron [GeV] :				
West forward	1	51	1	1
West plug	1	51	1	1
Central	1	51	1	1
East plug	1	51	1	1
East forward	1	51	1	1
L1 sums [GeV] :				
EM	25	15	0	0
Had	25	127	0	0
Total	25	127	0	0

Trigger condition = 2	BUFFET_30			
STT - EM [GeV] : Sum	A	B	C	D
West forward	1	5	1	1
West plug	1	5	1	1
Central	1	5	1	1
East plug	1	5	1	1
East forward	1	5	1	1
STT - Hadron [GeV] :				
West forward	1	51	1	1
West plug	1	51	1	1
Central	1	51	1	1
East plug	1	51	1	1
East forward	1	51	1	1
L1 sums [GeV] :				
EM	30	15	0	0
Had	30	127	0	0
Total	30	127	0	0

Trigger condition = 3	BUFFET_30_CMU			
STT - EM [GeV] : Sum	A	B	C	D
West forward	1	5	1	1
West plug	1	5	1	1
Central	1	5	1	1
East plug	1	5	1	1
East forward	1	5	1	1
STT - Hadron [GeV] :				
West forward	1	51	1	1
West plug	1	51	1	1
Central	1	51	1	1
East plug	1	51	1	1
East forward	1	51	1	1
L1 sums [GeV] :				
EM	30	15	0	0
Had	30	127	0	0
Total	30	127	0	0

Trigger condition = 4	BUFFET_30_FMU			
STT - EM [GeV] : Sum	A	B	C	D
West forward	1	5	1	1
West plug	1	5	1	1
Central	1	5	1	1
East plug	1	5	1	1
East forward	1	5	1	1
STT - Hadron [GeV] :				
West forward	1	51	1	1
West plug	1	51	1	1
Central	1	51	1	1
East plug	1	51	1	1
East forward	1	51	1	1
L1 sums [GeV] :				
EM	30	15	0	0
Had	30	127	0	0
Total	30	127	0	0

Trigger condition = 5	BUFFET_30_CMUEM			
STT - EM [GeV] : Sum	A	B	C	D
West forward	1	5	1	1
West plug	1	5	1	1
Central	1	5	1	1
East plug	1	5	1	1
East forward	1	5	1	1
STT - Hadron [GeV] :				
West forward	1	51	1	1
West plug	1	51	1	1
Central	1	51	1	1
East plug	1	51	1	1
East forward	1	51	1	1
L1 sums [GeV] :				
EM	30	15	0	0
Had	30	127	0	0
Total	30	127	0	0

Trigger condition = 6				
STT - EM [GeV] : Sum	A	B	C	D
West forward	1	2	1	1
West plug	1	5	1	1
Central	1	5	1	1
East plug	1	5	1	1
East forward	1	2	1	1
STT - Hadron [GeV] :				
West forward	1	51	1	1
West plug	1	51	1	1
Central	1	51	1	1
East plug	1	51	1	1
East forward	1	51	1	1
L1 sums [GeV] :				
EM	30	15	0	0
Had	30	127	0	0
Total	30	127	0	0

Trigger condition = 7	BUFFET_30_CMUEM_FEM_1_5			
STT - EM [GeV] : Sum	A	B	C	D
West forward	1	5	1	1
West plug	1	5	51	1
Central	1	5	51	1
East plug	1	5	51	1
East forward	1	5	1	1
STT - Hadron [GeV] :				
West forward	1	51	51	1
West plug	1	51	51	1
Central	1	51	51	1
East plug	1	51	51	1
East forward	1	51	51	1
L1 sums [GeV] :				
EM	30	15	5	0
Had	30	127	127	0
Total	30	127	127	0

Trigger condition = 8	BUFFET_30_CMUEM_FEM_1_10			
STT - EM [GeV] : Sum	A	B	C	D
West forward	1	5	1	1
West plug	1	5	51	1
Central	1	5	51	1
East plug	1	5	51	1
East forward	1	5	1	1
STT - Hadron [GeV] :				
West forward	1	51	51	1
West plug	1	51	51	1
Central	1	51	51	1
East plug	1	51	51	1
East forward	1	51	51	1
L1 sums [GeV] :				
EM	30	15	10	0
Had	30	127	127	0
Total	30	127	127	0

Trigger condition = 9	BUFFET_30_CMUEM_FEM_1_15			
STT - EM [GeV] : Sum	A	B	C	D
West forward	1	5	1	1
West plug	1	5	51	1
Central	1	5	51	1
East plug	1	5	51	1
East forward	1	5	1	1
STT - Hadron [GeV] :				
West forward	1	51	51	1
West plug	1	51	51	1
Central	1	51	51	1
East plug	1	51	51	1
East forward	1	51	51	1
L1 sums [GeV] :				
EM	30	15	15	0
Had	30	127	127	0
Total	30	127	127	0

Table 3-2 Systematic errors of the PEM energy scale calibration

Type	Source	Error (%)
Overall energy scale	Monitor tube electronics	5
	H.V. dependence	1.9
	Gas gain monitoring	0.4
Channel by channel	Mapping	1.3
	Source capacitance (linearity)	1

Trigger condition = 19 BUFFET_MEDIUM

STT - EM [GeV] :	Sum	A	B	C	D
West forward		1	51	1	1
West plug		1	51	1	1
Central		1	7.4	51	1
East plug		1	51	1	1
East forward		1	51	1	1
STT - Hadron [GeV] :					
West forward		1	51	51	1
West plug		1	51	51	1
Central		1	51	51	1
East plug		1	51	51	1
East forward		1	51	51	1
L1 sums [GeV] :					
EM		30	7	15	0
Had		30	127.75	127.75	0
Total		30	127.75	127.75	0

Trigger condition = 20 BUFFET_MEDIUM_ELEC_9

STT - EM [GeV] :	Sum	A	B	C	D
West forward		1	51	1	1
West plug		1	51	1	1
Central		1	9	51	1
East plug		1	51	1	1
East forward		1	51	1	1
STT - Hadron [GeV] :					
West forward		1	51	51	1
West plug		1	51	51	1
Central		1	51	51	1
East plug		1	51	51	1
East forward		1	51	51	1
L1 sums [GeV] :					
EM		30	9	15	0
Had		30	127.75	127.75	0
Total		30	127.75	127.75	0

Trigger condition = 21 BUFFET_MEDIUM_ELEC_12

STT - EM [GeV] :	Sum	A	B	C	D
West forward		1	51	1	1
West plug		1	51	1	1
Central		1	12	51	1
East plug		1	51	1	1
East forward		1	51	1	1
STT - Hadron [GeV] :					
West forward		1	51	51	1
West plug		1	51	51	1
Central		1	51	51	1
East plug		1	51	51	1
East forward		1	51	51	1
L1 sums [GeV] :					
EM		30	12	15	0
Had		30	127.75	127.75	0
Total		30	127.75	127.75	0

Trigger condition = 22 BUFFET_MEDIUM_ELEC_7

STT - EM [GeV] :	Sum	A	B	C	D
West forward		1	51	1	1
West plug		1	51	1	1
Central		1	7.4	51	1
East plug		1	51	1	1
East forward		1	51	1	1
STT - Hadron [GeV] :					
West forward		1	51	51	1
West plug		1	51	51	1
Central		1	51	51	1
East plug		1	51	51	1
East forward		1	51	51	1
L1 sums [GeV] :					
EM		30	7.50	15	0
Had		30	127.75	127.75	0
Total		30	127.75	127.75	0

Trigger condition = 23 BUFFET_LOW

STT - EM [GeV] :	Sum	A	B	C	D
West forward		1	51	1	1
West plug		1	51	1	1
Central		1	7.4	51	1
East plug		1	51	1	1
East forward		1	51	1	1
STT - Hadron [GeV] :					
West forward		1	51	51	1
West plug		1	51	51	1
Central		1	51	51	1
East plug		1	51	51	1
East forward		1	51	51	1
L1 sums [GeV] :					
EM		20	7	10	0
Had		20	127.75	127.75	0
Total		20	127.75	127.75	0

Trigger condition = 24 BUFFET_MEDIUM

STT - EM [GeV] :	Sum	A	B	C	D
West forward		1	51	1	1
West plug		1	51	1	1
Central		1	9	51	1
East plug		1	51	1	1
East forward		1	51	1	1
STT - Hadron [GeV] :					
West forward		1	51	51	1
West plug		1	51	51	1
Central		1	51	51	1
East plug		1	51	51	1
East forward		1	51	51	1
L1 sums [GeV] :					
EM		30	9	15	0
Had		30	127.75	127.75	0
Total		30	127.75	127.75	0

Trigger condition = 25 BUFFET_MEDIUM

STT - EM [GeV] :	Sum	A	B	C	D
West forward		1	51	1	1
West plug		1	51	1	1
Central		1	9	51	1
East plug		1	51	1	1
East forward		1	51	1	1
STT - Hadron [GeV] :					
West forward		1	51	51	1
West plug		1	51	51	1
Central		1	51	51	1
East plug		1	51	51	1
East forward		1	51	51	1
L1 sums [GeV] :					
EM		30	9	15	0
Had		30	127.75	127.75	0
Total		30	127.75	127.75	0

Trigger condition = 26 BUFFET_HIGH

STT - EM [GeV] :	Sum	A	B	C	D
West forward		1	51	1	1
West plug		1	51	1	1
Central		1	10	51	1
East plug		1	51	1	1
East forward		1	51	1	1
STT - Hadron [GeV] :					
West forward		1	51	51	1
West plug		1	51	51	1
Central		1	51	51	1
East plug		1	51	51	1
East forward		1	51	51	1
L1 sums [GeV] :					
EM		40	9.50	20	0
Had		40	127.75	127.75	0
Total		40	127.75	127.75	0

Trigger condition = 27 BUFFET_BURN

STT - EM [GeV] :	Sum	A	B	C	D
West forward		1	51	1	1
West plug		1	51	1	1
Central		1	12	51	1
East plug		1	51	1	1
East forward		1	51	1	1
STT - Hadron [GeV] :					
West forward		1	51	51	1
West plug		1	51	51	1
Central		1	51	51	1
East plug		1	51	51	1
East forward		1	51	51	1
L1 sums [GeV] :					
EM		45	11.50	20	0
Had		45	127.75	127.75	0
Total		45	127.75	127.75	0

Trigger condition = 10 (Not used)

STT - EM [GeV] :	Sum	A	B	C	D
West forward		1	1	1	1
West plug		1	1	1	1
Central		1	1	1	1
East plug		1	1	1	1
East forward		1	1	1	1
STT - Hadron [GeV] :					
West forward		1	1	1	1
West plug		1	1	1	1
Central		1	1	1	1
East plug		1	1	1	1
East forward		1	1	1	1
L1 sums [GeV] :					
EM		0	0	0	0
Had		0	0	0	0
Total		0	0	0	0

Trigger condition = 11 BUFFET_30_ELEC_7

STT - EM [GeV] :	Sum	A	B	C	D
West forward		1	7.4	1	1
West plug		1	7.4	1	1
Central		1	7.4	1	1
East plug		1	7.4	1	1
East forward		1	7.4	1	1
STT - Hadron [GeV] :					
West forward		1	51	1	1
West plug		1	51	1	1
Central		1	51	1	1
East plug		1	51	1	1
East forward		1	51	1	1
L1 sums [GeV] :					
EM		30	15	0	0
Had		30	127	0	0
Total		30	127	0	0

Trigger condition = 12 BUFFET_30_ELEC_10

STT - EM [GeV] :	Sum	A	B	C	D
West forward		1	10	1	1
West plug		1	10	1	1
Central		1	10	1	1
East plug		1	10	1	1
East forward		1	10	1	1
STT - Hadron [GeV] :					
West forward		1	51	1	1
West plug		1	51	1	1
Central		1	51	1	1
East plug		1	51	1	1
East forward		1	51	1	1
L1 sums [GeV] :					
EM		30	15	0	0
Had		30	127	0	0
Total		30	127	0	0

Trigger condition = 13 BUFFET_30_CMUEM_PEM_1_10

STT - EM [GeV] :	Sum	A	B	C	D
West forward		1	5	51	1
West plug		1	5	1	1
Central		1	5	51	1
East plug		1	5	1	1
East forward		1	5	51	1
STT - Hadron [GeV] :					
West forward		1	51	51	1
West plug		1	51	51	1
Central		1	51	51	1
East plug		1	51	51	1
East forward		1	51	51	1
L1 sums [GeV] :					
EM		30	15	10	0
Had		30	127	127	0
Total		30	127	127	0

Trigger condition = 14 BUFFET_30_CMUEM_PEM_1_15

STT - EM [GeV] :	Sum	A	B	C	D
West forward		1	5	51	1
West plug		1	5	1	1
Central		1	5	51	1
East plug		1	5	1	1
East forward		1	5	51	1
STT - Hadron [GeV] :					
West forward		1	51	51	1
West plug		1	51	51	1
Central		1	51	51	1
East plug		1	51	51	1
East forward		1	51	51	1
L1 sums [GeV] :					
EM		30	15	15	0
Had		30	127	127	0
Total		30	127	127	0

Trigger condition = 15 BUFFET_30_CMUEM_PEM_FEM

STT - EM [GeV] :	Sum	A	B	C	D
West forward		1	5	1	1
West plug		1	5	1	1
Central		1	5	51	1
East plug		1	5	1	1
East forward		1	5	1	1
STT - Hadron [GeV] :					
West forward		1	51	51	1
West plug		1	51	51	1
Central		1	51	51	1
East plug		1	51	51	1
East forward		1	51	51	1
L1 sums [GeV] :					
EM		30	15	15	0
Had		30	127	127	0
Total		30	127	127	0

Trigger condition = 16 BUFFET_30_CMUEM_PEM_FEM_20

STT - EM [GeV] :	Sum	A	B	C	D
West forward		1	5	1	1
West plug		1	5	1	1
Central		1	5	51	1
East plug		1	5	1	1
East forward		1	5	1	1
STT - Hadron [GeV] :					
West forward		1	51	51	1
West plug		1	51	51	1
Central		1	51	51	1
East plug		1	51	51	1
East forward		1	51	51	1
L1 sums [GeV] :					
EM		30	15	20	0
Had		30	127	127	0
Total		30	127	127	0

Trigger condition = 17 (Not used)

STT - EM [GeV] :	Sum	A	B	C	D
West forward		1	5	1	1
West plug		1	5	1	1
Central		1	5	1	1
East plug		1	5	1	1
East forward		1	5	1	1
STT - Hadron [GeV] :					
West forward		1	51	1	1
West plug		1	51	1	1
Central		1	51	1	1
East plug		1	51	1	1
East forward		1	51	1	1
L1 sums [GeV] :					
EM		30	15	0	0
Had		30	127	0	0
Total		30	127	0	0

Trigger condition = 18 (Not used)

STT - EM [GeV] :	Sum	A	B	C	D
West forward		1	5	1	1
West plug		1	5	1	1
Central		1	5	51	1
East plug		1	5	1	1
East forward		1	5	1	1
STT - Hadron [GeV] :					
West forward		1	51	51	1
West plug		1	51	51	1
Central		1	51	51	1
East plug		1	51	51	1
East forward		1	51	51	1
L1 sums [GeV] :					
EM		30	15	15	0
Had		30	127.75	127.75	0
Total		30	127.75	127.75	0

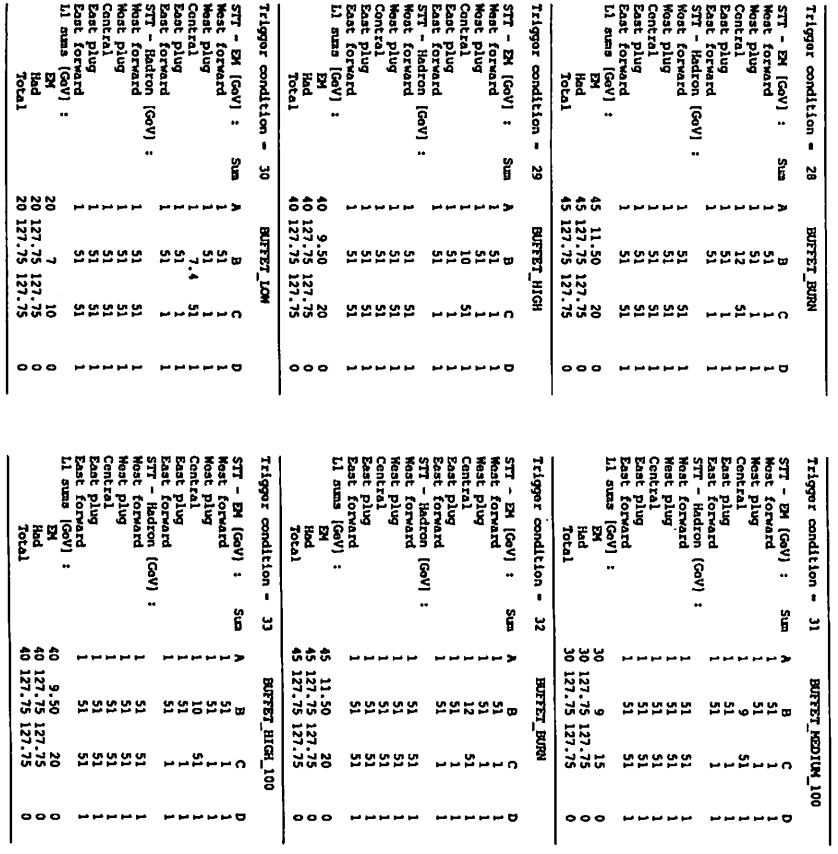

Trigger condition = 28 BUFFET_BURN

	Sum	A	B	C	D
STT - EM [GeV] :					
West forward	1	1	51	1	1
West plug	1	1	51	1	1
Central	1	1	12	51	1
East plug	1	1	51	1	1
East forward	1	1	51	1	1
STT - Hadron [GeV] :					
West forward	1	1	51	51	1
West plug	1	1	51	51	1
Central	1	1	51	51	1
East plug	1	1	51	51	1
East forward	1	1	51	51	1
L1 sums [GeV] :					
EM	45	11.50	20	0	0
Had	45	127.75	127.75	0	0
Total	45	127.75	127.75	0	0

Trigger condition = 29 BUFFET_HIGH

	Sum	A	B	C	D
STT - EM [GeV] :					
West forward	1	1	51	1	1
West plug	1	1	51	1	1
Central	1	1	10	51	1
East plug	1	1	51	1	1
East forward	1	1	51	1	1
STT - Hadron [GeV] :					
West forward	1	1	51	51	1
West plug	1	1	51	51	1
Central	1	1	51	51	1
East plug	1	1	51	51	1
East forward	1	1	51	51	1
L1 sums [GeV] :					
EM	40	9.50	20	0	0
Had	40	127.75	127.75	0	0
Total	40	127.75	127.75	0	0

Trigger condition = 30 BUFFET_LOW

	Sum	A	B	C	D
STT - EM [GeV] :					
West forward	1	1	51	1	1
West plug	1	1	51	1	1
Central	1	1	7.4	51	1
East plug	1	1	51	1	1
East forward	1	1	51	1	1
STT - Hadron [GeV] :					
West forward	1	1	51	1	1
West plug	1	1	51	51	1
Central	1	1	51	51	1
East plug	1	1	51	51	1
East forward	1	1	51	51	1
L1 sums [GeV] :					
EM	20	7	10	0	0
Had	20	127.75	127.75	0	0
Total	20	127.75	127.75	0	0

Trigger condition = 31 BUFFET_MEDIUM_100

	Sum	A	B	C	D
STT - EM [GeV] :					
West forward	1	1	51	1	1
West plug	1	1	51	1	1
Central	1	1	9	51	1
East plug	1	1	51	1	1
East forward	1	1	51	1	1
STT - Hadron [GeV] :					
West forward	1	1	51	51	1
West plug	1	1	51	51	1
Central	1	1	51	51	1
East plug	1	1	51	51	1
East forward	1	1	51	51	1
L1 sums [GeV] :					
EM	30	9	127.75	15	0
Had	30	127.75	127.75	0	0
Total	30	127.75	127.75	0	0

Trigger condition = 32 BUFFET_BURN

	Sum	A	B	C	D
STT - EM [GeV] :					
West forward	1	1	51	1	1
West plug	1	1	51	1	1
Central	1	1	12	51	1
East plug	1	1	51	1	1
East forward	1	1	51	1	1
STT - Hadron [GeV] :					
West forward	1	1	51	51	1
West plug	1	1	51	51	1
Central	1	1	51	51	1
East plug	1	1	51	51	1
East forward	1	1	51	51	1
L1 sums [GeV] :					
EM	45	11.50	20	0	0
Had	45	127.75	127.75	0	0
Total	45	127.75	127.75	0	0

Trigger condition = 33 BUFFET_HIGH_100

	Sum	A	B	C	D
STT - EM [GeV] :					
West forward	1	1	51	1	1
West plug	1	1	51	1	1
Central	1	1	10	51	1
East plug	1	1	51	1	1
East forward	1	1	51	1	1
STT - Hadron [GeV] :					
West forward	1	1	51	51	1
West plug	1	1	51	51	1
Central	1	1	51	51	1
East plug	1	1	51	51	1
East forward	1	1	51	51	1
L1 sums [GeV] :					
EM	40	9.50	20	0	0
Had	40	127.75	127.75	0	0
Total	40	127.75	127.75	0	0

Table 4-2 The integrated luminosity for each trigger type in the 1987 CDF run.

Trigger type		# of Trigger	Integrated Luminosity (nb)
1	BUFFET_25	3046	0.142E+00
2	BUFFET_30	11968	0.702E+00
3	BUFFET_30_CMU	25234	0.195E+01
4	BUFFET_30_FMU	6824	0.409E+00
5	BUFFET_30_CMUEM	164350	0.861E+01
6		1337	0.514E-01
7	BUFFET_30_CMUEM_FEM_1_5	539	0.610E-02
8	BUFFET_30_CMUEM_FEM_1_10	1254	0.677E-01
9	BUFFET_30_CMUEM_FEM_1_15	848	0.544E-01
10		0	0.000E+00
11	BUFFET_30_ELEC_7	733	0.462E-01
12	BUFFET_30_ELEC_10	751	0.435E-01
13	BUFFET_30_CMUEM_PEM_1_10	753	0.359E-01
14	BUFFET_30_CMUEM_PEM_1_15	756	0.393E-01
15	BUFFET_30_CMUEM_PEM_FEM	752	0.492E-01
16	BUFFET_30_CMUEM_PEM_FEM_20	750	0.487E-01
17		0	0.000E+00
18		2569	0.109E+00
19	BUFFET_MEDIUM	5009	0.151E+00
20	BUFFET_MEDIUM_ELEC_9	1211	0.460E-01
21	BUFFET_MEDIUM_ELEC_12	1268	0.458E-01
22	BUFFET_MEDIUM_ELEC_7	245	0.712E-02
23	BUFFET_LOW	18603	0.254E+00
24	BUFFET_MEDIUM	5368	0.194E+00
25	BUFFET_MEDIUM	54058	0.246E+01
26	BUFFET_HIGH	18149	0.172E+01
27	BUFFET_BURN	12559	0.188E+01
28	BUFFET_BURN	36887	0.481E+01
29	BUFFET_HIGH	45576	0.407E+01
30	BUFFET_LOW	9276	0.165E+00
31	BUFFET_MEDIUM_100	15158	0.776E+00
32	BUFFET_BURN	6838	0.856E+00
33	BUFFET_HIGH_100	5829	0.515E+00

Table 5-2 Event list of the 9 plug $W \rightarrow e\nu$ candidates

Run	Event	Ne	Et	Eta	Phi	ArTr	Tw	H/EM	Iso4	E/p	ζ	Chi5	Nc	Xph	Nv	XR	Djet	MET	SIG	Mtev
7317	1445	1	35.3	-1.80	4.59	1	1	12	0.01	0.06	9.99	0.9	2.5	0	0.2	1	0.1	0.0	34.6	24.8	69.4
7342	4524	1	25.6	-1.25	4.14	1	1	4	0.00	0.03	0.96	1.8	1.5	1	0.0	1	-1.6	0.0	23.9	20.0	49.3
7728	1980	1	36.0	1.66	4.06	1	1	9	0.01	0.02	1.84	1.4	1.9	1	0.1	1	-3.1	0.0	33.0	21.8	68.9
7757	772	1	28.5	1.40	4.93	1	2	4	0.03	0.03	1.07	0.8	1.9	1	0.0	2	-2.3	0.0	27.3	18.5	54.2
7768	159	1	46.7	-1.71	2.16	1	1	11	0.02	0.01	6.58	0.8	1.3	1	-0.9	1	0.3	0.0	36.1	21.5	82.1
7770	1990	1	44.7	1.32	4.07	1	1	9	0.01	0.02	0.77	1.0	2.7	1	-0.2	1	-10.0	0.0	39.1	22.3	83.6
7788	2931	1	33.3	-1.65	1.20	1	1	15	0.02	0.02	2.21	0.8	1.2	1	0.0	1	-0.6	0.2	20.5	10.0	52.2
7789	5493	1	43.4	1.69	1.88	1	1	11	0.01	0.01	1.67	1.4	1.6	1	-0.1	1	-1.1	0.0	47.7	48.6	90.9
7790	3086	1	29.3	-1.98	1.70	1	1	11	0.02	0.05	66.84	3.9	3.4	1	-1.2	1	0.9	0.0	31.3	24.9	60.2

Table 5-3 Event list of the 6 $Z^0 \rightarrow e^+e^-$ candidates

Run	Evt	Ne	Et	Eta	Phi	ArTr	Tw	H/EM	Iso4	E/p	ChiL	Chi5	Nc	Xph	Nv	XR	Zvtx	M12	M123	Pt2	Pt3
7288	1276	2	19.3	0.26	1.02	0	1	1	0.02	0.03	1.11						11.8	63.7		13.8	
			8.3	3.43	3.48	2	0	13	0.00	0.51	-9.99										
7377	830	2	45.5	0.03	0.26	0	1	2	0.01	0.07	0.95						83.7	69.0		21.8	
			23.8	0.65	3.37	0	1	3	0.01	0.11	0.70										
7614	4963	2	54.0	0.53	0.17	0	1	2	0.01	0.00	0.95						-18.5	98.4		21.8	
			32.3	1.71	3.35	1	1	13	0.01	0.21	0.98	5.2	4.1	1	-0.5	1	3.8				
7744	5364	2	21.7	0.19	4.81	0	1	2	0.01	0.01	0.97						53.4	81.4		2.8	
			21.6	2.69	1.54	2	0	9	0.00	0.22	-9.99										
7767	940	2	31.7	0.64	2.95	0	1	3	0.01	0.01	1.08						7.8	83.9		5.6	
			26.0	-1.21	6.09	1	1	3	0.00	0.06	0.89	0.0	63.6	1	-0.5	1	3.3				
7769	4235	3	35.3	1.79	2.14	1	1	12	0.00	0.04	4.36	2.8	3.5	1	0.0	1	-1.5	-16.4	80.1	95.2	15.5	5.5
			32.1	0.51	5.74	0	1	2	0.00	0.01	1.03										
			12.8	0.77	3.81	0	0	2	0.00	0.00	-9.99										

Table 5-1 Cuts used in the CDF electron DST production.

Class	Number of tracks	Cuts
Photon	0	$E_T(e) \geq 15$ GeV
		Had/EM ≤ 0.1
Electron	≥ 1	$E_T(e) \geq 5$ GeV
		Had/EM ≤ 0.1

Table 6-1 Backgrounds Estimate to the $W \rightarrow e\nu$ Event Sample in the Endplug region

1) Electrons from Tau Decay	
$W \rightarrow \tau\nu \rightarrow e\nu\nu$	0.3 ± 0.1 events
2) Electrons from Z^0 decay and one electron is undetected or mismeasured	
$Z \rightarrow ee$	0.12 ± 0.06 events
3) Electrons from Semi-leptonic Decay of Heavy Flavor Quarks.	
$b\bar{b} \rightarrow$ jets + $e\nu$	< 0.05 events
$t\bar{t} \rightarrow$ jets + $e\nu$	< 0.1 events
4) Other QCD Background	
Overlap of photons and charged hadrons and γ-conversions	0.30 ± 0.16 events
Total number of background	0.7 ± 0.2 (stat.)

Table 6-2 Set of cuts used to produce a "Background sample of Z"

1) Primary photon cuts

CEM region (Tower 9 veto)

$E_T(e) \geq 15$ GeV

Had/EM ≤ 0.05

I(R=0.4) ≤ 0.1

Number of tracks = 0

2) Secondary photon cuts

$E_T(e) \geq 5$ GeV

Had/EM ≤ 0.1

Number of tracks = 0

Table 6-3 Backgrounds Estimate to the $Z^0 \rightarrow e^+e^-$ Event Sample

1) QCD Overlapping Background		0.35 ± 0.08 events
2) Heavy Flavor Background ($b\bar{b} \rightarrow e^+e^-$ + jets)		< 0.003 events
Number of events in which $E_T(e)$ is greater than 15 GeV	329 events	
Number of events remained after Z cuts	none	
Equivalent integrated luminosity	8.6 pb^{-1}	

Table 7-1 Trigger and algorithm efficiencies of the W selection

Central electrons [Ref.5-4]	
CEM Geometrical Acceptance	$0.49 \pm 0.01 \pm 0.05$
$E_T(e) \geq 15$ GeV	0.91 ± 0.01
Had/EM ≤ 0.05	0.98 ± 0.01
I(R=0.4) ≤ 0.1	0.99 ± 0.01
Missing $E_T / \sqrt{\sum E_{T_{pc}}} \geq 2.8$	0.97 ± 0.01
Dijet veto	0.98 ± 0.01
	$0.41 \pm 0.01 \pm 0.04$
Trigger Efficiency	0.99 ± 0.01
Radiative	0.97 ± 0.01
Tracking Efficiency from Data	0.98 ± 0.01
Total cutting efficiency	$0.37 \pm 0.02 \pm 0.08$
	stat. syst.
Plug electrons	
ϵ_{geom}^{PEM}: PEM Geometrical Acceptance	$0.30 \pm 0.01 \pm 0.02$
ϵ_{15}: Trigger acceptance of Total E_T 15 GeV	$0.90 \pm 0.04 \pm 0.03$
ϵ_{20}: Trigger acceptance of Total E_T 20 GeV	$0.82 \pm 0.04 \pm 0.03$
Cluster finding efficiency ($E_T \geq 15$ GeV)	0.92 ± 0.05
Had/EM ≤ 0.05	$0.92 \pm 0.06 \pm 0.02$
Longitudinal shower shape $\zeta \leq 4$	$0.95 \pm 0.01 \pm 0.01$
Lateral shower shape $\chi^2_{lateral} \leq 10$	$0.93 \pm 0.01 \pm 0.03$
I(R=0.4) ≤ 0.1	$0.99 \pm 0.05 \pm 0.01$
Dijet $D < 0.3$	$0.97 \pm 0.05 \pm 0.02$
$\not{E}_T^2 / \sum E_{T_{pc}} \geq 7.8$ GeV	$0.90 \pm 0.05 \pm 0.02$
Number of associated tracks ≥ 1	$0.88 \pm 0.05 \pm 0.03$
$\Delta\varphi_{CTC} \leq 1°$	0.97 ± 0.03
$\Delta R_{VTPC} \leq 4$ cm	0.95 ± 0.05
Fiducial tracking volume	0.95 ± 0.02
ϵ_{algo}: Total algorithm efficiency	$0.49 \pm 0.07 \pm 0.04$
	stat. syst.

Table 7-2 Trigger and algorithm efficiencies of the Z selection

Geometrical and trigger Acceptance	0.59 ± 0.02
Primary electron cuts	
CEM electron cuts	0.95 ± 0.03
Secondary electron cuts	
CEM electron cuts	0.70 ± 0.04
PEM electron cuts	0.90 ± 0.03
FEM electron cuts	0.86 ± 0.08
Overall efficiency	0.46 ± 0.02

Table 7-3 χ^2 of the W transverse mass fitting for various generated mass

Generated W mass [GeV/c^2]	χ^2 data weighted	χ^2 prediction weighted
77.2	13.5	12.7
78.9	11.3	10.4
80.1	7.3	6.5
81.1	7.9	7.3
82.1	7.4	7.0
82.5	6.4	7.0
83.4	7.5	7.9
84.0	6.4	6.4
85.0	7.3	9.7
86.0	8.4	10.3

Table 7-4 Corrected Z^0 Mass

Run	Event	$N_{e,\gamma}$	E_T^c	ΔE_T^c	correction	η	φ	M_Z	ΔM_Z	P_{Tz}
7288	1276	3	19.3	0.9		0.26	1.02	75.2	6.7	11.9
			8.3	1.0		3.43	3.48			
			3.3	0.4	photon	3.40	3.72			
7377	830	2	45.7	1.7		0.03	0.26	85.7	3.5	10.0
			36.7	2.7	CTC	0.65	3.37			
7614	4963	2	54.0	2.0		0.53	0.17	98.4	4.5	21.8
			32.3	2.7		1.71	3.35			
7744	5364	2	21.7	1.0		0.19	4.81	86.1	5.1	3.8
			22.7	2.5	φ-boundary	2.69	1.54			
7767	940	2	31.7	1.3		0.64	2.95	99.5	10.8	5.0
			36.7	7.8	30°-crack	-1.21	6.09			
7769	4235	3	35.3	2.9		1.79	2.14	95.2	5.1	5.5
			32.1	1.3		0.51	5.74			
			12.8	0.7		0.77	3.81			

FIGURE CAPTIONS

Fig.1-1 A lowest order Feynman diagrams which produce (a) W boson and (b) Z boson.

Fig.1-2 R, defined by Eq.1-1, as a function of top quark mass for various choice of number of light neutrinos, together with the combined experimental results from UA1/UA2. Taken from Ref.1-10.

Fig.1-3 A perspective view of the CDF detector showing the central detector and the forward and backward detector. The forward/backward detector covers $2° < \theta < 10°$ and $170° < \theta < 178°$. The central detector covers $10° < \theta < 170°$.

Fig.1-4 A cut through view of the half of the CDF detector. A full view of the forward detector is shown in left of the figure and the half of the central detector in right.

Fig.1-5 A CTC endplate. 84 layers of sense wires are grouped into five axial super layers and four stereo super layers.

Fig.1-6 Schematic drawing of two octagonal VTPC modules. One module is rotated to another by 11.5° in φ to prevent a charged particle totally missed due to the dead spaces near the octant boundaries.

Fig.1-7 Radiation length of the amount of material as a function of the polar angle.

Fig.1-8 An isometric view and a section view of a FTC module configuration.

Fig.1-9 One of two modules of the BBC counter. Beam runs perpendicular to the paper.

Fig.1-10 CDF hadron calorimeter tower segmentation in one of eight identical quadrants ($\Delta\varphi$=90°, η>0). Bold lines indicate module or chamber boundaries.

Fig.1-11 Schematic drawing of a CEM module. The coordinates shown here are called "local coordinates" and used in the CEM response map.

Fig.2-1 Cross sectional view of the Endplug electromagnetic calorimeter.

Fig.2-2 Exploded view of a layer of the proportional tube array.

Fig.5-9 $\chi^2_{lateral}$ distribution of electrons from test beam data at 100 GeV.

Fig.5-10 Electron efficiencies at $\chi^2_{lateral} \leq 10$ cut as a function of (a) electron energy and (b) polar angle. Observed shower shape depends on the tower threshold and therefore the $\chi^2_{lateral}$ distribution varies at lower electron energies. A difference of the test function F (see the text for the definition) from the actual shower shape generates a systematics on the $\chi^2_{lateral}$ distribution as the tower sizes (the polar angle in the detector) vary.

Fig.5-11 Scatter plot of the missing E_T v.s. electron E_T for the Central $W \rightarrow e\nu$ sample (22 events).

Fig.5-12 Scatter plot of the missing E_T v.s. electron E_T of the loose cut plug electron sample (134 events) and their projections.

Fig.5-13 (a) Isolation I(R=0.4) versus missing E_T significance χ of the event sample before making χ and I(R=0.4) cuts. QCD backgrounds appear in low χ and larger I(R=0.4) region, while the real $W \rightarrow e\nu$ events appear in high χ and smaller I(R=0.4) region.
(b) Missing E_T significance for I(R=0.4) ≤ 0.1 sample.

Fig.5-14 Scatter plot of the missing E_T v.s. electron E_T for the final sample of the plug W electron sample (9 events) and their projections.

Fig.5-15 Event display of the 9 events of $W \rightarrow e\nu$ candidates.

Fig.5-16 Distribution of the various quantities used in the cuts for the Endplug electron sample. The data is from the 1987 electron DST tapes and only the clusters in the Endplug electromagnetic calorimeter is shown in the plots. Solid line is the loose cut sample (134 events) and dashed line is the final sample of the W candidates (9 events). (a) Had/EM, (b) Isolation with cone radius R = 0.4, (c) $\chi^2_{longitudinal}(\zeta)$, (d) $\chi^2_{lateral}$ (5×5 towers) distribution, (e) track-calorimetry position matching (CTC and VTPC are combined in this figure according to their standard deviations: $\sigma(\Delta\varphi_{CTC}) = 0.79°$, $\sigma(\Delta R_{VTPC}) = 0.87$ cm, and offsets, -0.15° and 0.84 cm respectively), and (f) Dijet.

Fig.5-17 Dielectron mass distribution of the 12 events remained after "Z cuts" which have $M_{ee} \geq 20$ GeV/c^2.

Fig.5-18 Event display of the 6 events of $Z^0 \rightarrow e^+e^-$ candidates.

Fig.6-1 (a) Electron E_T spectrum from the process $W \rightarrow \tau\nu \rightarrow e\nu\nu$ by ISAJET V-6.10.
(b) after the detector simulation.

Fig.6-2 Scatter plot of the missing E_T versus the E_T of the primary electron for the process $Z^0 \rightarrow e^+e^-$. Events were generated with ISAJET V-6.10 and the detector simulation was done by CDFSIM V-4.4 (V-4.5 for the tracking simulation).

Fig.6-3 Missing E_T significance distribution for the background event sample which passed the same set of calorimetry cuts as the electron sample but has no associated tracks. The slope is fitted with $y = e^{-a\chi}$.

Fig.6-4 Electron (photon) pair mass distribution. Histogram shows the mass distribution of 12 events in the Z sample above $M_{ee} \geq 20$ GeV/c^2. Crosses are the QCD background sample (see Table 6-2 for the definition) normalized at the mass range 20 GeV/c$^2 \leq M_{ee} \leq 60$ GeV/c^2.

Fig.7-1 W total production cross sections in $\bar{p}p$ as a function of $\sqrt{s}$. B($W \rightarrow e\nu$) = 0.089 (m_t = 40 GeV/c^2) is assumed. The statistical and systematic errors are added quadrature. Of three curves in the plot, the center curve is the theoretical predictions by Altarelli *et al* [Ref.1-4]. The upper and lower curves reflect their theoretical uncertainty.

Fig.7-2 Z total production cross sections in $\bar{p}p$ as a function of $\sqrt{s}$. B($Z^0 \rightarrow e^+e^-$) = 0.032 (m_t = 40 GeV/c^2) is assumed. The statistical and systematic errors are added quadrature. Of three curves in the plot, the center curve is the theoretical predictions by Altarelli *et al* [Ref.1-4]. The upper and lower curves reflect their theoretical uncertainty.

Fig.7-3 Transverse mass distribution of the $W \rightarrow e\nu$ sample. Solid line is the 22 events from the Central electron analysis and the hatched area shows the 9 events from the plug electron analysis. Dotted cross is Monte Carlo data with the ISAJET V-6.10 at M_W = 81 GeV/c^2.

Fig.7-4 χ^2 of the transverse mass fitting (NDF = 11) as a function of the weak boson mass M_W. Transverse mass plot of 31 events of $W \rightarrow e\nu$ were fitted with the Monte Carlo transverse mass distribution. ISAJET V-6.10 and CDFSIM V-4.4

were used to generate W transverse mass distribution with various mass M_W. This χ^2 plot was further fitted parabolically and minimized χ^2 was obtained.

Fig.7-5 W mass together with the results from the UA1/UA2 experiments [Ref.1-16]. The statistical and systematic errors are added quadrature.

Fig.7-6 Mass of the electron pair or $ee\gamma$ system of 6 $Z^0 \rightarrow e^+e^-$ candidates after the energy correction. Error bars include the resolution of the energy/momentum measurements and the uncertainty in the energy correction for the electrons near detector boundaries.

Fig.7-7 Electron pair mass distribution of 6 $Z^0 \rightarrow e^+e^-$ candidates after the energy correction. Solid curve is the Monte Carlo with ISAJET V-6.10 and CDFSIM V-4.4 simulation at M_Z = 93 GeV/c^2.

Fig.D-1 The PEM spike noise seen by the PEM anode signals: (a) Anode energy sum v.s. single layer anode energy. (b) $E_{i-1}^{anode} + E_{i+1}^{anode}$ v.s. E_i^{anode}, as defined in Eq.D-1a.

Fig.D-2 PEM spike energies seen by pads vs anodes.

Fig.D-3 PEM spike pad/anode ratio as a function of η (a) and (c) and φ (b) and (d). Figures (a) and (b) are of west side (anti-proton direction) plug and (c) and (d) are of east side (proton direction) plug.

FIGURES

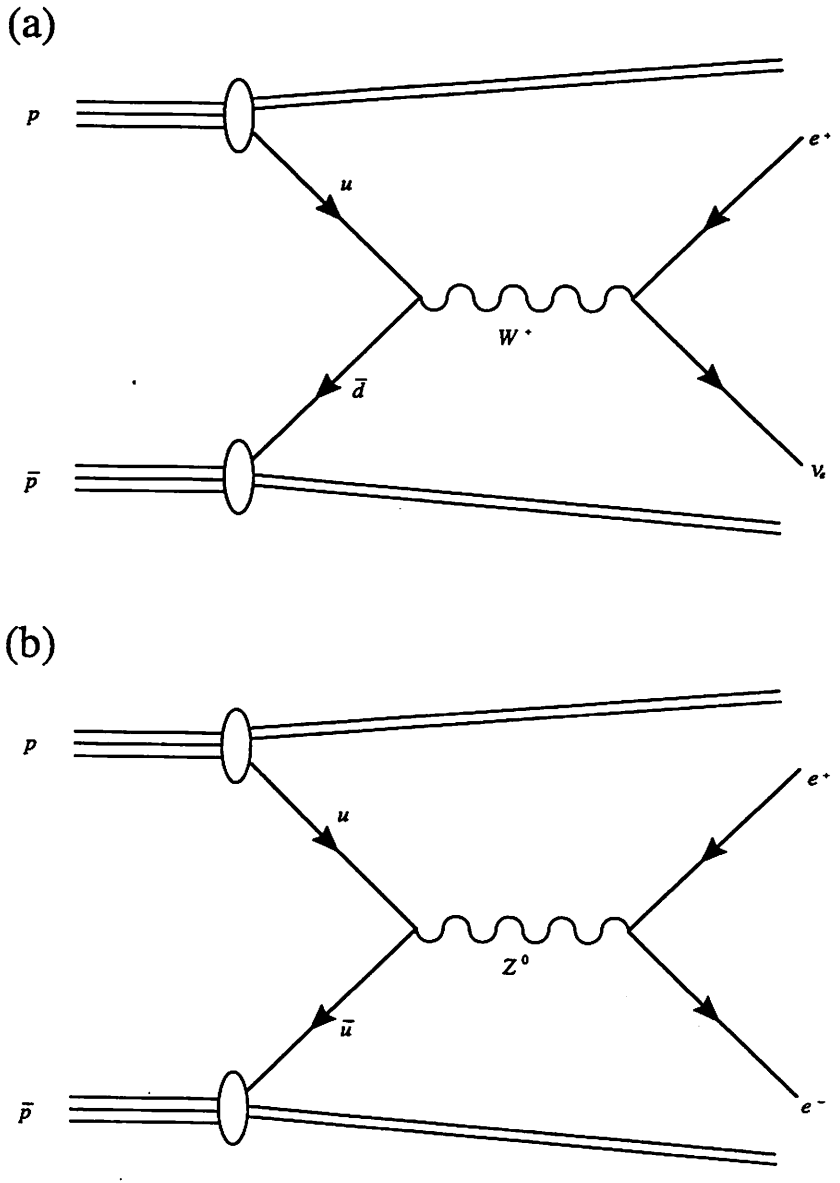

Fig.1-1

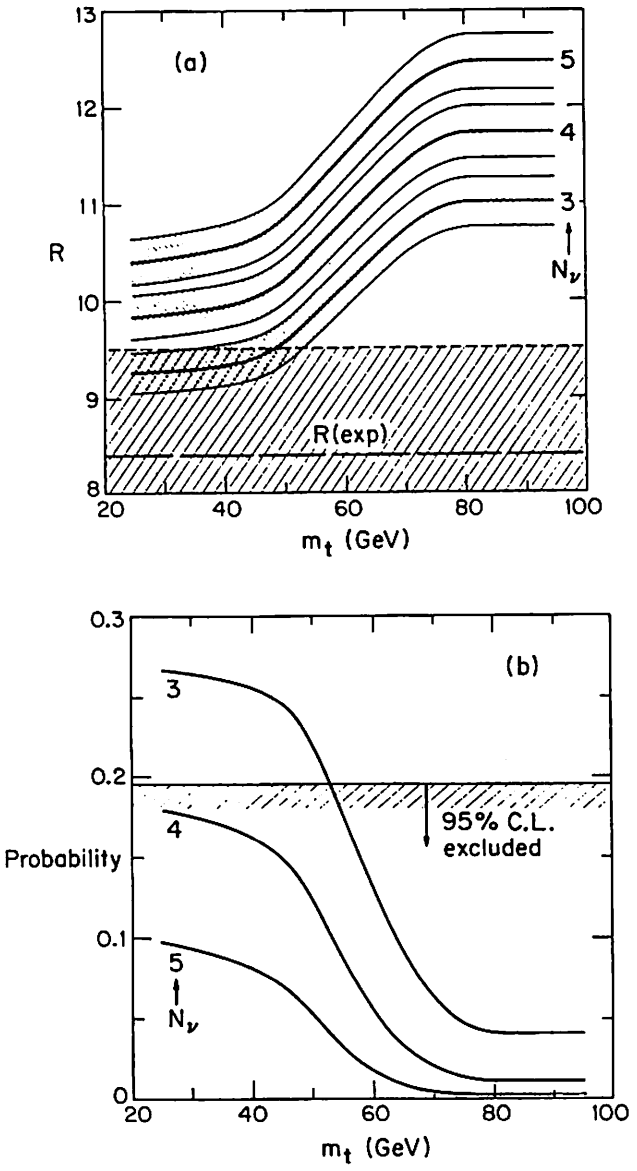

Fig.1-2. (a) R, defined by Eq.1-1, as a function of top quark mass for various choice of number of light neutrinos, together with the combined experimental results R(exp) from UA1/UA2; (b) overlap probability of R(theory) and R(exp) from (a). Taken from Ref.1-10.

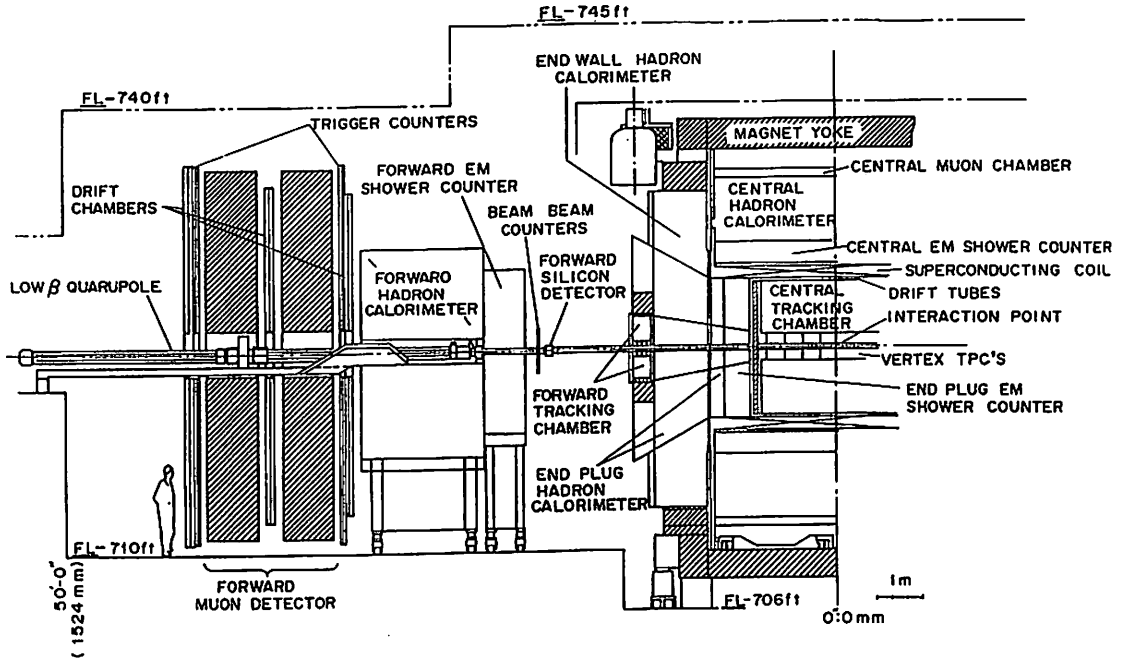

Fig.1-4 The CDF detector

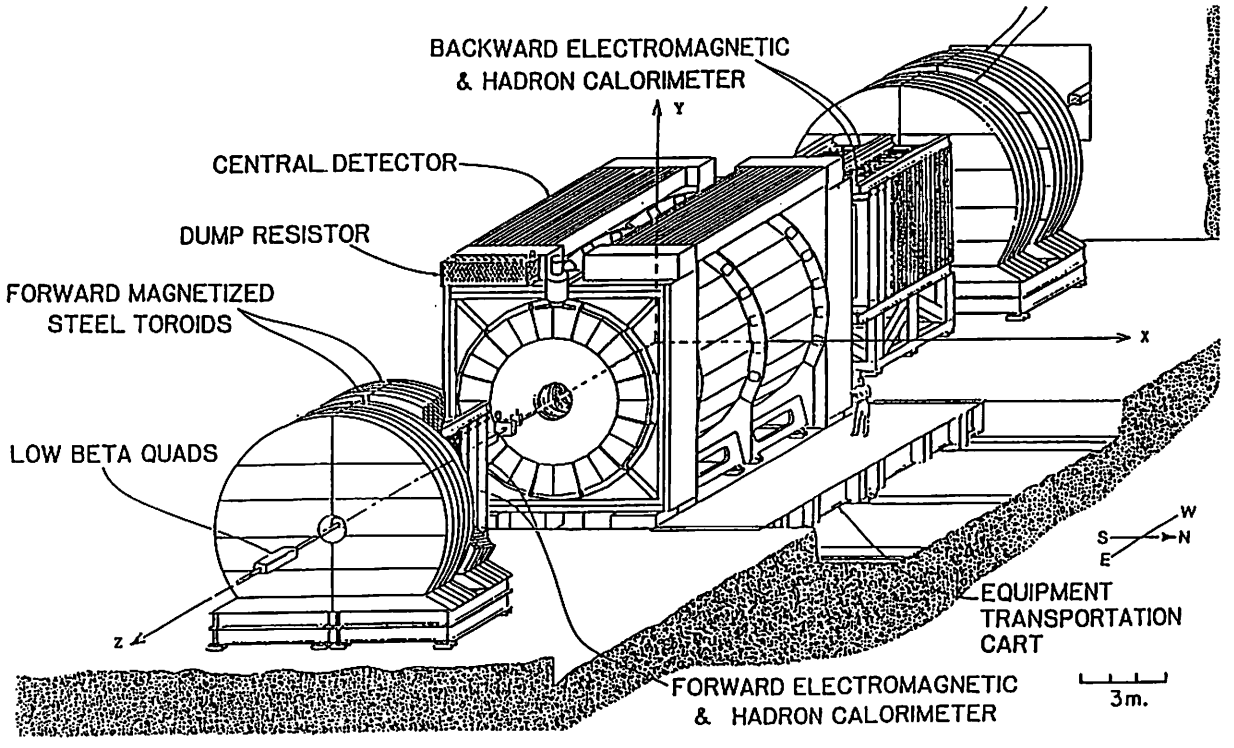

Fig.1-3 The CDF detector

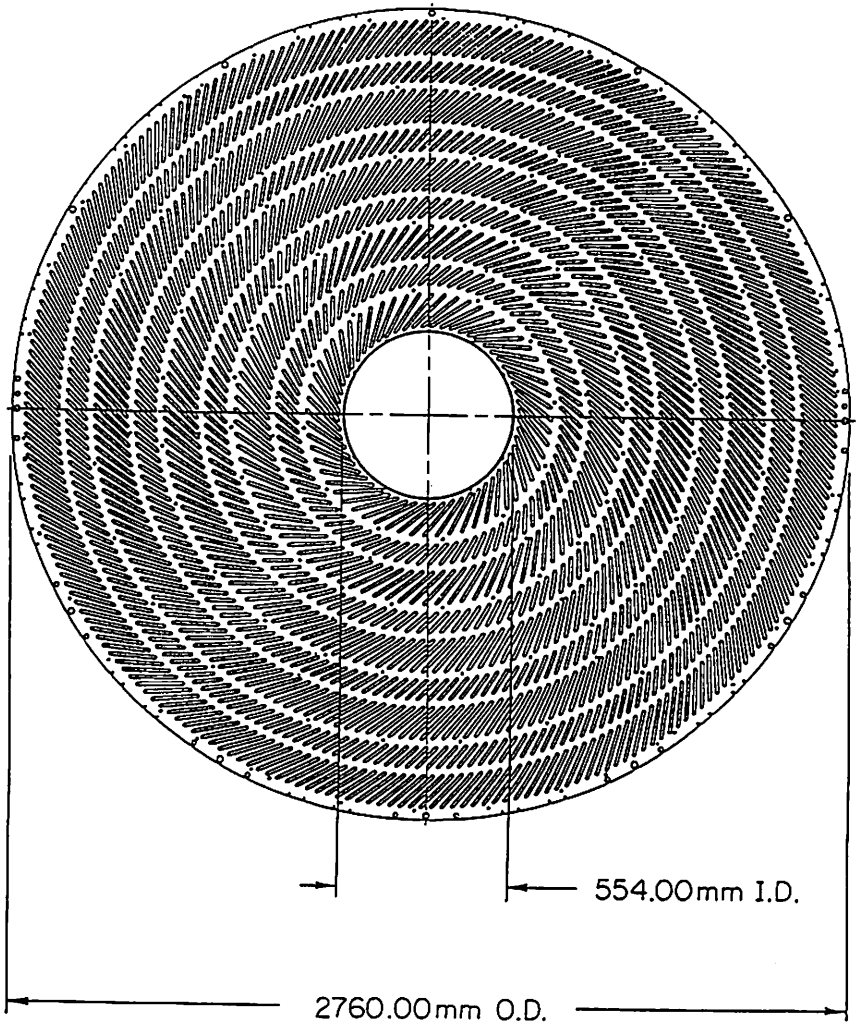

Fig.1-5 A CTC endplate

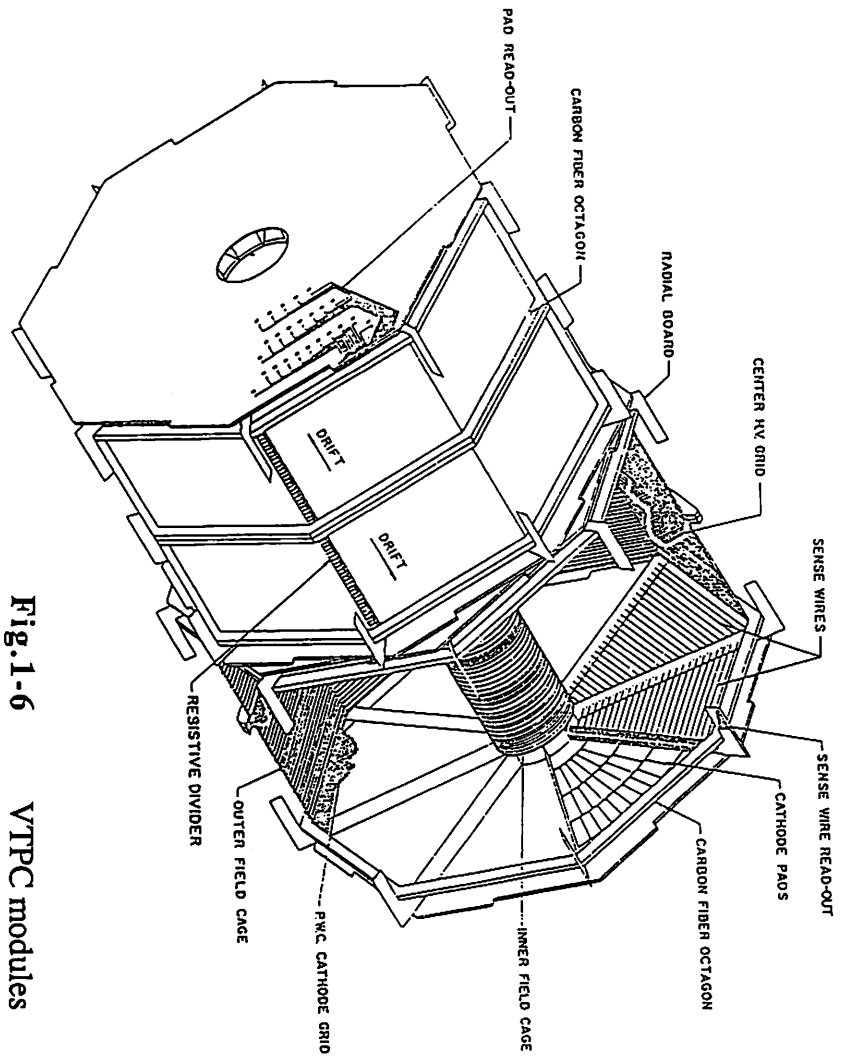

Fig.1-6 VTPC modules

Fig.1-8 A FTC module

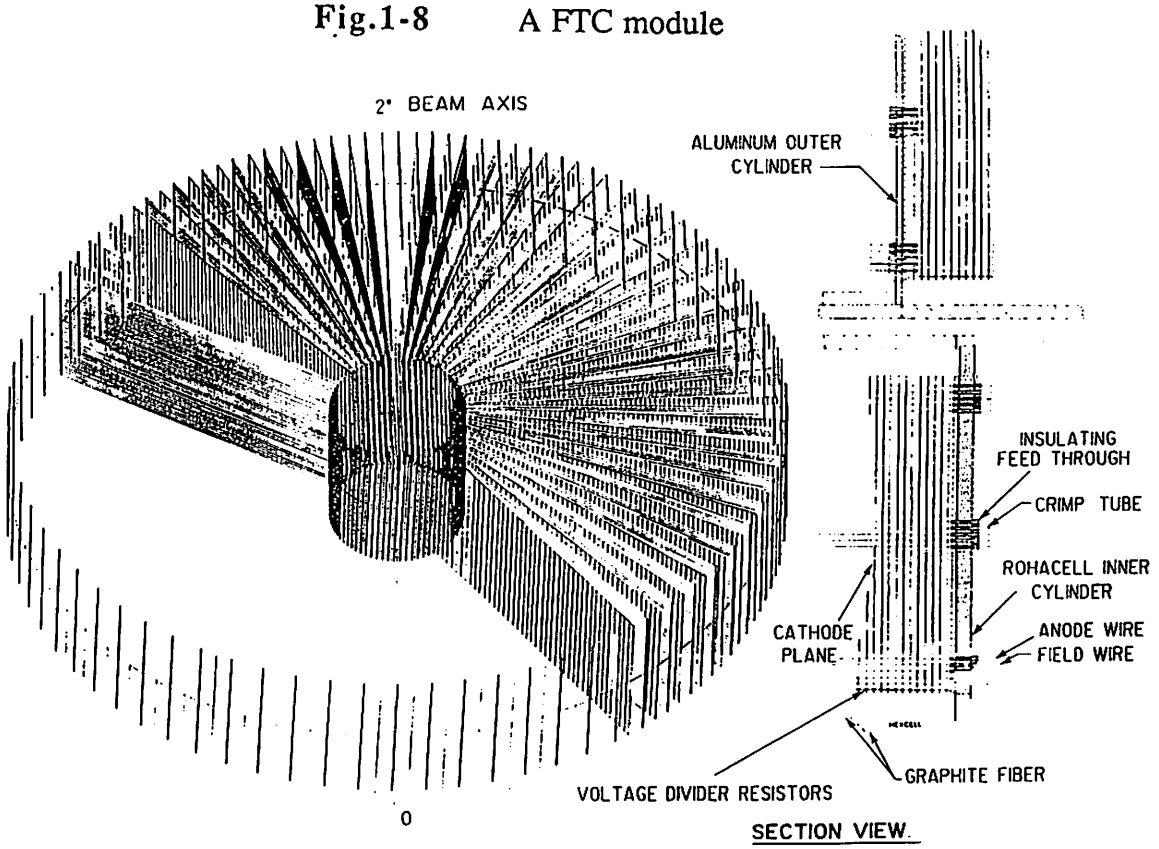

Fig.1-7 % RADIATION LENGTH λ VS POLAR ANGLE θ

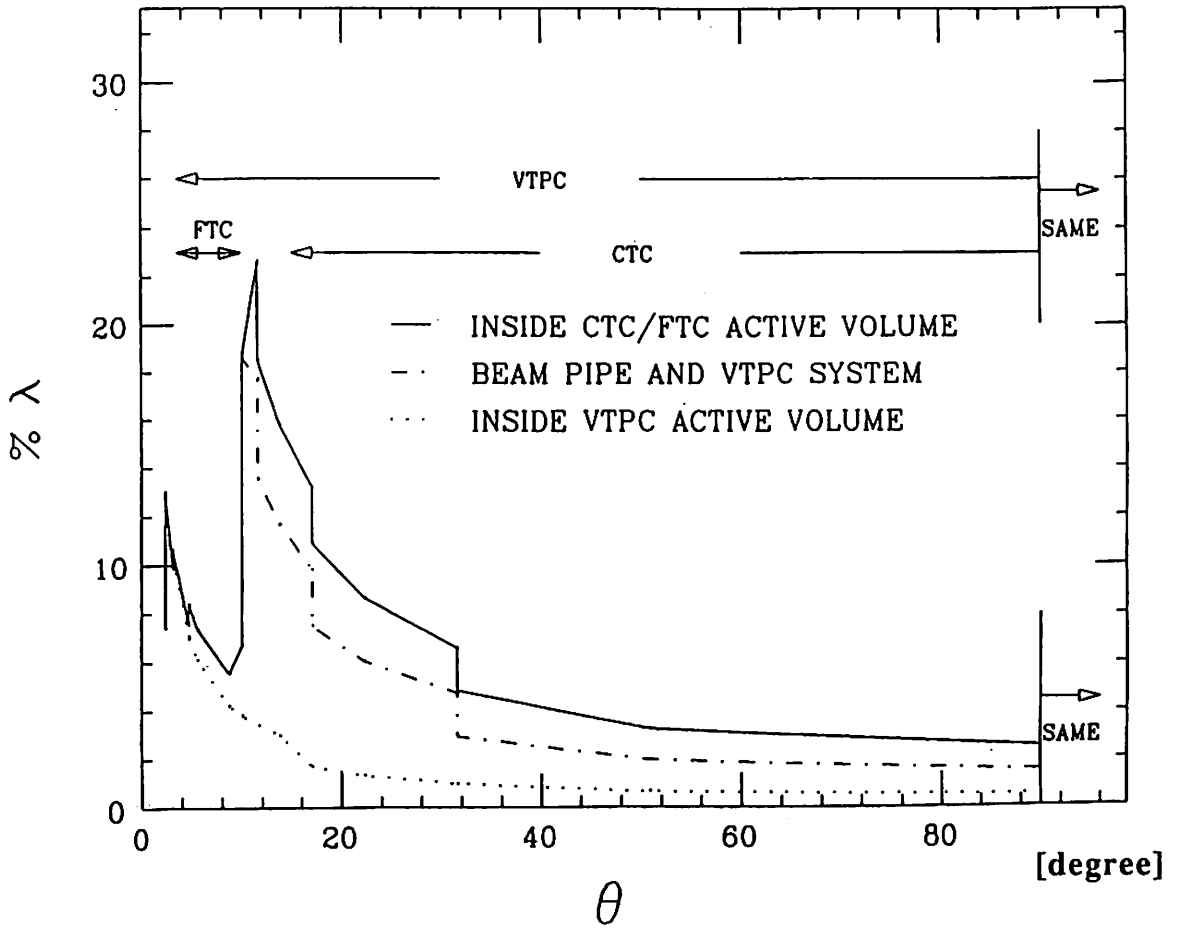

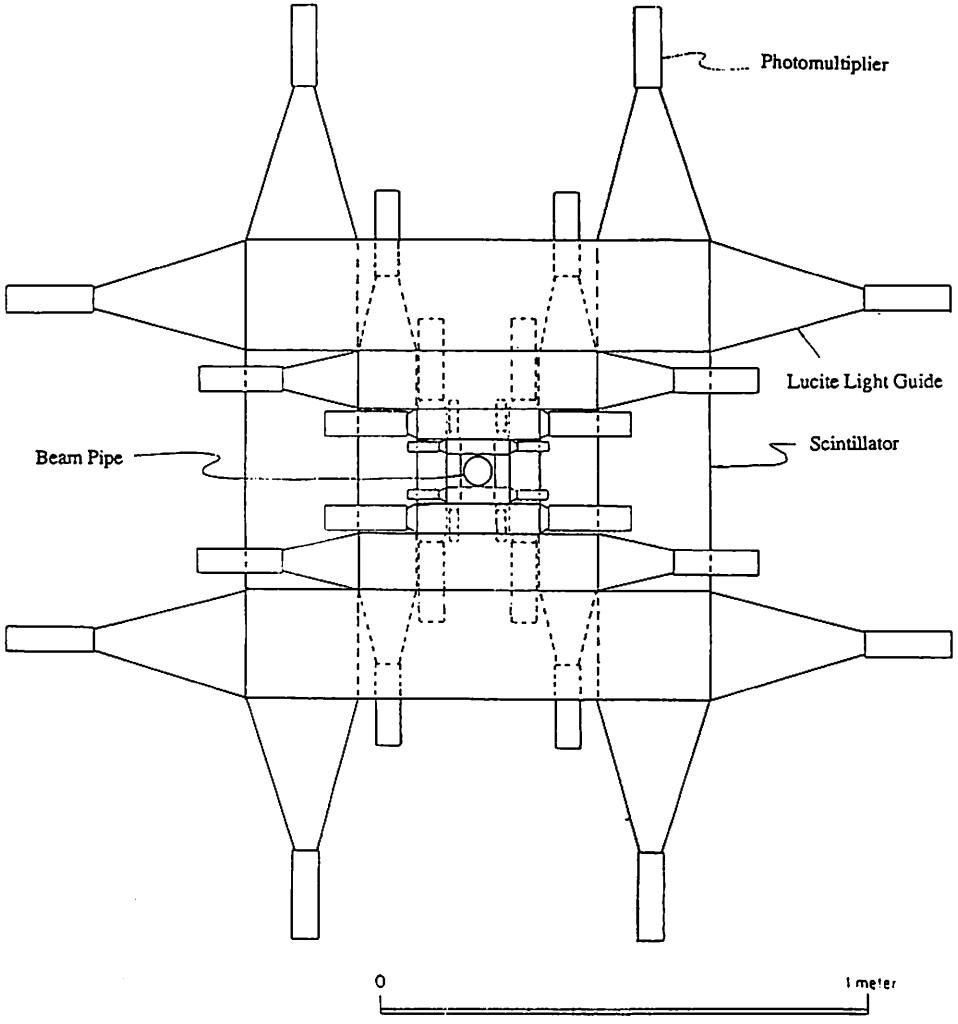

Fig.1-9 A BBC module

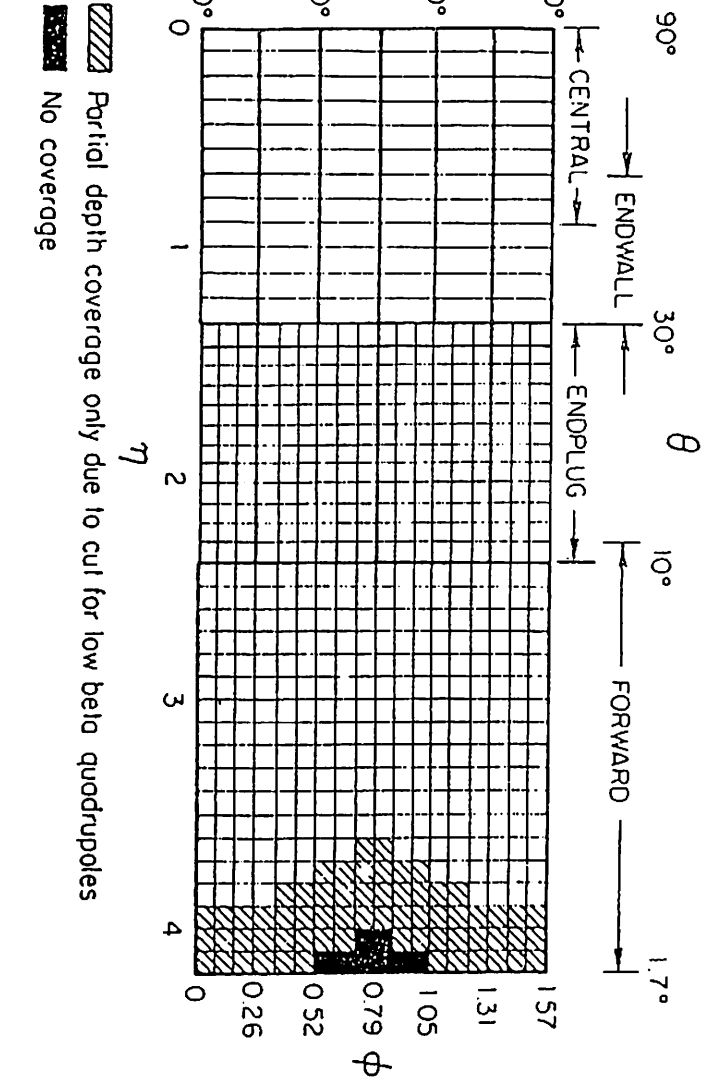

Fig.1-10 CDF calorimetry tower segmentation

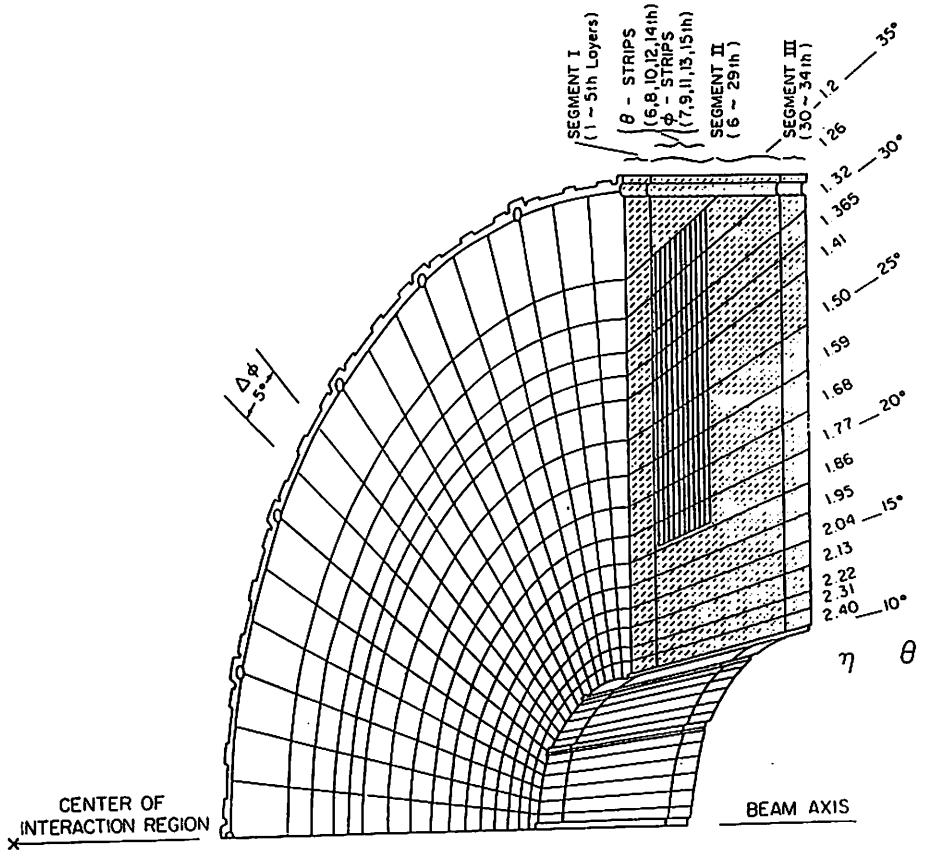

Fig.2-1

Endplug Electromagnetic Calorimeter

One quadrant module

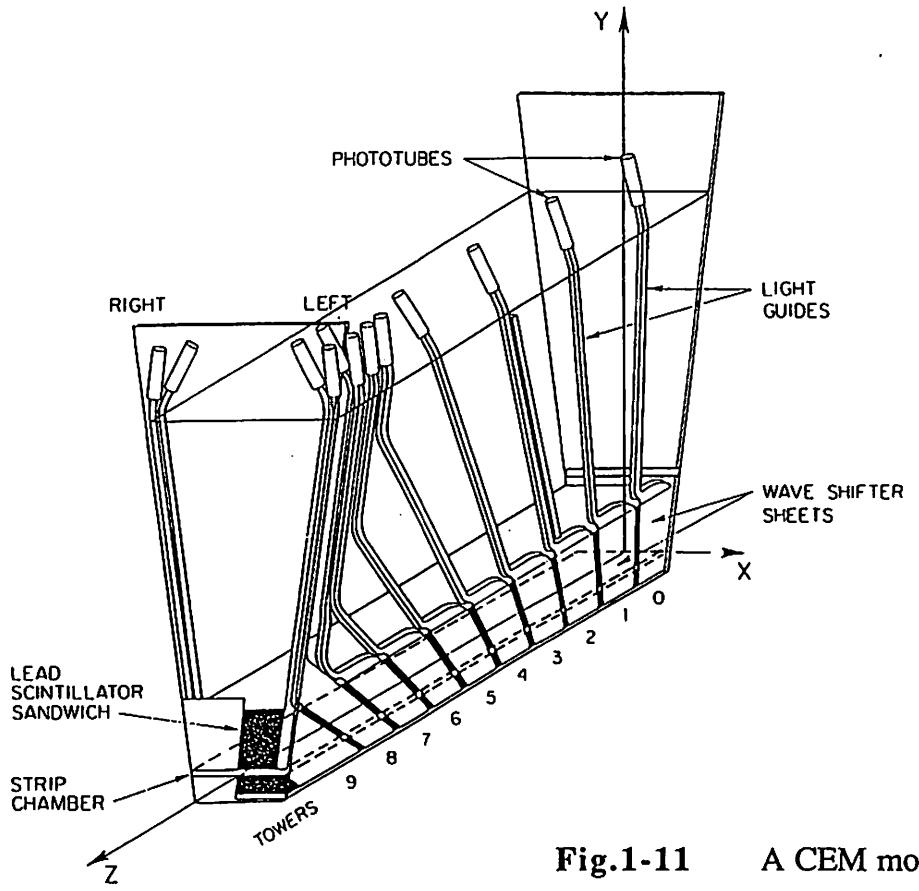

Fig.1-11 A CEM module

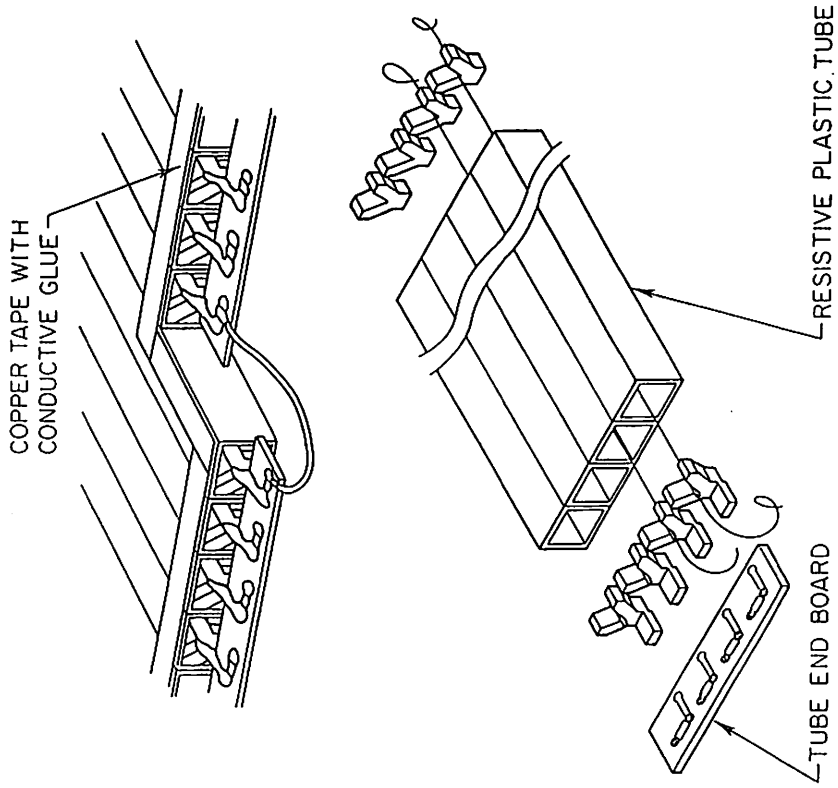

Fig.2-3

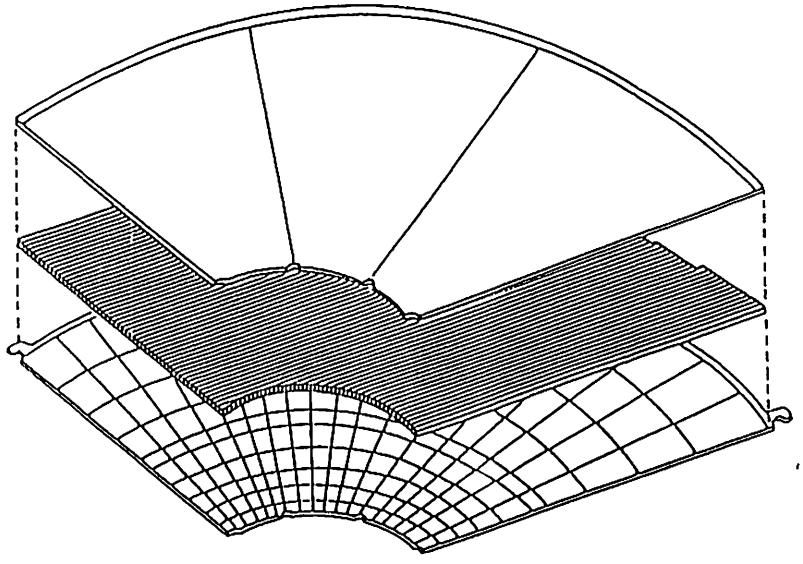

G10 boards

Proportional tube array

G10 boards

Fig.2-2

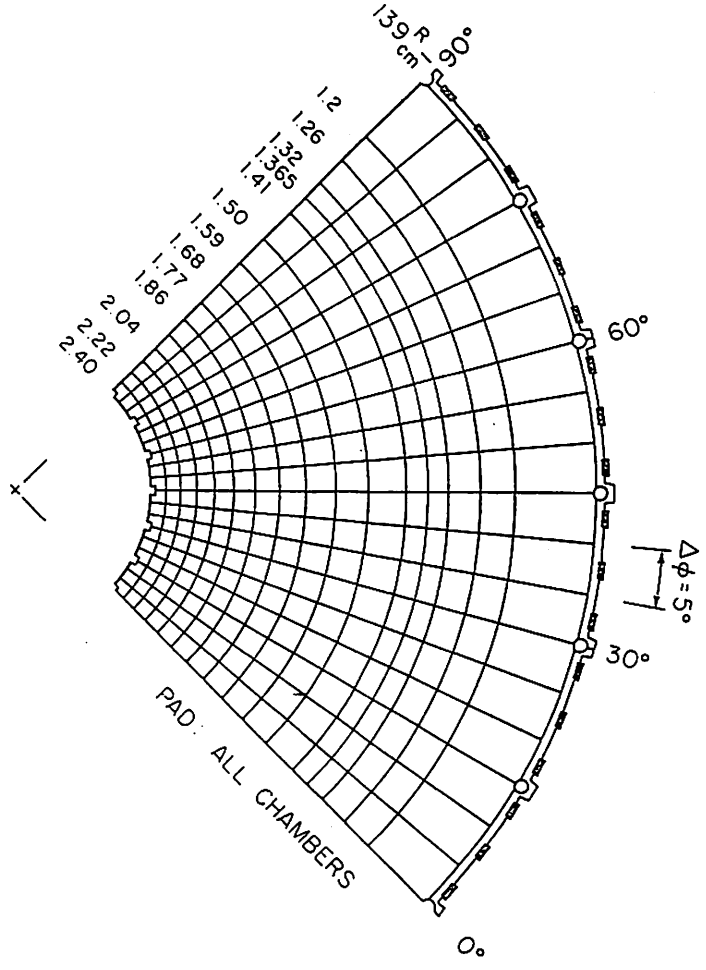

Fig.2-4 (a)

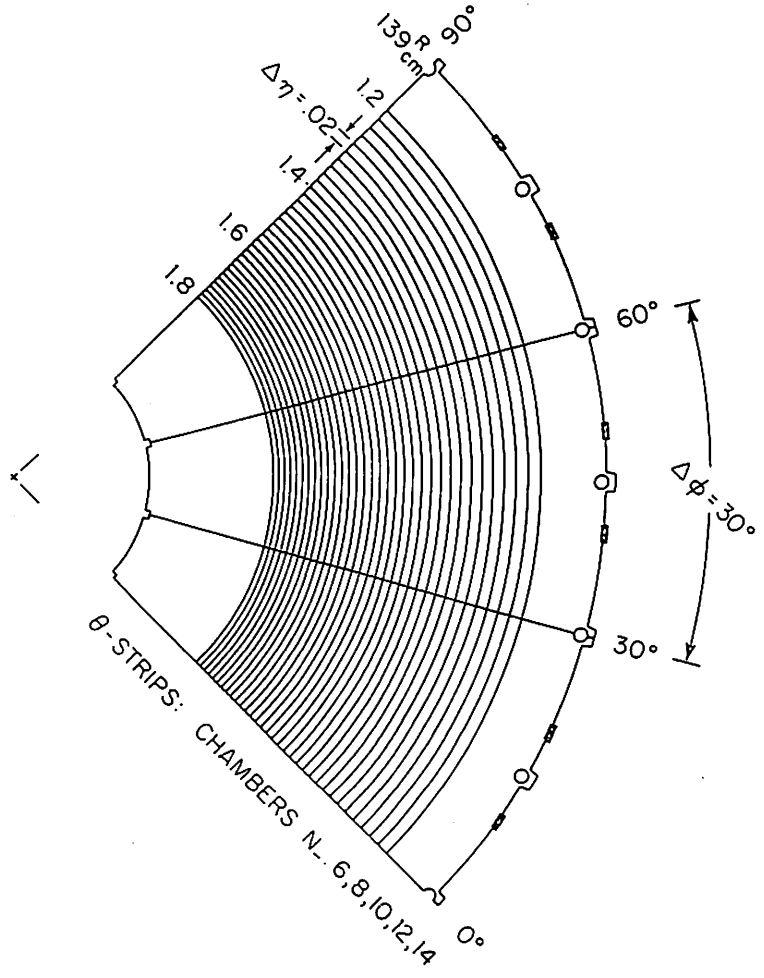

Fig.2-4 (b)

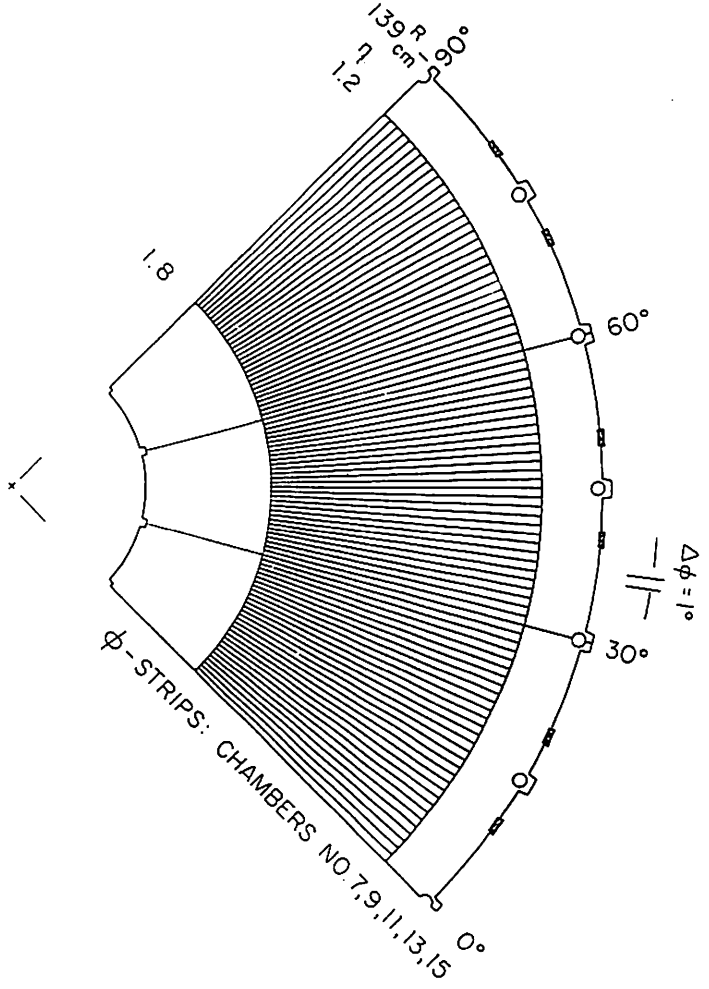

Fig.2-4 (c)

Assembling Jig of Conductive Tube Array

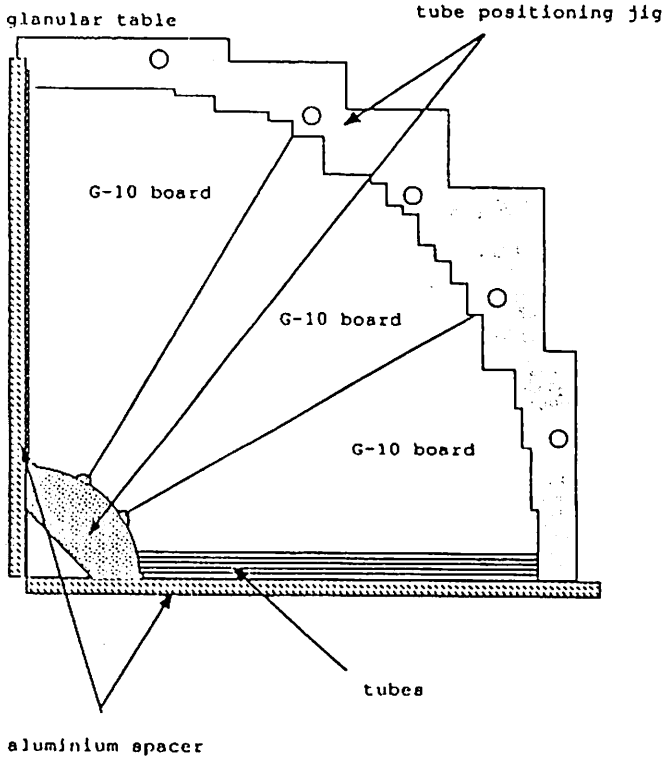

Fig.2-5

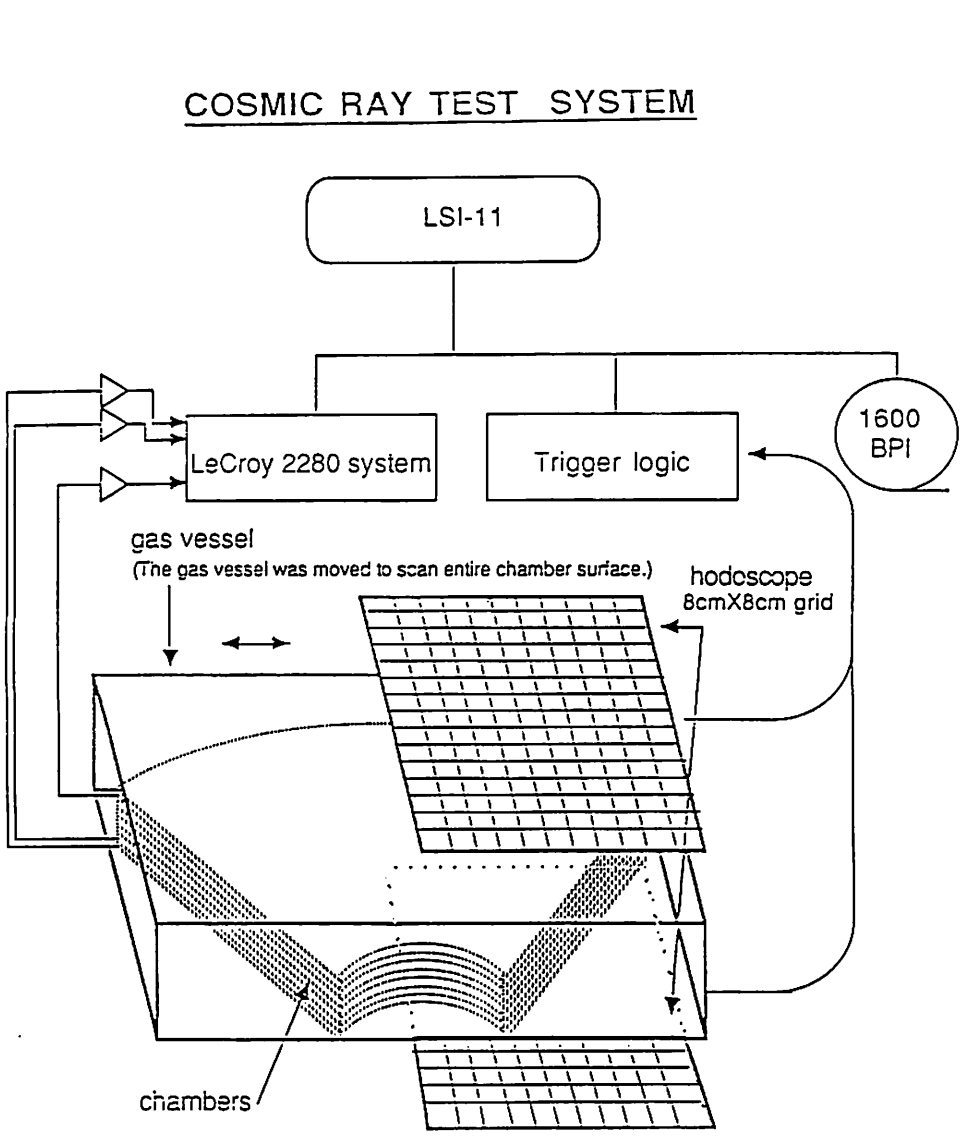
COSMIC RAY TEST SYSTEM
LSI-11
LeCroy 2280 system
Trigger logic
1600 BPI
gas vessel
(The gas vessel was moved to scan entire chamber surface.)
hodoscope
8cmX8cm grid
chambers

Fig.2-6

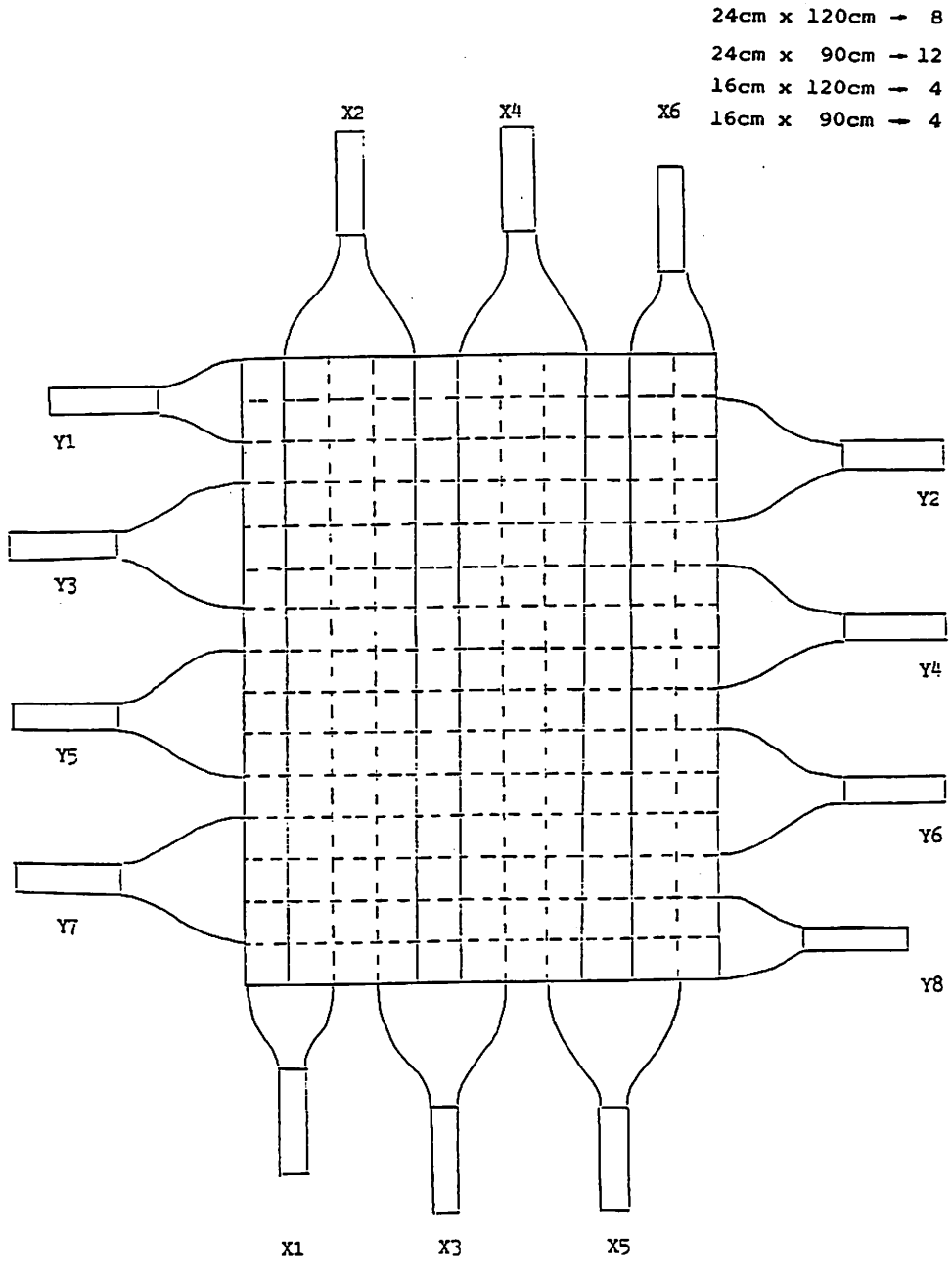
24cm x 120cm → 8
24cm x 90cm → 12
16cm x 120cm → 4
16cm x 90cm → 4
X2
X4
X6
Y1
Y2
Y3
Y4
Y5
Y6
Y7
Y8
X1
X3
X5

Fig.2-7

Fig.2-8 (a)

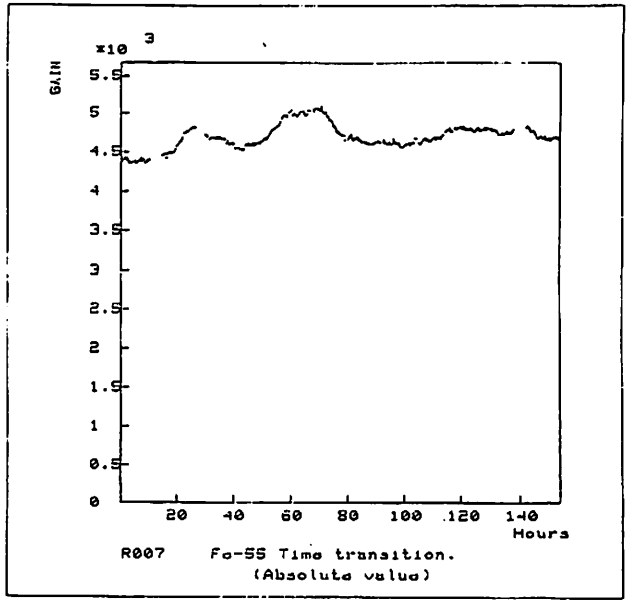

Fig.2-8 (b)

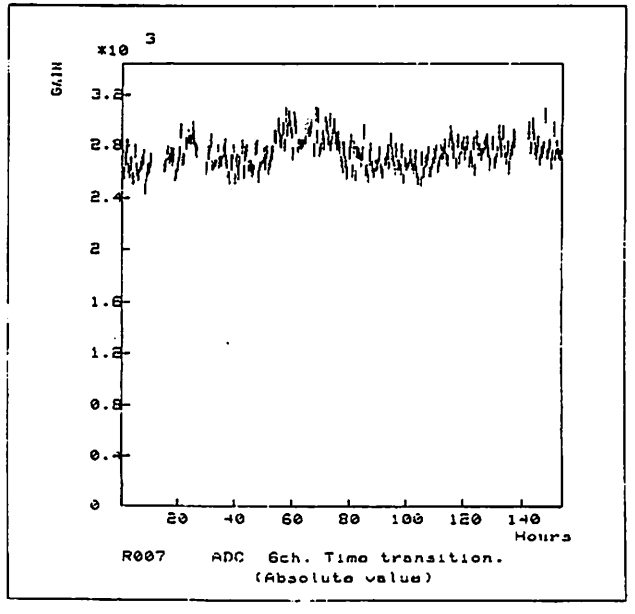

Fig.2-8 (c)

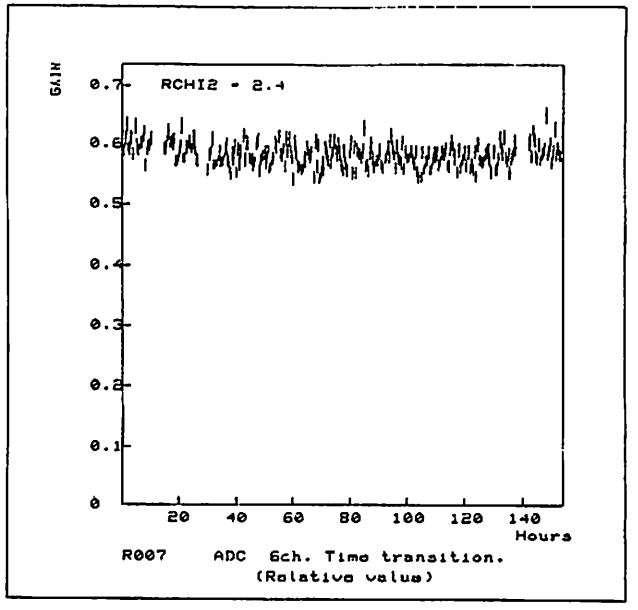

Fig.3-9(c)

Fig.2-9

Fig.2-10 RABBIT Hutch

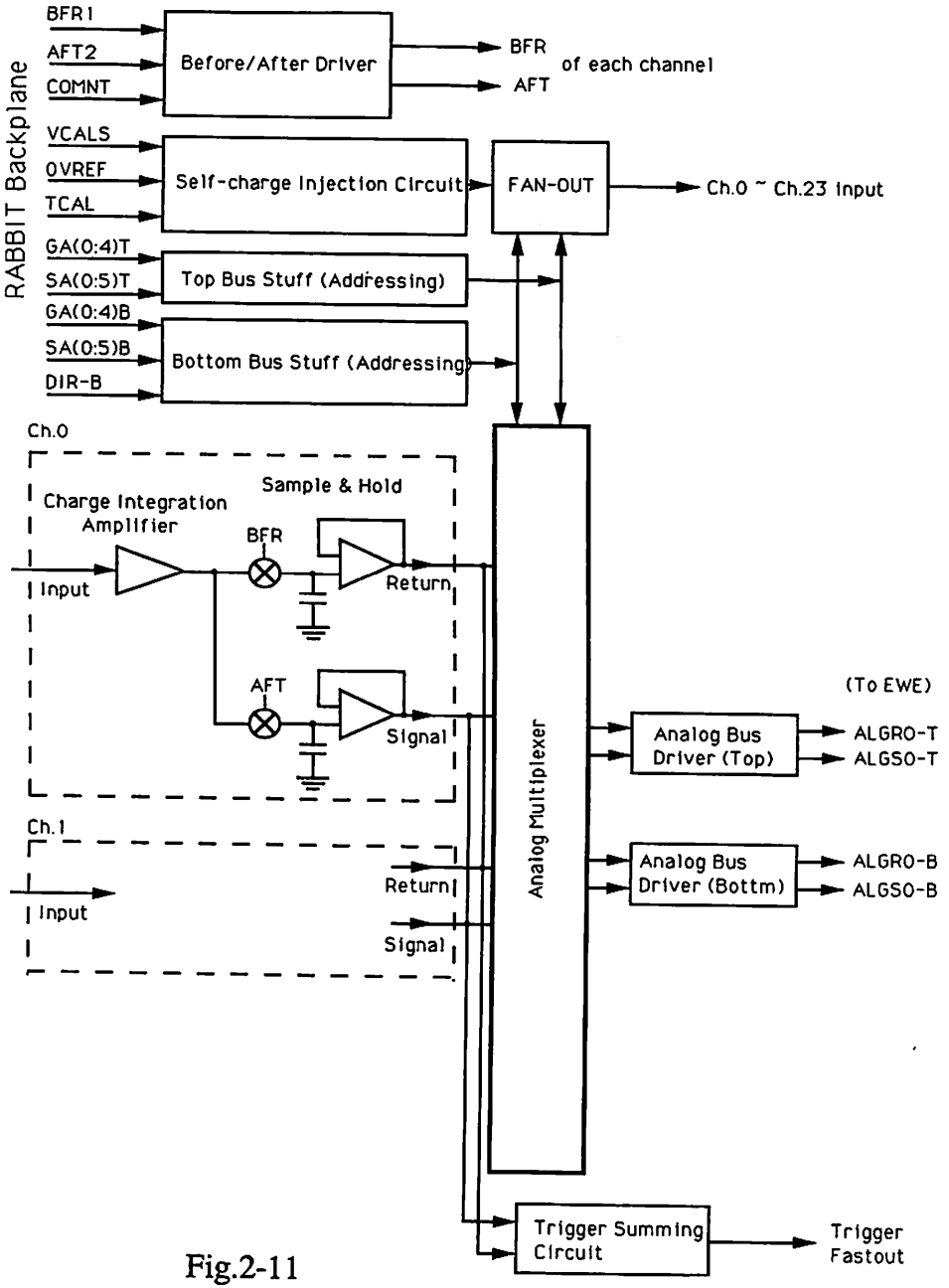

Fig.2-11

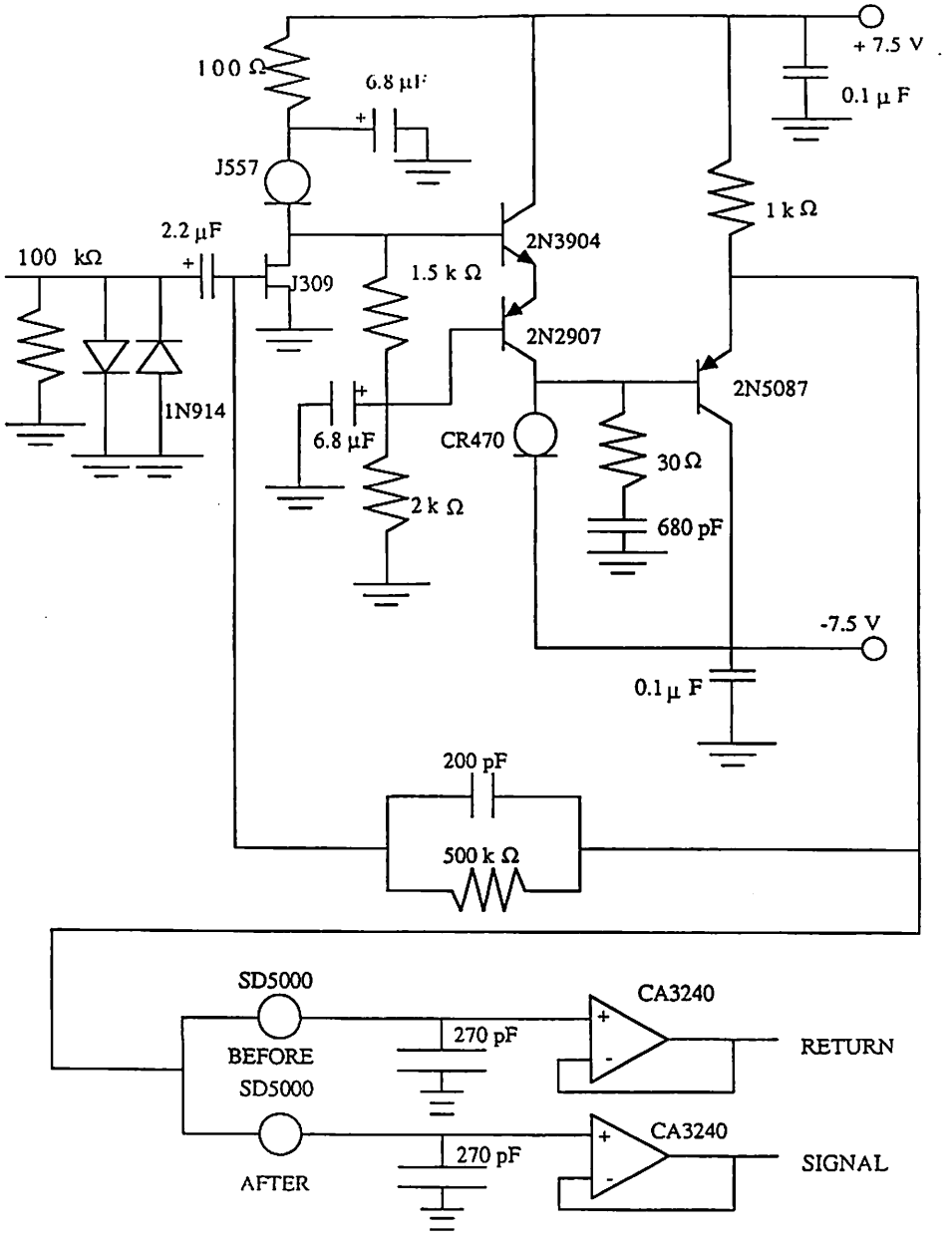

Fig.2-12 (a)

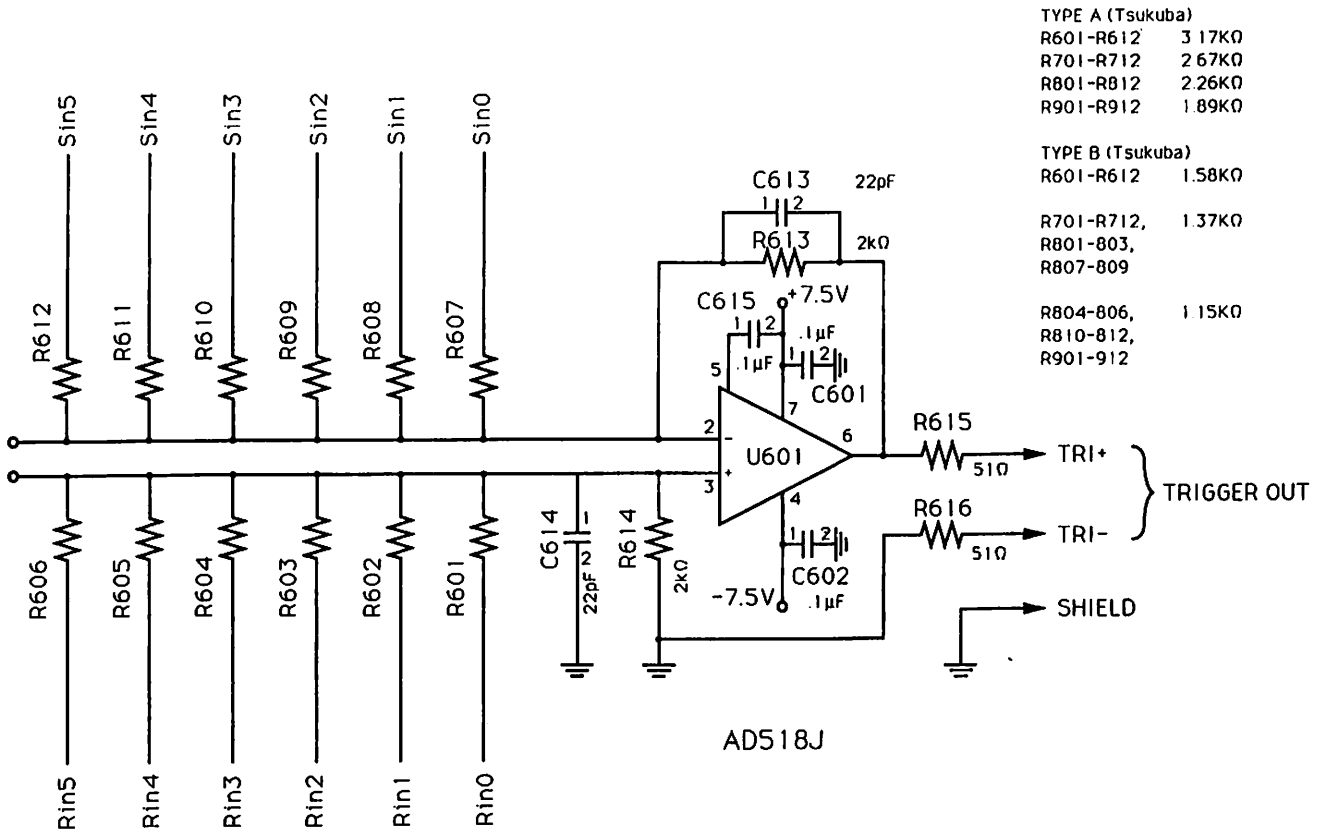

Fig.2-12 (c)

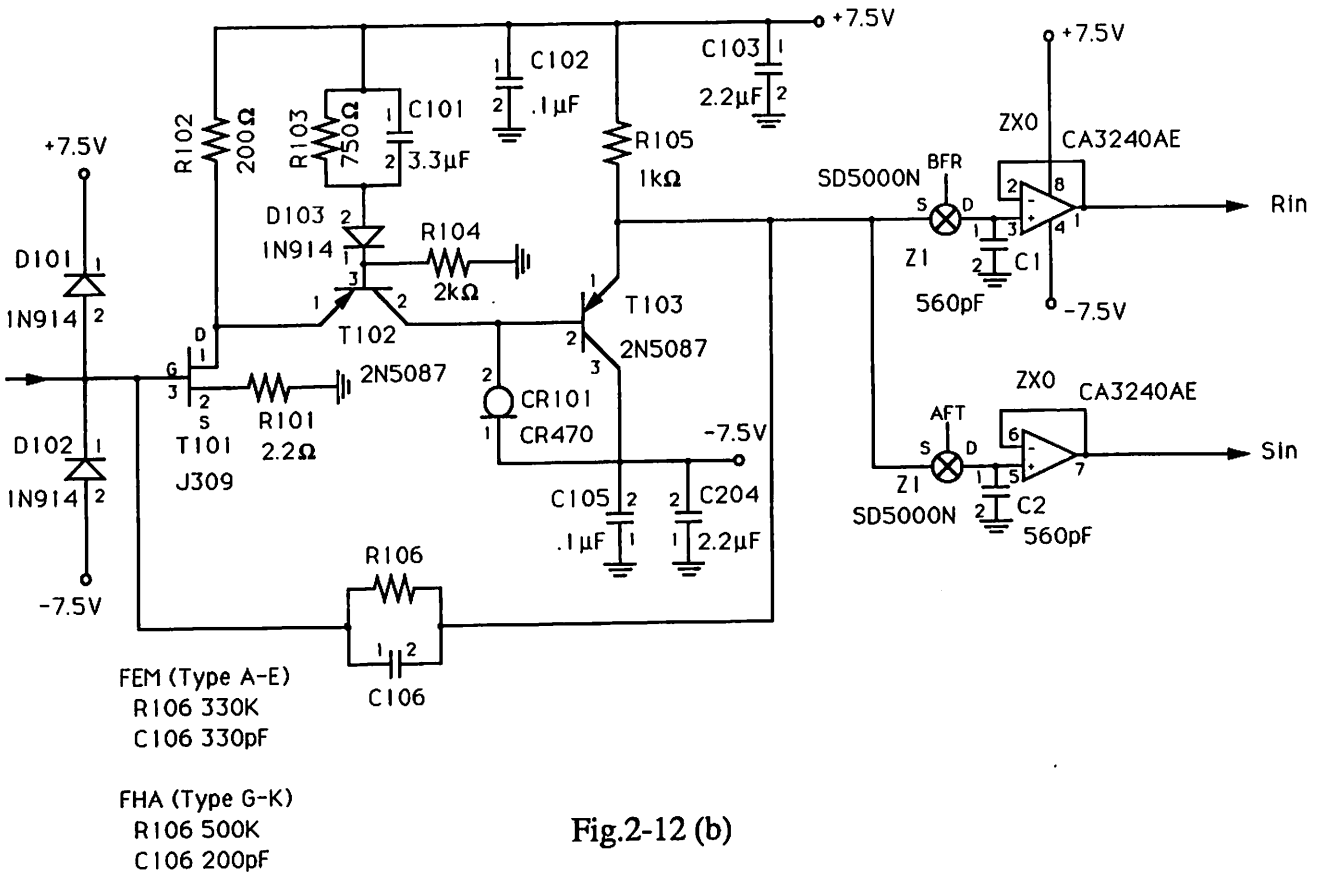

Fig.2-12 (b)

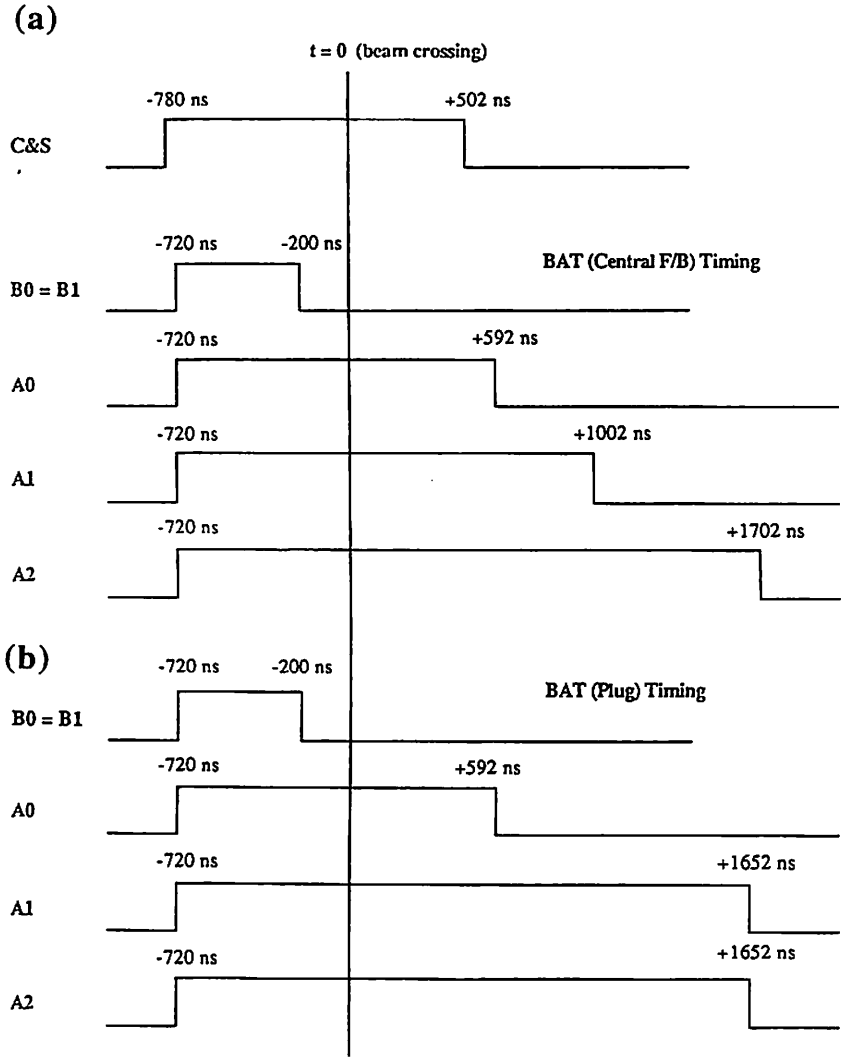

Fig.2-13

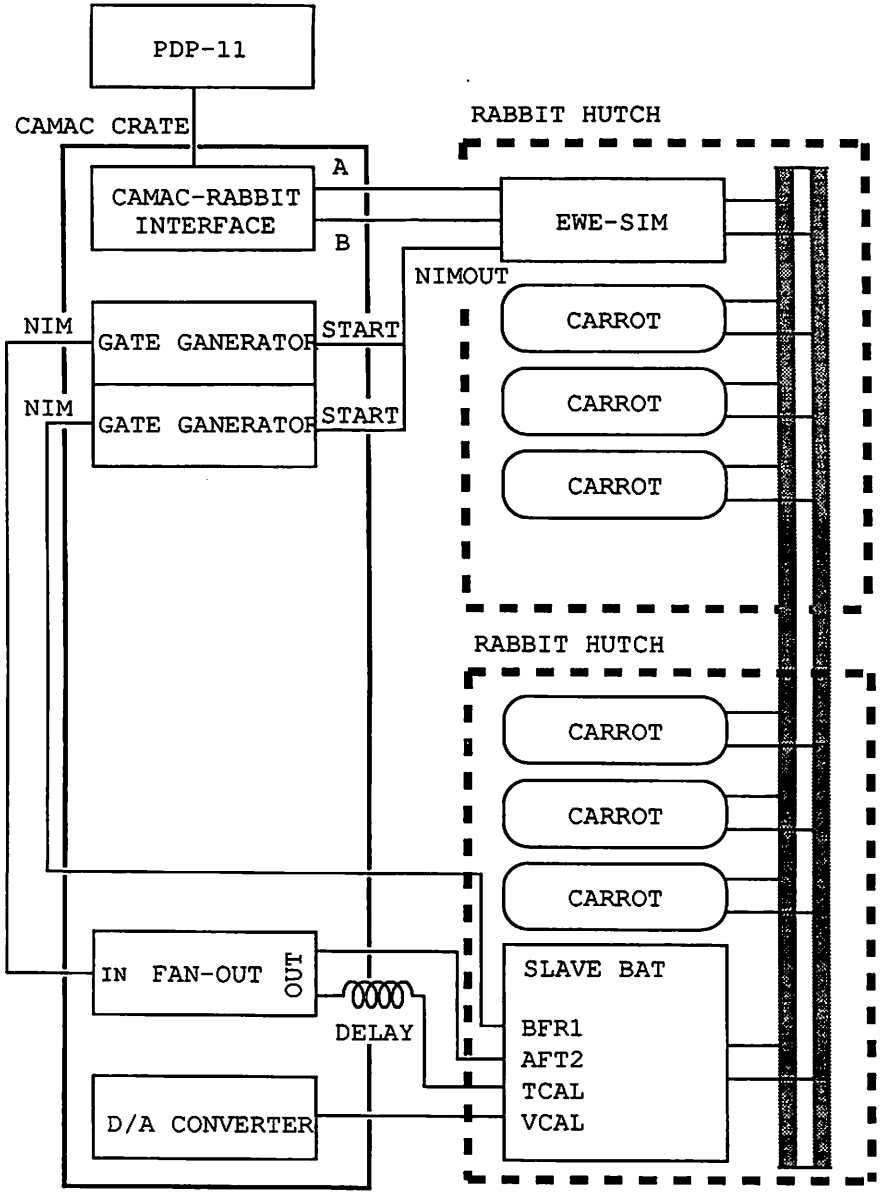

Fig.2-14

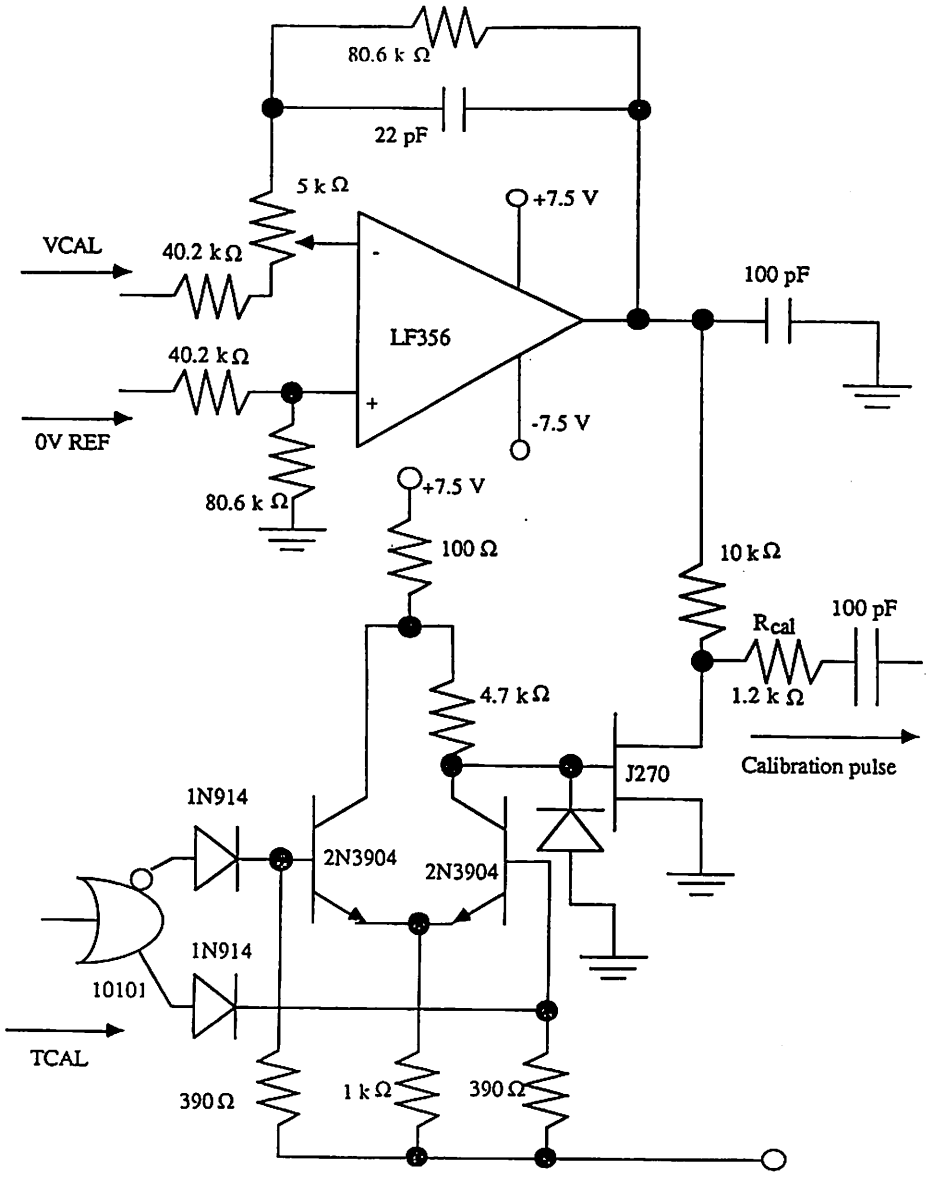

Fig.2-15

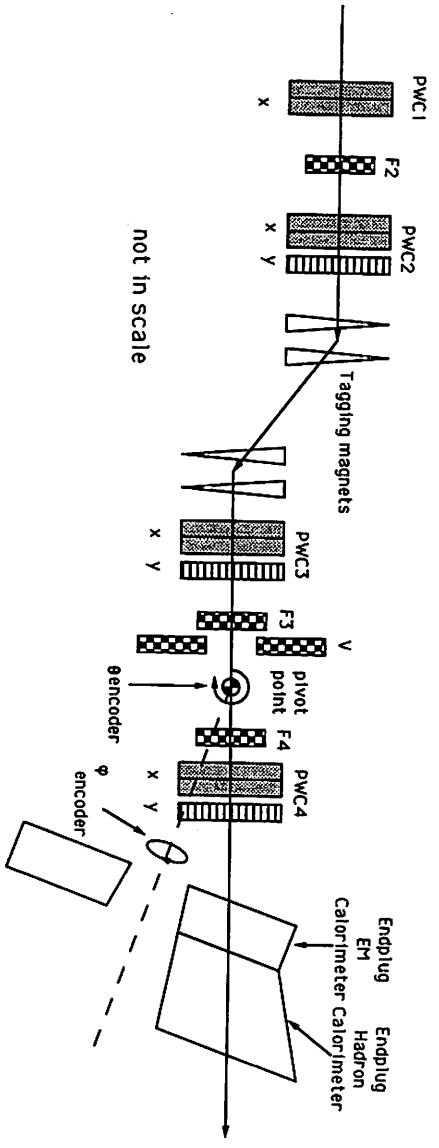

Fig. 3-1

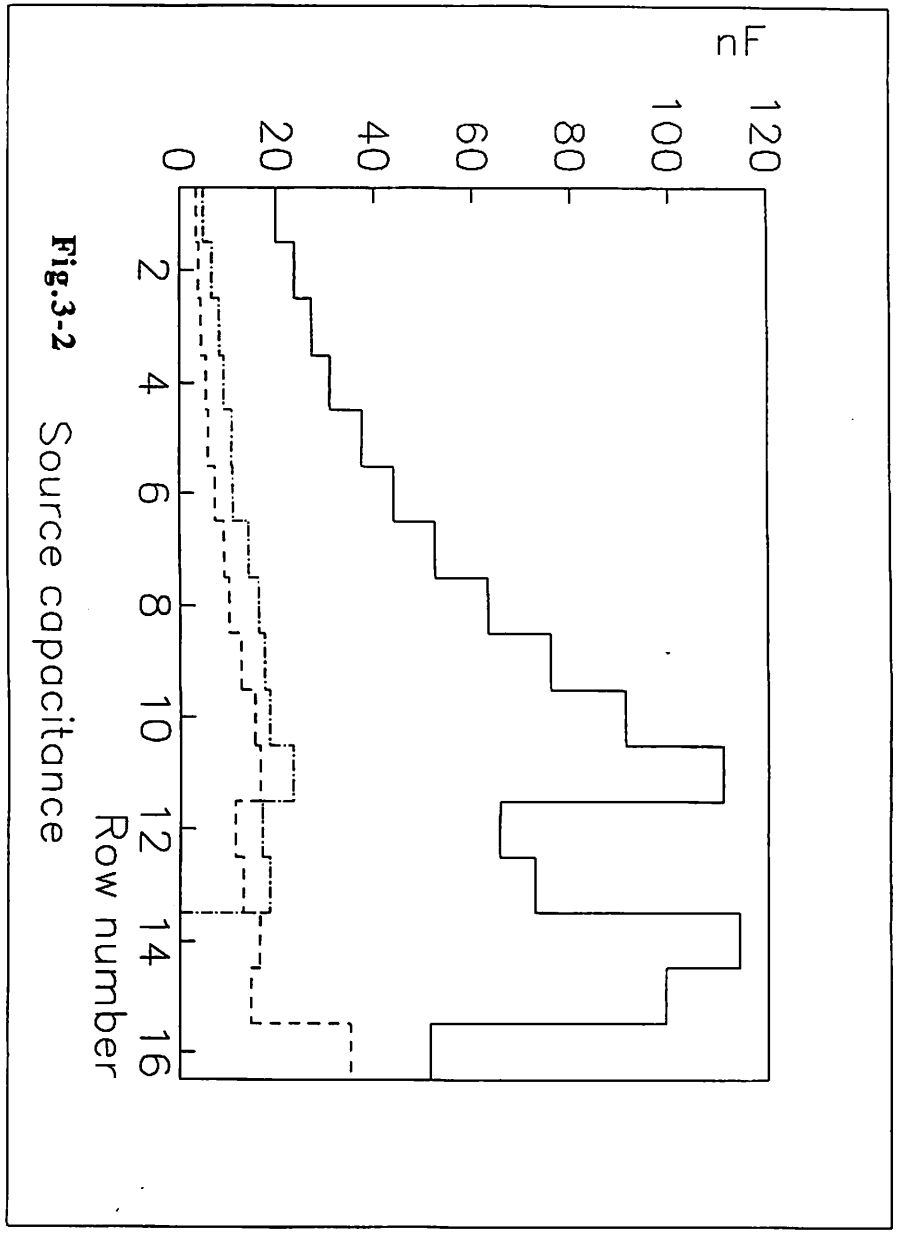
nF
120
100
80
60
40
20
0
2
4
6
8
10
12
14
16
Row number
Source capacitance

Fig.3-2

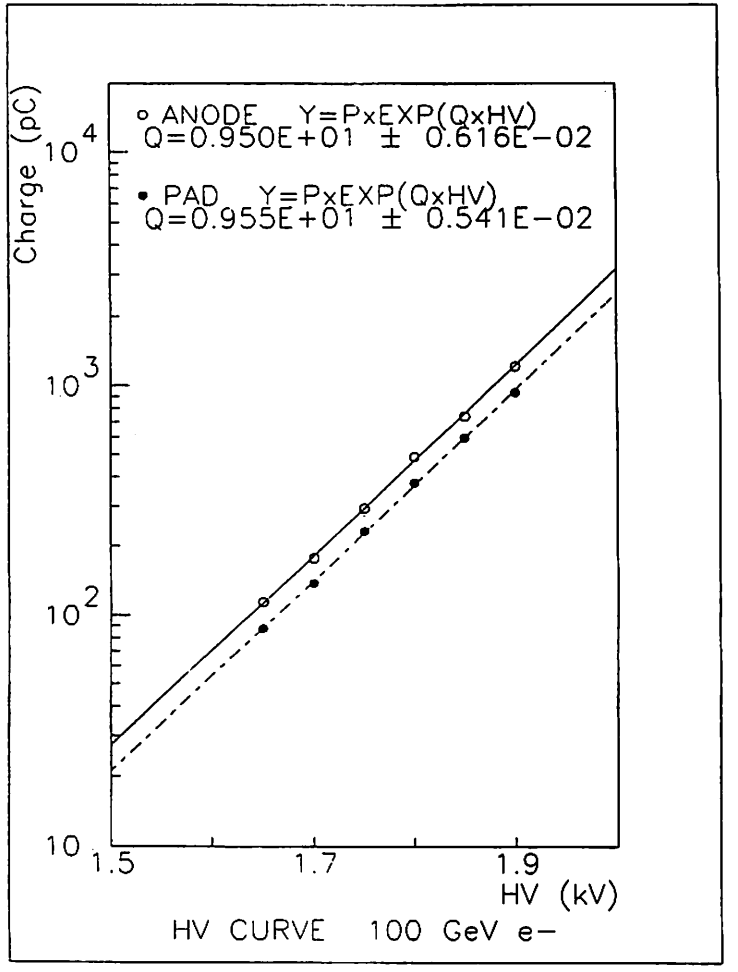
ANODE Y=PxEXP(QxHV)
Q=0.950E+01 ± 0.616E-02
PAD Y=PxEXP(QxHV)
Q=0.955E+01 ± 0.541E-02
Charge (pC)
10^4
10^3
10^2
10
1.5
1.7
1.9
HV (kV)
HV CURVE 100 GeV e-

Fig.3-3

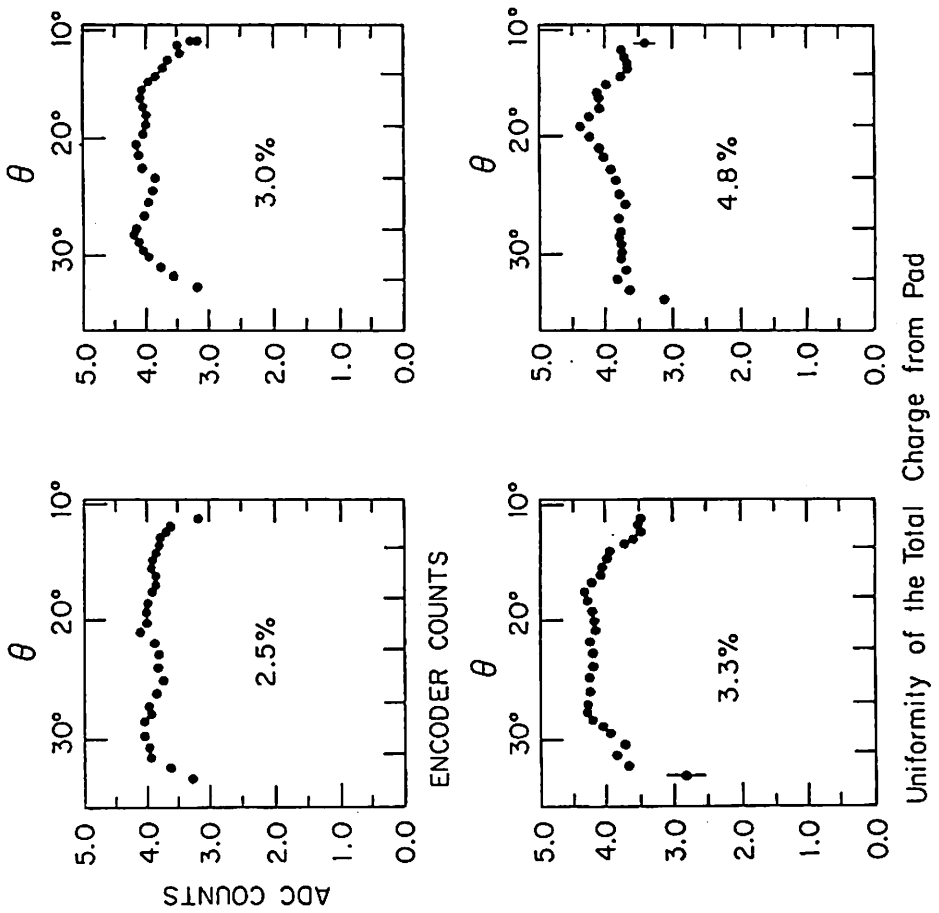

Fig.3-4 (a)

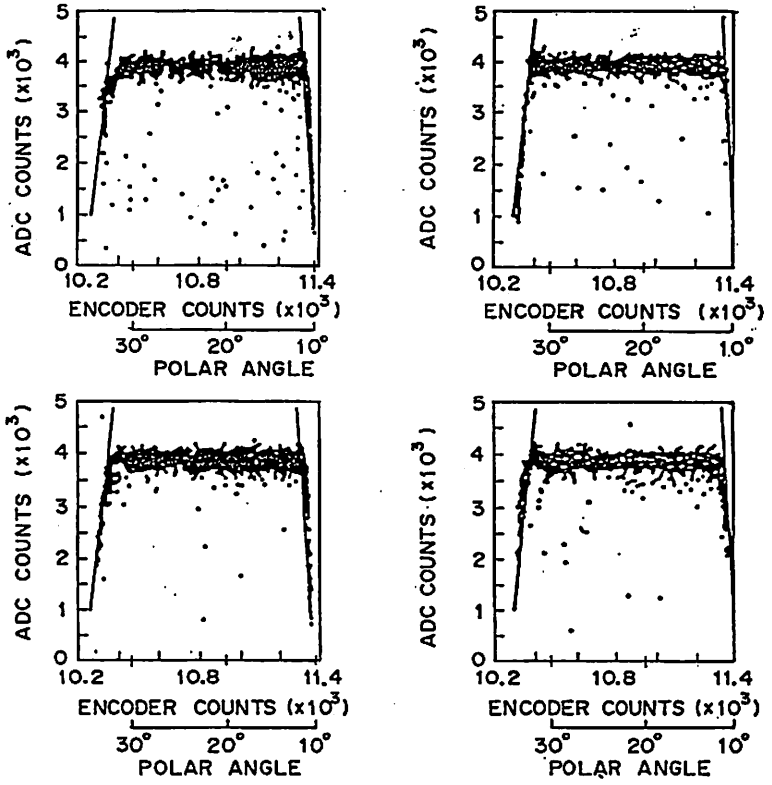

Fig.3-4 (b)

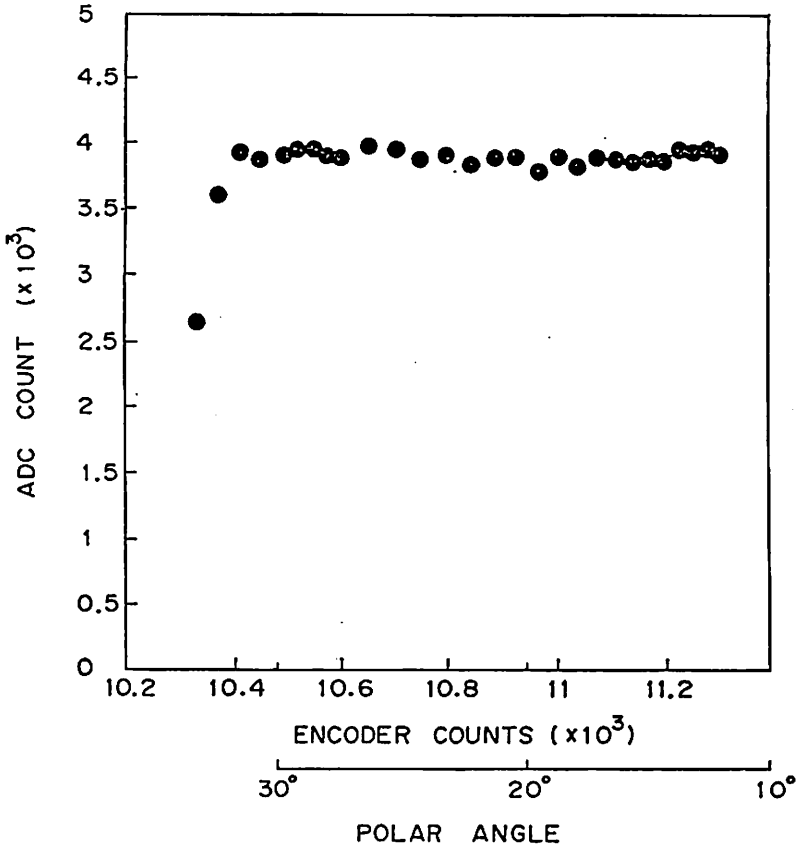

Fig.3-5

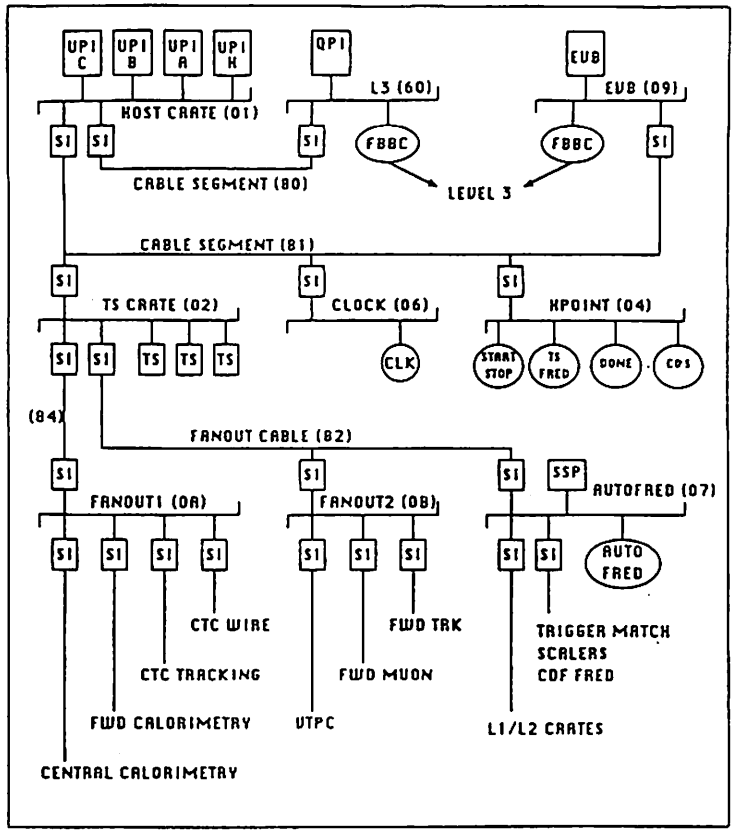

Fig.4-1 CDF data acquisition system

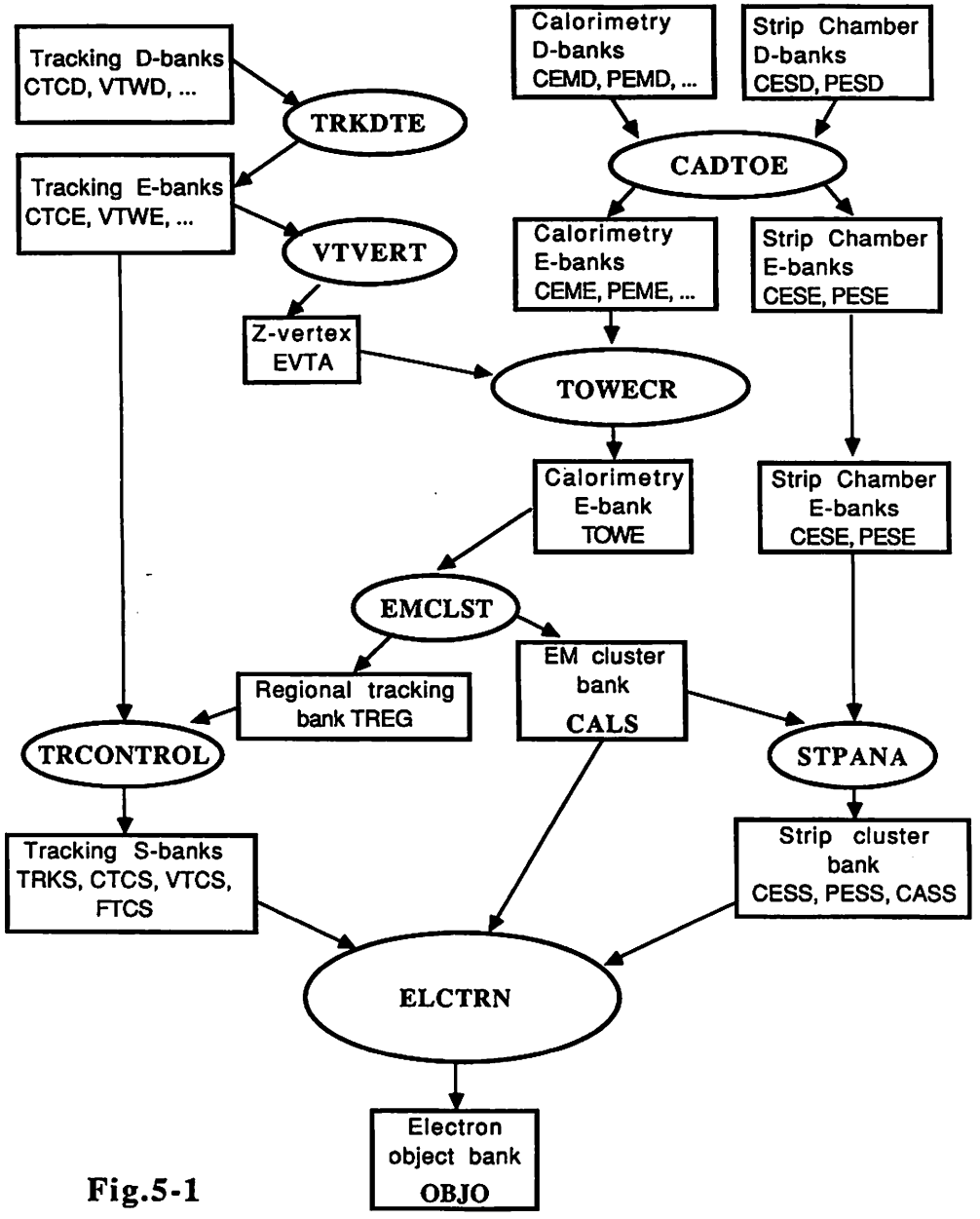

Fig.5-1

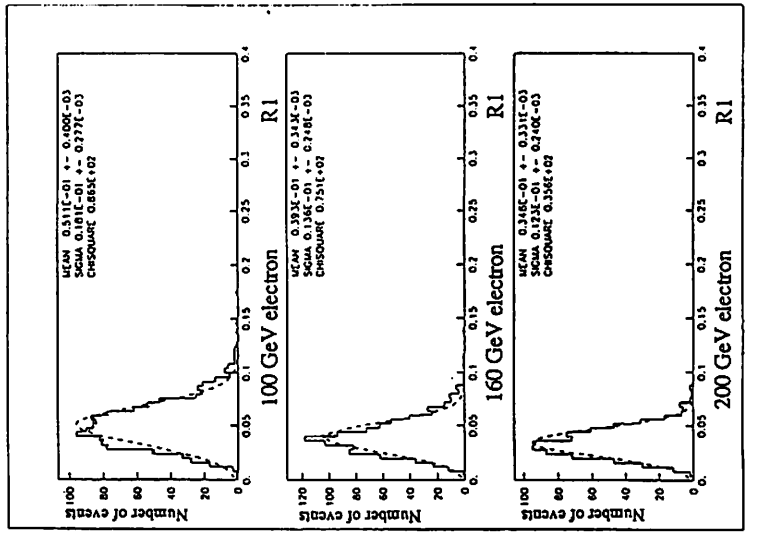

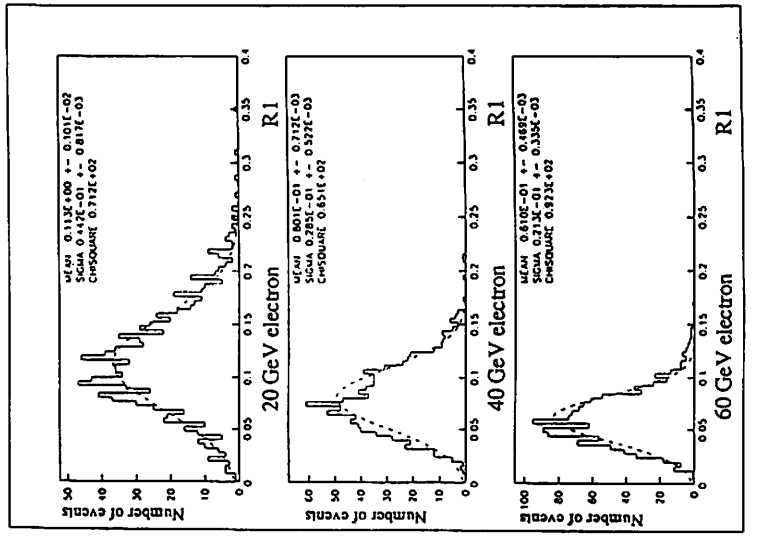

Fig.5-2 (a)

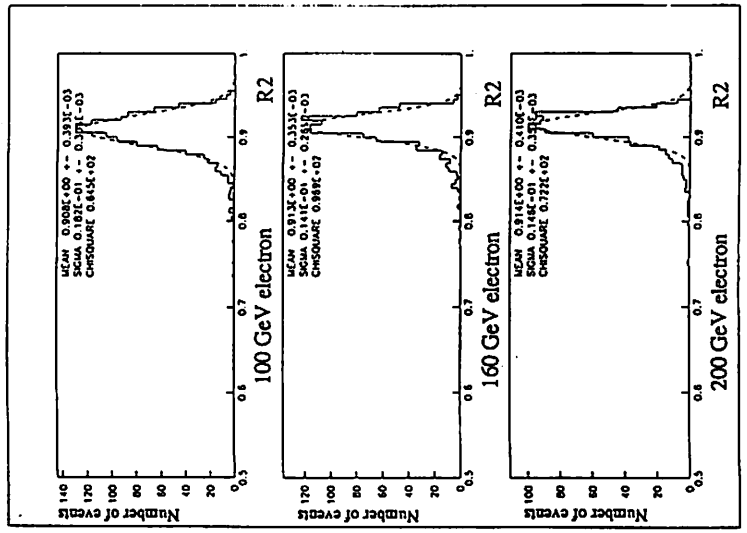

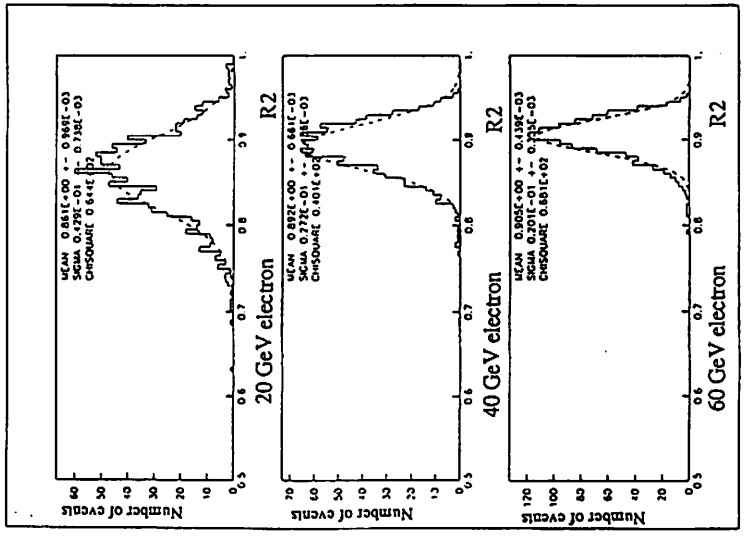

Fig.5-2 (b)

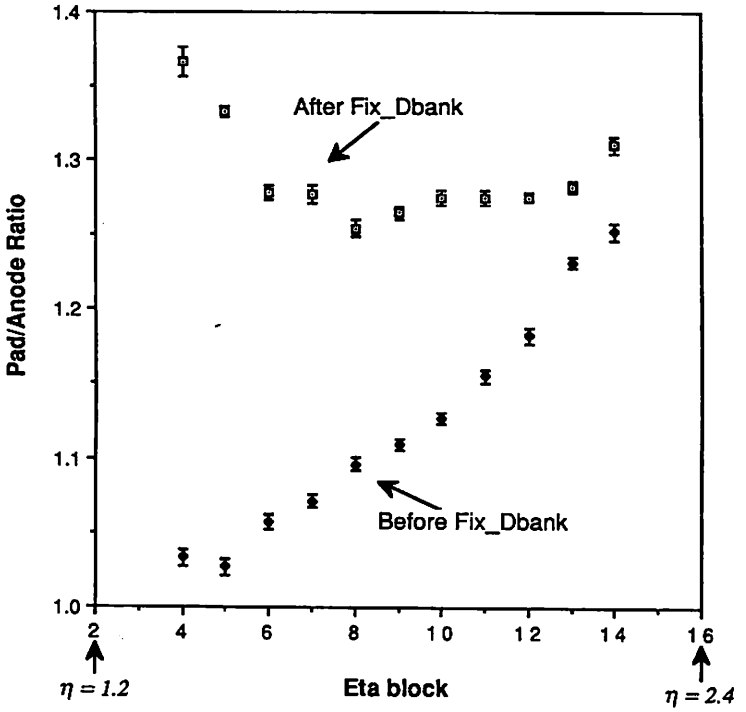

Fig.5-3

CDF electromagnetic clustering algorithm

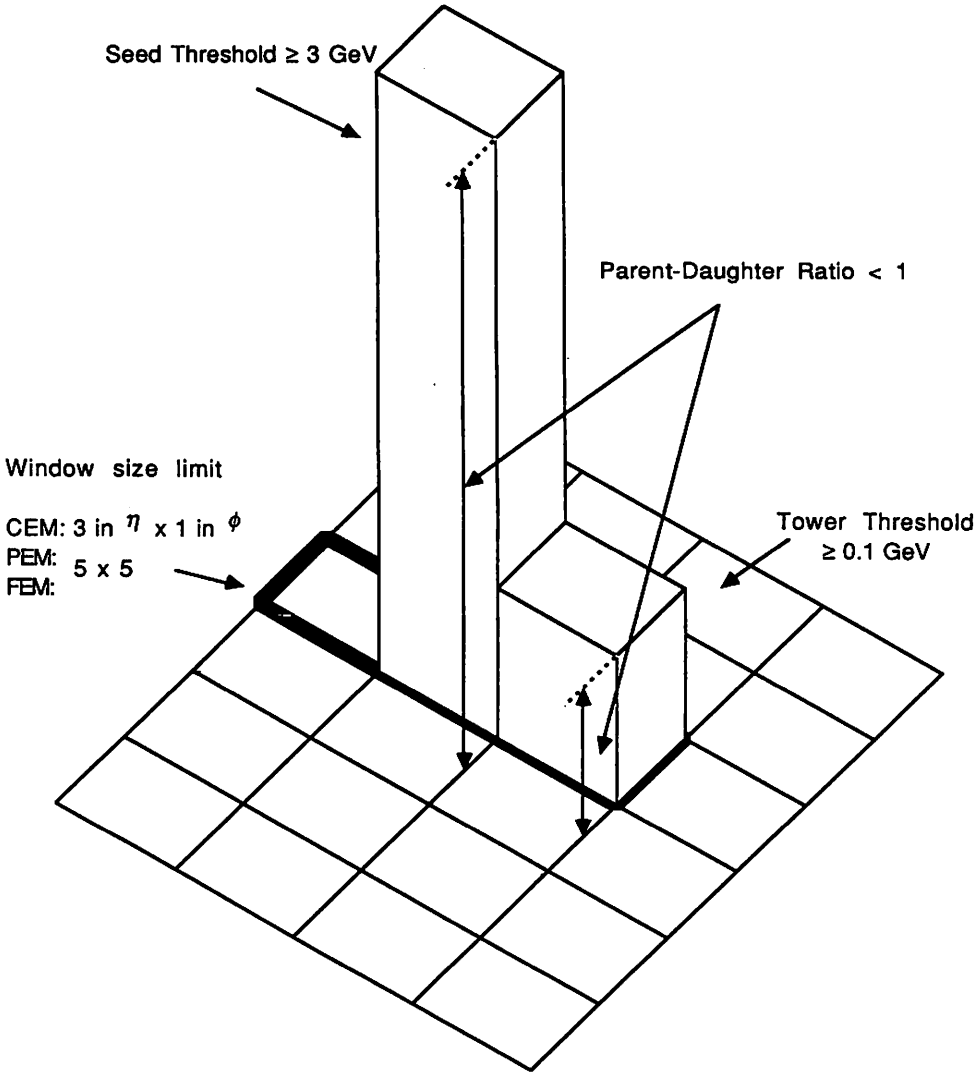

Fig.5-4

Fig. 5-5

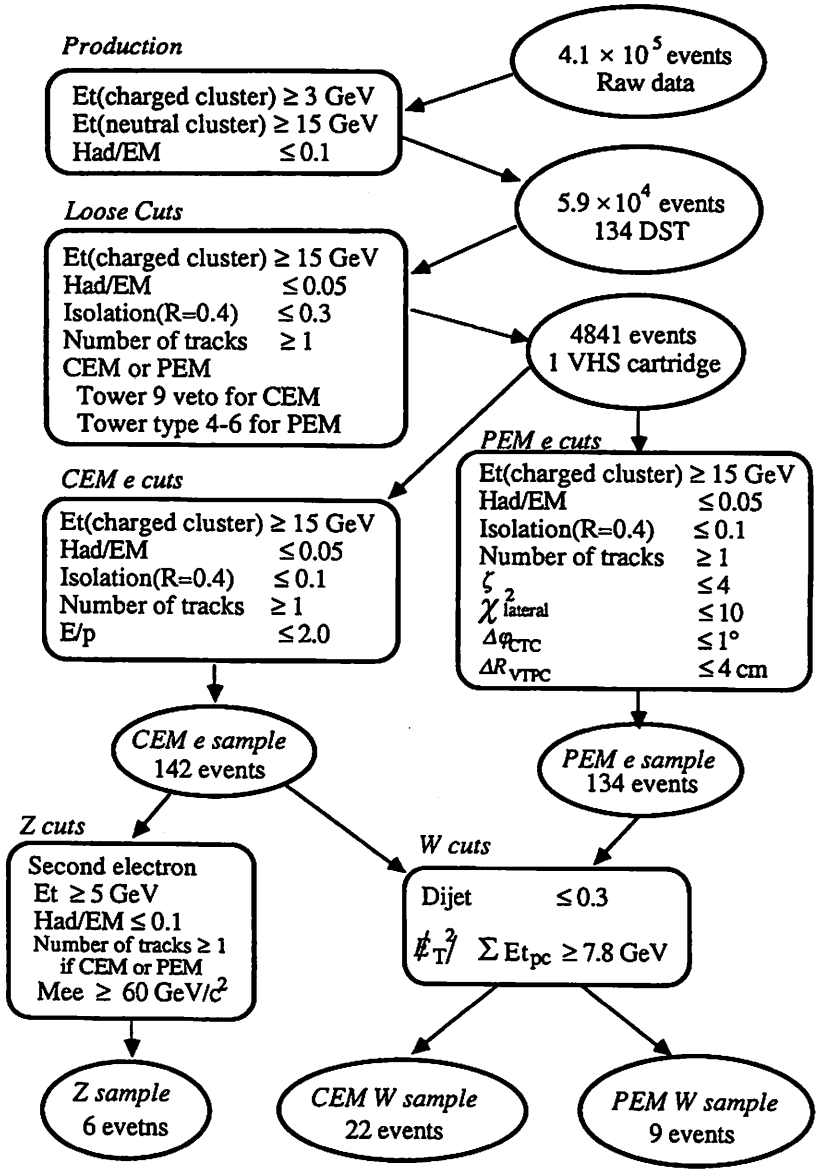

(a)

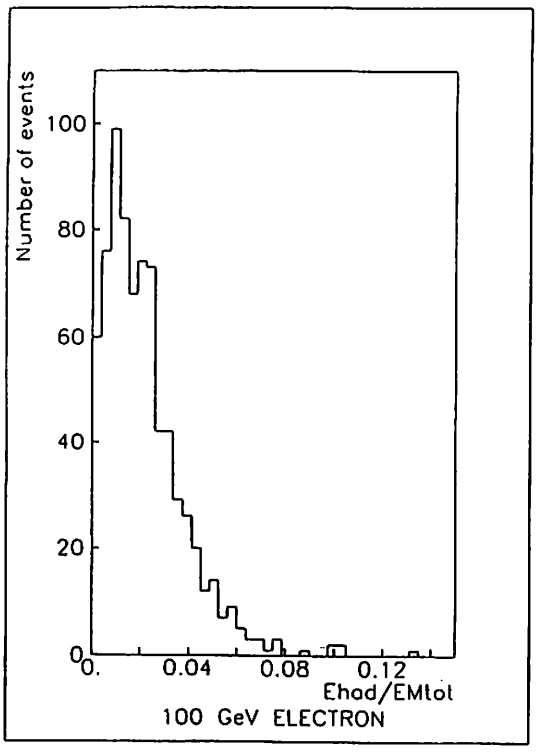

(b)

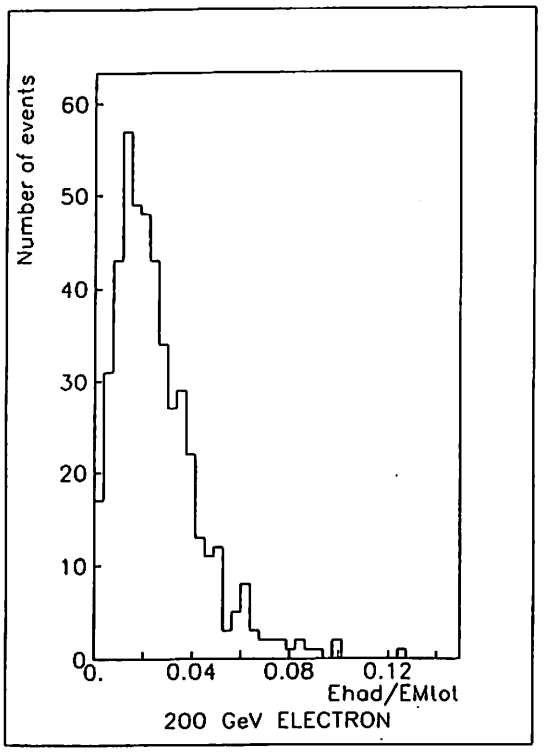

Fig.5-7

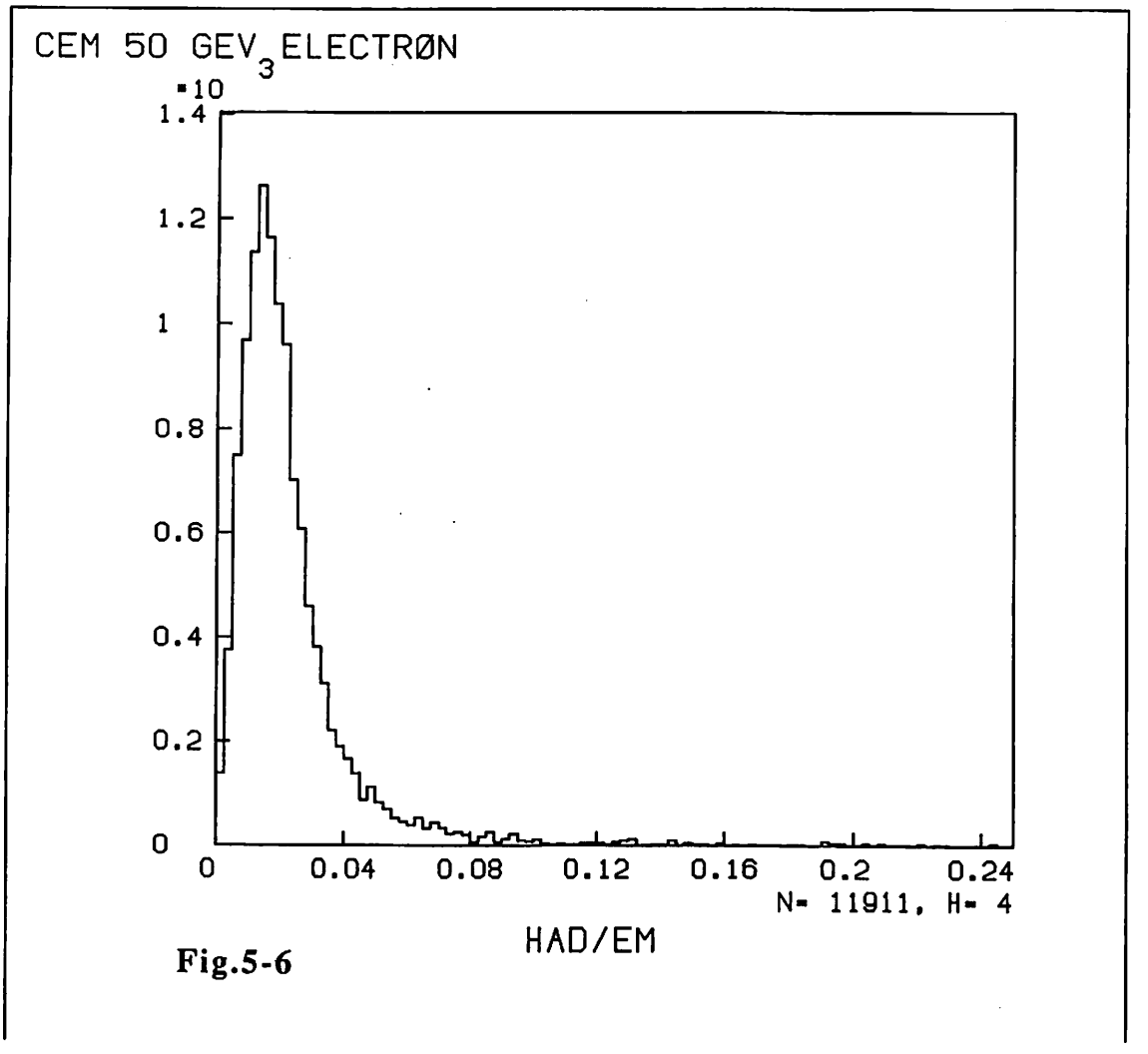

Fig.5-6

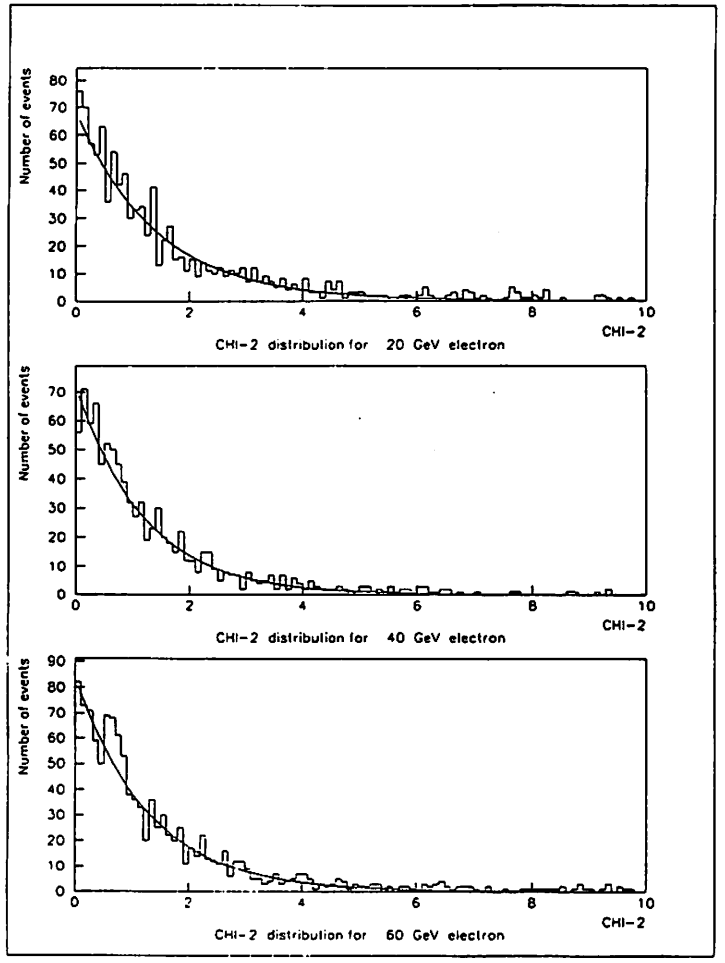

Fig.5-8

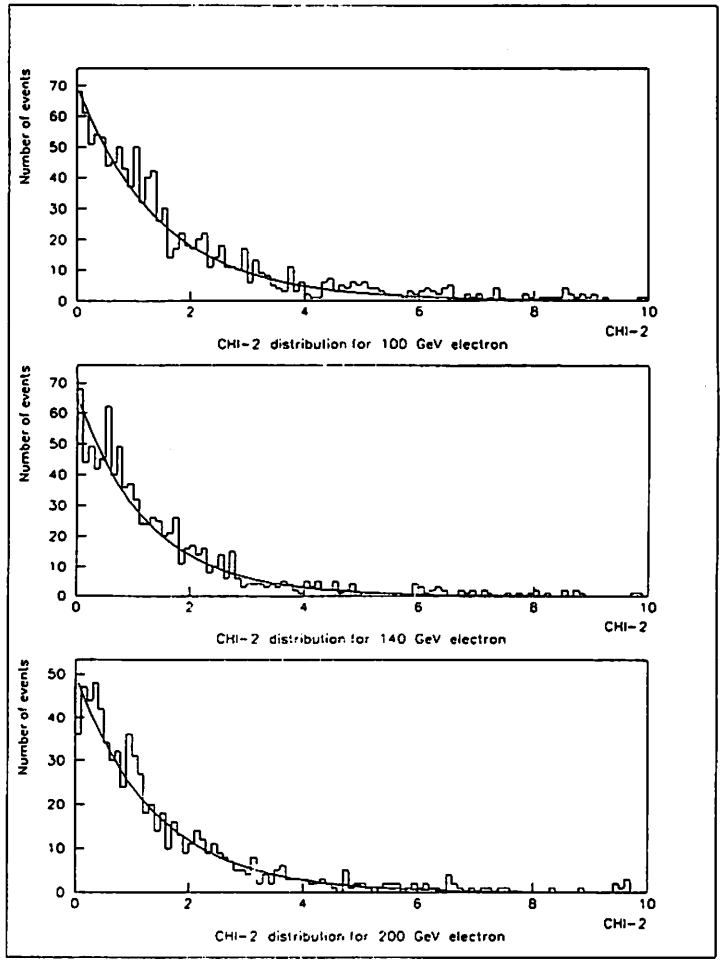

Fig.5-8 cont'd

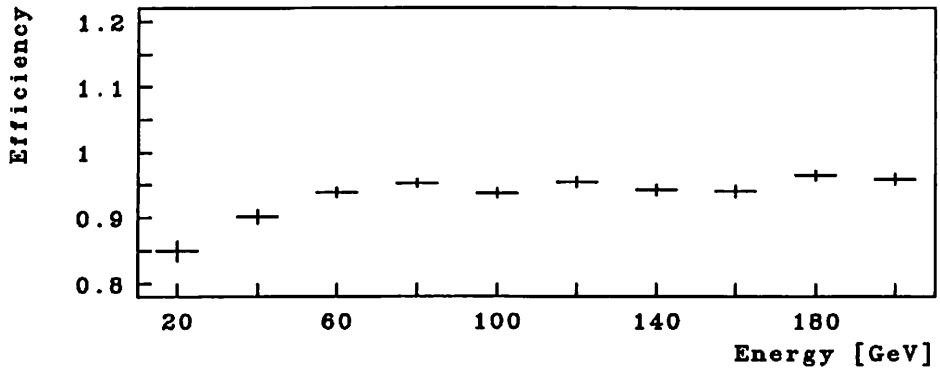

Fig.5-10 (a)

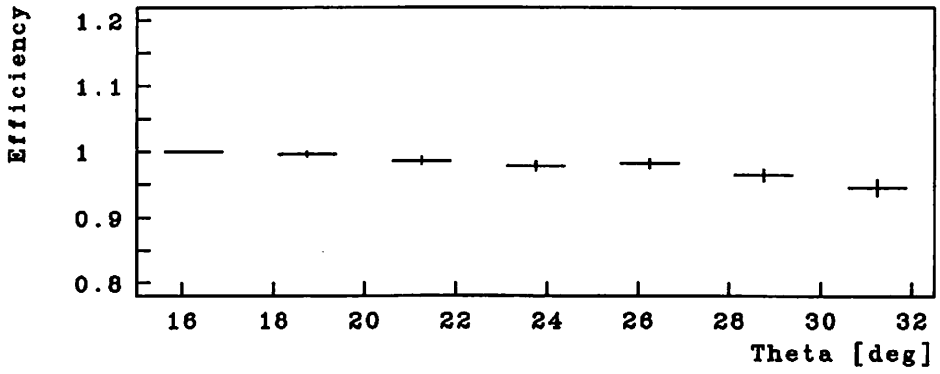

Fig.5-10 (b)

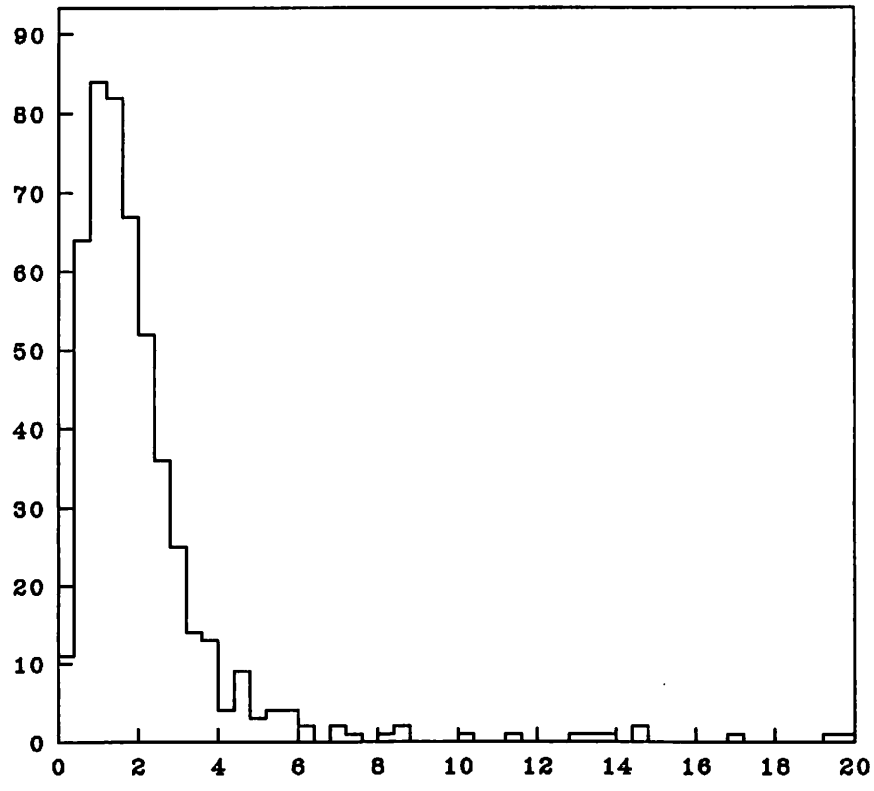

Fig.5-9 Lateral Chi-square

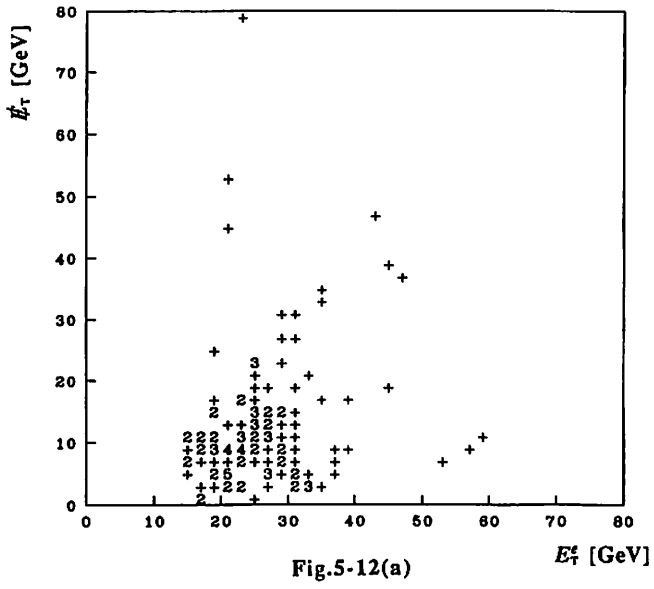

Fig.5-12(a)

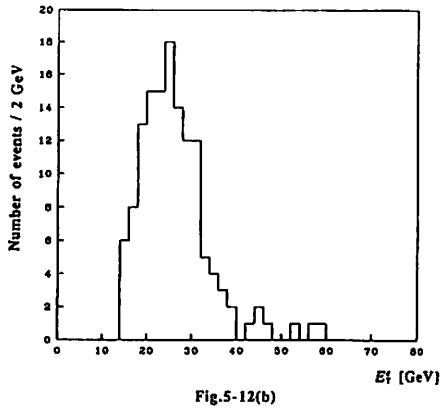

Fig.5-12(b)

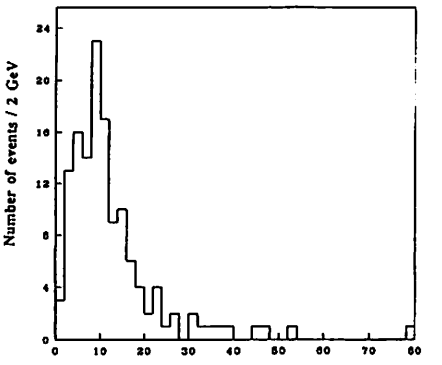

Fig.5-12(c)

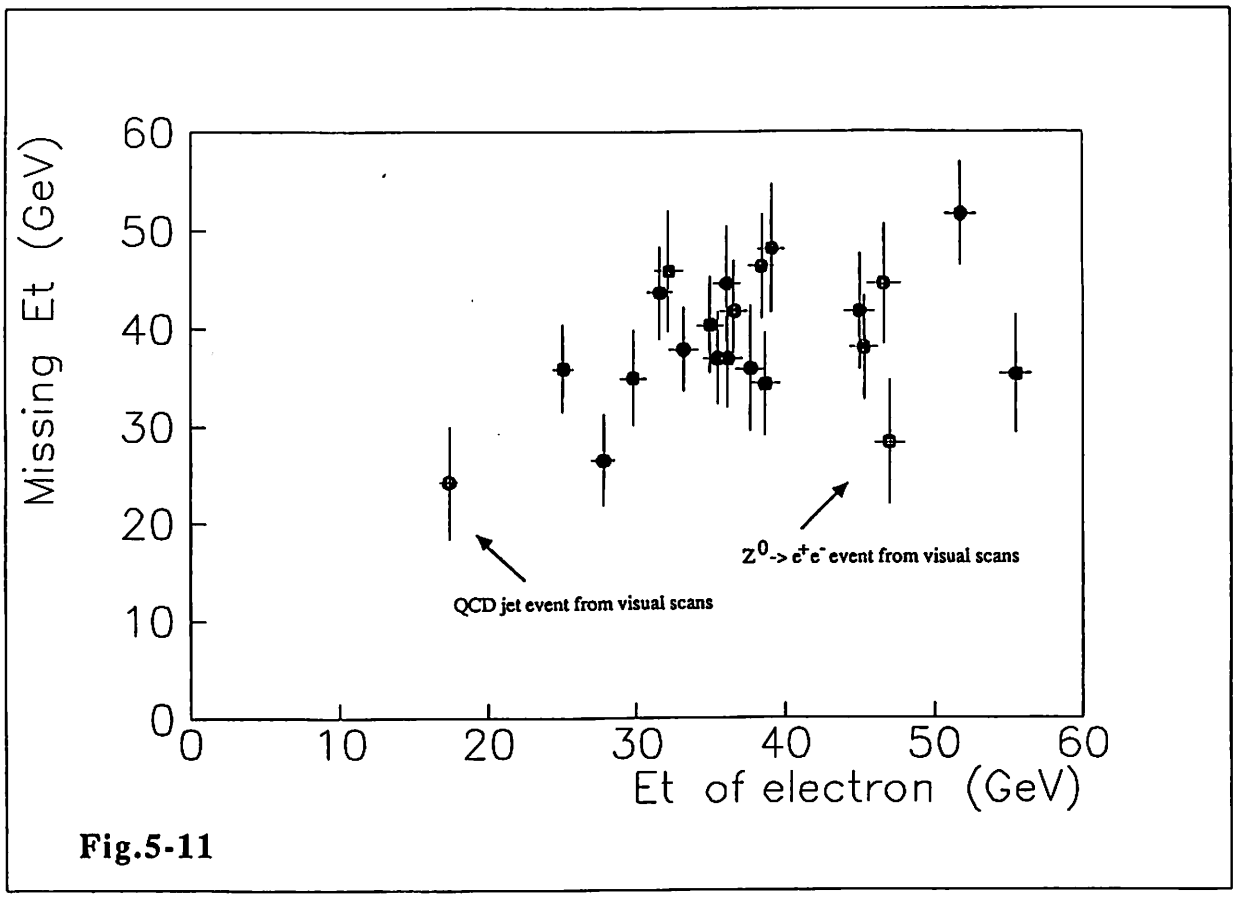

Fig.5-11

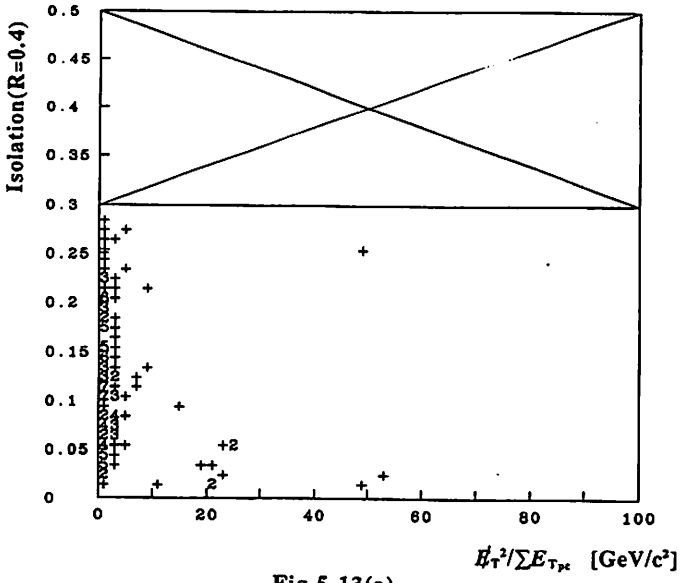

Fig.5-13(a)

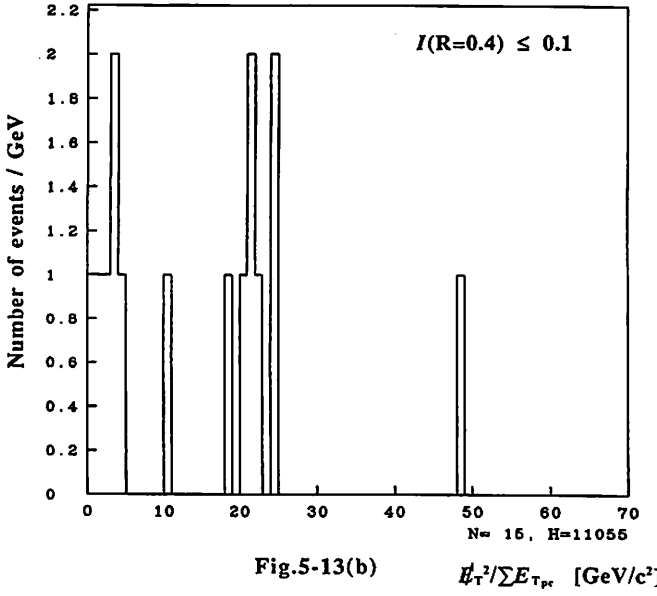

Fig.5-13(b)

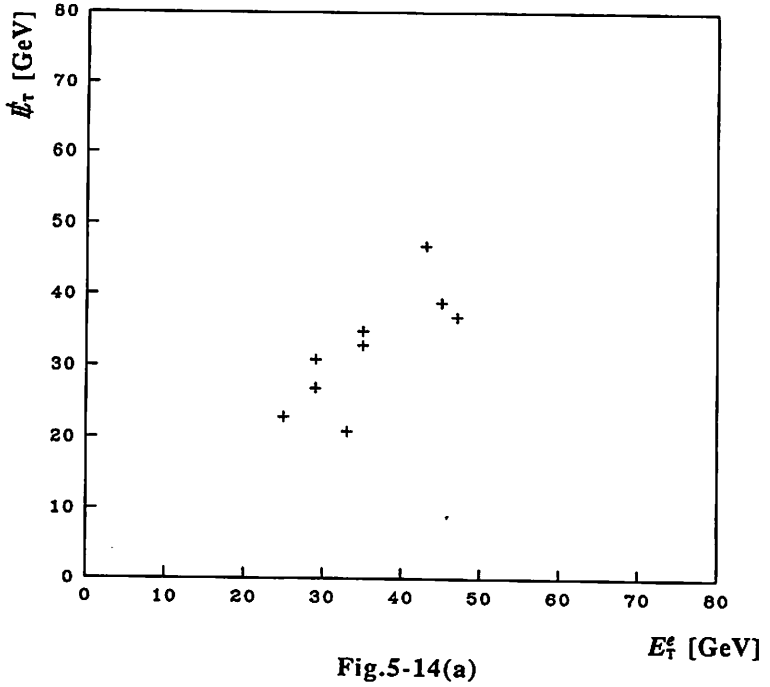

Fig.5-14(a)

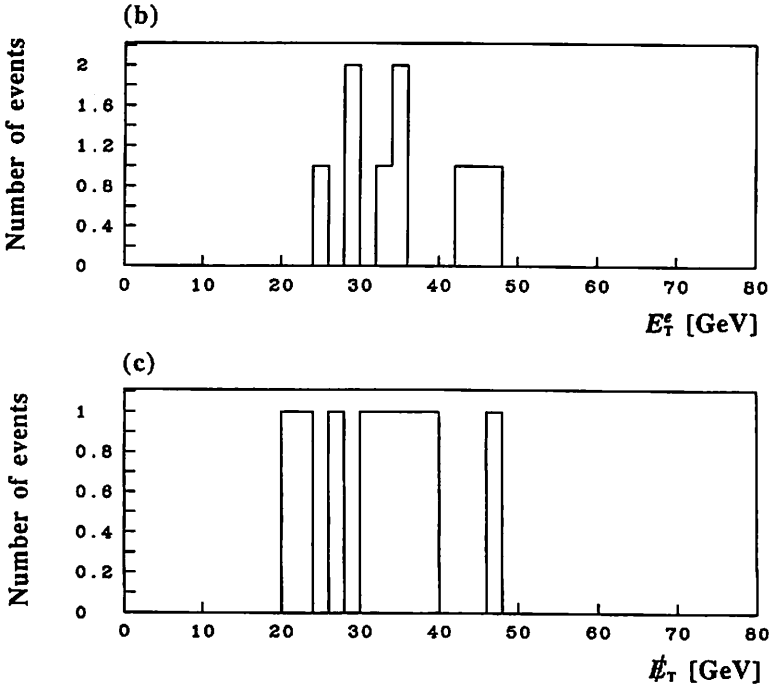

Fig.5-14

Fig.5-15 (a) cont'd

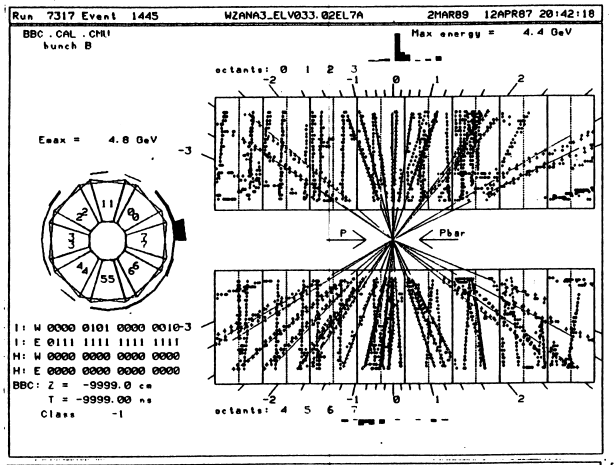

Fig.5-15 (b)

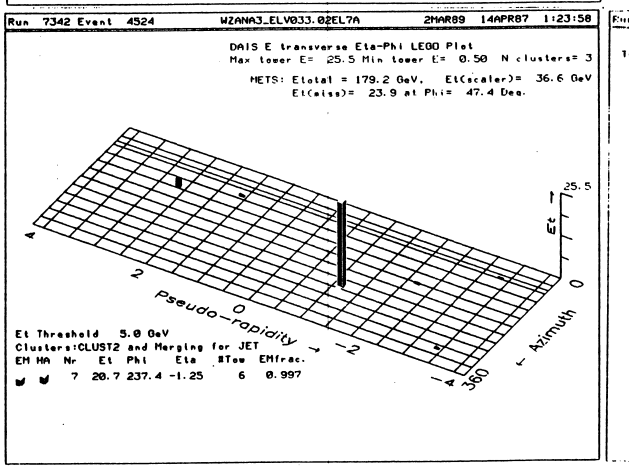

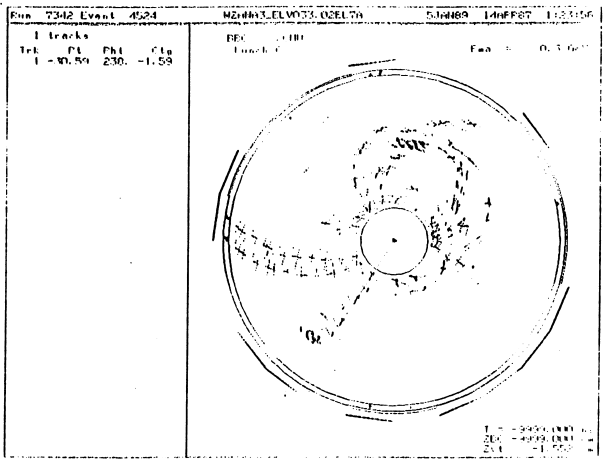

Fig.5-15 (a)

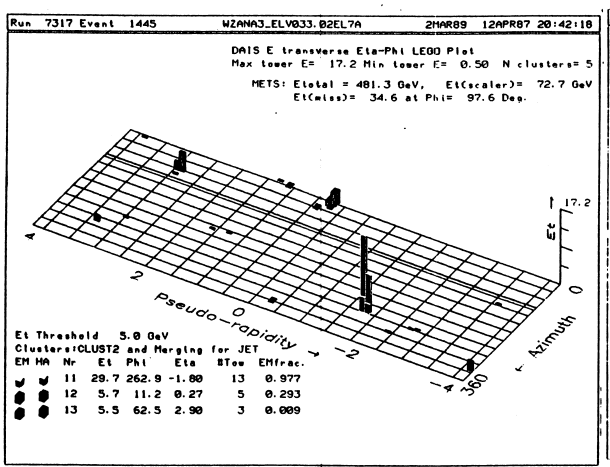

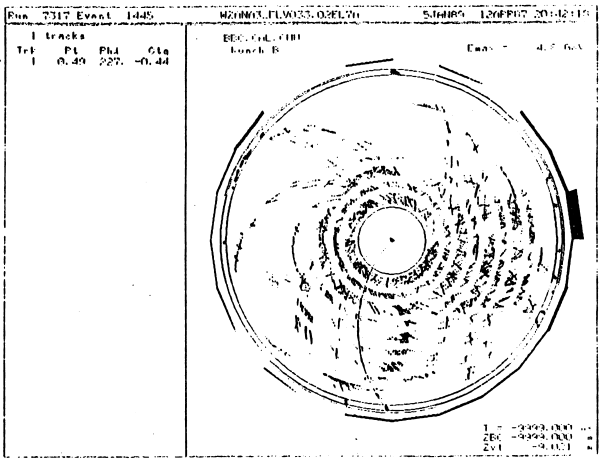

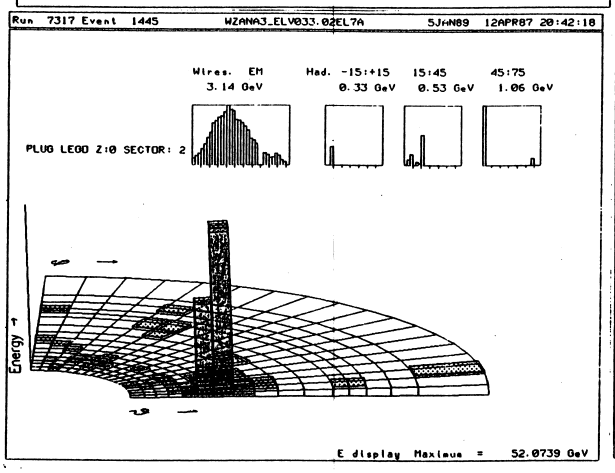

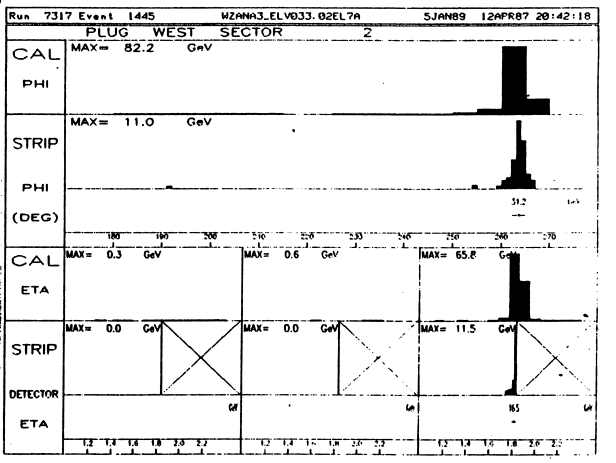

Fig.5-15 (c)

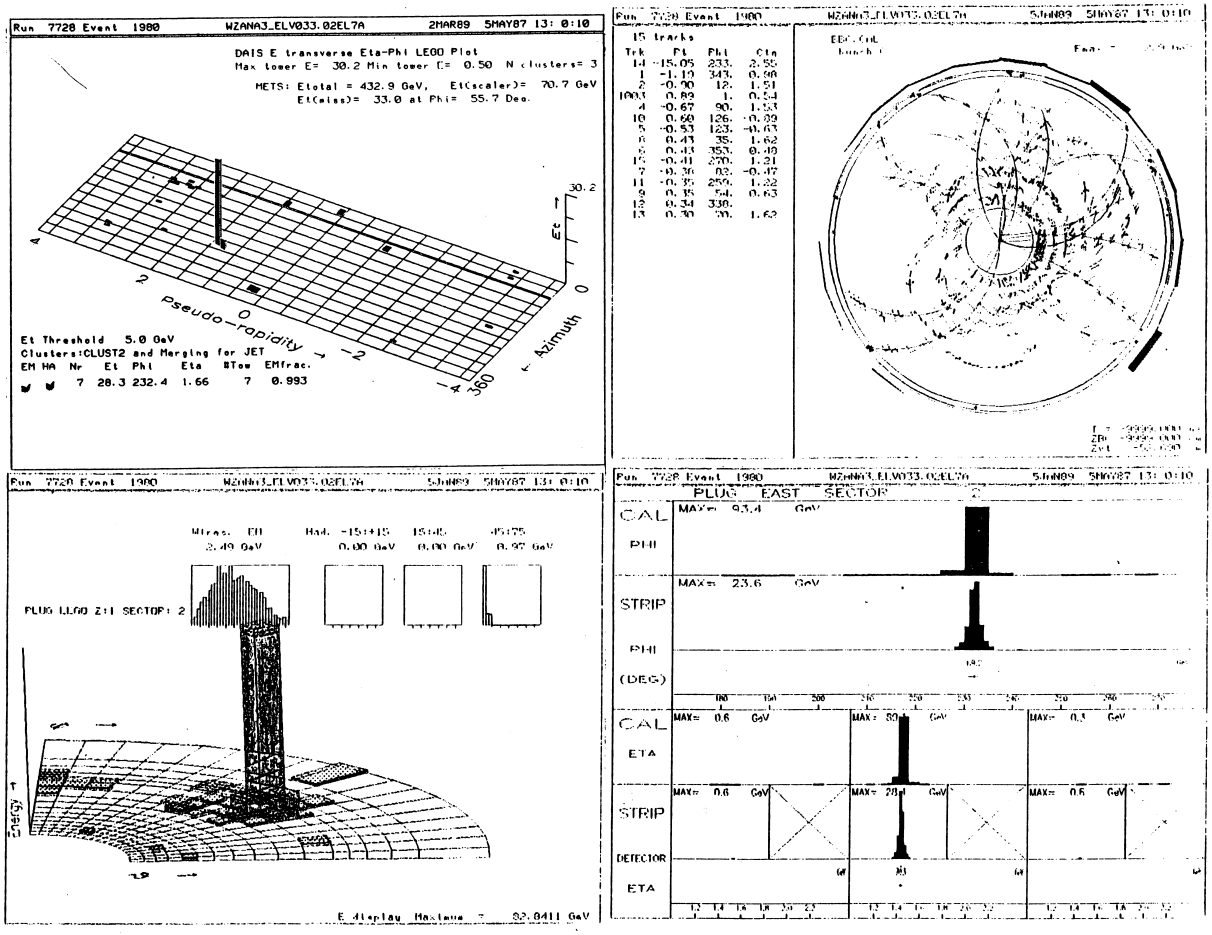

Fig.5-15 (b) cont'd

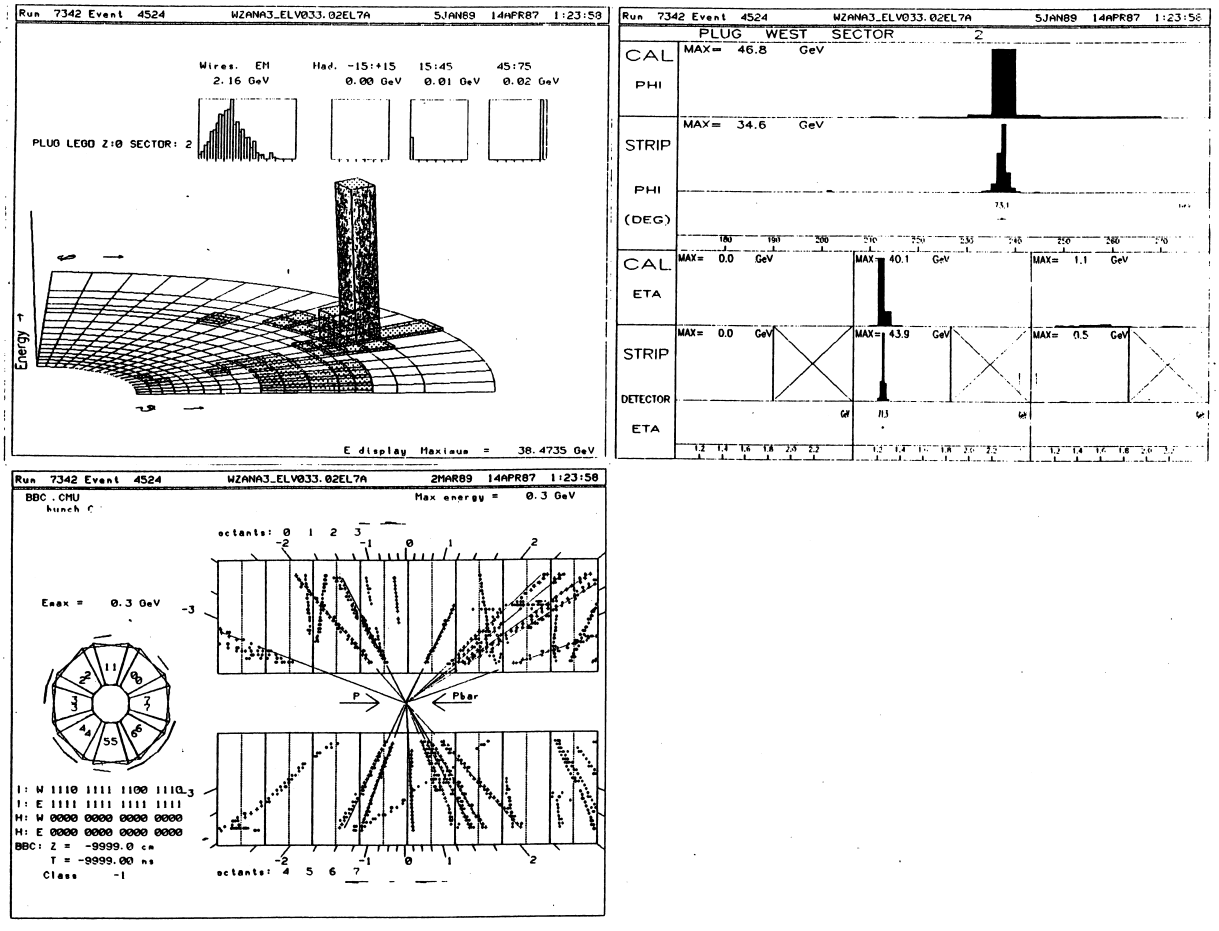

Fig.5-15 (d) cont'd

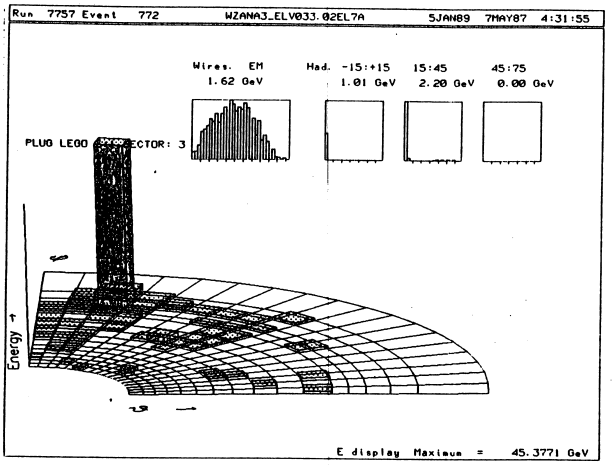

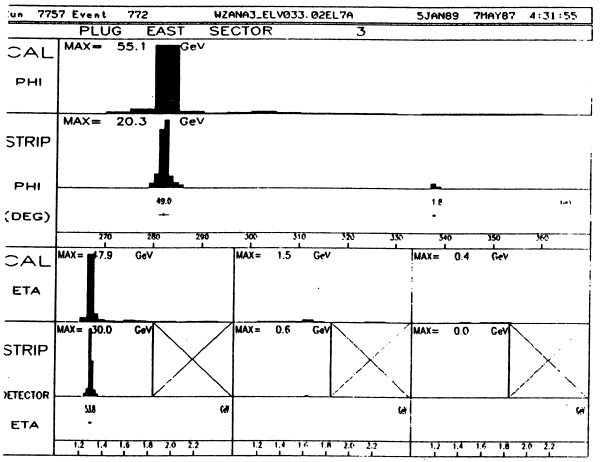

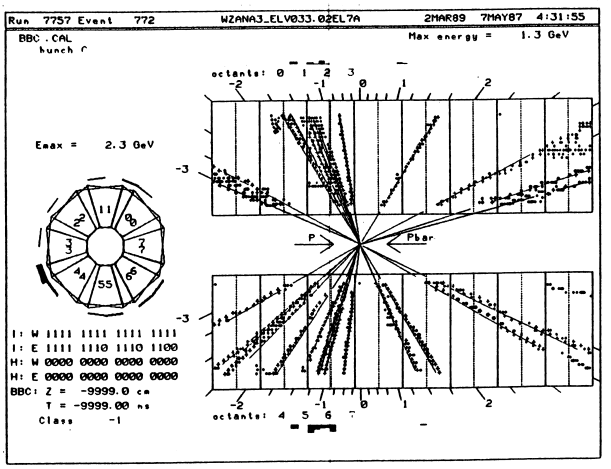

Fig.5-15 (c) cont'd

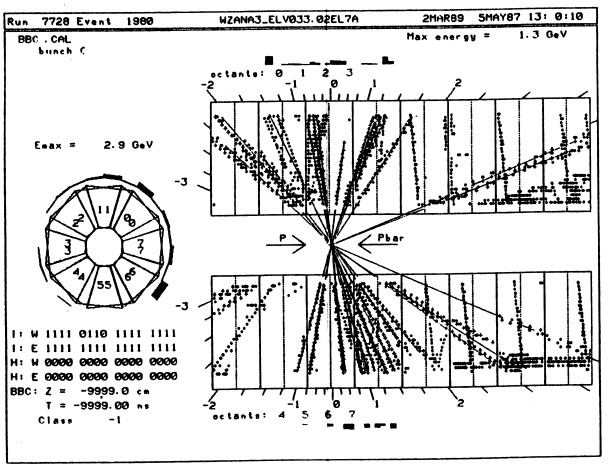

Fig.5-15 (d)

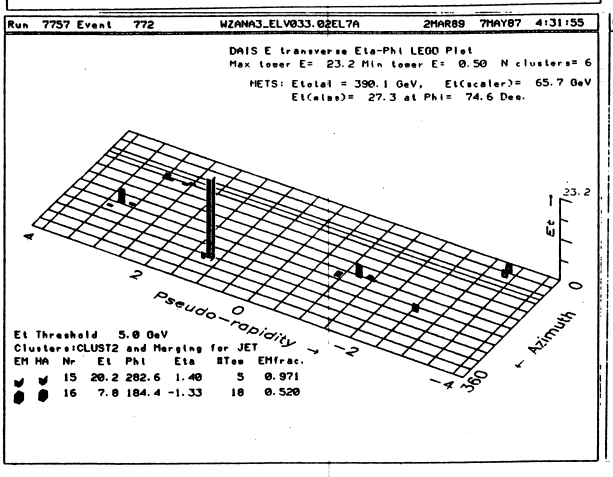

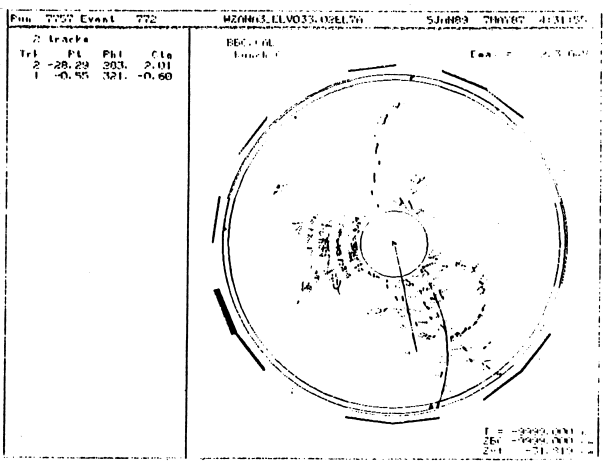

Fig.5-15 (e) cont'd

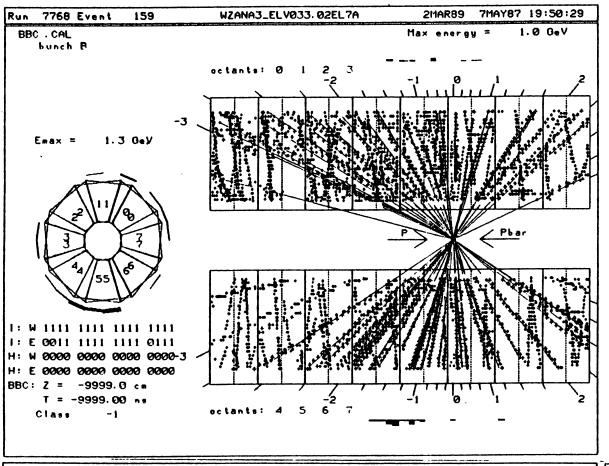

Fig.5-15 (f)

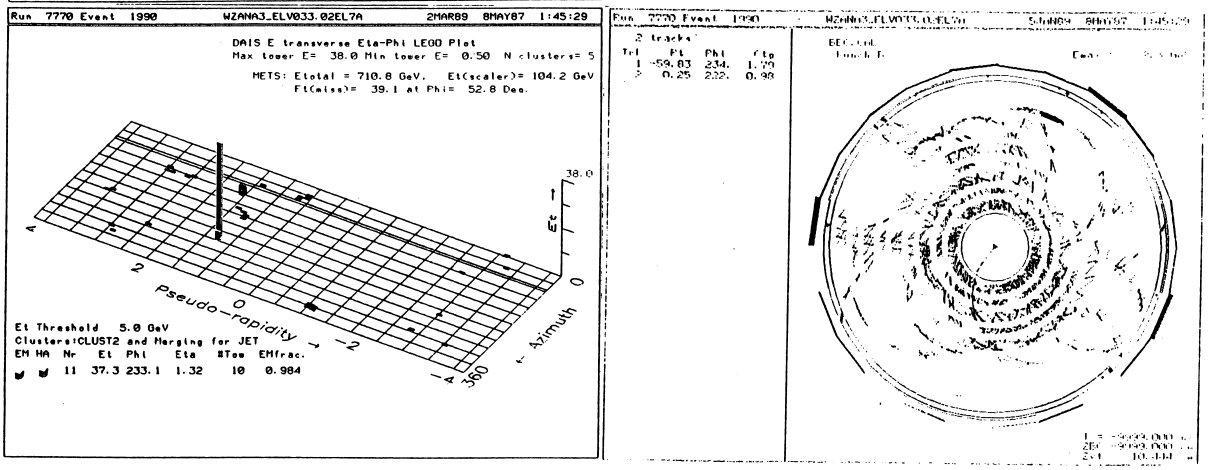

Fig.5-15 (e)

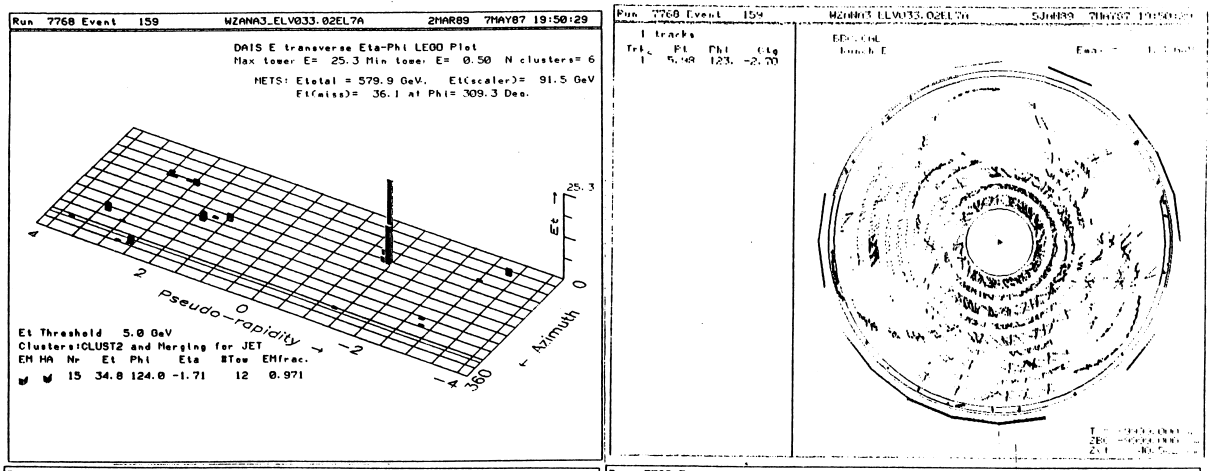

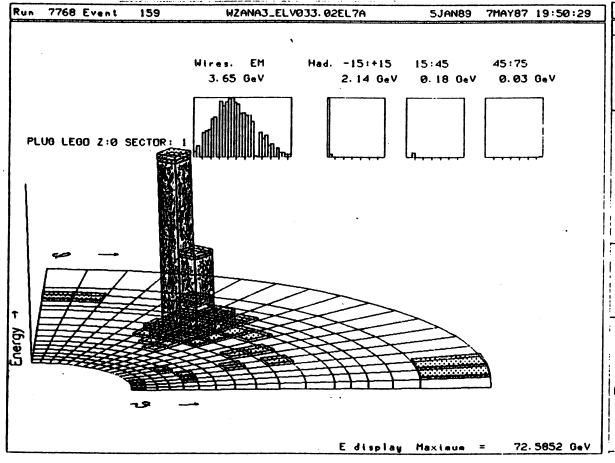

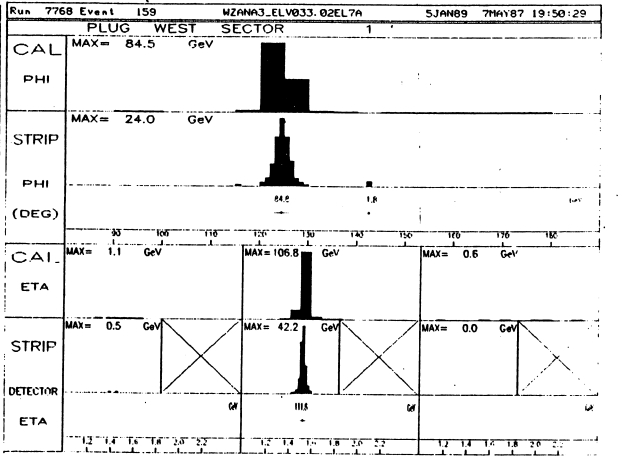

Fig.5-15 (g)

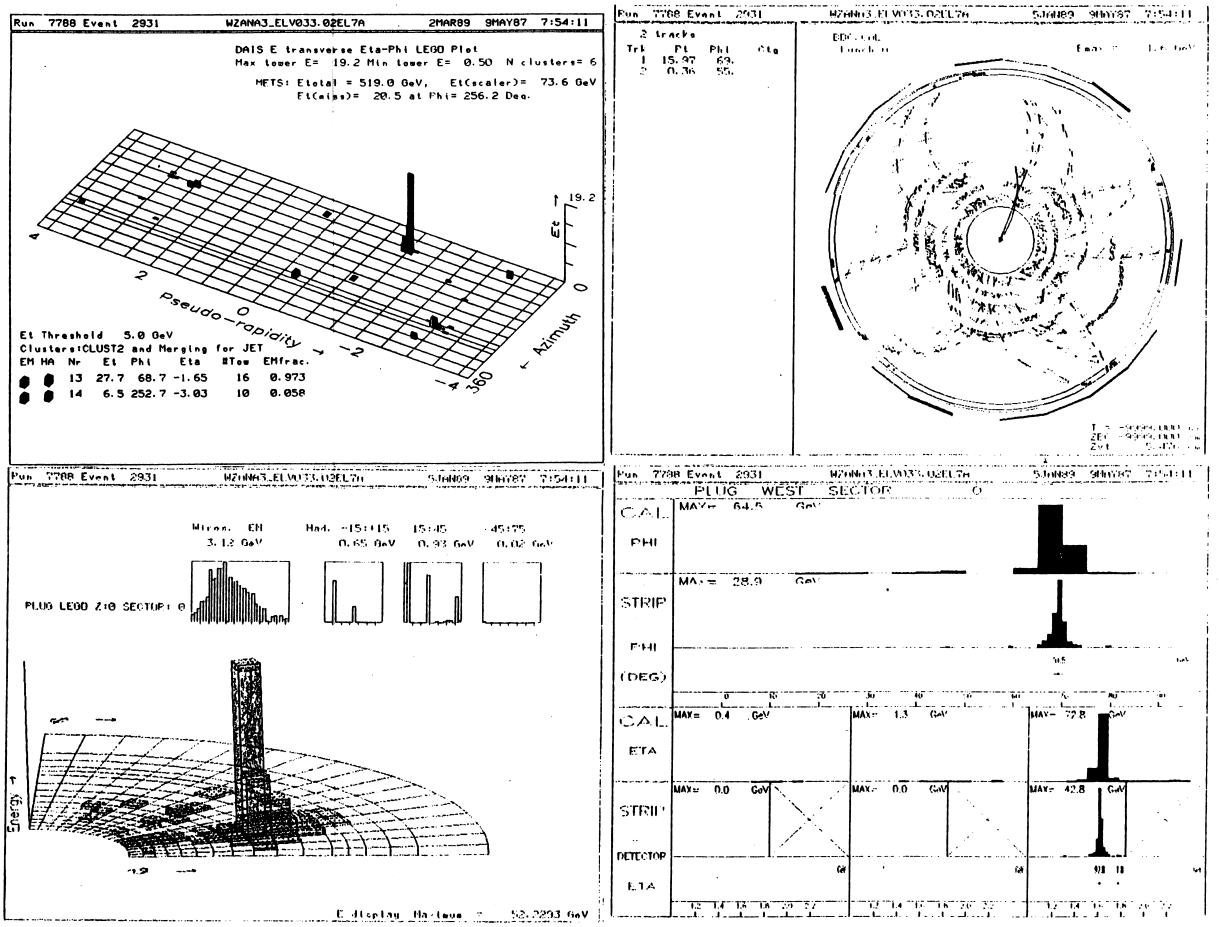

Fig.5-15 (f) cont'd

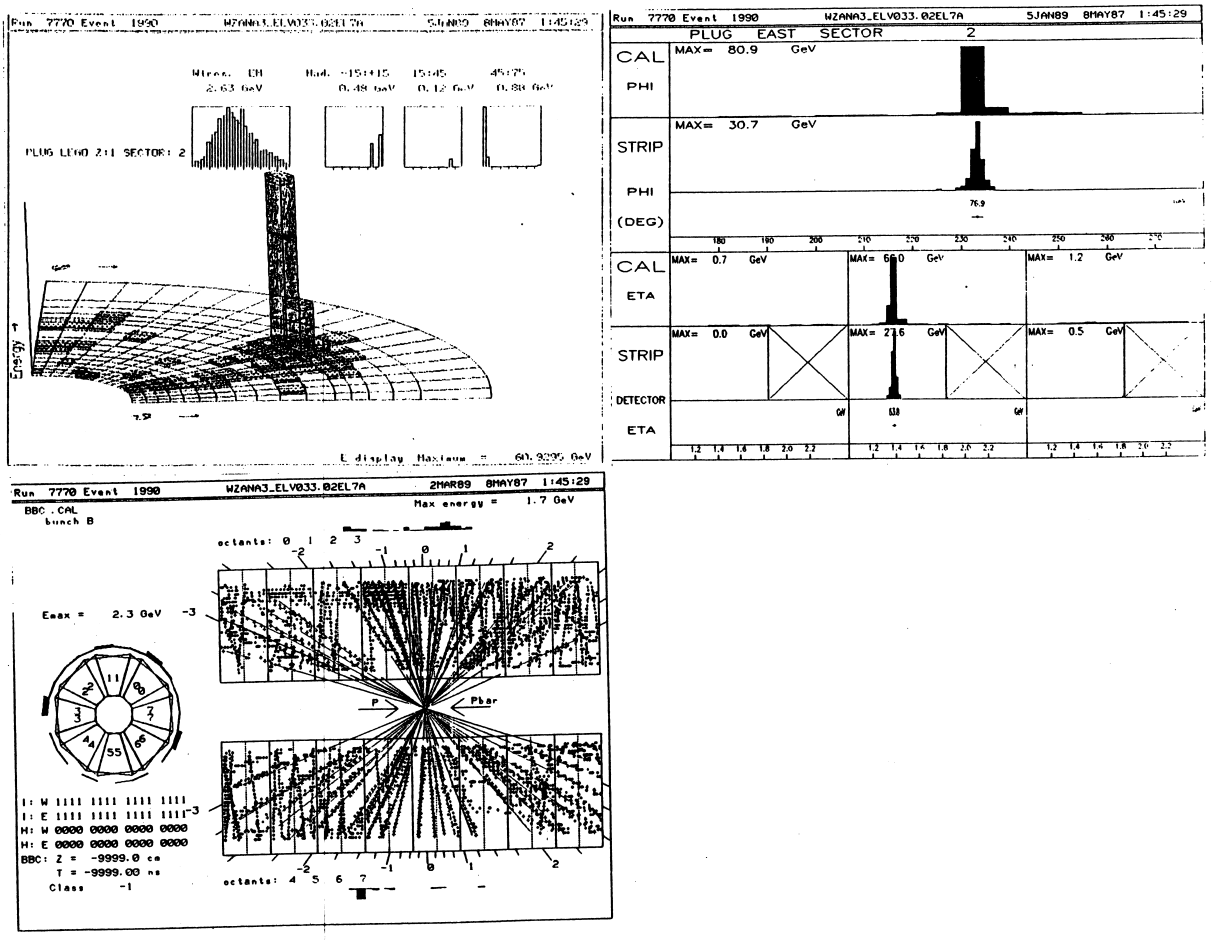

Fig.5-15 (h) cont'd

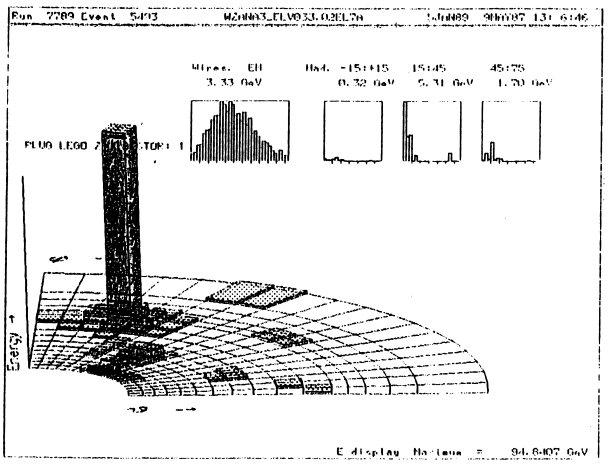

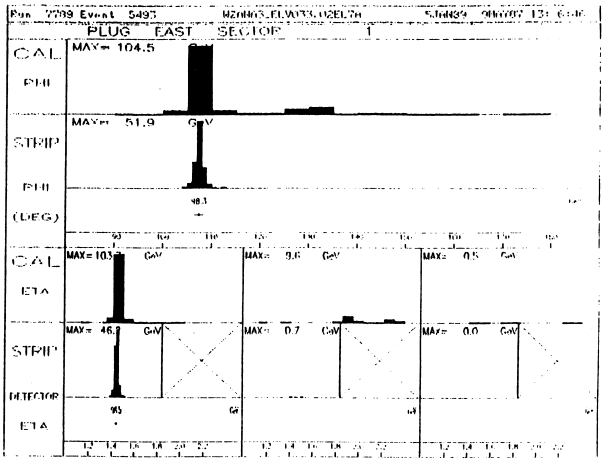

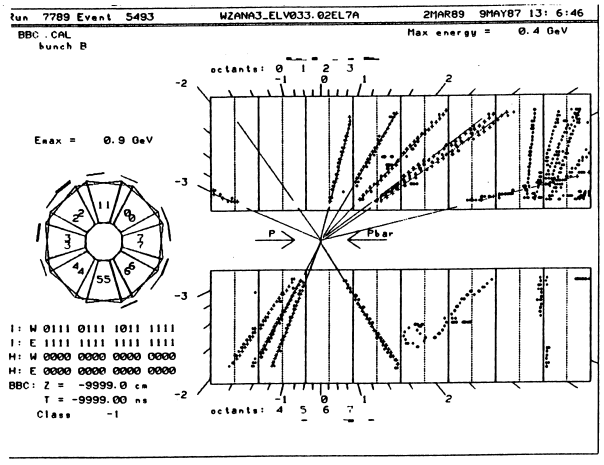

Fig.5-15 (g) cont'd

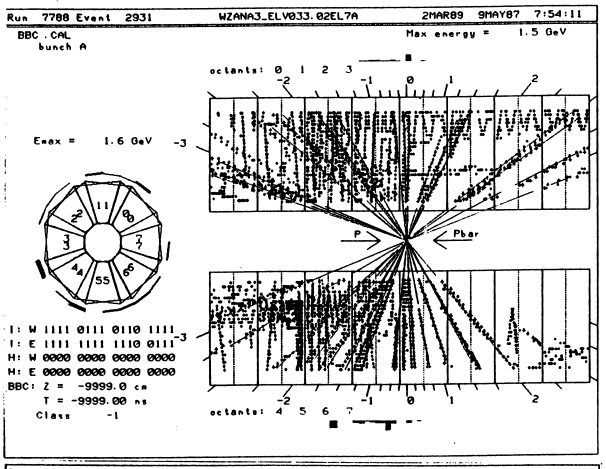

Fig.5-15 (h)

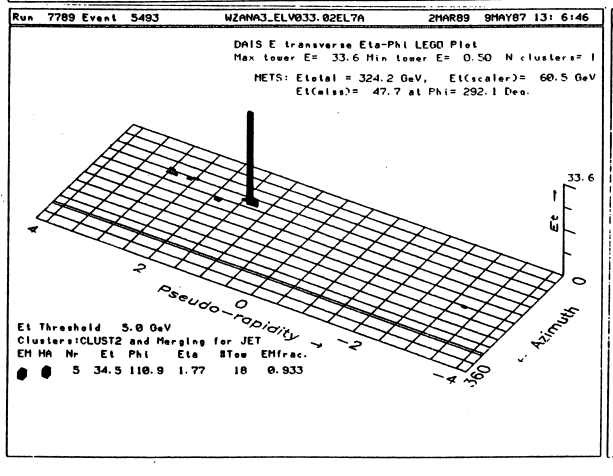

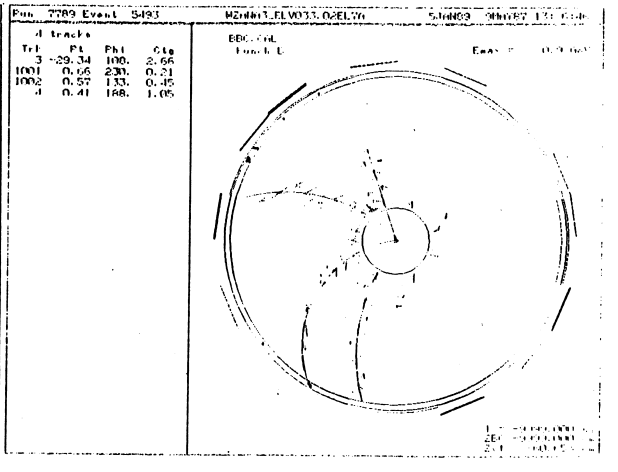

Fig.5-15 (i) cont'd

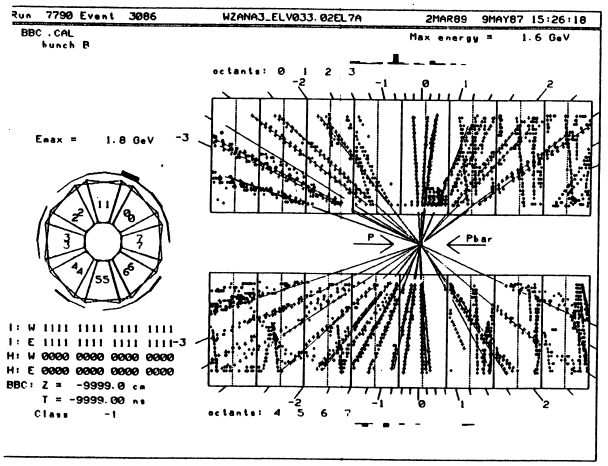

Fig.5-15 (i)

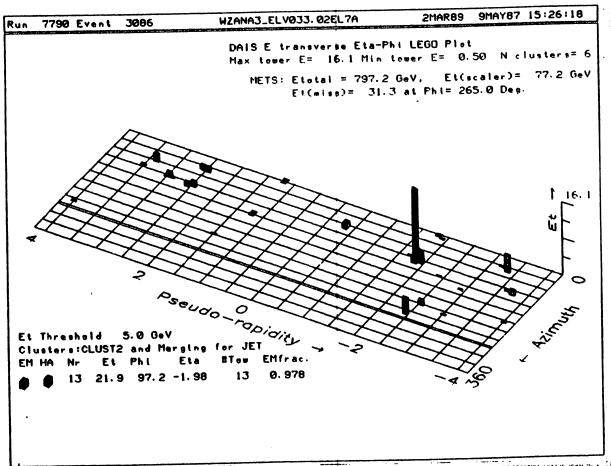

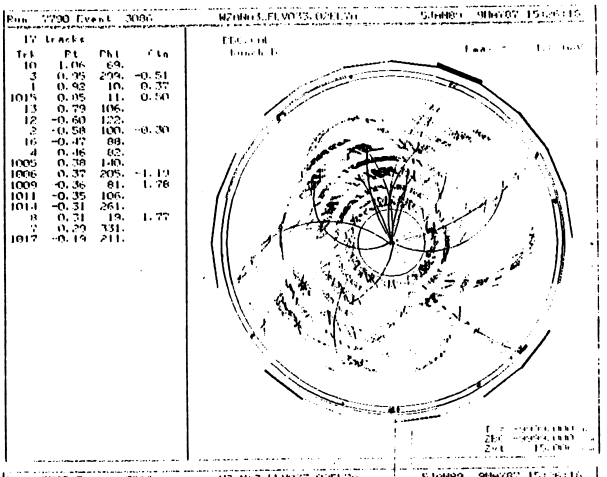

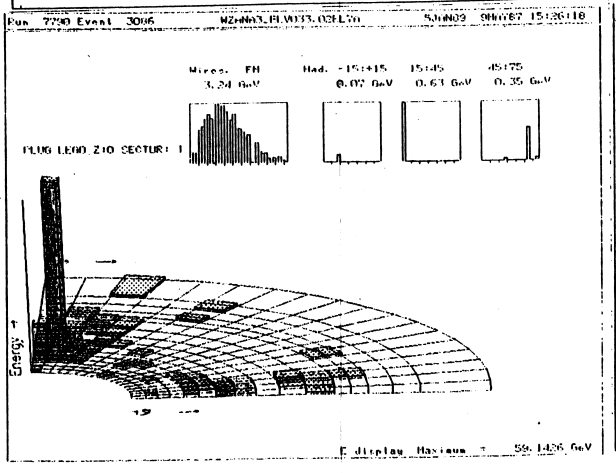

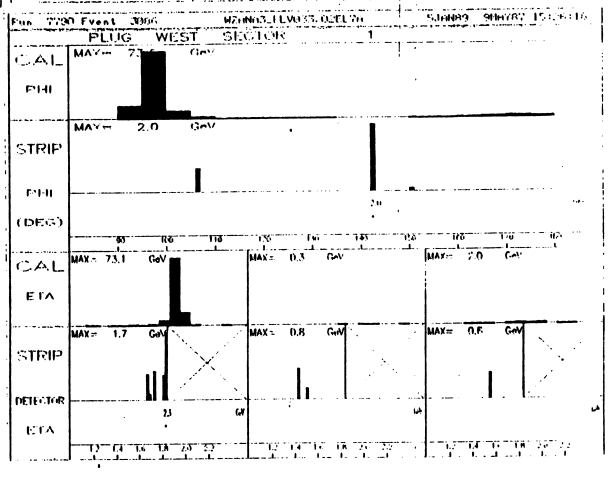

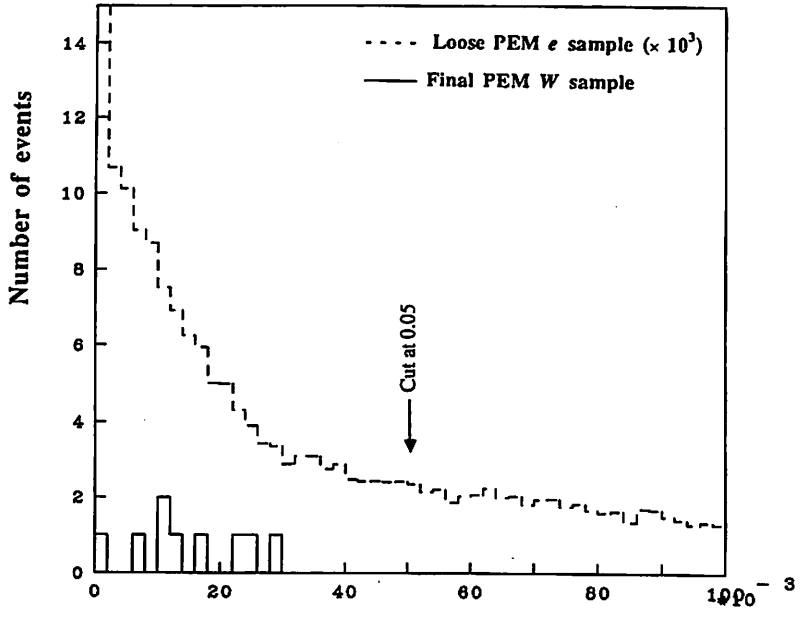

Fig.5-16(a)

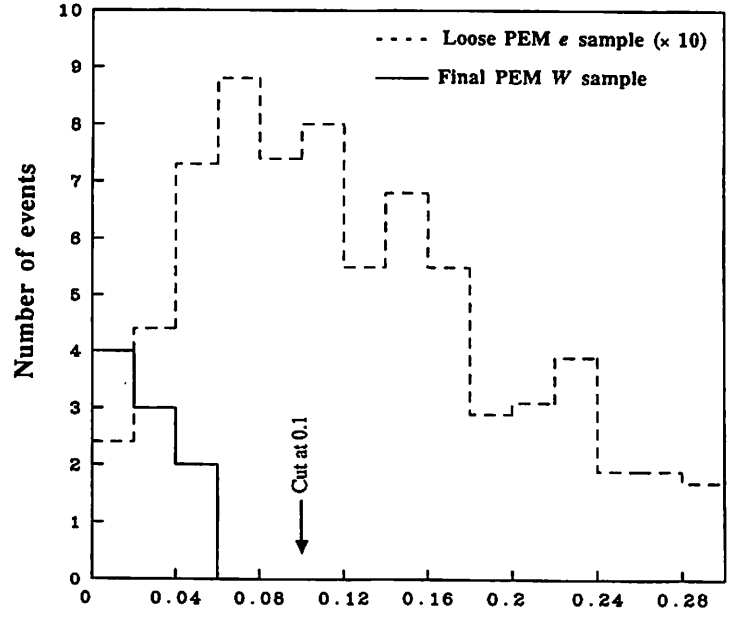

Fig.5-16(b)

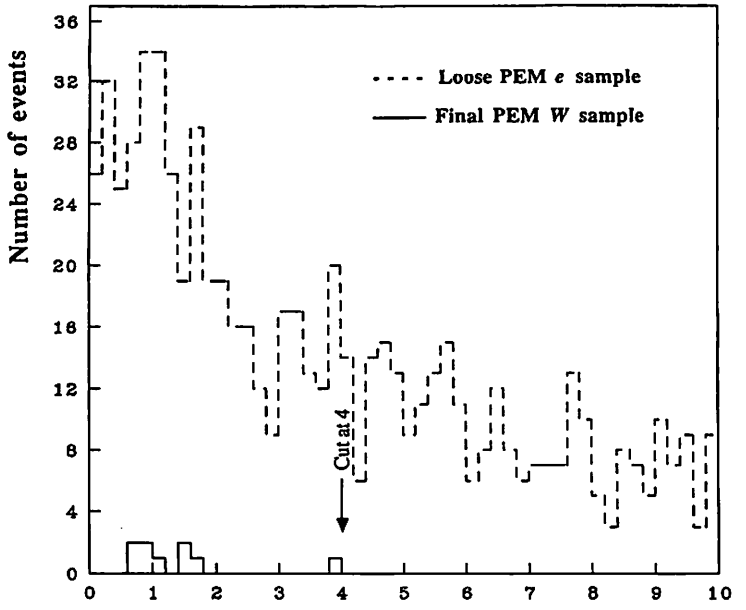

Fig.5-16(c)

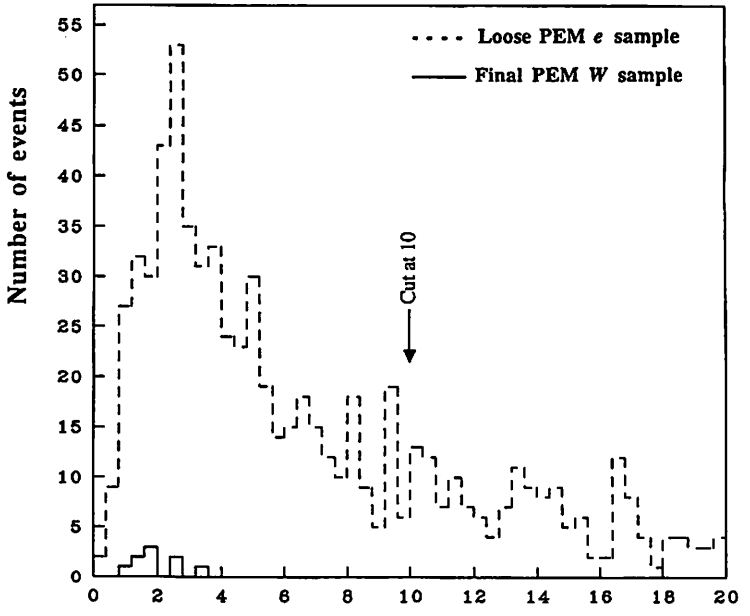

Fig.5-16(d)

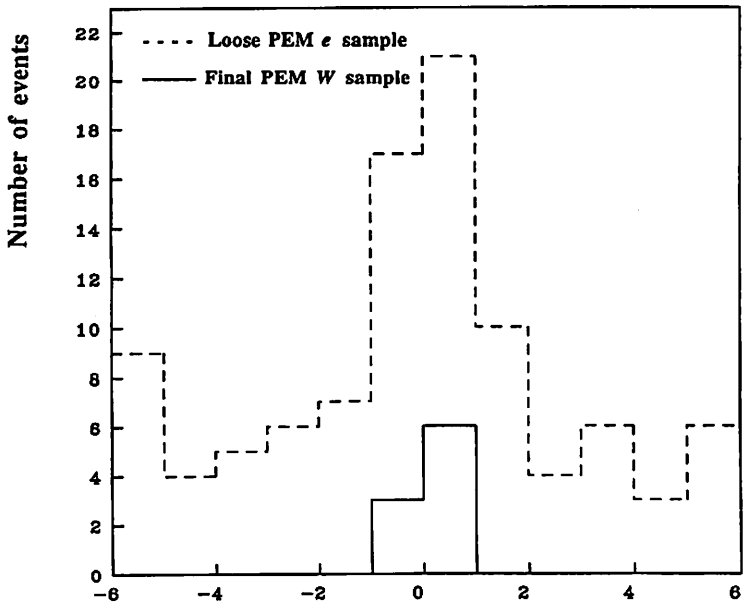

Fig.5-16(e) PEM - track matching

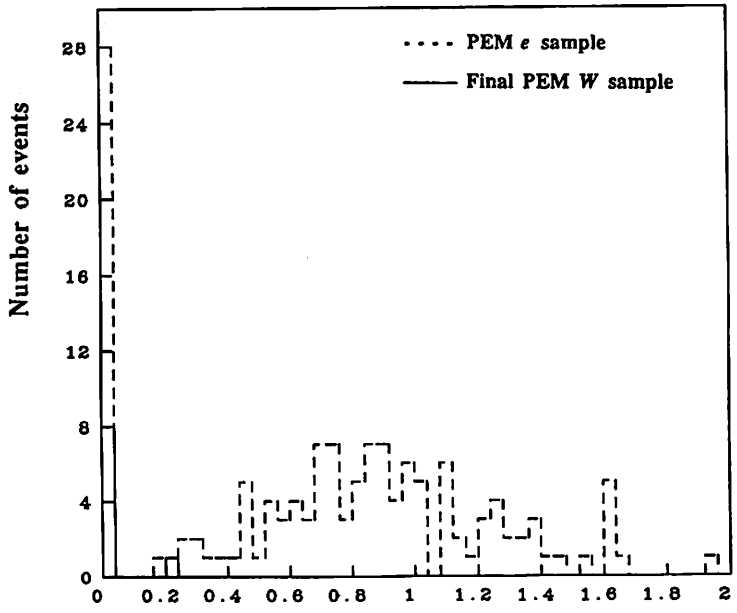

Fig.5-16(f) Dijet

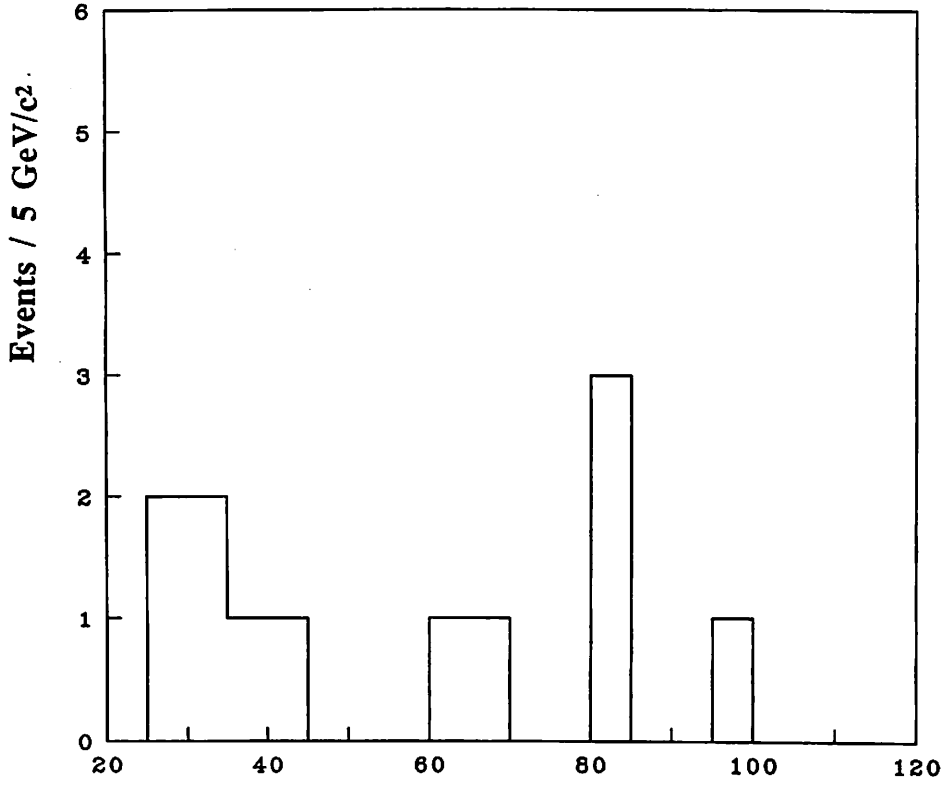

Fig.5-17

Fig.5-18 (a) cont'd

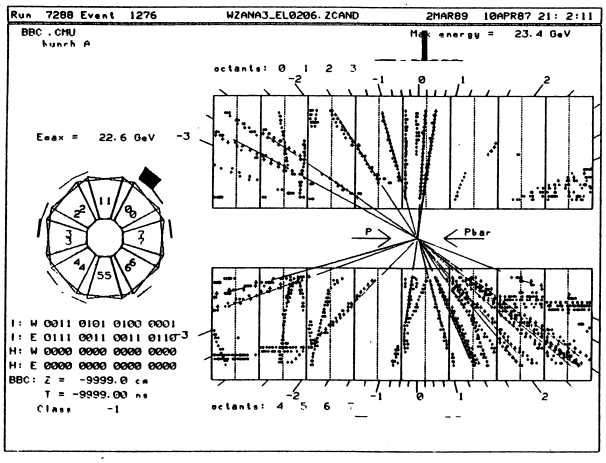

Fig.5-18 (a)

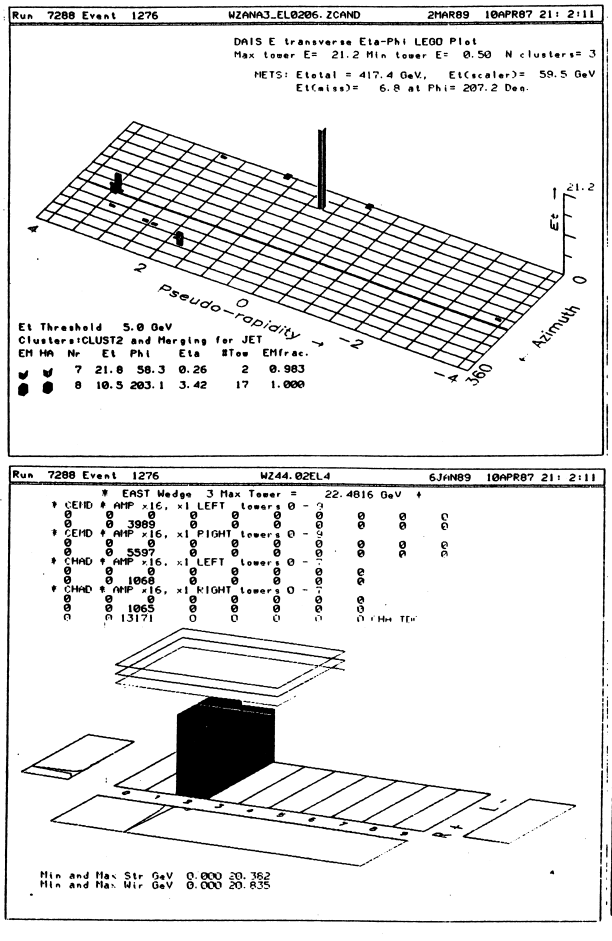

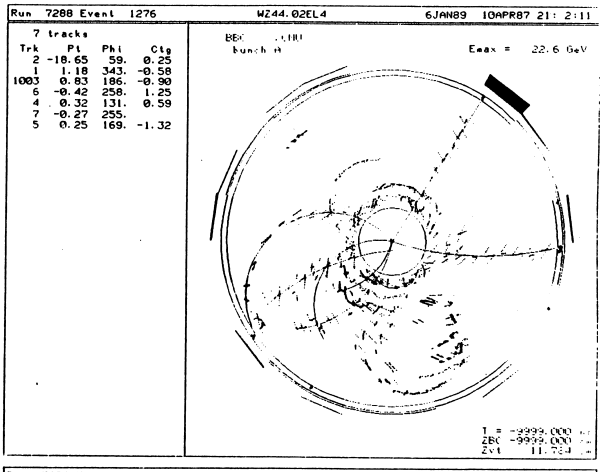

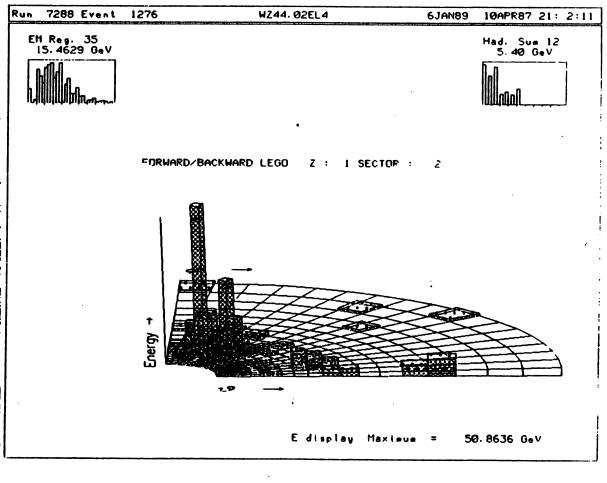

Fig.5-18 (b) cont'd

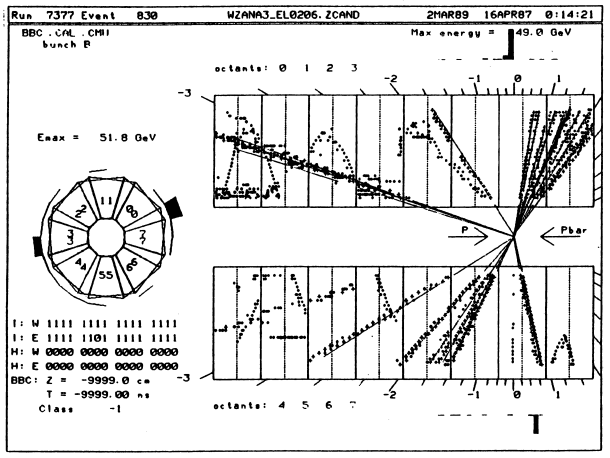

Fig.5-18 (b)

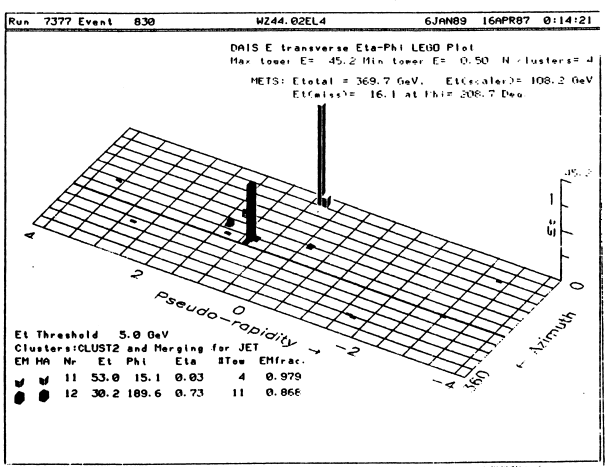

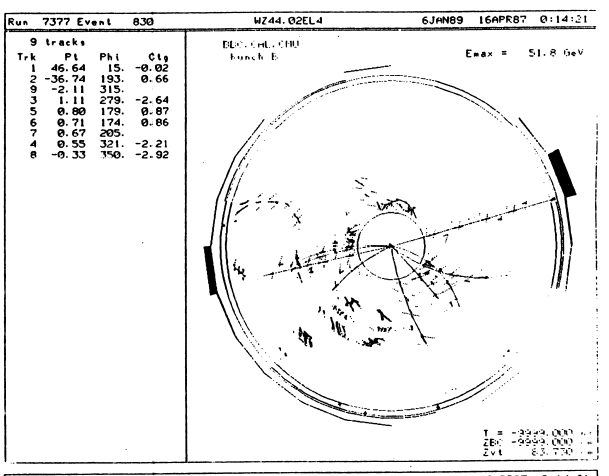

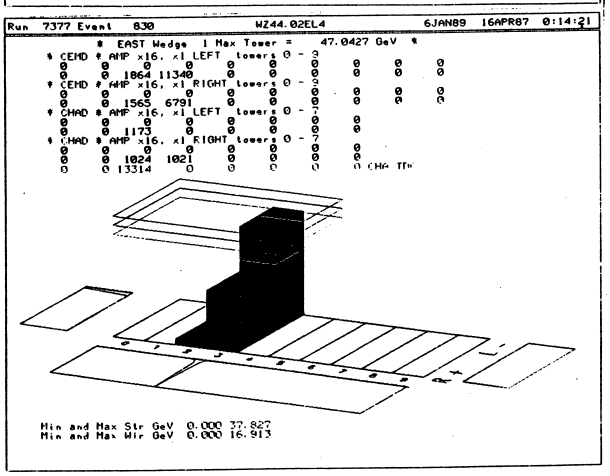

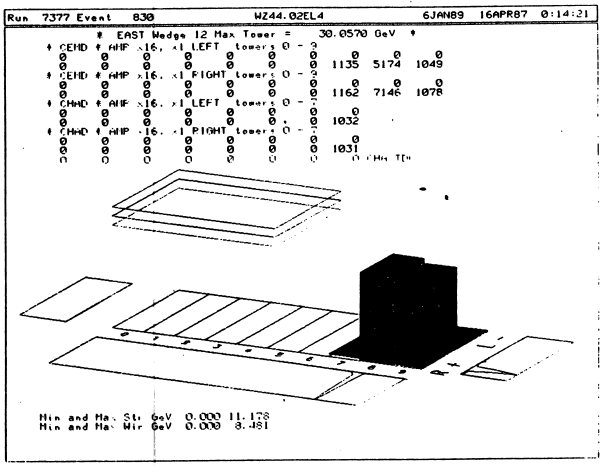

Fig.5-18 (c) cont'd

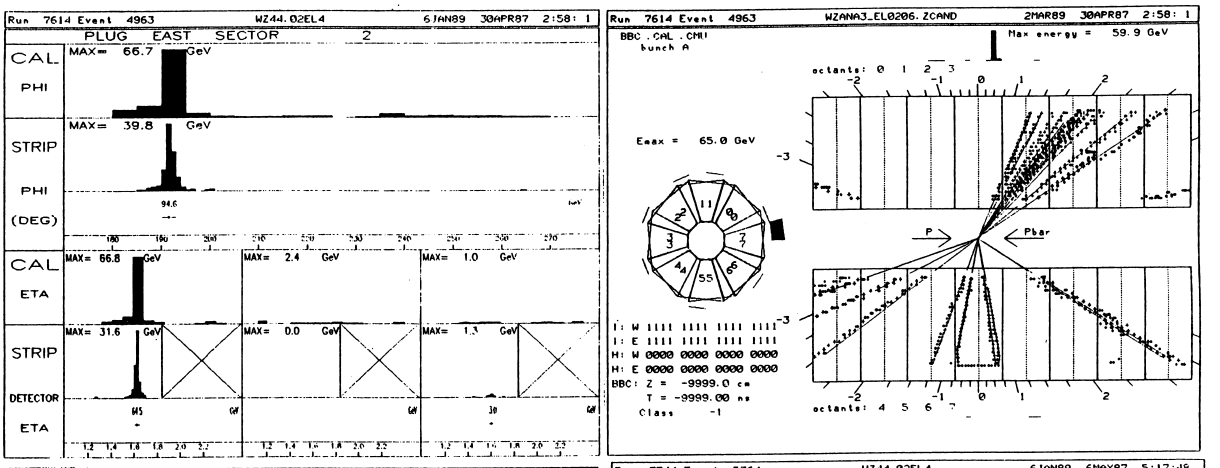

Fig.5-18 (d)

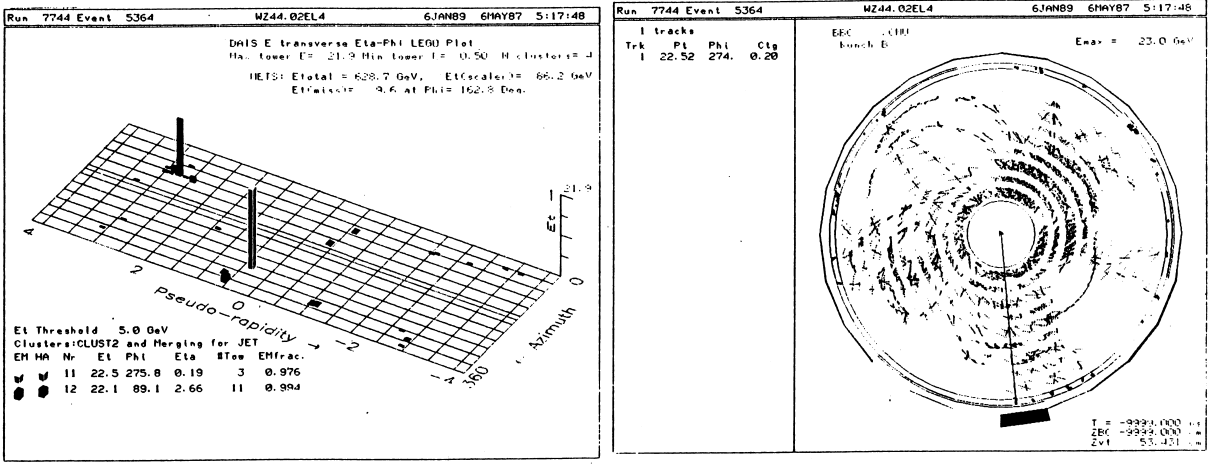

Fig.5-18 (c)

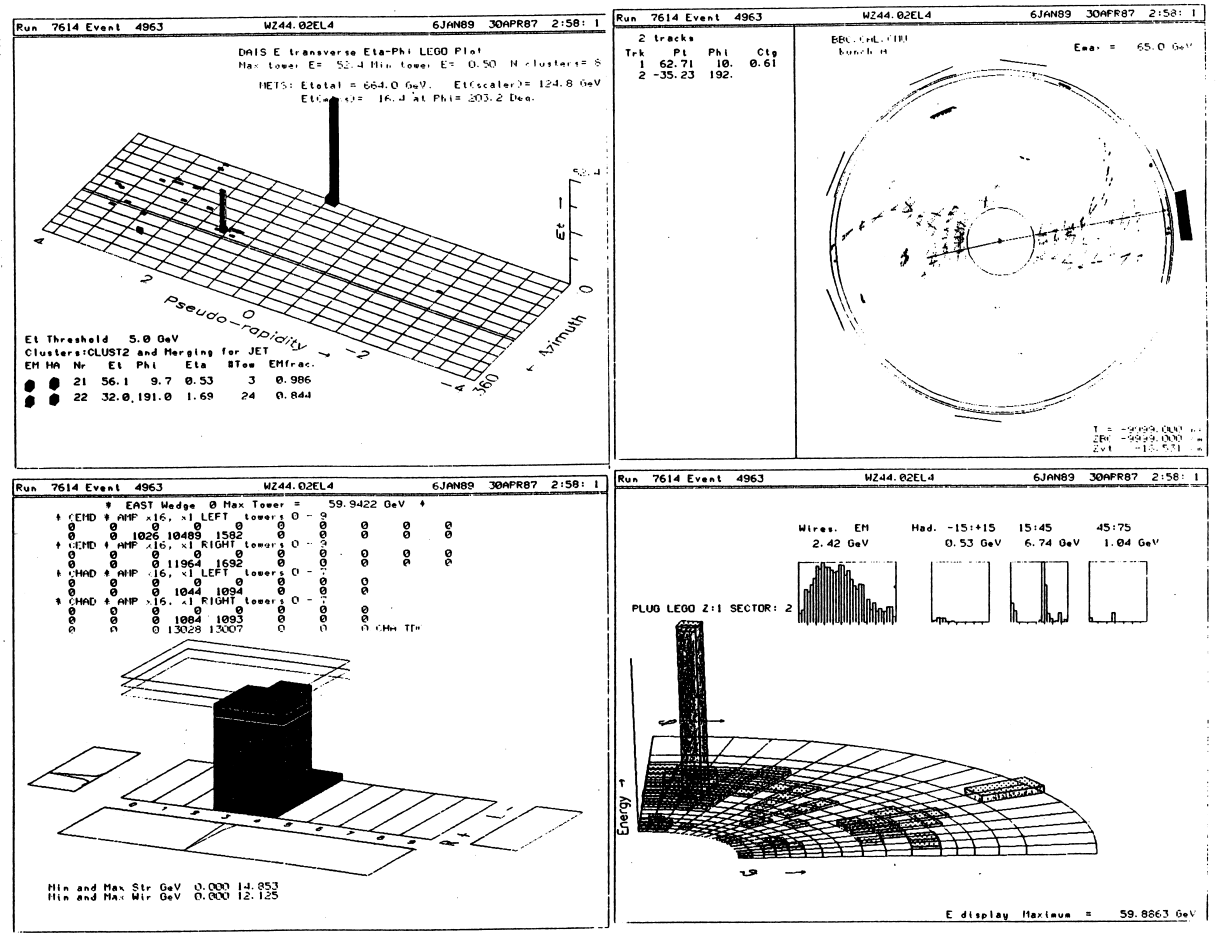

Fig.5-18 (e)

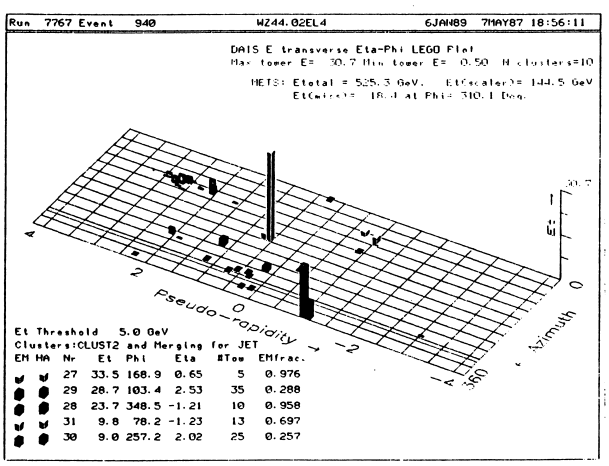

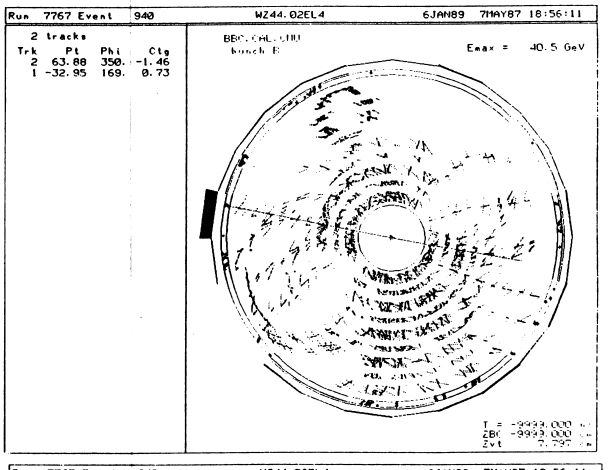

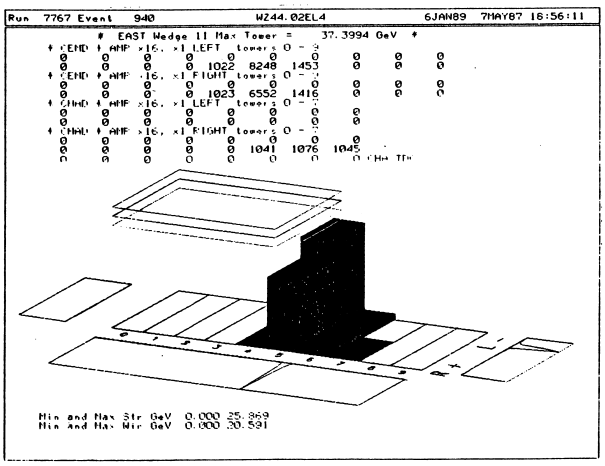

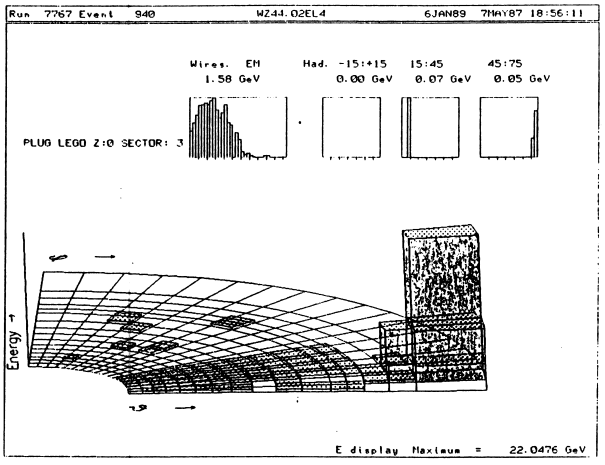

Fig.5-18 (d)

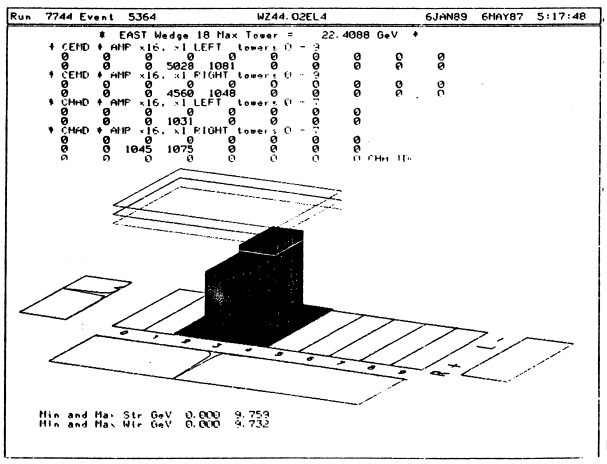

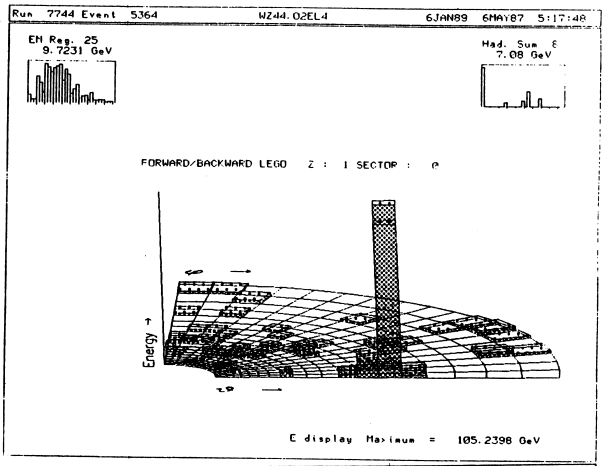

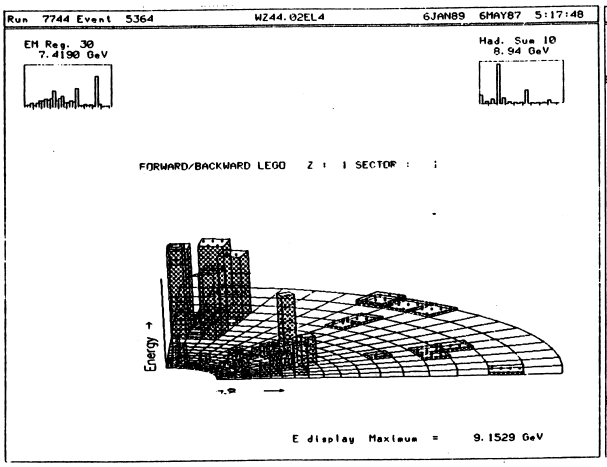

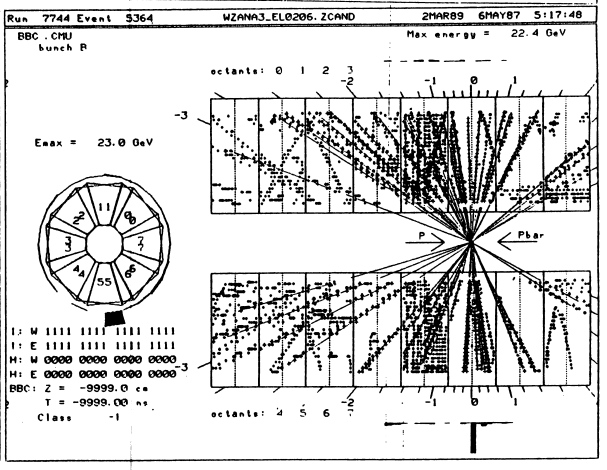

Fig.5-18 (f)

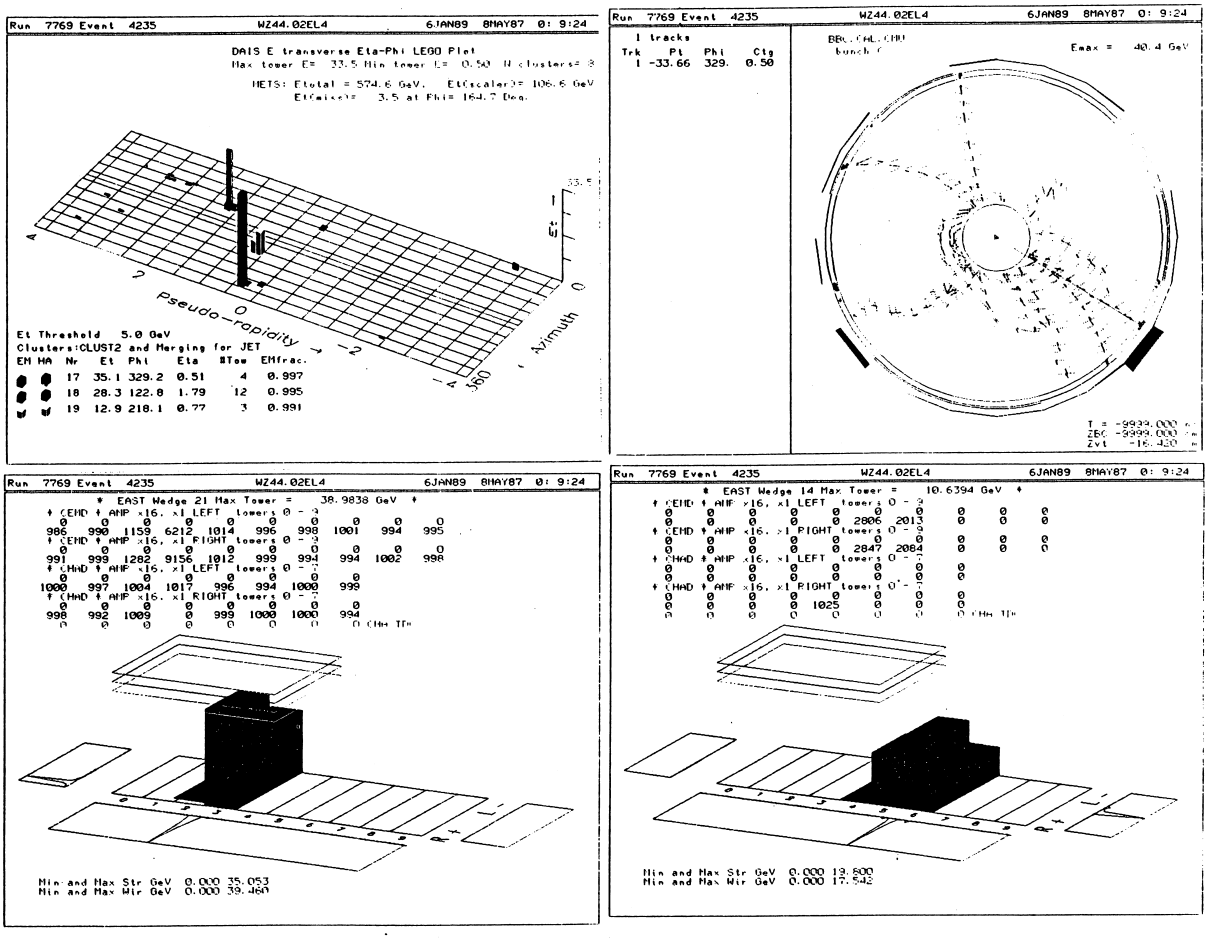

Fig.5-18 (e) cont'd

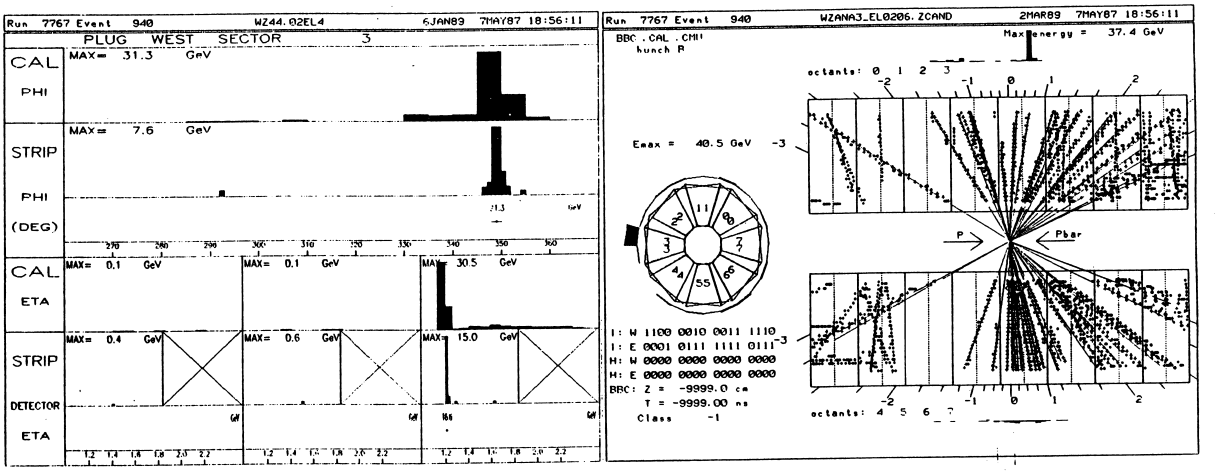

Fig.6-1(a)

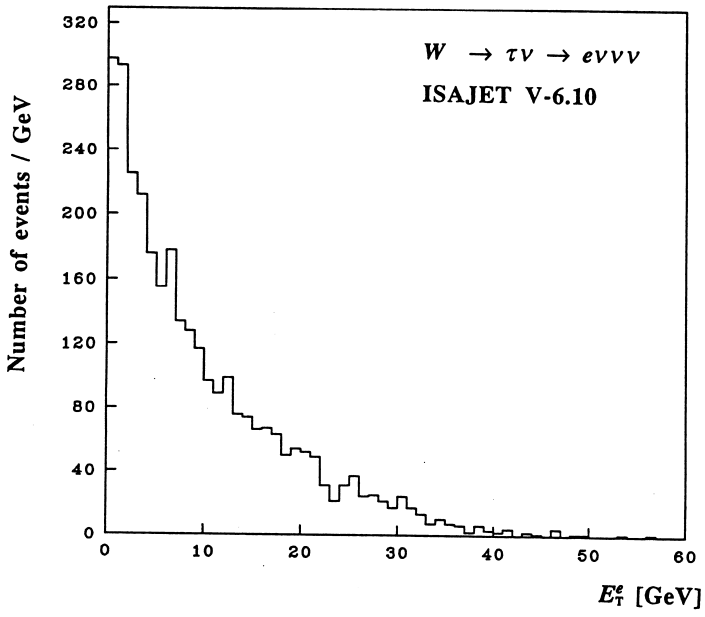

Fig.6-1(b)

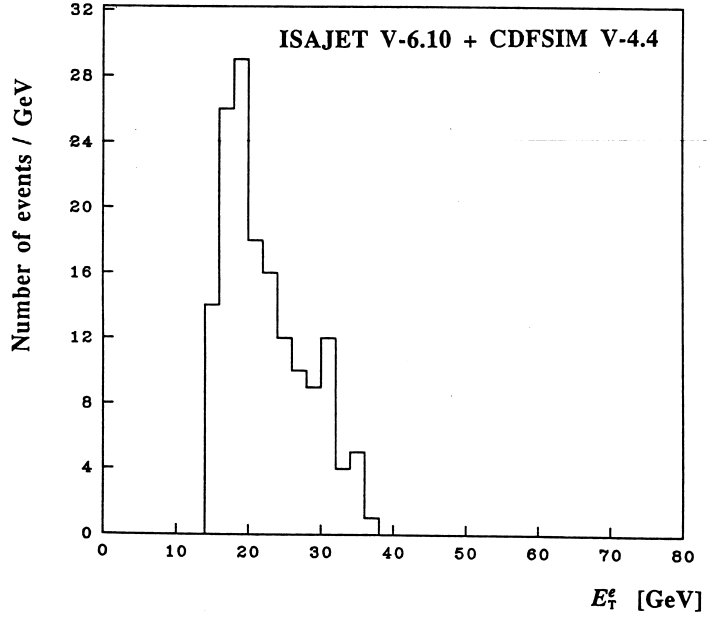

Fig.5-18 (f) cont'd

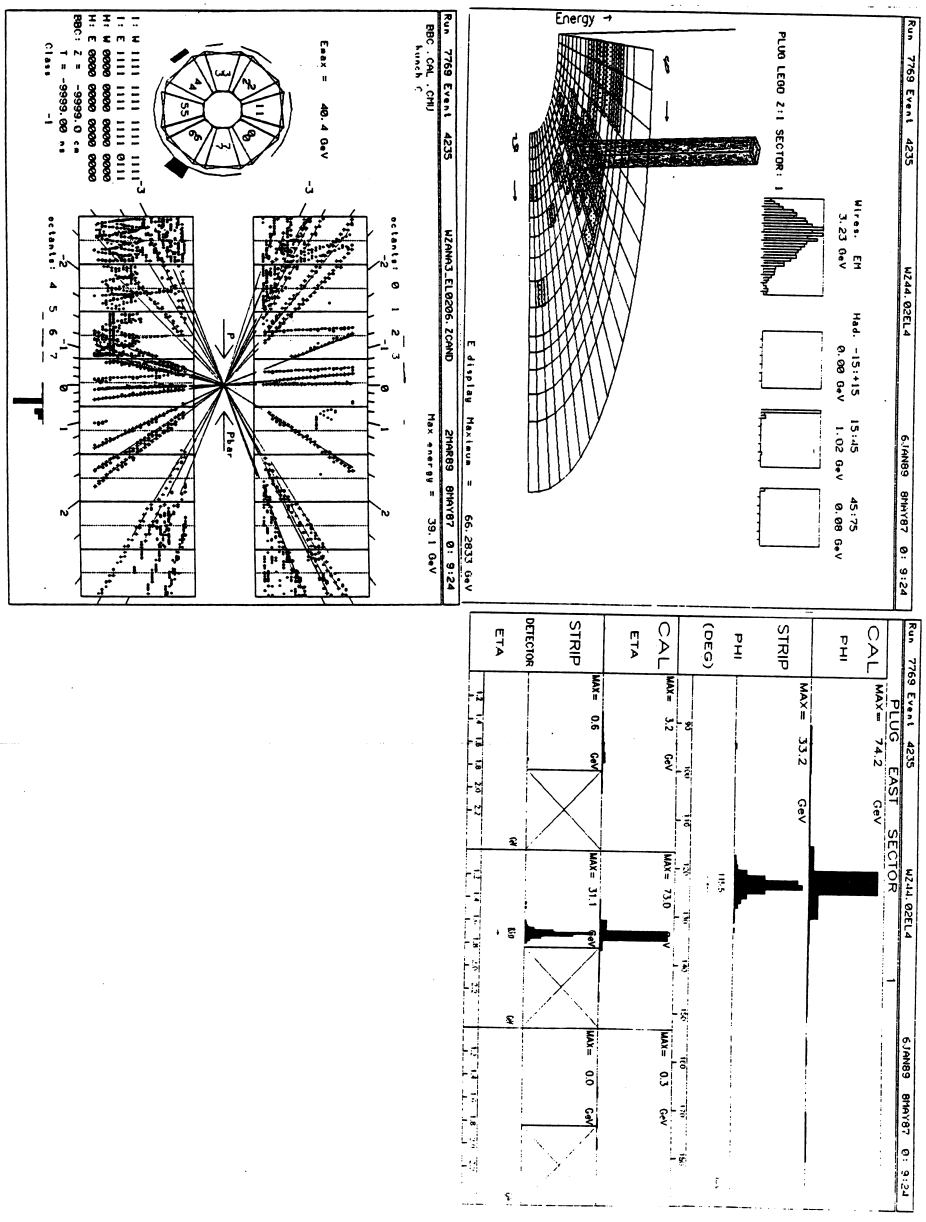

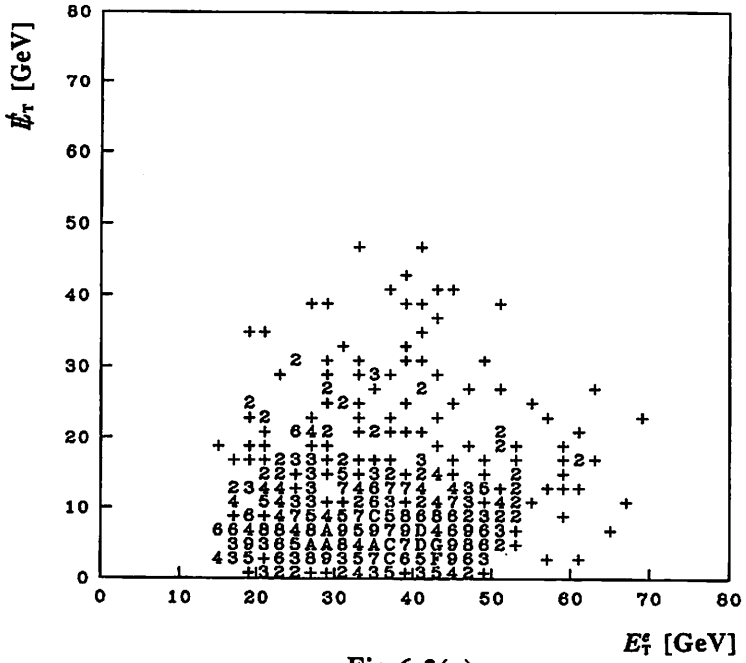

Fig.6-2(a)

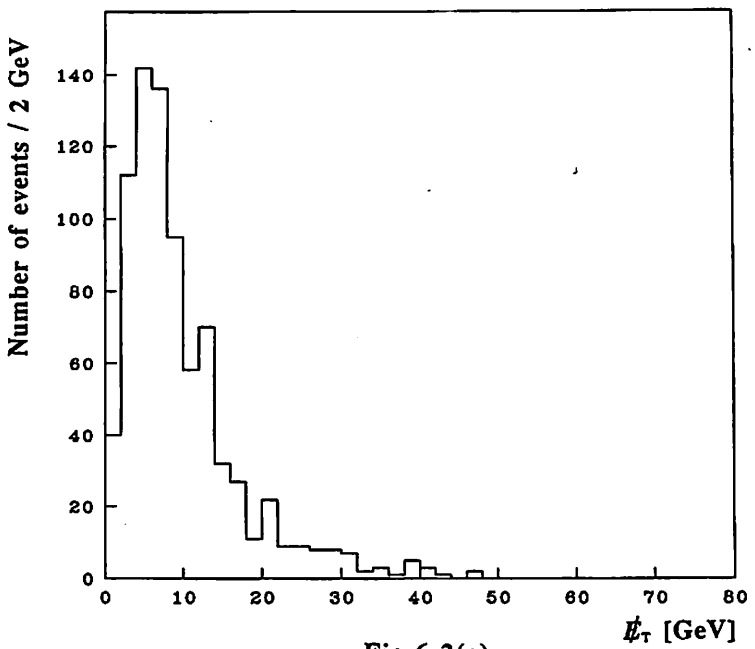

Fig.6-2(c)

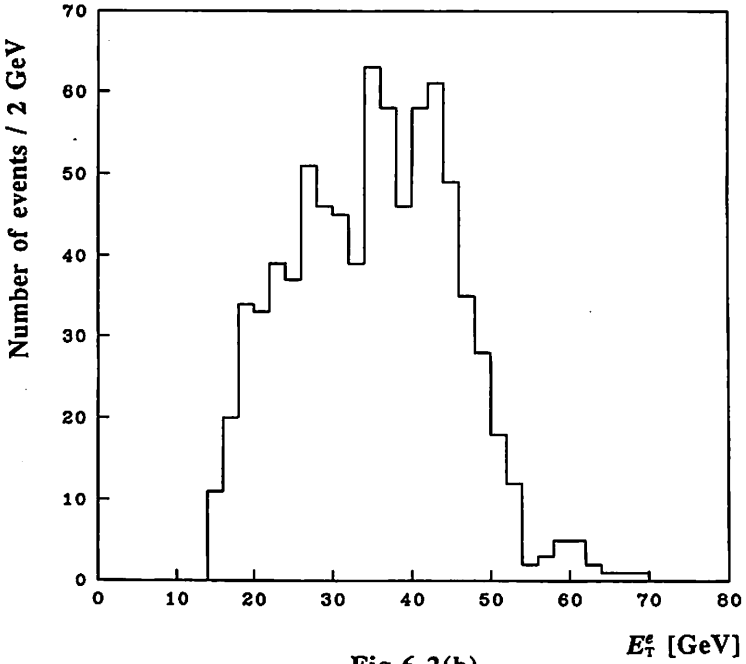

Fig.6-2(b)

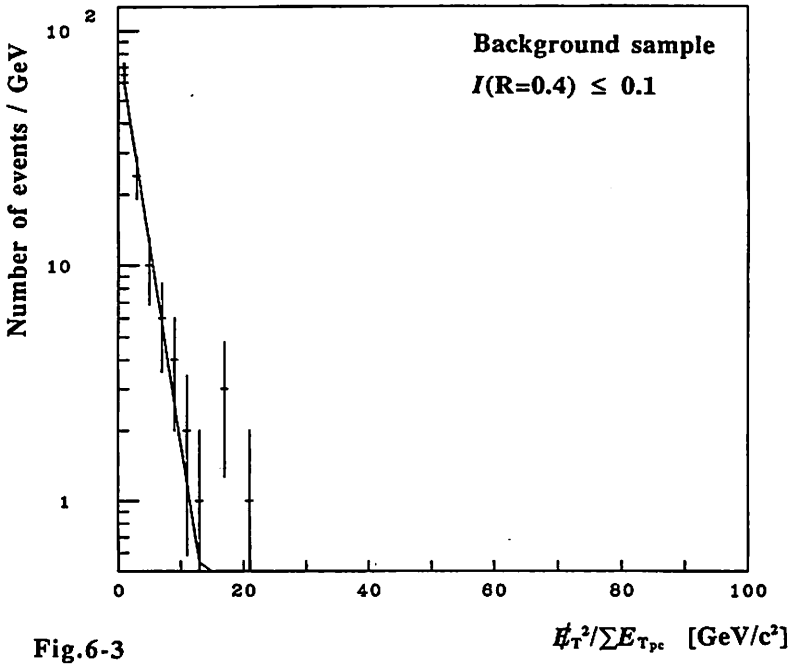

Fig.6-3

Fig.6-4

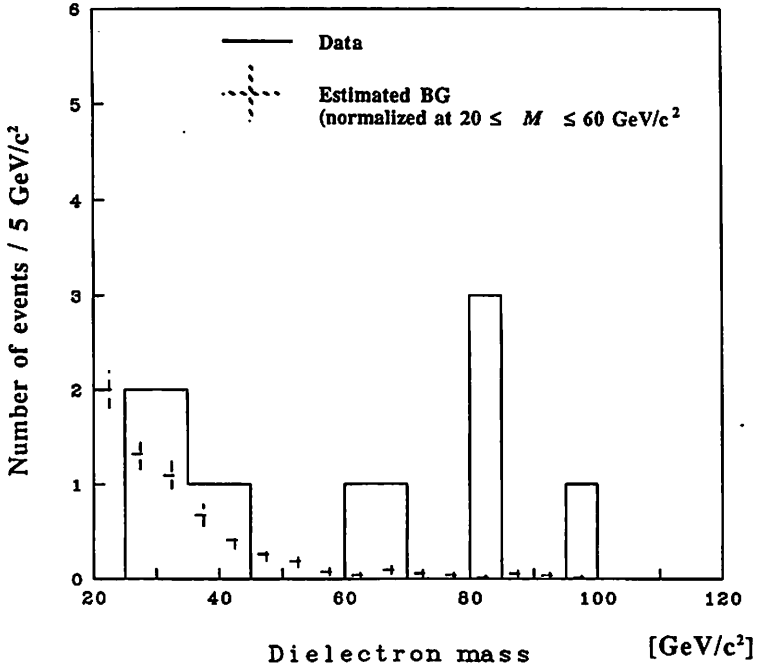

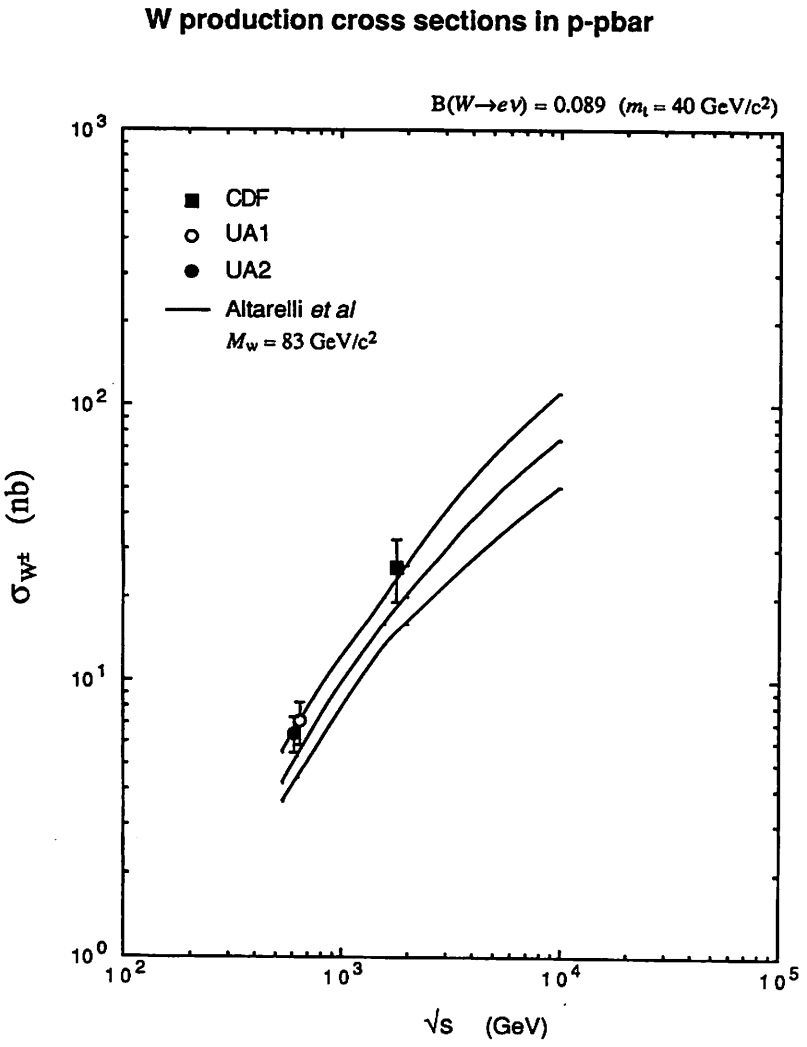

Fig.7-1

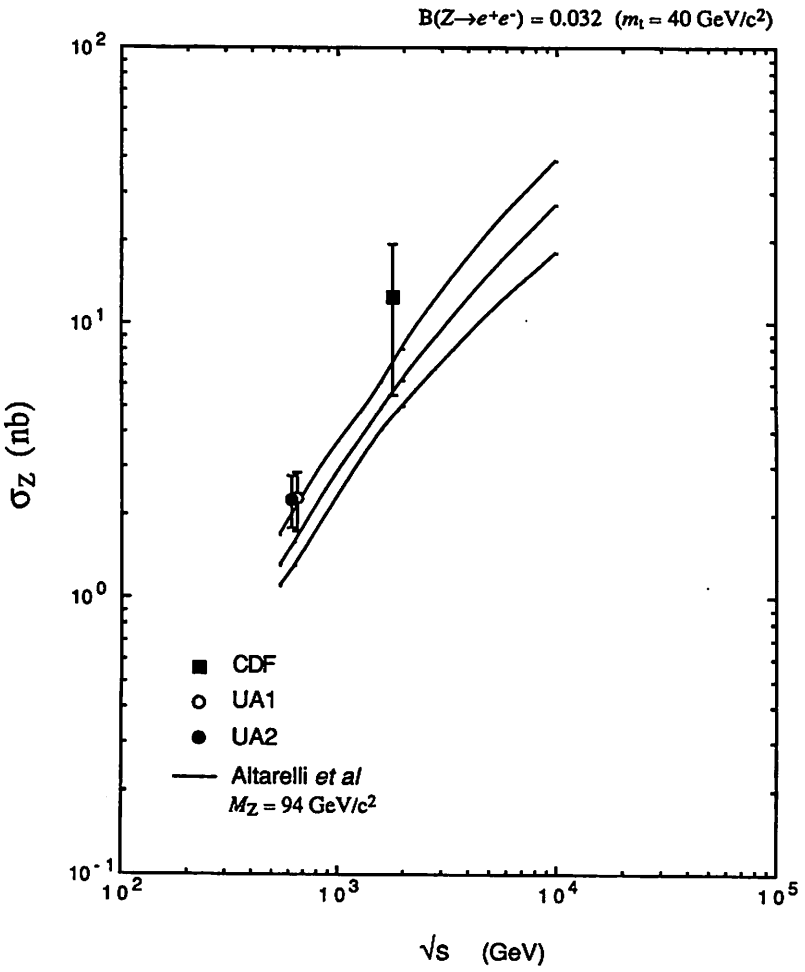

Fig.7-2

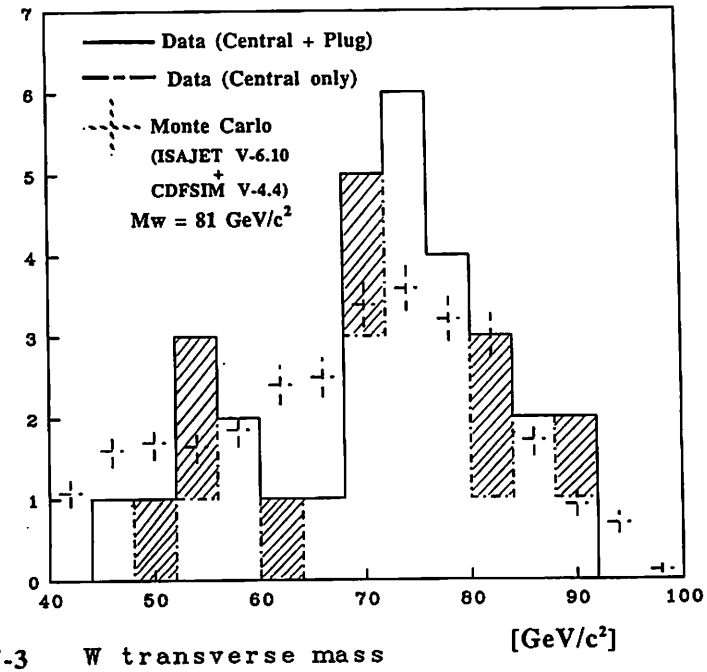

Fig.7-3 W transverse mass

Fig.7-4 χ^2 of the W transverse mass fitting

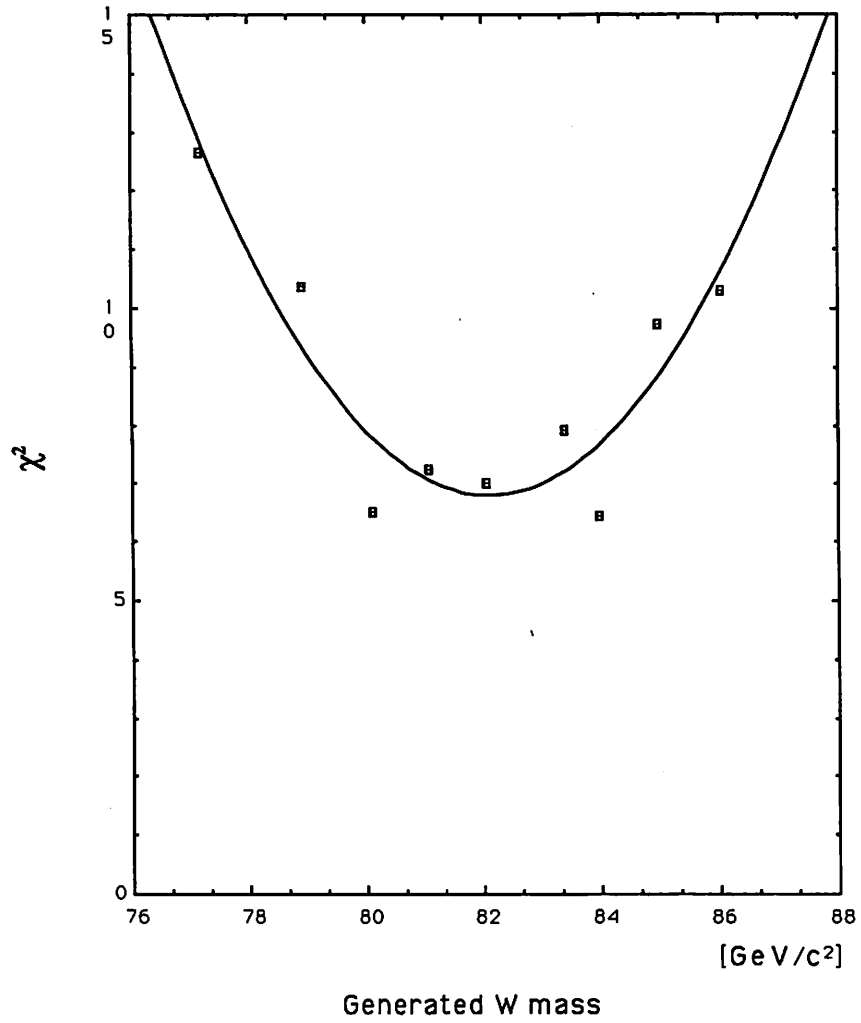

Fig.7-5

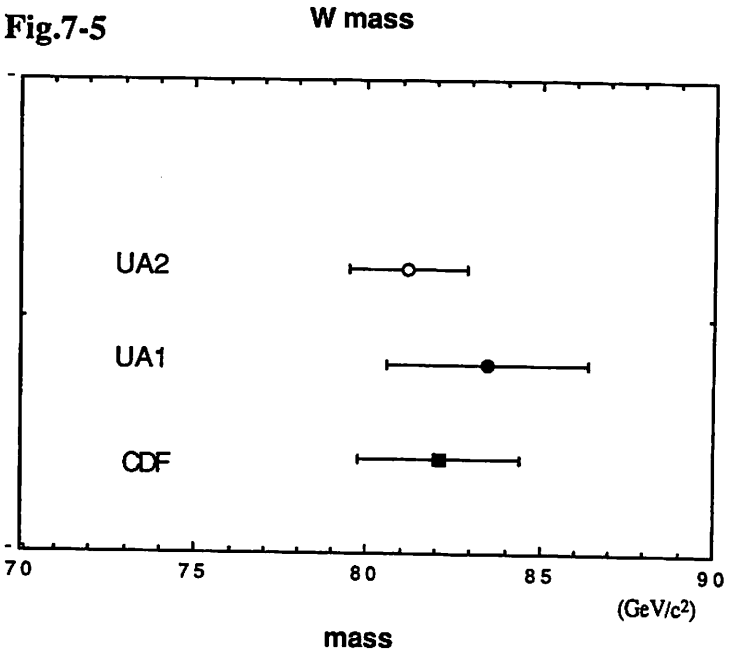

Fig.7-6 Mass of 6 Z candidates

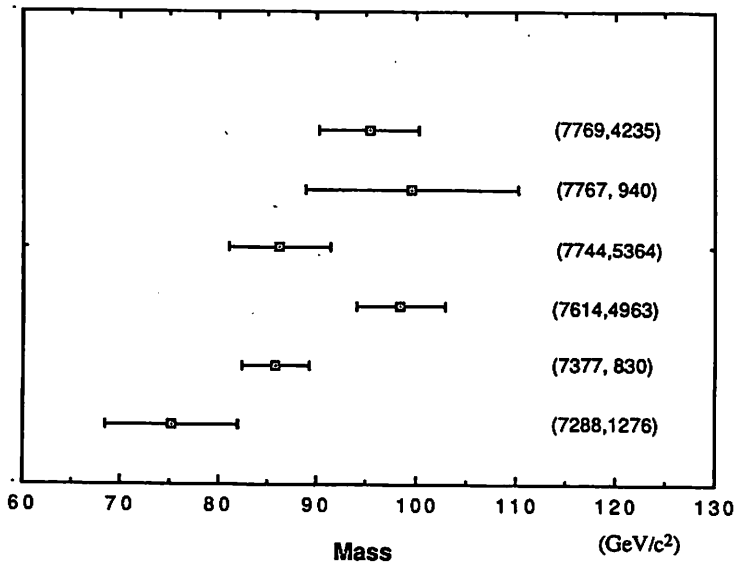

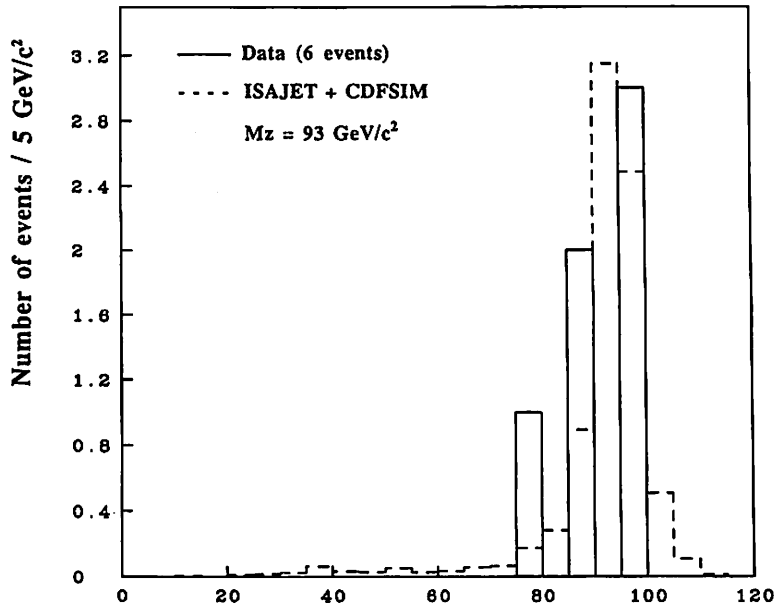

Fig.7-7

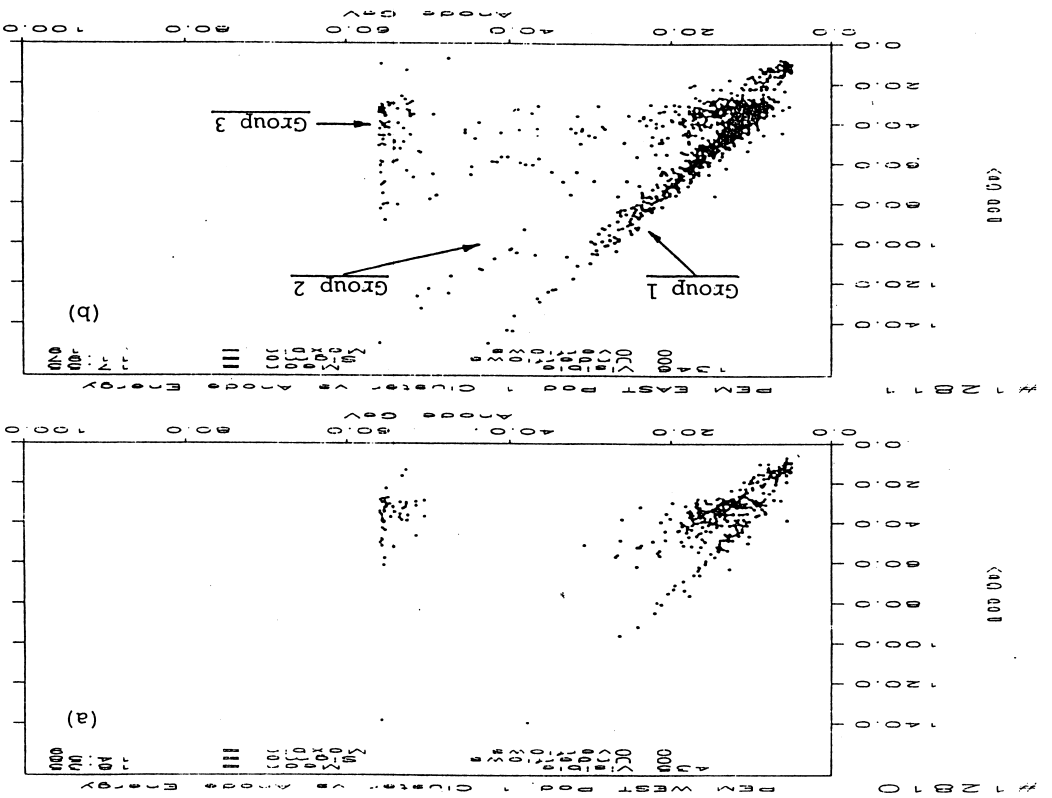
Group 3
Group 2
Group 1
(b)
(a)

Fig.D-2

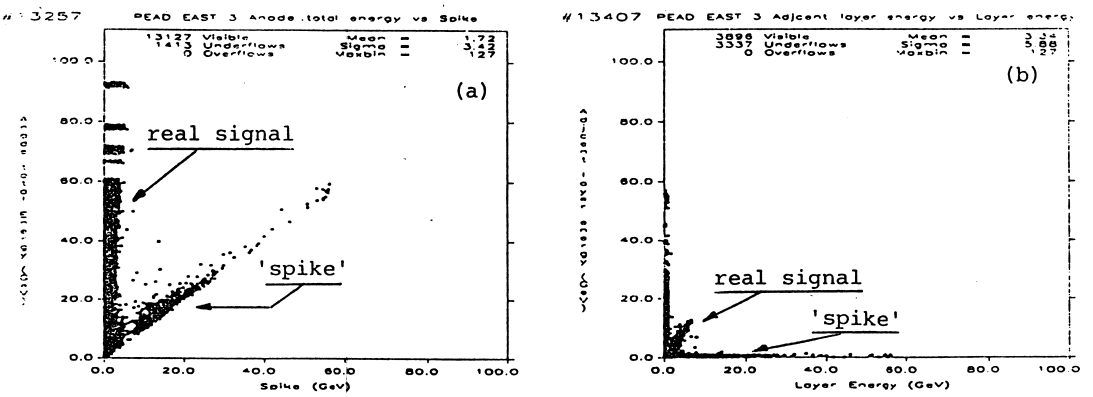
real signal
'spike'
(a)
Spike (GeV)
real signal
'spike'
(b)
Layer Energy (GeV)

Fig.D-1

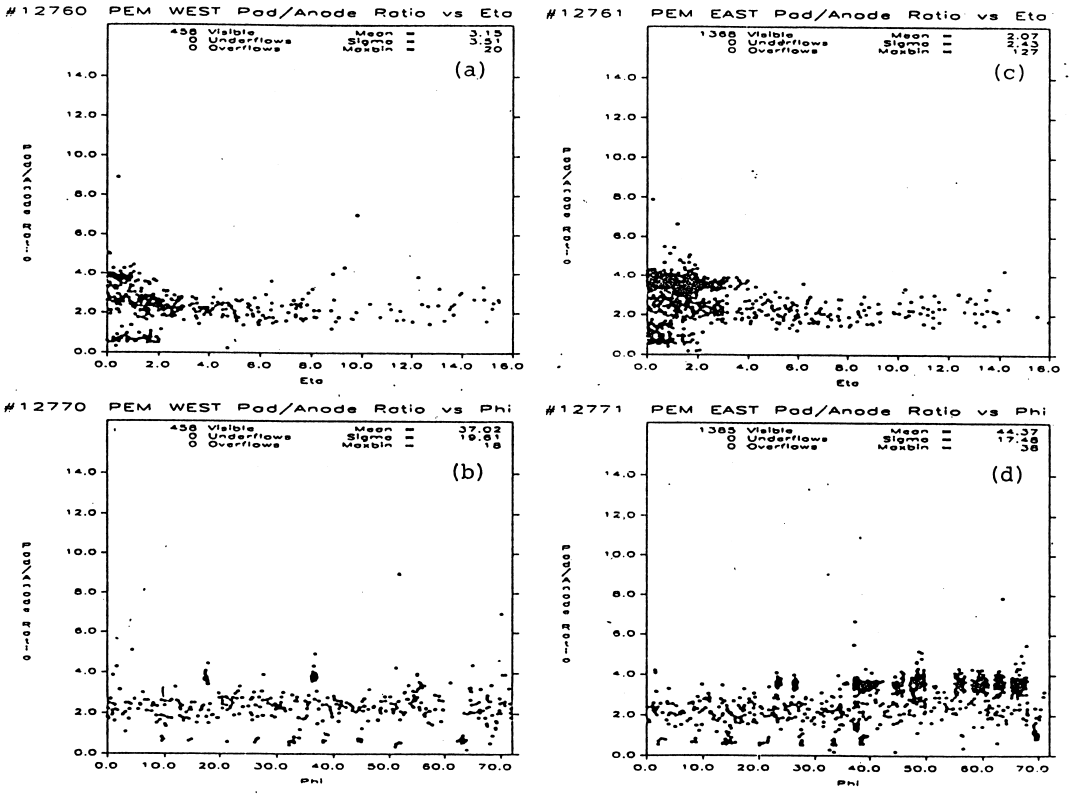
#12760 PEM WEST Pod/Anode Ratio vs Eto
458 Visible
0 Underflows
0 Overflows
Mean = 3.15
Sigma = 3.51
Maxbin = 20
(a)
Eto
#12761 PEM EAST Pod/Anode Ratio vs Eto
1368 Visible
0 Underflows
0 Overflows
Mean = 2.07
Sigma = 2.45
Maxbin = 127
(c)
Eto
#12770 PEM WEST Pod/Anode Ratio vs Phi
458 Visible
0 Underflows
0 Overflows
Mean = 37.02
Sigma = 19.61
Maxbin = 18
(b)
Phi
#12771 PEM EAST Pod/Anode Ratio vs Phi
1383 Visible
0 Underflows
0 Overflows
Mean = 44.37
Sigma = 17.48
Maxbin = 38
(d)
Phi

Fig.D-3